Low Temperature Plasma Etching Control through Ion Energy Angular Distribution and 3-Dimensional Profile Simulation

by

Yiting Zhang

A dissertation submitted in partial fulfillment
of the requirements for the degree of
Doctor of Philosophy
(Electrical Engineering)
in the University of Michigan
2015

Doctoral Committee:

Professor Mark J. Kushner, Chair
Associate Professor John E. Foster
Professor Brian E. Gilchrist
Professor Yogesh B. Gianchandani
Associate Professor Steven C. Shannon, North Carolina State University
Professor Fred L. Terry, Jr

DEDICATION

To my parents, Shuiping Zhang 张水平 and Meijuan Shao 邵梅娟.

"谁言寸草心，

报得三春晖。"

-唐·孟郊《游子吟》

ACKNOWLEDGEMENTS

Table of Contents

List of Figures

List of Appendices

List of Acronyms

2-d	2-dimensional	LIF	Laser Induced Fluoresces
3-d	3-dimensional	*LF*	Low Frequency
AR	Aspect Ratio	LTP	Low Temperature Plasma
ARDE	Aspect Ratio Dependent Etching	MCS	Monte-Carlo Simulation
CCP	Capacitively Coupled Plasma	MCFPM	Monte-Carlo Feature Profile Model
CD	Critical Dimension		
CDR	Critical Dimension Ratio	MEMS	microelectromechanical system
dc	direct current	MOSFET	Metal-oxide-semiconductor field-effect
DF	Dual-frequency		
dLL	digital phase-lock loop	PCMCM	Plasma Chemistry Monte- Carlo Module
eMCS	electron Monte-Carlo Simulation		
EAE	Electrical Asymmetry Effect	PIC	Particle-in-Cell
EED	Electron Energy Distribution	PR	Photoresist
EETM	Electron Energy Transport Module	rf	radio frequency
EMM	Electromagnetic Module	RIE	Reactive Ion Etching
FKPM	Fluid Kinetics-Poisson Module	RFEA	Retarding Field Energy Analyzer
HF	High Frequency		
HPEM	Hybrid Plasma Equipment Model	SEM	Scanning Electron Microscope
ICP	Inductively Coupled Plasma	SOR	Successive over Relaxation
IED	Ion Energy Distribution	TF	Triple-frequency
IEAD	Ion Energy and Angular Distribution	TSV	Through-Silicon-Via
IVD	Ion Velocity Distribution	VLSI	Very Large Scale Integration

ABSTRACT

Plasma etching has become a major part of semiconductor processing because it enables the production of smaller electronics with increased computational power. Plasma etching produces highly anisotropic features, which are needed to maintain feature size critical dimensions (CDs) through directional ion wafer bombardment. As the semiconductor industry moves towards smaller feature sizes and higher aspect ratios, a better understanding of ion dynamics and control of the plasma etching processes becomes increasingly necessary.

Multi-frequency capacitively coupled plasmas were investigated as a mean to provide separate control of ion fluxes and energies. The high frequency (*HF*, tens of MHz to hundreds of MHz) is intended to control the plasma density and ion fluxes, while the low frequency (*LF*, hundreds of kHz to 10 MHz) is intended to control the ion energies. However, recent research has shown that the *LF* can also influence the magnitude of ion fluxes and both frequencies can determine the ion energies. Hence, achieving separate control of fluxes and ion energies is both important and highly complex.

In prior plasma etching technology nodes, 2-dimensional (2-d) feature profile models served very well to help optimize features and connect reactor scale properties to feature scale CDs. As CDs continue to shrink, the current technology nodes must utilize 3-dimensional (3-d) structures, whose optimization is considerably more difficult and not well represented by 2-d profile simulators.

This dissertation investigated the plasma physics and plasma surface interactions in plasma etching chambers using a hybrid plasma equipment model to predict plasma properties and a Monte Carlo feature profile model to predict feature evolution. The computational models are validated with collaborated experimental measurements. Algorithms for capturing ion sheath dynamics, controlling dual frequency powers on the same substrate and describing 3-d plasma surface kinetics have been developed and integrated into the models. With the addition of these new algorithms, three challenging areas have been investigated: ion multi-frequency sheath dynamics, control of ion energy angular distributions and 3-d plasma etching. The ion kinetics is found to be controlled through several critical parameters, such as shifting phases, tuning frequencies, and adjusting rf voltage ratios. The 3-d profile model addresses the complex feature pattern layout and aids in the physical understanding of ion 3-d bombardment on surfaces. With this improved capability, correlations of the variability of plasma tool performance with variability of feature dimensions are investigated.

Chapter 1 INTRODUCTION

1.1   An Introduction to Low Temperature Plasma in Semiconductor Fabrication

Plasma is defined as a quasi-neutral gas of charged and neutral particles that exhibits collective behavior.[1] It is often called the fourth state of matter. As molecules become more energetic, they transform their states: from solid to liquid to gas and finally to plasma. In the plasma state, molecules also dissociate.[2] Plasmas occur naturally on and around the Earth in various forms, such as lightning, the Aurora Borealis and the ionosphere. Plasmas can also be generated by applying external power to breakdown gases, as in neon lights and arc jets. Both natural and manmade plasmas occur over a wide range of pressures, and it is customary to classify them in terms of electron temperatures and densities, as shown in Fig. 1.1.[3] Although the current research on plasmas extends to all operation regions, the low temperature and high plasma density region is the focus of this dissertation, since as the plasma-assisted microelectronic fabrication is performed in this region. Low temperature plasmas (LTPs) [gas temperature 300-500 K, 0.1 mTorr to 10 Torr] are ubiquitous in semiconductor fabrication, especially for plasma surface treatments.[4]

Plasma surface interactions involve positive ions, energetic electrons, neutrals and photons. When a solid surface is bombarded with these particles, the surfaces can be activated. For example, when an energetic ion strikes the surfaces, it can release its energy to the lattice atoms. This kind of bombardment can also affect the chemical reactions occurring at the surface

of the substrate and their rates. Electron and ion bombardment are effective in changing and catalyzing surface chemical reactions when the bombardment energy is sufficient to break chemical bonds. Ion bombardment also promotes the mixing of atoms near the surface, which improves the quality of the thin film deposition.[5]

In addition to its advantage in thin film deposition, ion bombardment can also stimulate the surface etching.[6] This was observed experimentally by Coburn and Winters in 1979, who demonstrated that the etching of silicon by active gases was enhanced by argon ion bombardment, as shown in Fig. 1.2. The etch rate obtained with the simultaneous use of XeF_2 and Ar^+ was eight times higher than the etch rates with the individual gases alone. The XeF_2 dissociative chemisorption rate at the silicon surface was enhanced by the argon ion bombardment.[6] Similar enhancing effects were observed for plasma etching of Si with F_2 or Cl_2 and SiO_2 with F or CF_x.[7,8]

Ion bombardment is much more effective in enhancing surface reactions than electron bombardment. This occurs because of the large momentum of ions. However, the energetic electron can also cause the emission of secondary electrons, enhancing the chemical reactions and inducing dissociation of adsorbed molecules.[9] Moreover, the densities of radicals or atoms which participate in the surface reaction are mainly produced by collision of energetic electrons with molecules. High electron density plasma is usually desired, because it can ensure that large reactant fluxes reach the surfaces, and increase the rate of etching or deposition.

The fabrication of integrated circuits usually requires removing selected areas from wafer substrates. Wet etching and plasma etching are two common choices for this process. Wet etching is inexpensive and fast. However, it can lead to undercutting, which is undesirable because it results in an isotropic etch profile where the vertical and horizontal etch rates are

approximately equal, as shown in Fig. 1.3 a. As semiconductor manufacturers continue to shrink feature sizes, plasma etching becomes an indispensable part of semiconductor fabrication. In plasma etching, the electric field of the sheath region (a layer in plasma where charge neutrality begins to break down with greater density of positive ions that balances the opposite negative charges on the surface.) accelerates ions towards the surface and therefore the etching is anisotropic. That is, it creates a narrow trench and removes material from the bottom only, while leaving the material on the sidewalls unaffected, as shown in Fig. 1.3 b.[10] This directional etching is essential for achieving high resolution pattern transfer (one of the essential wafer fabrication steps).[11]

Overall, plasma processing is essential in the production of semiconductor chips for three main reasons. Firstly, electrons are used as a dissociation source for converting injected gas into atoms at low pressure and temperature. Secondly, the etch rate is enhanced by ion surface bombardment. With ions striking the wafer surface, the bonds in the first few monolayers will be broken, which allows the etchant atoms to react with substrate atoms to form volatile chemical products. Lastly, the plasma etching is anisotropic, allowing the creation of features at nanometer dimensions. This is also the most important advantage of plasma etching, when compared with the traditional wet etching.

1.2   Plasma Sources

As low temperature high density plasma does not occur naturally, it must be produced manually with vacuum and ionization systems. Plasma forms from when power is supplied to a gas mixture. The technique involves coupling of electrostatic or electromagnetic energy into the gas. In plasma processing semiconductor fabrication, the two main types of plasma reactors with

rf sources are used: Capacitively Coupled Plasmas or CCPs and Inductively Coupled Plasmas (ICPs), as illustrated in Fig. 1.4.

Capacitively coupled plasma reactors are the most commonly used approach in the design of industrial rf plasma reactors for dielectric etching. These systems couple the rf power to two parallel electrodes inserted inside the reactor. The rf power coupling to parallel electrodes usually produces uniform electric fields, and the discharge is mainly confined to the space between the electrodes as illustrated in Fig. 1.4 a. With this kind of configuration, high process uniformity over large areas is determined by the size of the electrodes. Ions in the bulk plasma can be accelerated by sheath potential to high energies, because they flow to the substrate, leading to energetic ion enhanced processing. However, CCP reactors with a single rf power supply also have a crucial limiting feature: the ion-bombarding flux and energy cannot be independently varied, which limits the process optimization window.[12] Consequently, CCP reactors with multiple rf power supplies have been used in industry since Goto *et al.* first introduced the dual frequency setup in the early 1990s.[13] With the addition of a low frequency (*LF*) source, the ion energy can be modified with a limited degree of independence Thus wafer damage due to high energy ion impingement can be partially eliminated.

In multi-frequency CCPs with complicated sheath dynamics, independent control could be obtained from the frequency scaling law: the ohmic heating scales with frequency, electron temperate and rf voltage as: $\bar{S}_{heating} \propto \omega^2 T_e^{1/2} V_{rf}$.[14] Thus, the high frequency (*HF*) source produces a much higher density than the *LF* source and controls the production of ions and radicals. On the other hand, the ion energy is controlled by the total rf voltage across the sheath. Hence, the *LF* with large voltage amplitude is intended to control the shape of the ion energy angular distribution (IEAD). The incensement in the *LF* voltage enlarges the sheath potential and

thus accelerates ions to high energy. For a wide separation of frequencies, both conditions can be met simultaneously and flexible independent control of flux and IEADs can be achieved.[14] Typically, the *LF* is in the range from hundreds of kHz to 10 MHz, the *HF* is in the range from tens of MHz to as much as 100-200 MHz under operational pressure range from tens of mTorr to hundreds of mTorr. Since a plasma has a nonlinear impedance, decoupling the mutual influence of the two frequencies often requires that the separation in frequency be at least tens of MHz.[15] Even with significant separation, recent studies have shown mutual interactions between the frequencies – that is, the IEADs are not unique functions of *LF* and the plasma density is not a unique function of *HF*. [16,17]

The increasing demands of high density etching systems have motivated the development of ICPs.[18] The antenna in an ICP is supplied by electric currents that produce time-varying magnetic fields. The electromagnetic fields are typically generated by external rf antennas, which have planer or cylinder coil configurations. An ICP with cylinder coil configuration is shown in Fig. 1.4 b. With these kinds of antenna placement, the time-varying magnetic field produces an electric filed in azimuthal direction, E_θ, which accelerates the electrons. The acceleration paths of the electrons in ICPs are circular and electrons can keep accelerating in one direction during a half cycle until collisions occur. In contrast, the electrons in CCPs are accelerated between the electrodes and a certain amount of them are lost to the electrodes. Unlike CCPs, therefore, ICPs are capable of producing high density ($> 10^{11}$ to 10^{12} cm^{-3}) plasmas at low pressure over large area wafers.[19] With high density plasmas, large radical and ion fluxes will bombard the wafer and induce a higher etch or deposition rate for semiconductor etching and deposition. Since the process rates depend not only on the fluxes on the wafer, but also on their energies, ICPs typically have additional rf/ dc biases applied on the electrodes to

accelerate ion incident energies. This configuration modulates the sheath potential and brings about independent control of ion energy distributions (IEDs).

Although both CCPs and ICPs have been industrial standards for many years, alternate reactor configurations are concurrently being investigated to meet critical dimension shrinking requirements implied by Moore's Law.[20] The goals of these efforts are to obtain more anisotropic etching and more control over etching profiles with higher degrees of uniformity over large areas. These results can be obtained through the modifications to the rf power supplies such as, multi-frequency biases on the substrate, pulsing, and phase shifting.[21,22] In these rf control approaches to chamber design, understanding rf coupling and ion sheath dynamic becomes essential. The challenges and recent studies in the control and customization of IEDs are reviewed in the next section.

1.3   Control and Customization of Ion Energy Distributions

The use of low pressure plasmas in microelectronics fabrication is essential to maintaining critical dimensions (CDs) through anisotropic etching and conformal deposition. In this regard, controlling the IEADs on the wafer is an important consideration for tuning CDs and optimizing material selectivity.[23,24]

One well-known critical parameter determining the shape of the IEDs is $\tau_{ion}/\tau_{rf,}$, where τ_{ion} is the transit time through the sheath and τ_{rf} is the rf period. Since the 1980s, following Metze *et al.,*[25] researchers have been predicting ion energy distributions by dividing the driving rf frequency into different regimes. Kawamura *et al.* [23] analyzed IEDs in a collisionless rf sheath in different frequency regimes. Because the sheath potential is the potential drop between the plasma and the biased electrode, it is time dependent with the instantaneous rf voltage on the electrode. They found that in the *LF* regime ($\tau_{ion}/\tau_{rf} \ll 1$), the

ions respond to the instantaneous electric field, and they reach the substrate with an energy nearly equal to the instantaneous sheath potential when they entered the sheath. Averaging over the rf period, the IED is broad and bimodal exhibiting a low energy, E_1, and high energy, E_2, peak. The separation between peaks, $\Delta E = E_2 - E_1$, approaches the maximum sheath potential during the rf period as shown in Fig. 1.5 a and b. In the *HF* regime ($\tau_{ion}/\tau_{rf} \gg 1$), the ions take many rf cycles to cross the sheath and they strike the wafer with the average sheath potential. The phases of the rf cycle at which they enter the sheath and the instantaneous sheath voltage at that instant are not particularly important for determining the shape of the IEDs. Starting at *LF*, with increasing τ_{ion}/τ_{rf}, ΔE shrinks until the two peaks cannot be resolved. Further experiments have confirmed the theoretical prediction that the ΔE is centered at the average sheath potential and it depends on the ion mass ($\Delta E \sim m_{ion}^{-1/2}$) as shown in Fig. 1.5 c and d.[23,32]

In the intermediate frequency regime ($\tau_{ion}/\tau_{rf} \approx 1$), inertia results in the ions partially responding to the time variation of the sheath potential, and thus obtaining analytic representations of the IEDs becomes difficult. A kinetic approach based on some form of Monte Carlo or particle-in-cell simulations is typically used to obtain IEDs in this intermediate regime, particularly in the dual-frequency CCPs.[26]

In order to better understand the dual-frequency (DF) CCPs, several recent studies have focused on ion dynamics in the sheath and ion energy distributions to the substrate.[27-30] Lee *et al*. used particle-in-cell Monte Carlo simulations to study the control of IEDs in asymmetric single (27 MHz) and double frequency (*LF*=2 MHz, *HF* varied from 27.12 to 189 MHz) CCPs sustained in Ar. They investigated the influence of rf voltage and frequencies for various neutral gas pressures and electrode gap distances. They showed a manner that the IEDs can be controlled through bias frequencies. For their conditions, an increase in the *LF* voltage produced

a decrease in plasma density, while the sheath width, the plasma potential, and the dc self-bias increased.[31]

In their investigation of DF-CCPs, Liu *et al.* measured IEDs of Ar^+ and O_2^+ on the wafer for varying discharge parameters in an $Ar/O_2 = 90/10$ mixture.[32] They found that the IEDs are primarily influenced by the frequency and power of the *LF*. When the *LF* power increases, more power will be preferentially dissipated in the sheath, producing a broader IED extending to higher energies. However, an increase in *LF* frequency increases the ratio of ion transit time through the sheath to the rf period, and this results in a decrease in the energy width of the IED. They also measured the electron density and IEDs in low pressure CCPs sustained in Ar/CF_4 and $Ar/O_2/CF_4$ mixtures.[33] They observed that the electron density linearly increased with increasing *HF* power and gradually decreased with increasing *LF* power. The addition of CF_4 plays an important role in determining the electron density at different pressures. They found that the *HF* power does affect the IEDs when the amplitude of the voltage of the *LF* and *HF* are comparable.

Booth *et al.* investigated DF-CCPs by measuring electron density and ion flux in Ar/O_2 (195/28 sccm) and $Ar/C_4F_8/O_2$ (160/16/8 sccm) mixtures at 50 mTorr while controlling power at both frequencies.[16] In Ar/O_2 mixtures, the electron density and ion flux increased nearly linearly with 27 MHz power and sub-linearly with 2 MHz power. For example, electron density increased by about a factor of 2 for a factor of 7 increase in 2 MHz power. The 2 MHz power was found to contribute to plasma heating and increased ionization by secondary electron emission. While keeping the 2 MHz power constant, the *LF* voltage decreased with increasing *HF* power as the ion current increased. Similar trends were observed in the $Ar/C_4F_8/O_2$ mixtures.

8

Although the frequencies of the *LF* and *HF* in DF-CCPs are usually selected with sufficient separation to avoid interference effects, Gans *et al*. observed frequency coupling with quite disparate frequencies.[17] With the lower electrode in a parallel plate CCP sustained in 490 mTorr of He/O$_2$ powered at 2 MHz and 27.12 MHz, they found that both frequencies influenced the ionization dynamics as shown in Fig. 1.6. Their results showed that the *LF* contributed to control of the plasma density, indicating that separate control of plasma density and ion energy remains challenging for DF-CCPs.

1.4   Modeling of Low Temperature Plasma

Modeling of low temperature plasma is increasingly viewed as a scientific tool to improve our understanding of the underlying fundamentals of physics and provide information often difficult to obtain from experiments.[34,35] Different platforms have been developed over the past several decades, and they have shown advantages as computer-aided design methods for the improving performance of plasma processes and equipment. [36-45]

Low temperature plasma modeling usually involves the solution of particle kinetics, radiation transport, Maxwell equations (Poisson's equation for the electrostatic simulation) and large numbers of plasma gas and surface reactions. Fluid, particle, and hybrid models are widely used as numerical techniques for simulating LTP properties in reactors. Fluid models calculate plasma density, mean velocity and mean energy of the constituent species by solving the continuity, the flux and the energy equation for each species in the plasma. In order to obtain self-consistent electromagnetic fields, Maxwell or Poisson's equations are also calculated in addition to solving the velocity moments of the Boltzmann equation.[36-38] Fluid models have the advantage of fast computational speed when the species number is large and plasma chemistries are complicated with numerous reactions. [35]

Particle models, or kinetic models, use interacting particles to represent physical phenomena.[39] The particle models (often called particle-in-cell, PIC) became a popular method for plasma simulation in the late 1950s and are still extensively used.[40-42] A comparison results from PIC and fluid models is shown in Fig. 1.7. Nitschke and Grave reported relatively good agreement between two models at pressures above 10 mTorr. Their PIC simulations accounts for heating occurring from the individual interactions between electron and sheath edge by including an analytic sheath heating expression in the electron energy balance equation. This predicted sheath heating is the main difference between their PIC and fluid models at low pressures.[43] In PIC models, one numerical particle typically represents 10^{5-7} real particles and the trajectories of the particles are obtained by solving the Newton- Lorentz equation for the motion of electrons and ions coupled with self-consistent calculation of electromagnetic fields. Kinetic models simulate particle collisions, and statistical processes in detail, and therefore have an advantage of kinetic fidelity. However, particle models typically require a longer computational time than fluid models for resolving several thousands of rf cycles to obtain meaningful results from a steady state. Because a large number of particles is needed to simulate each species, particle simulations are not preferred for simulating complex plasma chemistry.[35]

Hybrid models are a combination of the fluid and kinetic models. By combining the fast speed of fluid models with the accuracy of particle models, the hybrid models are able to run faster than particle models and describe non-local kinetics more precisely than fluid models.[44] The design of a hybrid model typically depends on the particular physics to be modelled. For example, Sommerer and Kushner[45] modeled ions as fluid and electrons in a Monte Carlo scheme for their investigation of the kinetics and chemistry of He, N_2, O_2, He/N_2/O_2, He/CF_4/O_2

and SiH_4/NH_3 in a CCP reactor. Alternatively, the hybrid model from Wang *et al.*[46] contains a fluid model to simulate the bulk plasma region and a Monte Carlo model to describe the physics of the electron, ions, and fast neutrals in the sheath region. The main challenge of implementing hybrid models is that the time step for transferring coefficients between the fluid and the particle parts needs to be properly chosen. Overall, the flexibility of mixing fluid and particle models allows hybrid models to deal with a wide range of physical phenomena.

Modeling of surface profile evolution in plasma processing is another complex undertaking, because it involves numerous plasma surface reactions. Due to their differencing in time and spatial scales, feature profile simulation is typically separated from reactor scale modeling. Cell-based Monte Carlo method is one of the most commonly-used technologies for tracking topological evolutions for arbitrary geometries.[47] By assigning each cell a material identity and launching pseudo-particles according to fluxes obtained from a reactor scale model, cell-based models allow the incorporation of complete reaction schemes based on the surface composition. Compared with other profile simulation methods, cell-based models have the advantage of straightforward implementation and are capable of handling simultaneous composition-dependent etching and deposition as features evolve. However, this kind of model also has challenges in determining surface curvature and normal direction and usually involves a tradeoff between fast computational speed and precise particle reflection and sputtering directions.[48]

Osano and Ono[49] applied a fast four-point check method for surface advancement. They only checked the nearby four cells and calculated the normal direction when a particle hit a cell. With this method, the computational speed was fast while the reflection angle resolution was rough. Kawai[50] recorded boundary-cells within a 3-cell range of the hit cell and fitted

their positons into a polynomial curvature as shown in Fig. 1.8. With this curvature, the model was sensitive to particle injection velocity and position. However, this method largely increased CPU resources and might over-estimate statistical surface roughness. Least square fit method, a lower order method than the polynomial fit method, is the mostly used method of determining surface normal. It also searches boundary-cells, but fits with a linear line which saves computational time.

Although current computational models are capable of addressing many physics phenomena, there are improvements needed to be incorporated into models, such as spatial- and phase- resolved ion sheath dynamics and distinguishing harmonic currents with non-sinusoidal rf waveform in reactor scale models. As for profile simulation, current feature sizes of 14 nm also bring new challenges. With processes for smaller critical dimensions with 3-dimensional (3-d) features being developed, a profile simulator that can address 3-d structures is desirable to speed new process development.[47,51] Non-planer double-gate MOSFETs (FinFETs, as shown in Fig. 1.9) have provided an innovative strategy for shrinking of the CD.[52] However, the fabrication of vertical Si fins has brought its own set of challenges using conventional plasma etching techniques. While 2-dimensional (2-d) simulators have facilitated the understanding of plasma surface interactions and profile evolution to date, these simulators are challenged to represent the 3-d topography of modern structures, and capture defects such as re-deposition from sputtering, line-edge-roughening and clearing of corners.[53] To address these more complex 3-d profile evolution, extending current 2-d profile simulation into 3-d is highly desired.

1.5   Plasma Experimental Diagnostics

Modeling investigations are commonly performed in collaboration with experiments. By collaborating with experimental expertise, both modelers and experimentalists can validate their

methodologies and understand complex physics which cannot be explained by computational or experimental methods alone. This part of the introduction only focuses on the experimental diagnostic techniques used by collaborators in this dissertation.

Of all plasma diagnostics, the Langmuir probe is the most commonly-used method to measure electron density, electron temperature and plasma potential by analysis of the I-V characteristic of the Debye sheath.[54] Probes come with one or multiple electrodes and a wide range of designs and shapes. The single probe is the simplest configuration. Unfortunately, it has a drawback which is difficult to overcome when the reference electrode is ill defined. When the probe is close to the space potential, the probe area may not be small enough for validating the orbital motion limited theory.[55] Therefore, single probes may disturb the discharge condition by drawing large electronic current. Although adding extra electrodes complicates the system, double probes can reduce perturbation and provide accurate data in a wide range of discharge conditions.[56] Since neither electrode is ever far above the floating potential, the theoretical uncertainties caused by large electron currents can be avoided. In a double probe system, there is no reference to the vessel, so the disturbance of probe insertion in rf plasmas can be reduced.[57] In this dissertation, double probe systems were used to measure ion saturation current in single- and dual-frequency CCPs by collaborators in Chapter 5. A referenced single probe was used to measure electron density in Chapter 6.

Inserting Langmuir probes into the plasma sheath region will generate an extra shielding region and perturb ion sheath dynamics. Therefore, probe measurements are not suitable for sheath characterization; a non-invasive diagnostic method is needed for measuring ion properties in the sheath. Laser-induced-fluorescence (LIF) is a powerful non-invasive diagnostic technique that is capable of measuring ion densities, velocities and energy distributions in both rf and dc

sheaths.[58] In LIF, a neutral or ion species in a particular electronic state is excited via lasers. The fluorescence that results from the decay of the excited state can be detected with photomultiplier tubes or CCD cameras. A schematic of LIF measurement of z direction ion velocities in an ICP chamber is shown in Fig. 1.10. The strength of the fluorescence photon signal is proportional to the initial state density before laser excitation. By calculating the Doppler shift between the frequencies of the incident photon of reference of the metastable atom in states transition, relative velocity of the atom with respect to the direction of the laser beam can be detected with the formula: [59]

$$\Delta\lambda = \lambda_0 - \lambda_L = v_{//}\lambda_0 / c, \tag{1.1}$$

where $\lambda_0 = c / v_0$ the rest ion resonance wavelength, λ_L is the laser wavelength, $v_{//}$ is the ion velocity parallel to the laser propagation direction and c is the speed of light.

Due to the shadowing effect of the surface, the LIF is unable to measure ion velocities very close to the substrate where atom density is low. The fluorescence signal is weak and signal to noise ratio is high. In order to obtain IEDs on the substrate, the Retarding Field Energy Analyzer (RFEA) was invented in the 1960s and has been applied extensively.[60-62] A REFA consists of a series of (concentric) grids. The grids can be planer or hemisphere. The first grid is usually grounded and lower grids are biased to certain voltages to filter ions at a certain energy level as illustrated in Fig. 1.11 a. The RFEA is normally placed on the electrode with a small aperture, which allows a sample of the ions to pass through for analysis. By collecting ion fluxes and measuring ion currents passing through the grids, the IED can be achieved as a function of the grid potential. An example of IED measurement with the RFEA placed on a 2 MHz biased electrode is shown in Fig. 1.11 b.[63]

1.6   Summary

Low temperature plasmas are extensively used and irreplaceable for semiconductor wafer fabrication. However, since the critical dimension continues to shrink, there are increasing demands on flexible controlling of IEDs, understanding multi-frequency sheath dynamics and 3-dimensional profile simulation. With the assistance of collaborating experiments, this thesis addresses these needs through computational investigations. The organization of this thesis is as follows: the algorithms developed in this work are incorporated in the following two chapters. In Chapter 2, the Hybrid Plasma Equipment Model (HPEM), used for simulating plasma properties in etching reactors, is discussed in detail with an emphasis on the modification made for Plasma Chemistry Monte Carlo and power control algorithm with harmonic currents. The profile scale model- Monte Carlo Feature Profile Model (MCFPM) is summarized in Chapter 3. The model addresses reaction mechanisms resulting in etching, sputtering, mixing and deposition on the surface to predict 2-d and 3-d profile evolution based on fluxes of radicals, ions and photons provided by an equipment scale simulators, such as HPEM.

In Chapter 4, results from a two-dimensional computational investigation of Ar/O_2 plasma properties in an industrial reactor are discussed. The IEADs are tracked as a function of height above the substrate and phase within the rf cycles from the bulk plasma to the presheath and through the sheath with the goal of providing insights to this complexity. Comparison is made to LIF experiments. The rf voltages and driving frequency are critical parameters in determining the shape of the IEADs, both during the transit of the ion through the sheath and when ions are incident onto the substrate. To the degree that contributions from the *HF* can modify plasma density, sheath potential and sheath thickness, this may provide additional control for the IEADs.

Chapter 5 includes a computational investigation of customizing and controlling IEADs in a DF-CCP resembling those industrially employed with both biases applied to the substrate holding the wafer. The ratio of the low-frequency to high-frequency power is found to control the plasma density, provide extra control for the angular width and energy of the IEADs, and to optimize etch profiles. If the phases between the low frequency and its higher harmonics are changed, the sheath dynamics are modulated, which in turn produces modulation in the ion energy distribution. With these trends, continuously varying the phases between the dual-frequencies can smooth the high frequency modulation in the time averaged IEADs. For validation, results from the simulation are compared with Langmuir probe measurements of ion saturation current densities in a DF-CCP.

In Chapter 6, the computational and experimental investigations of IED control in dual-frequency and triple-frequency (TF-) CCPs where the phase between the frequencies is used as a control variable are performed and discussed. The operating conditions were 5 - 40 mTorr in Ar and Ar/CF_4/O_2 gas mixtures. By changing the phase between the applied rf frequency and its second harmonic, the electrical asymmetry effects (EAE) was significant. When changing phases of higher harmonics, IEDs was maximized at controllable energies. With the addition of a 3rd high frequency rf source, the plasma density increased with better uniformity. By adjusting the phases and powers, IEDs can be customized over a large range of energy and with different shapes. Computed results for IEDs were compared with rf phase locked harmonic experimental results measured using an ion energy analyzer.

Chapter 7 addresses evolving CD control issues. The current technology nodes utilize 3-d structures such as FinFETs and Tri-Gate transistors, whose optimization is considerably more difficult and not well represented by 2-d profile simulators. For example, etching of 3-d

structures typically require longer over-etch to clear corners, which then places additional challenges on selectivity to maintain CD. Prior CD control techniques are evolving to address these issues. Results from the model will be used to compare etching of 2-d and 3-d structures. Ar/Cl_2 and $Ar/CF_4/O_2$ plasmas are used for Si and SiO_2 etching in representative 2-d and 3-d feature topographies relevant to etch applications in advanced technology nodes.

In Chapter 8, an overview of the research discussed in previous chapters is given with general conclusions. The chapter also contains suggestions of possible future work that could be performed.
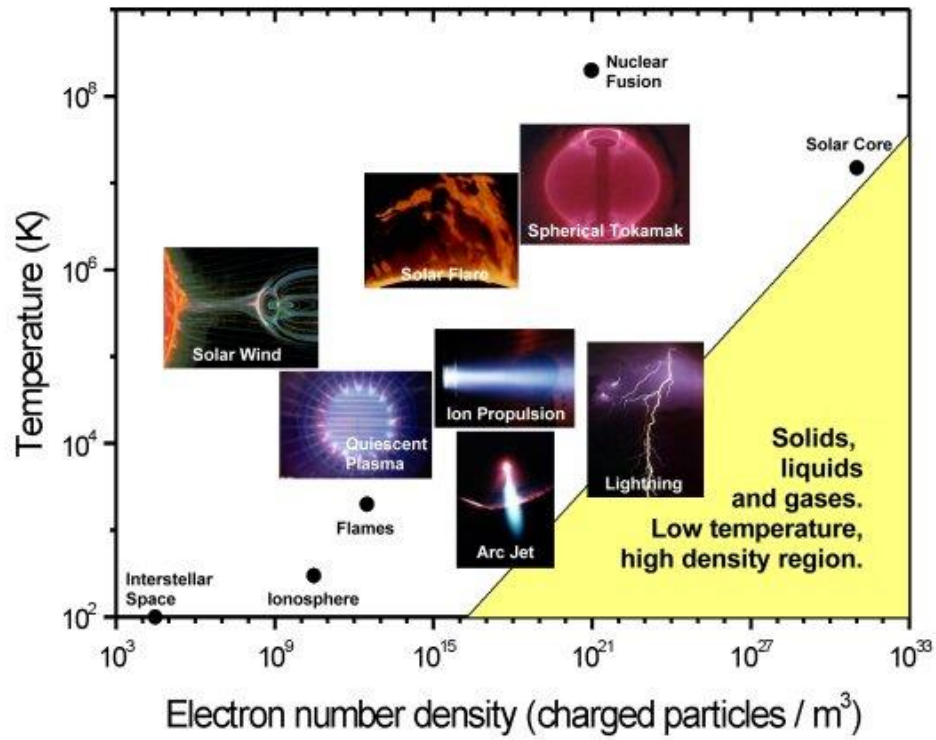
Fig. 1.1. Electron temperature and density of natural and manmade plasma.[3]
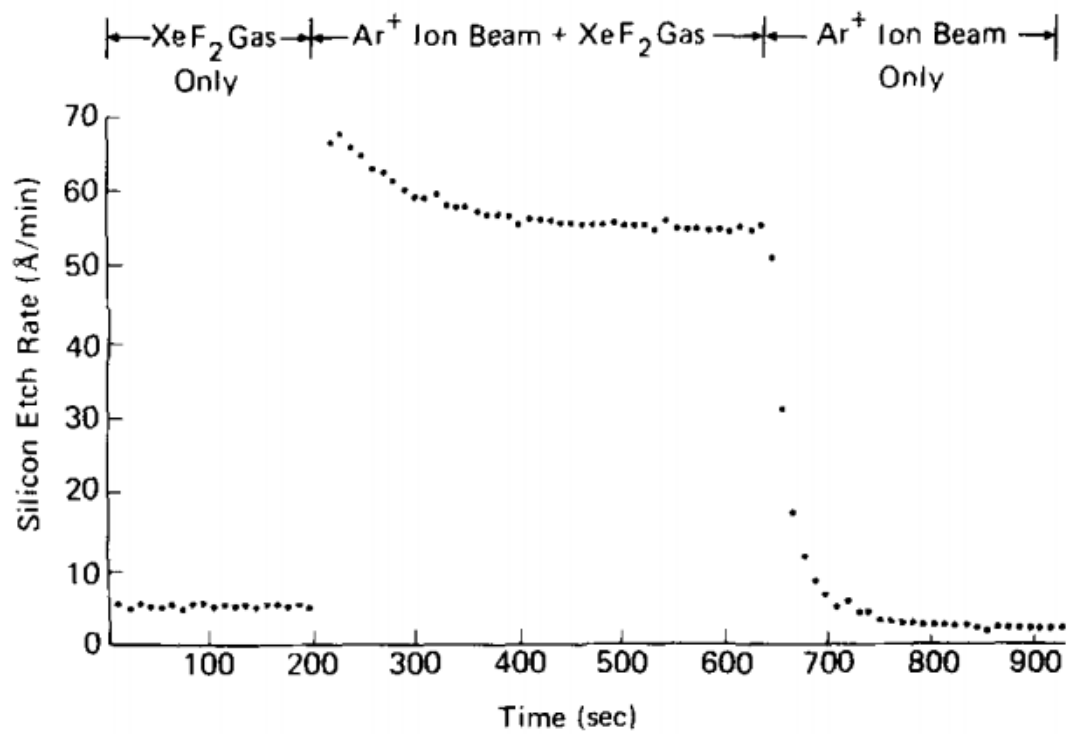
Fig. 1.2. Ion-assisted gas-surface chemistry using Ar^+ +XeF_2 on silicon. [6]

Desired Pattern

W

D

W<D
Impossible

Wet Etch (etch rate isotropic)

Dry Etch (etch rate anisotropic)

radicals

E-field
in sheath
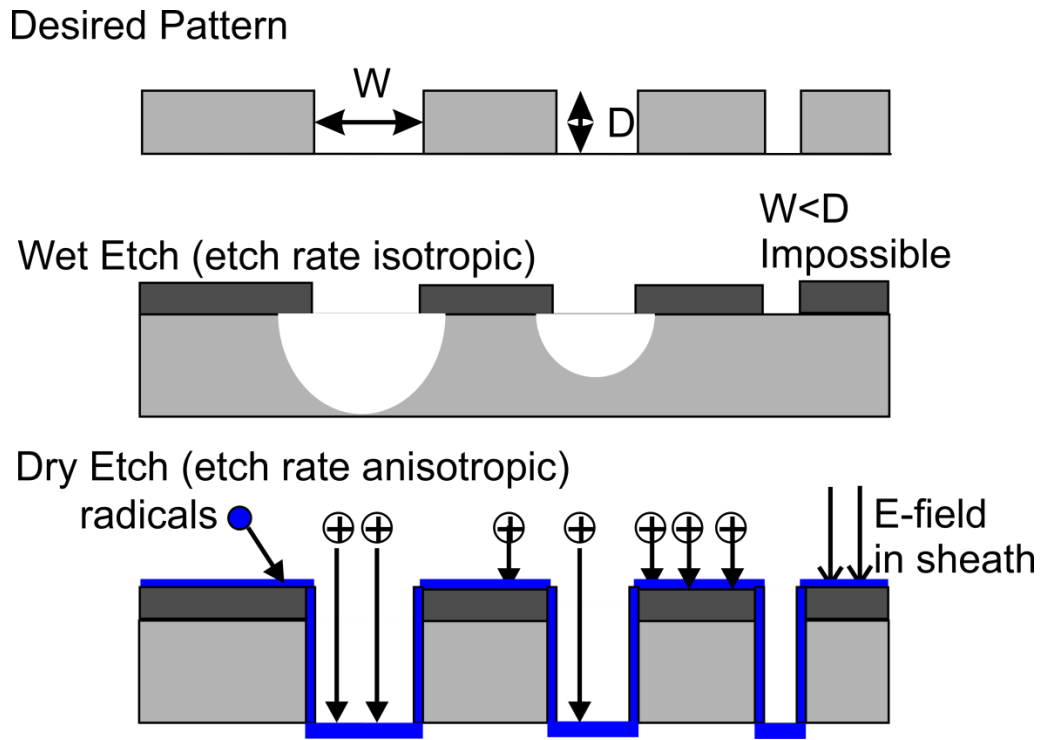
Fig. 1.3. Illustration of wet etching limitation and anisotropic dry etching.
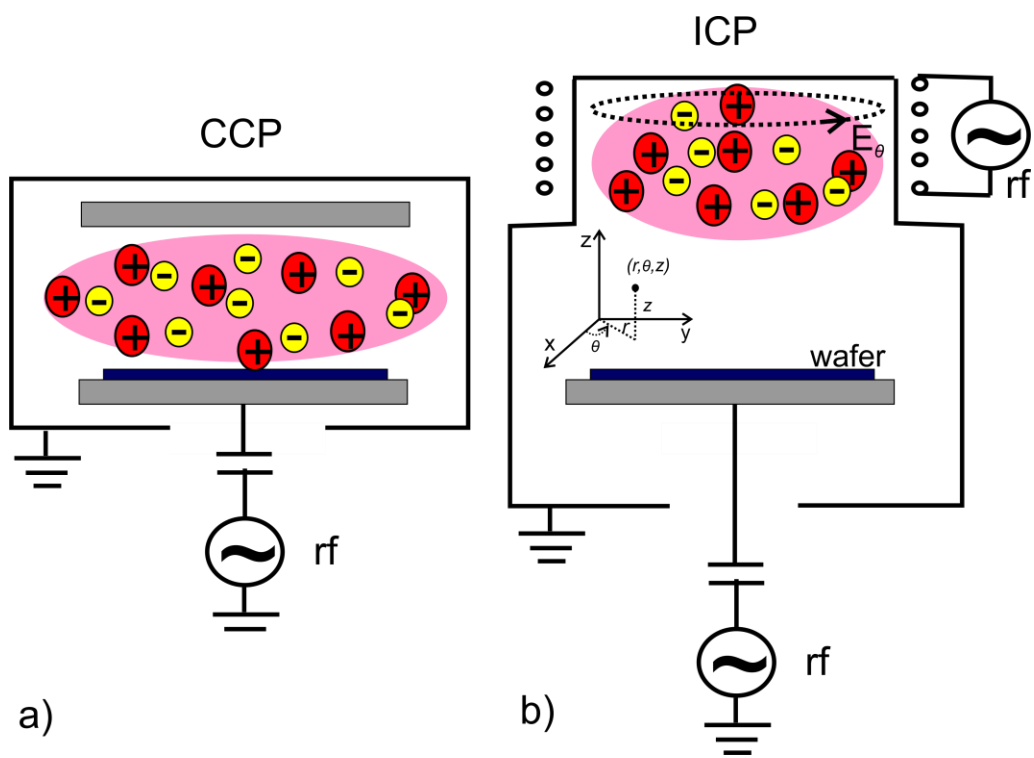
Fig. 1.4. Plasma rf sources: a) Capacitively Coupled Plasma and b) Inductively Coupled Plasma with cylinder coil antenna.
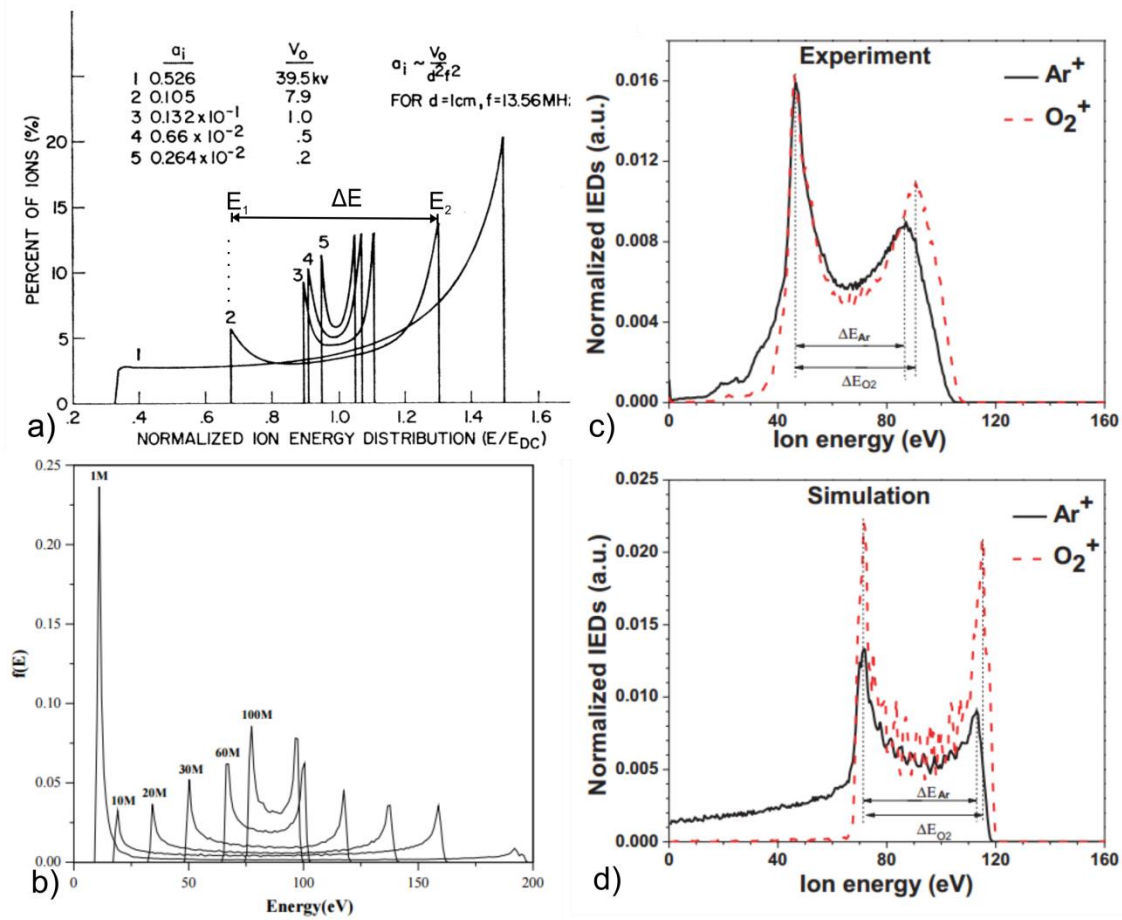
Fig. 1.5. a) IEDs from Tsui[64] for different values of $a_i \approx (\tau_{rf}/\tau_{ion})^2$. The unexpected disappearance of the low-energy peak at higher a1 is due to Tsui's assumption of constant sheath width.[23] b) PDP1 Modeled results from Kawamura *et al.*[23] showing IEDs of He$^+$ at bias frequencies from 1 MHz to 100 MHz. c) Experiments and d) simulation for IEDs of Ar$^+$ and O$_2^+$ from Liu *et al.*[32]
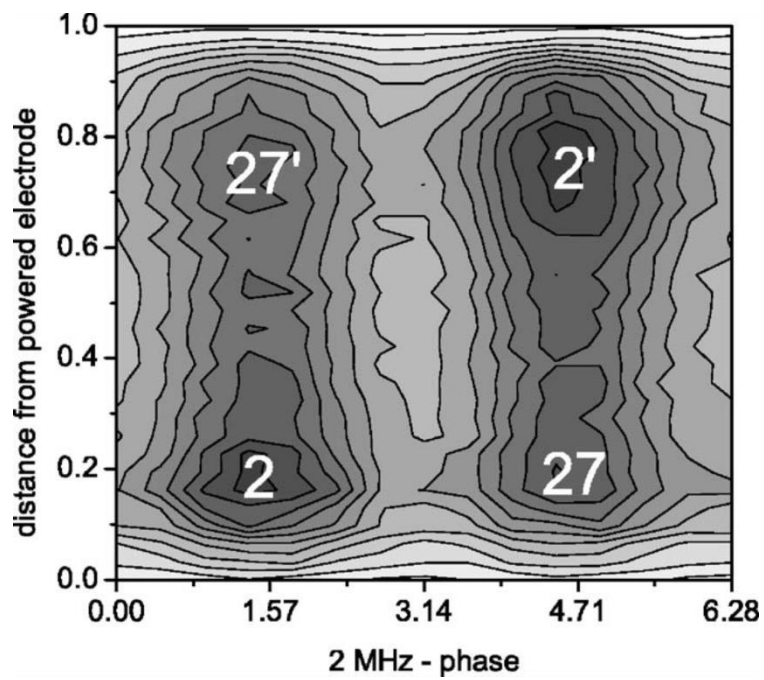
Fig. 1.6. Space and phase resolved optical emission measured by Gans *et al*.[17] The produced electron dynamics exhibits a strong coupling of both 2 and 27 MHz. The emission maxima indicated as 2 and 2' scale with the 2 MHz power relative to the 27 MHz power while the maxima indicated as 27 and 27' scale vice versa.
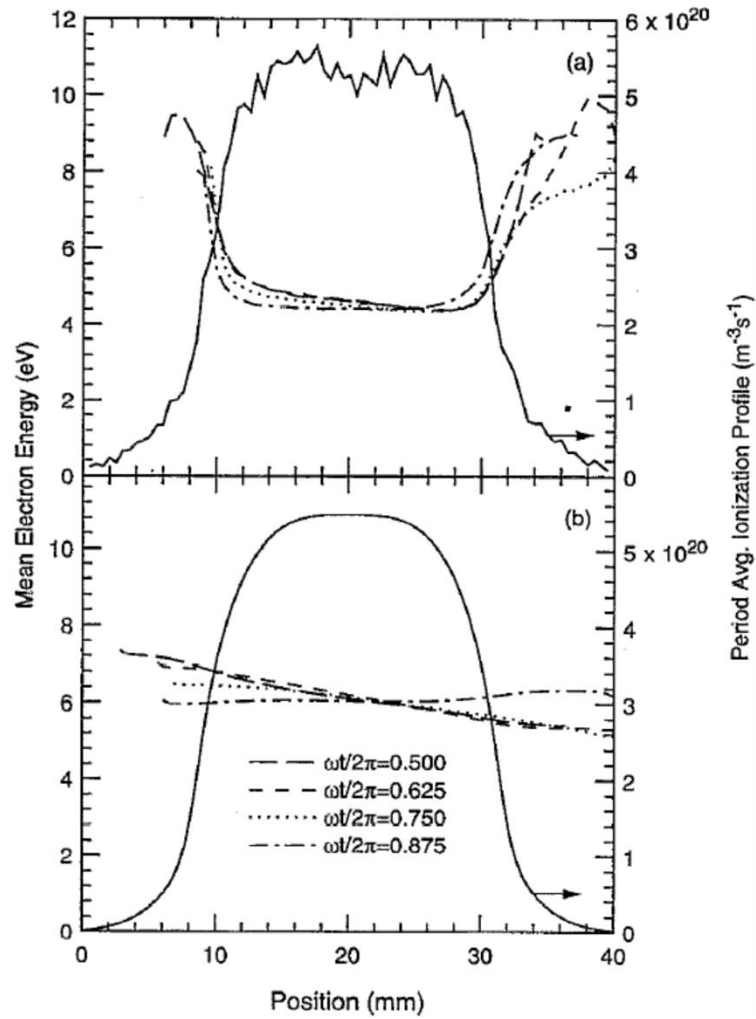
Fig. 1.7. Mean electron energy at four times in the rf period and period average ionization profile from a) the PIC model and b) the fluid model.[43]
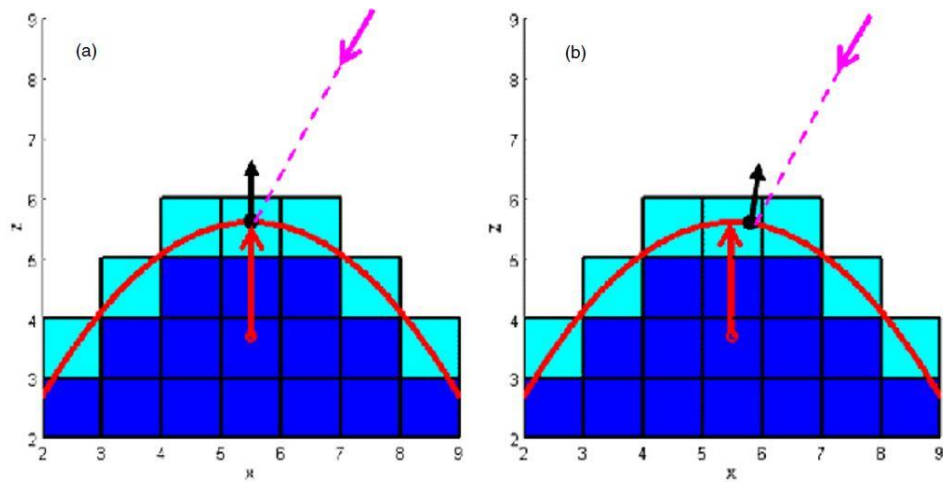
Fig. 1.8. Surface normal is determined at the interaction of particle tractor and fitted polynomial surface.   Slight difference in the intersection results in different angles of incidence.[50]
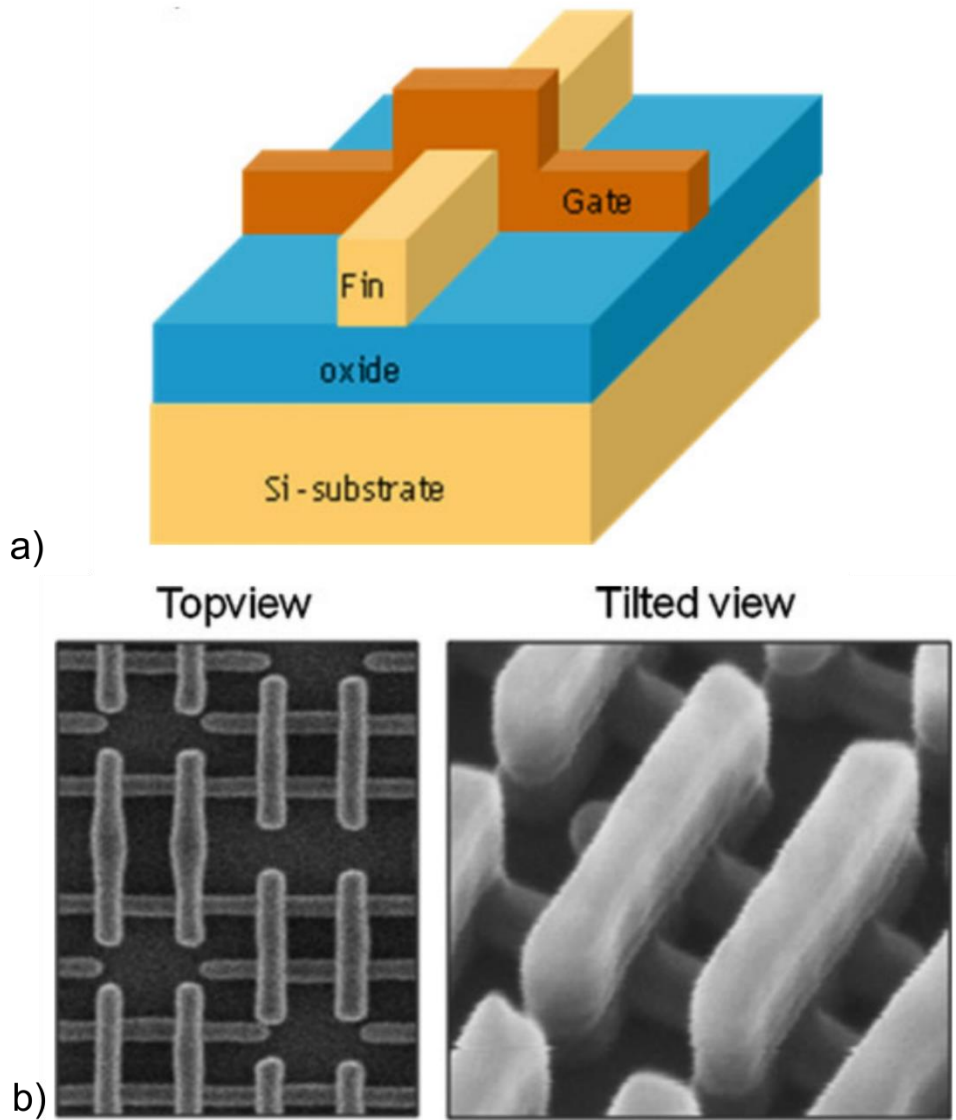
Fig. 1.9. a) Device structure of FinFet, which has a double gate structure. b) Top view and tilted view SEM pictures of gate double pattering in sub 0.1 um^2 FinFET 6T-SRAM.[52]
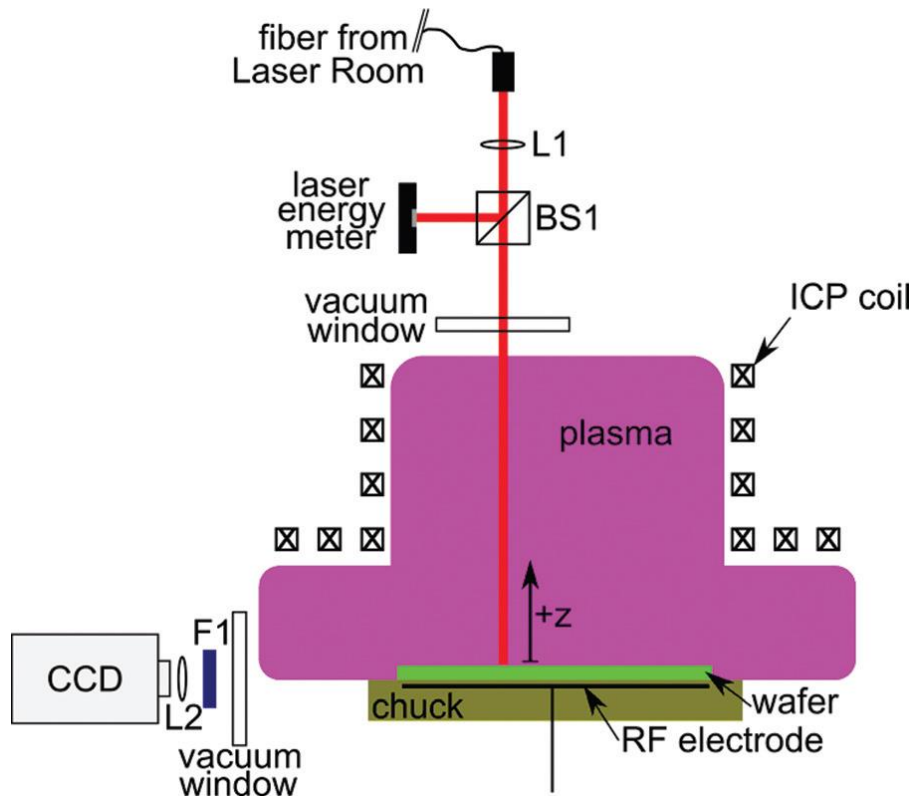
Fig. 1.10. LIF schematic: The laser beam passes through a quartz vacuum window on the top of the chamber and strikes the wafer at normal incidence to measure z component of the ion velocity distribution.[59]
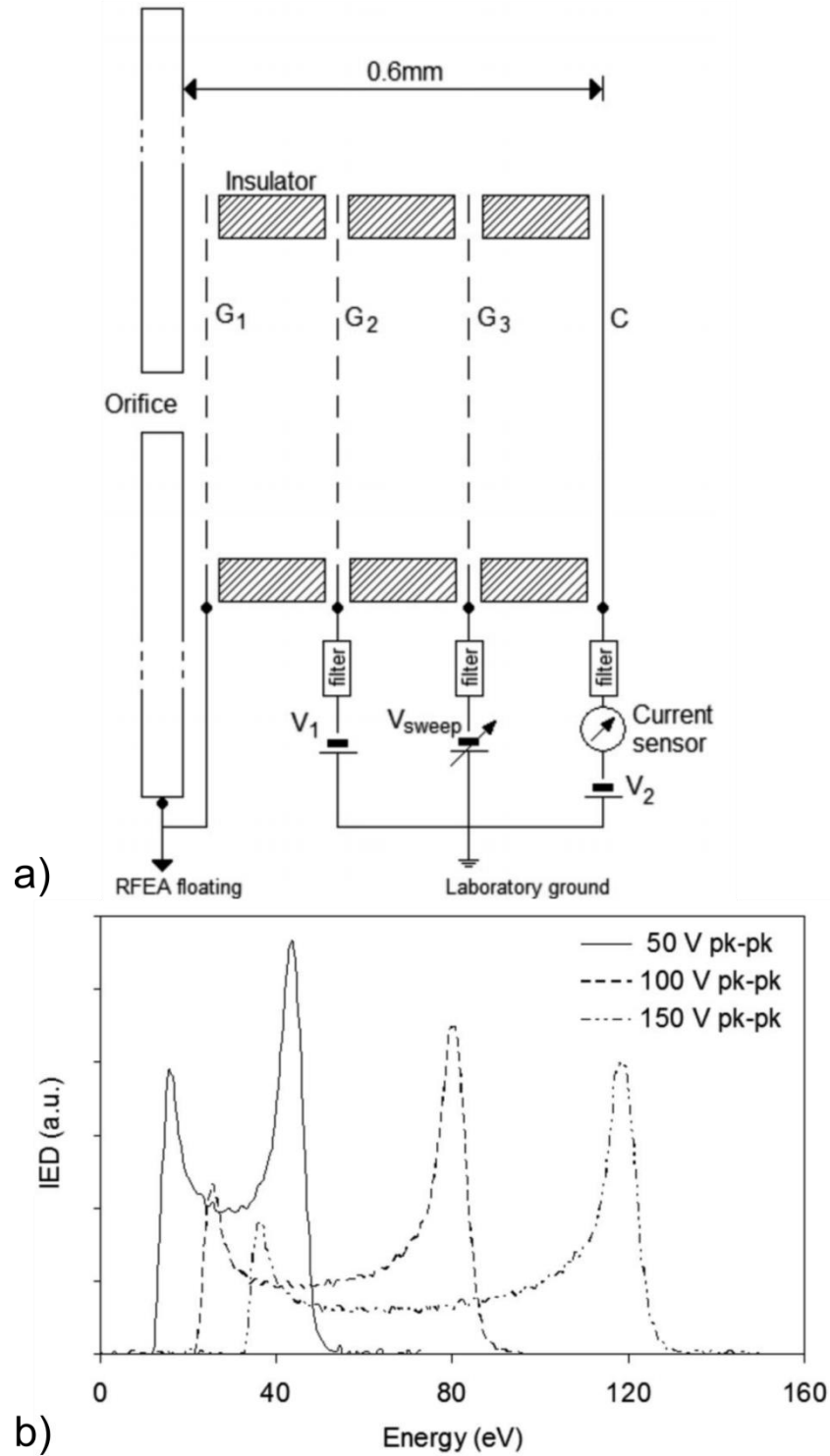
Fig. 1.11. a) Schematic of the retarding field energy analyzer structure. b) An example of normalized IEDs for various 2 MHz rf bias potentials measured by the RFEA.[63]

1.8   References

1. F. F. Chen, "*Introduction to plasma physics and controlled fusion",* (Plenum Press, New York, 1984), p. 3.
2. A. Fridman and L. A. Kennedy, "*Plasma Physics and Engineering",* (Taylor & FRANCIS Books, New York, 2004), p. 3.
3. http://www.plasma.inpe.br/LAP_Portal/LAP_Site/Text/Variety_of_Plasmas.htm
4. D. Economou, J. Vac. Sci. Technol. A **31**, 050823 (2013).
5. A. Grill, "*Cold Plasma in Materials Fabrication: from Fundamentals to Applications",* (IEEE Press, New York, 1993), p. 68-75.
6. J. W. Coburn and H. F. Winters, J. Appl. Phys **50**, 3189 (1979).
7. D. L. Flamm, V. M. Donnelly and D. E. Ibbotson, J. Vac. Sci. Technol. B. **1**, 23 (1983).
8. J. W. Coburn and H. F. Winter, J. Vac. Sci. Technol **16**, 381 (1979).
9. M. M. Shamim, J. T. Scheeuer, R. P. Fetherston and J. R. Conrad, J. Appl. Phys. **70**, 4756 (1991).
10. F. F. Chen, Chap. 6 "*Advanced Plasma Technology".* Ed. by Riccardo d'Agostino, Pietro Favia, Yoshinobu Kawai, Hideo Ikegami,Noriyoshi Sato, and Farzaneh Arefi-Khonsari (WILEY-VCH, 2008).
11. V. Donnelly and A. Kornblit, J. Vac. Sci. Technol. A **31**, 050825 (2013).
12. X. Xu, H. Ge, S. Wang, Z. L. Dai, Y. N. Wang, and A. M. Zhu, Prog. Nat. Sci. **19**, 677 (2009).
13. H. H. Goto, H. D. Lowe and T. Ohmi, J. Vac. Sci. Technol.A **10**, 3048 (1992).
14. M. A. Lieberman and A. J. Lichtenberg, "*Principles of Plasma Discharges and Materials Processing"*, (WILEY-INTERSCIENCE, New Jersey, 2005), p. 410-417.
15. T. Kitajima, Y. Takeo, Z. Lj. Petrović and T. Makabe, Appl. Phys. Lett. **77**, 489 (2000).
16. J. P Booth, G. Curley, D. Marić and P Chabert, Plasma Source Sci. Technol. **19**, 015005 (2010).
17. T. Gans, J. Schulze, D. O'Connell, U. Czarnetzki, R. Faulkner, A. R. Ellingboe and M. M. Turner, Appl. Phys. Lett. **89**, 261502 (2006).
18. R. Patrick, P. Schoenborn, H. Toda and F. Bose, J. Vac. Sci. Technol. A. **11**, 1296 (1993).
19. L. J. Mahoney, A. E. Wendt, E. Barrios, C. J. Richards, and J. L. Shohet, J. Appl. Phys. **76**, 2041 (1994).
20. R. R. Schaller, IEEE Spectrum **34**, 52 (1997).
21. R. W. Bosewell and R. K. Porteous, J. Appl. Phys. **62**, 3123 (1987).
22. QZ. Zhang, SX Zhao, W. Jiang and YN Wang, J. Phys. D: Appl. Phys. **45** 305203 (2012).
23. E. Kawamura, V. Vahedi, M.A. Lieberman and C.K. Birdsall, Plasma Sources Sci. Technol. **8**, R45 (1999).
24. W. J. Goedheer, Plasma Sources Sci. Technol. **9**, 507 (2000).
25. A. Metze, D. W. Ernie and H. J. Oskam, J. Appl. Phys. **65**, 993 (1989).
26. M. Olevanov, O. Proshina, T. Rakhimova and D.Voloshin, Phys. Rev. E **78**, 026404 (2008).
27. S.-B. Wang and A. E. Wendt, J. Appl. Phys. **88**, 643 (2000).
28. T. Lafleur, P. A. Delattre, E. V. Johnson and J. P. Booth, Appl. Phys. Lett. **101**, 124104 (2012).
29. A. Ushakov, V. Volynets, S. Jeong, D. Sung, Y. Ihm, J. Woo and M. Han, J. Vac. Sci. Technol. A. **26**, 1198 (2008).
30. G. A. Curley, D. Marić, J-P. Booth, C. S. Corr, P. Chabert and J. Guillon, Plasma Sources Sci.

Technol. **16**, S87 (2006).

31. J. K. Lee, O. V. Manuilenko, N. Y. Babaeva, H. C. Kim and J. W. Shon, Plasma Sources Sci. Technol. **14**, 89 (2005).

32. J. Liu, Q-Z. Zhang, Y-X. Liu, F. Gao and Y-N. Wang, J. Phys. D: Appl. Phys. **46**, 235202 (2013).

33. J. Liu, Y-X. Liu, Z-H. Bi, F. Gao and Y-N Wang, J. Appl. Phys. **115**, 013301 (2014).

34. S. Samukawa, M. Hori, S. Rauf, K. Tachibana, P. Burggeman, G. Kroesen, J. C. Whitehead, A. B. Murphy, A. F. Gutsol, S. Starikovskaia, U. Kortshagen, J-P. Boeuf, T. J. Sommerer, M. J. Kushner, U. Czarnetzki and N. Mason, J. Phys. D: Appl. Phys. **45,** 253001 (2012).

35. H. C. Kim, F. Iza, S. S. Yang, M. Radmilovic-Radjenovic and J. K. Lee, J. Phys. D: Appl. Phys. **38**, R283 (2005).

36. E. Golant, A. P. Zhilinsky, and I. E. Sakharov, *"Fundamentals of Plasma Physics"* (Wiley, New York, 1980).

37. A. Stewart, P. Vitello, and D. B. Graves, J. Vac. Sci. Technol. B. **12**, 478(1994).

38. A. Stewart, P. Vitello, D. B. Graves, E. F. Jaeger, and L. A. Berry, Plasma Sources Sci. Technol. **4**, 36 (1995).

39. R. W. Hockney and J. W. Eastwood, *"Computer Simulation Using Particles",* (McGraw-Hill, New York, 1981).

40. C. K. Birdsall, IEEE Trans. Plasma Sci. **19**, 65(1991).

41. V. Vahedi, M. Surendra, Computer Physics Communication. **87**, 179 (1995).

42. G. Wakayama and K. Nanbu, IEEE Trans. Plasma Sci. **31**, 638 (2003).

43. T. E. Nitschke and D. B. Graves, J. Appl. Phys., **76** 5646(1994).

44. M. J. Kushner, J. Phys. D. **43**, 185206 (2010).

45. T. J. Sommerer and M. J. Kushner, J. Appl. Phys. **71**, 1654 (1992).

46. S. Wang, X. Xu, and Y-N. Wang, Phys. Plasmas. **14**, 113502 (2007).

47. W. Guo and H. H. Sawin, J. Phys. D: Appl. Phys. **42,** 194014 (2009).

48. R. J. Hoekstra, M. J. Grapperhaus and M. J. Kushner, J. Vac. Sci. Technol. A. **15**, 1913 (1997).

49. Y. Osano and K. Ono, Japan. J. Appl. Phys. Part 1, **44** 8650 (2005).

50. H. Kawai, PhD Thesis MIT, (2008)

51. D. J. Cooperberg, V.Vahedi and R. A. Gottscho, J. Vac. Sci. Technol. A. **20,** 1536 (2002).

52. N. Horiguchi *et al.* "*Semiconductor- On- Insulator Materials for Nanoelectronics Applications, Engineering Materilas",* ed. by A. Nazarov *et al.* (Springer-Verlag Berlin Heidelberg, 2011), p. 141-153

53. M. Dalvie, R. T. Farouki and S. Hamaguchi, IEEE Trans. Electron Devices. **39,** 1090 (1992).

54. F.F. Chen, Chap. 4 *Electric Probes*, in "*Plasma Diagnostic Techniques*", ed. by R.H. Huddlestone and S.L. Leonard (Academic Press, New York, 1965), p. 113-200

55. M. Lampe, J. Plasma Physics. **65** 171 (2001).

56. M. Y. Naz, A. Ghaffar, N. U. Rehman, S. Naseer and M. Zakaullah, Progress In Electromagnetics Research, **114**, 113 (2011).

57. Langmuir Probe, Wikipedia page online at http://en.wikipedia.org/wiki/Langmuir_probe.

58. L. Oksuz, M. Atta Khedr and N. Hershkowitz, Phys. Plasmas **8**, 1729 (2001).

59. B. Jacobs, W. Gekelman, P. Pribyl and M. Barnes, Phys. Plasmas **18**, 053503 (2011).

60. J. W. Coburn and E. Kay, J. Appl. Phys. **43**, 4965 (1972).

61. A. D. Kuypers and H. J. Hopman, J. Appl. Phys. **67**, 1229 (1990).

62. D. Gahan, B. Dolinaj and M. B. Hopkins, Rev. Sci. Instrum. **79**, 033502 (2008).

63. W. J. Goedheer, Plasma Sources Sci. Technol. **9**, 507 (2000).

64. R. T. C. Tsui, Phys. Rev. **168** 107 (1968).

Chapter 2 HYBRID PLASMA EQUIPMENT MODEL

2.1   Introduction

In this chapter, the modules and techniques used for the reactor scale simulator, Hybrid Plasma Equipment Model (HPEM), are described. The HPEM is a 2-dimensional plasma equipment model for low pressure and low temperature plasma processing reactor investigation. As a hybrid model, the HPEM has a hierarchical structure in which different modules address different physical processes.[1-15] For this study, the Electron Magnetic Module (EMM), the Electron Energy Transport Module (EETM), the Fluid Kinetics-Poisson Module (FKPM), and the Plasma Chemistry Monte Carlo Module (PCMCM) were employed.

In the HPEM, an iteration represents one cycle through the modules with modules sequentially receiving and providing data between them. A flow chart showing modules information exchange for this thesis is shown in Fig. 2.1. The sequencing of modules in the simulation process begins with an estimation of species densities, which provides conductivities to solve the frequency domain form of wave equation for the inductively coupled fields in the EMM. The electromagnetic fields $\vec{E}(\vec{r}, \phi)$ and $\vec{B}(\vec{r}, \phi)$ calculated by EMM are then transported to the EETM. In the EETM, the electron Monte Carlo simulation provides electron energy distributions of bulk electrons. A separate Monte Carlo simulation is used for secondary sheath accelerated electrons. The outputs of EETM, electron impact rate coefficients $k_e(\vec{r}, \phi)$ and

electron impact source functions $S_e(\vec{r}, \phi)$, are transferred to the FKPM. Within the FKPM,

densities $N(\vec{r})$, fluxes $\vec{\phi}(\vec{r})$ and temperatures $T(\vec{r})$ of neutral and charged species are produced.

The FKPM also calculates heavy particle reactions rate coefficients $k(\vec{r}, \phi)$ and their source

functions $S(\vec{r}, \phi)$. With the densities of charged particles, Poisson's equation is solved in FKPM

for the electrostatic potential $\Phi_s(\vec{r}, \phi)$ and electrostatic field $\vec{E}_s(\vec{r}, \phi)$. The FKPM exports

$k_e(\vec{r}, \phi)$, $S_e(\vec{r}, \phi)$, $N(\vec{r})$, $\vec{\phi}(\vec{r})$, $T(\vec{r})$, $k(\vec{r}, \phi)$, $S(\vec{r}, \phi)$ and $\vec{E}_s(\vec{r}, \phi)$ to the PCMCM to obtain

energy (or velocity) and angular distribution of ions and neutrals in the bulk plasma, presheath,

sheath and wafer. Pseudo-particles representing ions and neutrals are launched from the site of

their formation and their trajectories are integrated as a function of time using electric fields from

the FKPM recorded as a function of phase and position. Collisions are accounted for using

Monte Carlo techniques. This cycle constitutes an iteration. In order to model a phenomenon to

come to a steady state and numerically resolve the phenomenon in a stable manner, integrating

hundreds or thousands of iterations are typically required.

2.2   The Electromagnetics Module (EMM)

The EMM module resolve 3-d component of the inductively coupled electric field based

on applied magnetostatic fields and the azimuthal antenna currents. The electromagnetic fields

$\vec{E}$ are obtained by solving the following wave equation:

$$-\nabla(\frac{1}{\mu}\nabla \cdot \vec{E}) + \nabla \cdot (\frac{1}{\mu}\nabla \vec{E}) = \omega^2 \varepsilon^2 \vec{E} + i\omega(\vec{J}_{coil} + \overline{\overline{\sigma}} \cdot \vec{E}), \qquad (2.1)$$

where μ is permeability, ω is angular electromagnetic frequency, and ε is permittivity. The

current density has contributions from both the external antenna current $\vec{J}_{coil}$ and the conduction

current generated in the plasma. The conduction current is addressed through a conductivity tensor $\overline{\overline{\sigma}}$ with form as following:

$$\overline{\overline{\sigma}} = \frac{\sigma_0}{(\alpha^2 + |B|^2)} \times \begin{pmatrix} \alpha^2 B^2{}_r & \alpha B_z + B_r B_\theta & -\alpha B_\theta + B_r B_z \\ -\alpha B_z + B_r B_\theta & \alpha^2 + B^2{}_\theta & \alpha B_r + B_\theta B_z \\ \alpha B_\theta + B_r B_z & -\alpha B_r + B_\theta B_z & \alpha^2 + B^2{}_z \end{pmatrix}, \qquad (2.2)$$

and

$$\sigma_0 = \frac{q_e{}^2 n_e}{m_e} \frac{1}{v_m + i\omega}, \alpha = \frac{m_e}{q}(v_m + i\omega), \qquad (2.3)$$

where B is the applied static magnetic file, q_e is the unit electron charge, n_e is the electron density, m_e is the electron mass and v_m is the electron momentum transfer collision.[15]

When there is a coil generated electromagnetic fields in the reactor, the EMM is executed for computing inductively coupled electric and magnetic fields as a function of position and phase during the rf cycle. Due to the absence of a static magnetic field in the ICP chambers studied in this thesis, the conductivity tensor is equal to its isotropic value, σ_0 in Eq. (2.3) and only azimuthal electric field E_θ is produced. The electric field is normalized to provide total power deposition by calculating the product of $j_e \cdot \vec{E}$ if assuming collisional power deposition. In order to include non-collisional heating effects, the electron current, j_e, needs to be calculated kinetically in the eMCS, and fed back to the electromagnetics calculation.

With the electric field $\vec{E}(\vec{r}, \phi)$, the magnetic field $\vec{B}(\vec{r}, \phi)$ is computed by the equation:

$$\vec{B} = (i/\omega)\nabla \times \vec{E} \qquad , \qquad (2.4)$$

with the boundary condition that there is no tangential E field on all metal surface and let $E_\theta = 0$.

2.3   The Electron Energy Transport Model (EETM)

The EETM solves for electron impact sources and electron transport properties by using the electromagnetic fields $\vec{E}(\vec{r}, \phi)$ and $\vec{B}(\vec{r}, \phi)$ from EMM and the electrostatic field $\vec{E}_s(\vec{r}, \phi)$ from FKPM.   The electron properties can be computed in three ways: 1) electron Monte Carlo Simulation (eMCS, described in Sec. 2.3.1), 2) local field approximation based on local power deposition (not involved in this dissertation work), and 3) Solving a time dependent electron energy equation, which is implicitly integrated in the FKPM to provide electron temperature, impact and transport coefficients. (see Sec. 2.4.1).   In this thesis, the eMCS is used in the majority of the simulations. Due to computational time constraints, the results discussed in Chapter 4 are obtained by solving the time dependent electron energy equation.

2.3.1   The Electron Monte Carlo Simulation (eMCS)

The eMCS is a fully kinetic treatment, which resolves the transport of electron in electromagnetic fields. The electrons are launched with velocities randomly chosen according to Maxwellian distribution and positions randomly selected in the reactor weighted by electron density $N_e(\vec{r})$. Electron trajectories are computed using the Lorentz equation,

$$\frac{d\vec{v}}{dt} = \frac{q_e}{m_e}(\vec{E} + \vec{v}_e \times \vec{B}) \quad ,$$
(2.5)

where $\vec{v}_e$ is the electron velocity, $\vec{E}$ is the local electric field and $\vec{B}$ is the local magnetic field. The electric fields are composed of the inductive fields computed in the EMM and the time-dependent electrostatic fields computed from the FKPM and updated when the EMM, EETM and FKPM are sequentially and iteratively called during execution of the model. Time steps are chosen to be less than 0.01 period of the highest applied frequency. In this thesis, 4000 to a maximum of 25000 particles are integrated in time for more than 300 lowest frequency rf cycles

on each iteration. Separate Monte Carlo simulation is used for secondary sheath accelerated electrons. The trajectories of the secondary electrons are tracked by integrating the equation of motion while accounting for collisions. Each pseudo-particle is tracked until it is collected by a surface.

In this thesis, the energy grid technique is used to collect collision frequencies and statistics. The energy grid is composed of 500 bins with energy ranges of 0 - 5, 5 - 12, 12 - 50, 50 - 300, and 300 - 1000 eV. The high energy ranges are mainly used to capture energy of the sheath accelerated secondary electrons. Each range is divided into 100 bins. The total collision frequency, v_i of each energy bin i, is calculated by summing all possible collisions with every heavy particle plasma species using the following equation,

$$v_i = (\frac{2\varepsilon_i}{m_e})^{1/2} \sum_{j,k} \sigma_{ijk} N_j ,$$
(2.6)

where ε_i is the average energy within bin i, m_e is the electron mass, σ_{ijk} is the cross section at energy i, for species j and collision process k, and N_j is the number density of species j.[12]

Null collision cross sections are used to provide a constant collision frequency. In a particular energy range, the null collision frequency is equal to the difference between the actual collision frequency and its maximum value.[16]

The time step between collisions is determined by $\Delta t = -\ln(r)/v_{mj}$, where r is a random number distributed on (0, 1) and v_{mj} is the maximum collision frequency in energy range j. The type of collision is determined by generating a series of random numbers and comparing their values with normalized collision frequencies. If a collision is null, the electron energy and its trajectory are not changed. Otherwise, the electron energy is modified according to the inelastic or elastic nature of the collision and the electron trajectory is scattered.[12]

36

The statistics for the electron energy distributions are collected into an array for each energy bin i and spatial bin l, as

$$F_{il} = \sum_j w_j \delta[(\varepsilon_i \pm \frac{1}{2}\Delta\varepsilon_i) - \varepsilon_i]\delta[(\vec{r}_l \pm \Delta\vec{r}) - \vec{r}_j]$$ (2.7)

where w_j is the weighting of the particle by considering three factors: 1) the relative number of electrons each pseudo-particle represents, 2) the time step used to advance the particle trajectory, and 3) a spatial weighting. At the end of an eMCS execution, F_{il} is normalized for computing the electron energy distributions, $f_e(\varepsilon, \vec{r})$, at each spatial location.

$$\sum_i F_{ij}\Delta\varepsilon_i = \sum_i f_e(\varepsilon, \vec{r})\varepsilon_i^{1/2}\Delta\varepsilon_i = 1$$ (2.8)

With the electron energy distributions, the electron impact source and transport rate coefficients can be obtained.

2.4 The Fluid Kinetics-Poisson Module (FKPM)

The output of EMM and EETM are transferred to FKPM in the plasma transport equations are integrated for the duration of iteration.

2.4.1 Continuity and energy equation for electrons

As an alternative method of determining electron transport properties, the electron rate coefficients are computed by solving Boltzmann's equation for a range of values of electric field/total gas density (E/N). The Boltzmann equation is expressed as

$$\frac{\partial f_e}{\partial t} = -\vec{v}\nabla_r f_e - \frac{e(\vec{E} + \vec{v} \times \vec{B})}{m_e} \cdot \nabla_v f_e + (\frac{\partial f_e}{\partial t})_{collisions}$$ (2.9)

where $f_e = f_e(\vec{r}, \vec{v}, t)$ is the electron energy distribution, ∇_r is the spatial gradient, ∇_v is the velocity gradient, m_e is the electron mass and $(\frac{\partial f_e}{\partial t})_{collisions}$ represents the effect of collisions.

With the rate coefficients, the electron energy equation module is able to tabulate the electron energy distributions over the given range and allow the determination of electron transport properties by solving the following equation:

$$\frac{\partial(\frac{3}{2}n_e k_B T_e)}{\partial t} = \nabla k \nabla T_e + \nabla \cdot (\vec{\phi}_e T_e) = P, \tag{2.10}$$

where k is the thermal conductivity, $\vec{\phi}_e$ is the electron flux and T_e is the electron temperature equal to two thirds of average electron energy, which is determined from f_e. The right hand side of Eq. (2.10) represents the total power delivered to the electrons:

$$P = j \cdot \vec{E} = q_e(-D\nabla n_e - \mu_e n_e \vec{E}) \cdot \vec{E}. \tag{2.11}$$

$$\vec{\phi}_e = \mu_e q_e n_e \vec{E} - D_e \nabla n_e, \tag{2.12}$$

where μ_e is the electron mobility, q_e is the charge of electron , n_e is the electron density and D_e is the electron diffusion coefficient. The electric field $\vec{E}$ is the sum of both $\vec{E}_\theta$ from the EMM and $\vec{E}_S$ from the FKPM.

Electron continuity equation is solved in either a drift-diffusion formulation as shown in Eq. (2.12) or in the Scharfetter- Gummel (S-G) expression.

The S-G expression captures upwind-and-downwind properties.[17,18] The flux between mesh points (*i, i+1*) is given by:

$$\vec{\phi}_{i+\frac{1}{2}} = \frac{\alpha \overline{D}(n_{i+1} - n_i \exp(\alpha \Delta x))}{1 - \exp(\alpha \Delta x)}, \tag{2.13}$$

where

$$\alpha = -q\overline{\mu}\left(\frac{\Phi_{i+1} - \Phi_i}{\Delta x}\right) \tag{2.14}$$

and Δx is the distance between vertex i and $i+1$, Φ_i is the potential of vertex i, $\overline{D}$ and $\overline{\mu}$ are average diffusion coefficient and mobility in the interval.

2.4.2 Continuity, momentum and equation equations for heavy particles

Continuity, momentum, and energy equations are solved for all heavy particles (neutrals and ions) as:

$$\frac{\partial N_i}{\partial t} = -\nabla \cdot \vec{\phi}_i + S_i \tag{2.15}$$

$$\frac{\partial \vec{\phi}_i}{\partial t} = \frac{\partial (N_i \vec{v}_i)}{\partial t} = -\frac{1}{m_i} \nabla(kN_iT_i) - \nabla \cdot (N_i\vec{v}_i\vec{v}_i) + \frac{q_i}{m_i} N_i(\vec{E}_S + \vec{v}_i \times \vec{B})...$$
$$-\nabla \cdot \overline{\overline{v}}_i - \sum_j \frac{m_j}{m_i + m_j} N_i N_j (\vec{v}_i - \vec{v}_j) v_{ij} \tag{2.16}$$

$$\frac{\partial N_i \varepsilon_i}{\partial t} = -\nabla \cdot \overline{\overline{\kappa}} \nabla T_i - P_i \nabla \cdot \vec{v}_i - \nabla \cdot (N_i \vec{v}_i \varepsilon_i) + q_i \vec{\phi}_i \vec{E}...$$
$$-(\overline{\overline{\mu}}_i \nabla \cdot \nabla \vec{v}_i) - \sum_{m,j} k_{mij} N_i N_j \varepsilon_i + \sum_{m,j,l} k_{mjl} N_j N_l \Delta \varepsilon_{mjl} \tag{2.17}$$

where $\vec{\phi}_i$, N_i, $\vec{v}_i$, m_i, T_i, $\overline{\overline{\mu}}_i$, P_i and ε_i is the flux, density, velocity, mass, temperature, viscosity, pressure and total energy of species i.

2.4.3 Poisson's equation

The local electrostatic field $\vec{E}_S$ is needed for solving the Eq. (2.11, 2.12, 2.16 and 2.17). In this thesis, the $\vec{E}_S$ is calculated by solving Poisson's equation using a semi-implicit technique:

$$\nabla \cdot (\varepsilon \nabla \Phi(t + \Delta t)) = -\rho(t + \Delta t) = -\rho(t) - \Delta t \frac{\partial \rho}{\partial t} |^{t+\Delta t} \tag{2.18}$$

and

$$\rho(t) = \rho_m(t) + \sum_i q_i N_i(t), \tag{2.19}$$

$$\frac{\partial \rho}{\partial t}\Big|^{t+\Delta t} = \frac{\partial \rho_m(t')}{\partial t} - q_e \nabla \cdot \left(\vec{\phi}_e(t) + \frac{\partial \vec{\phi}_e}{\partial \Phi}[\Phi_S(t+\Delta t) - \Phi_S(t)] \right) \dots$$
$$- \sum_j q_j \nabla \cdot \left(\vec{\phi}_j(t) + \frac{\Delta t}{2}\frac{\partial \vec{\phi}_j(t)}{\partial t} \right) \qquad , \qquad (2.20)$$

where ρ_m is the charge density on material m, ε is the permittivity, Φ_s is the electrostatic potential, $\vec{\phi}_{e,j}(t)$ is species flux with e and j represent electron and ions. The t' donates that the charge density is evaluated at current time step t, and the potential is evaluated at future time $t+\Delta t$. With the semi-implicit method, the time step Δt for updating the charged-particle can be larger than the dielectric relaxation time, which is the time limit for solving Poisson's equation explicitly.[14] The Jacobian element $\dfrac{\partial \vec{\phi}_e}{\partial \Phi}$ in Eq. (2.20) is numerically evaluated by considering have a small fraction of potential change (typically $\Delta \Phi = 5\%$) within Δt by solving two first-order partial derivatives of the electron flux with respect to potential $\Delta \Phi_{ij}$, where i, j is radial and axial direction index. Eq. (2.20) can be solved either with the successive over relaxation method [19] or a direct sparse matrix technique [20], where the Jacobian element is derived from:

$$\frac{\partial \vec{\phi}_{i,j}}{\partial \Phi_{i+1,j}} = \frac{\vec{\phi}_{i,j}(\Phi_{i+1,j} + \Delta\Phi_{i+1,j}) - \vec{\phi}_{i,j}(\Phi_{i+1,j})}{\Phi_{i+1,j}} \qquad , \qquad (2.21)$$

where $\Delta\Phi_{i+1,j}$ is a predefined perturbation with a typical value $=0.05\Phi_{i,j}$.

The boundary condition of solving Poisson's equation on powered metals is the instantaneous applied potential with dc bias. With a blocking capacitor connected in series to the bottom electrode in geometry asymmetric chambers, a dc self-bias is naturally generated on the electrodes, which ultimately determines the mean ion energy onto the substrate. HPEM computes a dc self-bias to equalize rf currents to powered and ground area,

$$V_{dc} = \frac{1}{C} \int \sum_i m_i \left(\sum_j \vec{\phi}_j \left(q_j + q\gamma_{ij} \right) \cdot \hat{n}_i + \frac{\partial \left(\varepsilon \vec{E} \cdot \hat{n}_i \right)}{\partial t} \right) dt , \tag{2.22}$$

where C is the blocking capacitance, $\vec{\phi}_j$ is the flux of charged particle j having charge q_j incident onto metal i have local normal $\hat{n}_i$. γ_{ij} is the secondary electron emission coefficient for species j and metal i. The first summation is over metal surfaces where m_i is ±1 depending on whether the metal is on the grounded or powered side of the circuit. The second summation is over charged species.

The electric fields are recorded as a function of phase over the *LF* cycle with sufficient resolution to capture the *HF* dynamics for use elsewhere in the model. In multi-frequency CCPs, when the voltage of each frequency is specified and voltages are applied to separate electrodes, the time averaged power $\overline{P}_{rf}$ can be computed for each electrode by

$$\overline{P}_{rf} = \frac{1}{\tau} \iint V(t) [j(\vec{r},t) + \varepsilon \frac{d\vec{E}(\vec{r},t)}{dt}] dt dA, \tag{2.23}$$

where V is the voltage on the electrode, $j(\vec{r},t)$ is the conduction current density to the electrode, and ε is the permittivity. τ is the integration time, a multiple of the longer rf period and of sufficient length of time to average over the other frequency.

When there is more than one rf source applied to the same electrode, the previous method can only compute the total power on the electrode. If it is desired to control the power delivered by each frequency, then the power at each frequency must be separately computed so that voltage at that frequency can be adjusted. Given that the boundary condition on the electrodes is voltage, the current component of each frequency at the electrode must be distinguished. This can be achieved by computing the discrete Fourier components of bias current. The current components can be represented as

$$I_k = \sum_{n=0}^{N-1} i_n e^{-i2\pi k \frac{n}{N}}, k = 0,...,N-1, \tag{2.24}$$

where N is the number of time bins used in resolving the rf cycles of the *LF* and *HF* when computing the Fourier components. N is usually large enough to divide the *LF* period into at least 10^4 bins and the *HF* period into at least 10^3 bins. This Fourier transform maps current samples recorded as a function of time into the harmonic components that produce the time series. Knowing the supply frequencies and their higher harmonics, the current at frequency ω can be rewritten in amplitude and phase as

$$I(t) = \sum_{i=1}^{m} \sum_{j=1}^{n} I_{ij} \cdot \cos(j\omega_{ij}t + \phi_{ij}), \tag{2.25}$$

where m is the total number of rf frequencies and n is the number of harmonics included for each frequency. Thus, the time averaged power for each frequency can be calculated by

$$\overline{P}_{\omega i} = \frac{1}{\tau} \int I_{\omega i}(t) \cdot V(t)dt. \tag{2.26}$$

At the end of the iteration in the FKPM, electric fields, conductivities and densities are transferred to the EMM and EETM. A simple acceleration technique is applied in the FKPM to speed up the convergence of plasma properties. The species densities are periodically inspected and their long term rates of change are evaluated. When there is slow time evolution of species towards their steady states, the densities are linearly accelerated by the following equations. [10]

$$N_i(t + \Delta t) = N_i(t)(1 + \delta), \tag{2.27}$$

$$\delta = \xi \frac{N_i(t) - N_i(t - \Delta t)}{N_i(t)}, \tag{2.28}$$

$$\delta = \min(\delta, \delta_{max}), \delta = \max(\delta, \delta_{min}), \tag{2.29}$$

Where N_i is the density of specie i, δ is the fractional change, δ_{max}, δ_{min} are the upper and lower

limit on δ to prevent over (or under) acceleration. ξ represents an acceleration factor, which is typically set as a large value for low density plasma and a small value for high density plasma.

2.5 Plasma Chemistry Monte Carlo Module (PCMCM)

The energy and angular distributions onto surfaces as a function of position and phase are obtained using the PCMCM, which calculates the trajectories of charged and neutral species in the gas phase and their intersection with the substrate.[9] The PCMCM is a 3v-3d (3 velocity components, 3 dimensions) simulation which integrates heavy particles (ions and neutrals) trajectories in electric fields obtained from the FKPM. The PCMCM is executed after the periodic steady state is reached in the remainder of the model or optionally, after the FKPM cycle iteration. By that time, the continuity, momentum, energy equations for neutrals and ions, continuity equations for electrons and Maxwell's equations would have been integrated to convergence. The vector components of the electric field are recorded as a function of position and phase over a low frequency rf cycle, $\vec{E}(\vec{r},\phi)$, which also captures the *HF* variation. For convenience, the *HF* and *LF* are chosen to be multiples of each other. These recordings typically contain hundreds of phase points during the highest frequency period and are recorded on the same spatial mesh as the fluid portion of the model. Similar number of time bins is used in resolving the rf cycle when computing the Fourier components of bias current. The current and voltage phase information of each unique frequency are recorded for harmonics. The fluid module also records cycle-averaged densities of all charged and neutral species, $N_i(\vec{r})$ and source functions for these species. A set of collision probability arrays are computed which account for all possible collisions in the reaction mechanism and their energy dependence. In the absence of experimental data or theory, a generic energy dependence for the cross section for

43

elastic collisions of ions is specified as the form $\sigma(\varepsilon) = \dfrac{\sigma_0}{1 + \varepsilon/\varepsilon_0}$. The maximum collision

frequency for each PCMCM species, i, over the entire computational domain, V_{im}, is determined,

$$V_{im} = \sum_j V_{ij}, \quad V_{ij} = \max\left(\left(v\sigma_j(v)\right)_m N_{jm}\right), \tag{2.30}$$

where the sum is over collisions j, $(v\sigma_j(v))_m$ is the maximum product of speed and cross section,

and N_{jm} is the maximum value of the collision partner in the computational domain. We also

define the normalized cumulative collision frequency as

$$\omega_{ij} = \frac{1}{V_{im}} \sum_{k=1}^{j} V_{ik}, \tag{2.31}$$

having range (0,1) which for species i represents the relative probability of each type of collision

based on the maximum possible collision frequency in the computational domain over the

expected range of energies.

Pseudo-particles representing ions and neutral species are launched from computational

cells at times randomly chosen in the rf period in proportion to the source function for each

species. The initial velocities are randomly chosen from a Maxwell-Boltzmann distribution

having the temperature of that species as computed by the FKPM. The randomly chosen time to

the next collision is then $t_c = t_0 - V_{im}^{-1} \ln(1 - r)$, where t_0 is the current time and r is a random

number distributed on (0, 1). The use of the maximum collision frequency, to be corrected later

through a null-cross section technique, enables the time step to be chosen independently of

changes in the density of the collision partner, velocity, and cross section. Note that a separate

random number generator is used for each process requiring random numbers to avoid aliasing

effects.[21,22]

The time step for integrating the trajectory of the particle is determined by the minimum of the randomly chosen time to the next collision, the time required to cross a specific fraction of the computational cell based on the current velocity and acceleration, and a fraction of shortest rf period. In the bulk plasma, the particle is allowed to traverse 0.2-0.5 of a computational cell in any given update. As a surface is approached and the ion enters the presheath and sheath, the fraction of the computational cell that can be traversed in any given time step is reduced so that the particle energy at the time the surface is intersected is more accurately represented. The equations of motion of the particle are integrated for this time step; using a second order predictor-corrector method while linearly interpolating the electric fields produced by the FKPM as a function of position and phase during the low frequency cycle.

A potential collision occurs when the particle time reaches t_c. At this time, a series of random numbers are chosen to determine whether the collision is null and, if not, what type of collision occurs. The first random number satisfying $\omega_{i,j-1} < r < \omega_{ij}$ selects process j as the possible collision. If for a second random number, $r > v\sigma_j(v)N_j(\vec{r})/\max\left((v\sigma_j(v))_m N_{jm}\right)$ the collision is null, where $N_j(\vec{r})$ is the actual local density of the collision partner for process j and $v\sigma_j(v)$ is the current value of velocity and cross section. The collision is rejected and called null because the actual collision frequency at location $\vec{r}$ and velocity v is smaller than was used to determine the time to the next collision. In a null collision, the particle is simply not collided. Another time to the next collision is chosen, and the integration of the trajectory is continued. In the case of a real collision, the type of collision determines the energy loss and scattering angle. In the event of an identity changing collision, such as a charge exchange, the trajectories of both the new ion and the new hot neutral are followed.

45

The velocity components of the particle are recorded as a function of position (radius and height, ($\vec{r}$) and phase during the rf cycle, ϕ, with each advance of the particle trajectory to produce an ion velocity distribution $f(\vec{v}, \vec{r}, \phi)$ throughout the plasma. The particle's contributions to the distribution are weighted by the time the particle spends in the phase space cell. The $f(\vec{v}, \vec{r}, \phi)$ is then post-processed after execution of the HPEM to produce IEADs.

The charge exchange collisions are assumed to be long range. For symmetric charge exchange, the trajectory of the original ion is retained while changing it to a neutral particle. The ion is initialized as a new particle at the site of the collision, with a speed randomly selected from Maxwell-Boltzmann distribution and with randomly selected angular distributions. The temperature of the new ion is that of the former neutral that was computed in the FKPM. If the collision is consuming, indicating that the velocity distribution of the product of the collision is not being followed, the particle is deactivated.

The spatial mesh upon which velocity distributions are recorded typically has a finer resolution than that used in the FKPM. In Chapter 4, a finer submesh was used within the PCMCM in order to resolve ion transport from the bulk, through the presheath and sheath, and onto the wafer. Statistics on the velocity components of the ion trajectories were recorded as a function of position (radius and height above the wafer) and phase during the rf cycle. Due to the potentially large arrays that resulted from the recording phase, energy, position, only a specified portion of the plasma was submeshed to provide $f(\vec{v}, \vec{r}, \phi)$.
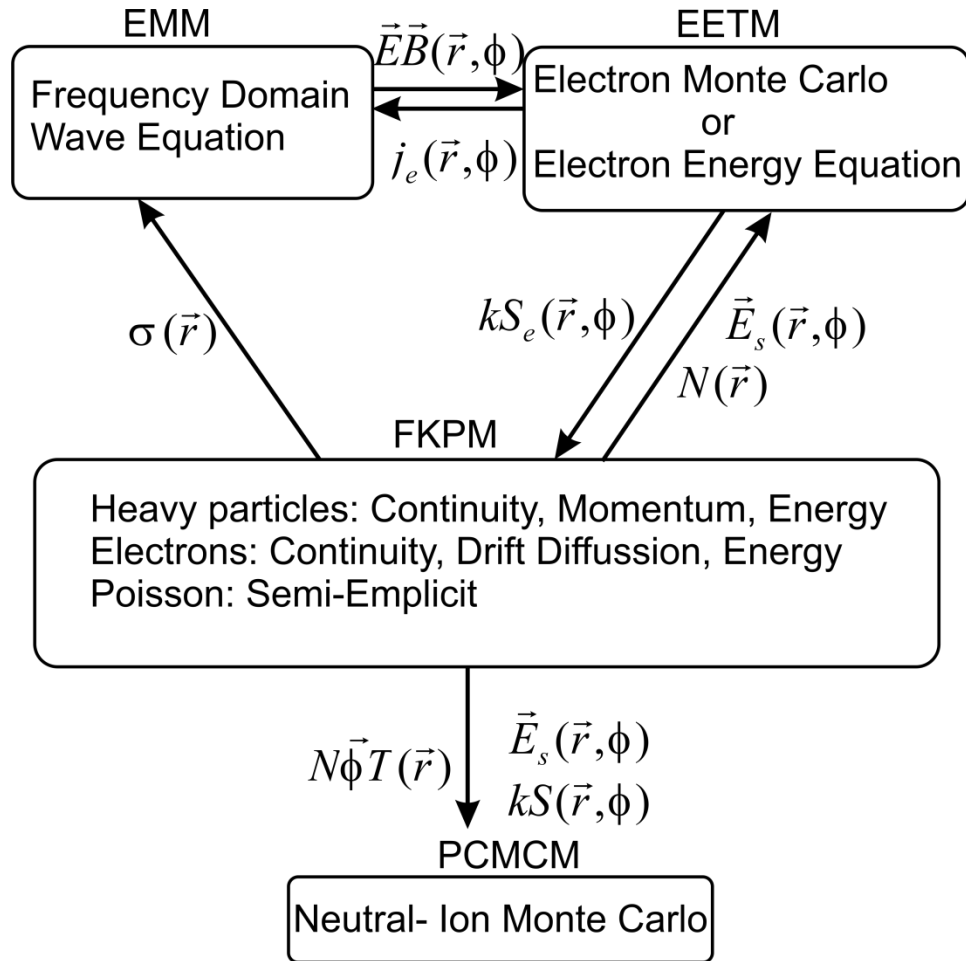
Fig. 2.1. Flow chart of modules information exchange used for this thesis.

2.7   References

1. V. Vyas and M. J. Kushner, J. Vac. Sci. Technol. A. **24**, 1955 (2004).
2. R. L. Kinder and M. J. Kushner, J. Vac. Sci. Technol. A. **17**, 76 (2001).
3. A. Agarwal and M. J. Kushner, J. Appl. Phys. **101**, 063305 (2007).
4. J. Lu and M. J. Kushner, J. Vac. Sci. Technol. A. **19**, 2652 (2001).
5. R. L. Kinder, A. R. Ellingboe and M. J. Kushner, IEEE Trans. Semicond. Manuf. **11**, 486 (1998).
6. M. J. Grapperhanus and M. J. Kushner, J. Appl. Phys. **81**, 569 (1997).
7. M. J. Grapperhanus, Z. Krivokapic and M. J. Kushner, J. Appl. Phys. **83**, 35 (1998).
8. M. J. Kushner, J. Appl. Phys. **94**, 1436 (2003).
9. D. Zhang and M. J. Kushner, J. Vac. Sci. Technol. A. **19**, 524 (2001).
10. M. J. Kushner, J. Phys. D. **42**, 194013 (2009).
11. Y. Yang and M. J. Kushner, Plasma Sources Sci. Technol. **19**, 055012 (2010).
12. S.-H. Song and M. J. Kushner, Plasma Sources Sci. Technol. **21**, 055028 (2012).
13. K. Rajaraman and M. J. Kushner, J. Phys. D: Appl. Phys. **37**, 1780 (2004).
14. P. L. G. Ventzek, T. J. Sommerer, R. J. Hoekstra and M. J. Kushner, Appl. Phys. Lett. **63**, 605 (1993).
15. R. L. Kinder and M. J. Kushner, J. Vac. Sci. Technol. A **17**, 2421 (1999).
16. S. L. Lin and J. N. Bardsley, J. Chem. Phys. **66**, 435 (1977).
17. C. M. Snowden. "*Introduction to semiconductor device modelling*", (World Scientific, Singapore, 1986).
18. D. L. Scharfetter and H. K. Gummel, IEEE Trans. Electronic Devices **ED-16**, 64 (1969).
19. W. H. Press, B. P. Flanney, S. A. Teukolsky and W. T. Vetterling, "*Numerical Recipes: The Art of Scientific Computing*", (Cambridge University Press, 1987).
20. SLAP Sparse Matrix Library, online at *www.netlib.org*.
21. H. R. Skullerud, J. Phys. B. **6**, 728 (1973).
22. M. J. Brennan, IEEE Trans. Plasma Sci. **19**, 256 (1991).

Chapter 3 MONTE CARLO FEATURE PROFILE MODEL

3.1   Introduction

The Monte Carlo Feature Profile Model (MCFPM) is a cell based Monte Carlo model, which simulates topographical on wafer feature evolution for semiconductor wafer fabrication.[1,2]   The model launches pseudo-particles with energy and angular distributions produced by the PCMCM in the HPEM for arbitrary radial locations on the wafer.   The pseudo-particles are statistically weighted to represent the fluxes of radicals and ions to the surface.   The model addresses various surface reaction mechanisms resulting in etching, sputtering, mixing, and deposition on the surface to predict profile evolution.   During the Monte Carlo integration, the trajectories of ion and neutral pseudo-particles are tracked within the feature until they either react or leave the computational domain.   To date, the MCFPM has advanced capabilities for predicting etching, stripping, atomic layer etching, ionized metal physical vapor deposition, and plasma enhanced chemical vapor deposition on various materials.[3-9]

With current feature dimension continue shrinking and new feature structures are being developed, developing a robust and accurate 3-d feature profile models is highly desired for semiconductor industry.   Some research attempts have been made.   Guo and Sawin studied surface roughening using a 3-d cellular Monte Carlo simulation.   The ion incidence angle was found a key parameter for forming the perpendicular and parallel ripple on planar feature surfaces.[10]   Tsuda *et al.* developed a 3-d Monte Carlo-based atomic-scale cellular model for

studying etching blank silicon substrate with Cl_2. The silicon surface roughness was found to be reduced by regulating the amount of etch-inhibitors.[11,12] The theoretical models such as level set method and string theory can also be used for studying surface evolution.[13,14] For example, Radjenović and Radmilović-Radjenović reported the surface roughness could be reduced by isotropic etching by demonstrating their 3-d simulation of surface topology evolution with level set method.[13] Besides the application in analyzing surface and line roughness, 3-d profile simulators have also been developed for optimizing complex processing such as atomic layer etching.[15] Although research has shown 3-d profile simulation has a great potential in reducing surface roughness and understanding plasma surface interaction, there is still a long way for investigating the 3-d ion incident influence of surface evolution and building up 3-d simulators which can address current and next generation feature patterns.

In this thesis, a 3-dimensional computational profile simulator (MCFPM 3-d) has been developed for plasma processing for complex feature layout patterns, in which 2-dimensional simulation may not be sufficient to resolve. The MCFPM 3-d inherits the platform of the MCFPM 2-d and contains a newly developed 3-d particle surface interaction algorithm. By doing so, the MCFPM 3-d is capable of evaluating 3-d pattern etching effects and switching between 2-d and 3-d simulation options.

An overview of MCFPM and the algorithms for particle motion are presented in Sec. 3.2. The new algorithms developed for MCFPM 3-d to address 3-d etching are described in Sec. 3.3. The surface reaction mechanisms applied in this dissertation for fluorocarbon etching of SiO_2/Si substrates and chorines etching of silicon are explained in Sec. 3.4.

3.2   Description of the Model

The MCFPM utilizes a rectilinear mesh in 2-d or 3-d having a fine enough resolution addresses the dimensions of the device. Each cell within the mesh may represent a different solid material or a mixture of materials. For example, a 2-d mesh can be used to resolve infinitely long trench in polysilicon as shown in Fig. 3.1 a and a circular via can be resolved in 3-d mesh as shown in Fig. 3.1 b. The mesh spacing can be adjusted from nanometer to micrometer. Each mesh cell is assigned a material identity (for example, photoresists, polysilicon and plasma), which may change during the profile evolution. Solid phase species are represented by the identity of the computational cell; gas phase species are represented by computational pseudo-particles.

3.2.1   Particle Initialization and Motion

In the MCFPM, pseudo-particles are launched to represent radicals and ions convecting towards the surface with their initial positions randomly chosen from several micrometers above the surface. The initial velocities of these particles are randomly selected from the given energy and angular distributions which are outputs of the HPEM. These distributions are flux weighted probability functions $F(\varepsilon,\theta,r)$ which are converted and normalized as cumulative distribution functions $f(\varepsilon,\theta,r)$ by:

$$f(\varepsilon,\theta,r) = \frac{F(\varepsilon,\theta,r)}{\iint F(\varepsilon,\theta,r)d\varepsilon d\theta},\tag{3.1}$$

where i is the species i, ε represents energy , θ represents angle and r represents location.

The particle launching frequencies are computed from the total flux of radicals or ions onto the substrate, so that each particle represents a fraction of the number of atoms in a mesh cell based on the gas-to-material weighting ratio:

$$W_g = \frac{1}{\gamma_{gs}} W_s,\tag{3.2}$$

where W_g is the gas particle weighting , W_s is the surface weighting, and γ is the gas-to-surface ratio, which was set to 1 for this dissertation.

After initialization, the pseudo-particle's trajectory is advanced in time with the electric fields produced by surface charging:

$$\vec{v}_i = \vec{v}_{i-1} + \frac{q\vec{E}}{m}\Delta t \text{ and } \vec{x}_i = \vec{x}_{i-1} + \vec{v}_i\Delta t,\tag{3.3}$$

where $\vec{v}$ and $\vec{x}$ represent the velocity and position of the particle, and subscripts indicate the former or current time step; q and m indicate the charge and mass of the particle, respectively; and Δt is the time-step taken by the particle. To date, the electric field $\vec{E}$ due to charging is set to be zero in the MCFPM 3-d because the effects of charging can be ignored in the majority of cases.[16] The MCFPM 2-d addresses the effects of surface charging on profile evolution by explicitly solving Poisson's equation with the Successive-Over- Relaxation method[17]: :

$$\nabla \cdot \varepsilon \nabla \Phi^{t+\Delta t} = -\rho^t .\tag{3.4}$$ where

Φ is the electrical potential in and around the feature for permittivity ε and charge density ρ. The charge density ρ is calculated by including the dispersal of charges due to conduction current by specifying conductivity σ for each material identity:

$$\frac{d\rho_j}{dt} = \frac{d}{dt}(\sum_i \frac{q_i}{V_j}) - (\nabla \cdot \sigma(-\nabla\Phi)),\tag{3.5}$$

where q_i is the charge of the incident particle i and V_j is the volume of mesh cell j.

When addressing the charging effect of the surface, electrons are simulated as low temperature isotropic fluxes which reach the feature during the low potential swing of the sheath

in order to macroscopically balance the ion currents. The top and bottom boundary conditions for potential are set to be Neumann boundary by assuming that the electric field above the feature matches the sheath field and the electric field below the feature is approximately zero. The left and right boundaries are assumed to follow a periodic Dirichlet condition.[18]

The following describes the lifetime of a particle. At any instant, the time step, Δt, is determined by the time required to move the minimum distance to a surface. Since the 3-d simulation uses a dynamic surface search algorithm, no surface information is available before a particle hits a solid cell. In the 3-d simulation, the time step is determined by limiting motion to a user-specified fraction of the mesh cell (typically, 1 mesh cell) for 3-d simulation. Based on this time step and the solution of Eq. (3.3), the new velocity and position of the particle is calculated. For the 2-d simulation, if the particle distance to a surface is still greater than one mesh cell, this new particle position is used to update the time step for its next move. Both MCFPM 2-d and 3-d contain an algorithm to avoid a gas phase particle for penetrating into the surface. If the particle is within one mesh cell of a surface, the particle is moved back to its previous position, the previous time step is halved, and the particle is moved again. This process is iterated until the particle moves within a fraction of the material containing cell, generally no longer than $0.2 \times$ cell width.

While the pseudo-particle is in the plasma, gas phase collisions are included in the particle trajectory calculation with a randomly chosen mean free path between collisions with an average value of user specified particle mean free path, which is determined by the process operating pressure. Although byproduct generation or gas phase particle consumption may modulate pressure inside the feature, the influence of pressure is not included in this work. The feature is etched with constant pressure. All gas phase collisions are assumed to be purely

elastic with isotropic scattering and no loss in energy. The final particle velocity after the collision is determined by applying a scattering matrix,

$$v_x = v \cdot (\cos\beta \cdot \cos\alpha \cdot \sin\theta \cdot \cos\phi + \cos\beta \cdot \sin\alpha \cdot \cos\theta - \sin\beta \cdot \sin\theta \cdot \sin\phi)$$
$$v_y = v \cdot (\sin\beta \cdot \cos\alpha \cdot \sin\theta \cdot \cos\phi + \sin\beta \cdot \sin\alpha \cdot \cos\theta + \cos\beta \cdot \sin\theta \cdot \sin\phi) , \quad (3.6)$$
$$v_z = v \cdot (-\sin\alpha \cdot \sin\theta \cdot \cos\phi + \cos\alpha \cdot \cos\theta)$$

where α and β are the polar and azimuthal Euler angles of the electron velocity prior to the collision; θ and ϕ are the polar and azimuthal scattering angles, and v is the particle velocity before the collision.

3.2.2   Energetic Particle Surface Interaction

The characteristics of the energetic particle surface interaction are determined by the energy and angular distributions and plasma surface mechanisms. The main source of energetic particles is from the ions accelerated through the sheath, which have hundreds eV of energies and angular spreads $<10^o$ from the vertical direction. With the assumption that the energetic ions neutralize upon interaction with the surface, there is no distinguishable difference between in-surface reaction mechanism of the energetic ions and the energetic neutrals.

In the MCFPM, a generalized reaction scheme of the ions and neutrals with the surface is applied for addressing any reactant-product combination reactions and energy dependent surface interactions. These processes are fed into the model through a list of the reactions in conventional chemical notation. Based on the specified reactions, the MCFPM constructs probability arrays for the reaction of plasma species with surface species. The classes of reactions include adsorption, passivation, ion activated etching, thermal etching, sputtering, ion surface neutralization, and re-emission. When a pseudo-particle hits a surface cell, a reaction is randomly chosen based on the probability arrays.

By referring to the work of Cheng *et al.*[19] and Graves *et al.*[20], the reaction probability for a particle of energy E incident onto a surface at an angle θ from the local vertical of the surface is assumed as:

$$p(\theta) = p_0 \left[\frac{E^n - E_{th}^n}{E_{ref}^n - E_{th}^n} \right] f(\theta), \tag{3.7}$$

where E_{th} is the threshold energy of the process n, E_{ref} is a reference energy, p_0 is the probability for a normal incidence at E_{ref} and $f(\theta)$ is the relative probability at the incidence angle θ, which is an empirical function typical of chemical enhanced sputtering with a maximum value near θ =60°. [20]

When a particle strikes a surface cell and does not participate in any surface reactions or it participates in a surface reaction that generates products in the gas phase, the particle or newly produced particles need to be reflected back into the plasma region. Both specular and diffusive particle reflections were considered. The particles which are desorbed or re-emitted from the surface are generally given thermal speeds and launched with a Lambertian angular distribution. When particles strike the surface at large angles with respect to the normal direction to the surface, specular reflection can occur.[21] To account for surface roughness on spatial scales not resolved by the model, the fraction between diffusive and specular reflection is specified. The energy of specular reflected particle is scaled such that the forward scattered particles retain the majority of their incident energy E_{inc}:

$$E_s(\theta) = E_{inc} \left(\frac{E_{inc} - E_{cutoff}}{E_{ts} - E_{cutoff}} \right) \left(\frac{\theta - \theta_{cutoff}}{90^o - \theta_{cutoff}} \right), \tag{3.8}$$

for $\theta > \theta_{cutoff}, E_{cutoff} < E_{inc} < E_{ts}$. In Eq. (3.8), E_{ts} represents the threshold for complete specular reflection, which is set to 100 eV. θ_{cutoff} represents the lower cutoff angle for specular reflection,

which is set to 60°. Particles having $\theta < \theta_{cutoff}$ or $E_{inc} < E_{cutoff}$ are assumed to experience diffusive scattering. Particles having $E_{inc} > E_{ts}$ are assumed to retain all of their energies subject to the angular correction. After determining the final reflected particle energy as a sum of both the specular and the diffusive reflected energies, the trajectories of reflected particles or re-emitted products are then tracked in the manner described by the particle motion section.

3.3   Surface Reaction Mechanisms

Because the surface reaction mechanism can be generally considered as an intrinsic property of the gas phase reactant species and the surface species, the reaction mechanism in the MCFPM is independent of process conditions. The process conditions such as the plasma source, operation pressures and gas chemistries, may determine the energies and magnitudes of the reactant fluxes. However, the surface reaction mechanism should persist.

In Chapters 5 and 6, the potential influence of controlling IEADs on plasma etching was studied through 2-d profile simulations of etching SiO_2/Si with an $Ar/CF_4/O_2$ gas mixture. The reaction mechanism for etching of SiO_2 and Si in fluorocarbon plasmas is described in detail in Refs. [4,5], and illustrated in Fig. 3.2.[22]   The etching of SiO_2 is dominantly through the formation of a fluorocarbon complex with SiO_2 on the surface activated by ion bombardment as the first step,

$$SiO_2(s) + I^+(g) \rightarrow SiO_2^*(s) + I^*(g),$$ (3.9)
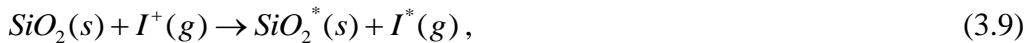
where SiO_2^* represents an activated site on surface, I^+ and $I*$ are ion and its hot neutral counterpart, respectively. The (s) and (g) indicate the phase of reactant or product, solid or gas. After surface activation, C_xF_y neutrals react with the activated SiO_2^* surface to produce a complex layer,

$$SiO_2^*(s) + C_xF_y(g) \rightarrow SiO_2C_xF_y(s)$$ (3.10)

Further deposition caused by C_xF_y neutrals produces a thicker polymer layer: $(C_xF_y)_n$. Energetic ions and hot neutrals penetrate this polymer layer and reach the complex to sputter it, with carbon from the polymer layer providing a means to remove the oxygen in the oxide,

$$SiO_2C_xF_y(s) + I^+(g) \rightarrow SiF_y(g) + CO_2(g) + I*(g) \tag{3.11}$$
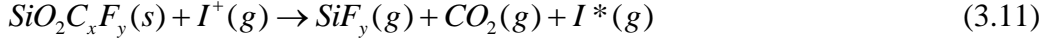
The remaining Si is etched dominantly by F atoms diffusing through the polymer layer, passivating the Si followed by ion activation, until the generation of SiF_4, which is a volatile product.

$$SiF_{n-1}(s) + F(g) \rightarrow SiF_n(s), \quad n < 4, \tag{3.12}$$

$$SiF_n(s) + I^+(g) \rightarrow SiF_n(g) + I*(g), \tag{3.13}$$

$$SiF_3(s) + F(g) \rightarrow SiF_4(g). \tag{3.14}$$

The thickness of the polymer layer can be controlled through the flux of the oxygen radicals O:

$$(C_xF_y)_n(s) + O(g) \rightarrow (C_xF_y)_{n-1}(s) + COF_x(g), \tag{3.15}$$

where the oxygen radical is generated by the electron impact dissociation of O_2.

Sputtering and re-deposition of the photoresist mask can be simulated with a similar mechanism. However, in this dissertation, all masks except for the experimental validation cases were assumed to be hard-masks (no reaction with any gas species).

In Chapter 7, 3-d patterning and circular via etching were investigated with the etching of Silicon in Ar/Cl_2 and He/Cl_2 plasmas. The inert gases in the gas mixture act as the source for energetic ions which deliver energy to the surface, but do not react with the surface. Therefore, surface contamination can be reduced. The reaction mechanism for silicon etching with chlorine plasma are modified from the work of Cheng *et al.*[13] and Meeks *et al.*[23] Briefly, the etching Si with Cl_2 occurs by first chlorinating the surface, forming $SiCl_n$. For example, the surface

chlorination with Cl atoms is expressed in Eq. (3.16).

$$Si(s) + Cl(g) \rightarrow SiCl(s)$$
$$SiCl_{n-1}(s) + Cl(g) \rightarrow SiCl_n(s), \quad n < 4,$$
(3. 16)

This surface chlorination is dominantly accomplished by Cl atoms, but can also be achieved by

Cl^+ and Cl_2^+. Etching of the poly-Si, $SiCl_n$, then occurs through subsequent ion activation which

generates a volatile product, $SiCl_4$:

$$SiCl_3(s) + Cl^+(g) \rightarrow SiCl_4(g),$$
(3. 17)

In this dissertation, the probability for an ion of energy ε activating an etch is dependent on the

scale of $\sqrt{\varepsilon - \varepsilon_0}$, where ε_0 is a threshold energy. Its value is assumed based on Cheng *et al.*. [19]

3.4   Three-Dimensional Monte Carlo Feature Profile Model (MCFPM 3-d)

As an extension of the MCFPM 2-d, the MCFPM 3-d is functionally equivalent to the 2-d

model with added dimensionality. Its coordinate is Cartesian (x-y-z). In order to simulate

complex 3-d features with multi-layer materials, a new mesh initialization algorithm was

developed which allows the model to adapt meshes generated by a commercial mesh generator.

Besides extending computational cell dimension from 2-d to 3-d, there exist other challenges in

performing 3-d simulation. For example, the computational burden of the 3-d Monte Carlo

method increases from $O(n^2)$ to $O(n^3)$, where n is the average mesh cell number in one

dimension. Moreover, the 2-d surface advancement technique needs to be extended to 3-d.

Determining particle reflection and sputtering direction in 3-d is also time consuming, expensive,

and complicated for surface represented by rectilinear mesh, which is considered as statistically a

rough surface. Therefore, a new surface advancement algorithm was developed to determine 3-d

surface and particle reflection. Overall, the MCFPM 3-d is built upon the MCFPM 2-d

considering particle trajectory in 3-d. A flowchart of current MCFPM, which supports both 2-d

and 3-d profile simulations, is shown in Fig. 3.3 a. In the next two sub-sections, the newly developed mesh input algorithm and the 3-d surface advanced algorithm will be described in detail.

3.4.1 3-d Mesh Generation

The mesh type for 3-d geometries needs to be generic enough such that reasonably arbitrary shapes representing multi-layer complex 3-d structures can be modeled. The simple 2-d mesh is adequate for analyzing a long trench. Typically, constructing a 2-d mesh is through a text file. In order to address 3-d meshes efficiently, the model provides two alternative methods for simulating different kinds of features. When the features contain complex structures, generating a 3-d mesh may be difficult and time consuming. The MCFPM 3-d is capable of importing a mesh in plot3d format, which can be generated by a commercial mesh generator such as CFD-GEOM[24]. With an interactive development environment, a 3-d mesh can be easily constructed and exported to MCFPM. If the pattern is simple and largely repeated in one-dimension, several 2-d slices with different patterns can be used through a text file, and MCFPM 3-d can duplicate those slices to generate a 3-d mesh, whose resolution and geometric scale can be adjusted via several parameters. With the 3-d mesh input algorithm, 3-d feature patterns (e.g. self-aligned contact and FinFET) can be simulated as shown in Fig. 3.4.

3.4.2 3-d Surface Advancement

In the MCFPM 2-d, all surface information (slope, position) is recorded in a lookup table, which is updated at a specified frequency. When a particle strikes a surface cell, the slope information can be used to reflect the particle. As a 3-d mesh typically contains more than 10^6 cells, calculating and recording surface through the entire computational domain is expensive. As the local surface information is only needed when a particle hits a solid cell, a dynamic

surface advancement algorithm was developed in the MCFPM 3-d as shown in Fig. 3.5. When a particle strikes a solid cell, a boundary-point-search is performed within the nearby cells. This search distance can be a small value to represent a rough surface or a large value for a smooth surface. Within the search region, if a cell has at least one face exposed to the plasma, it is considered as a boundary point and its positon is recorded. After searching all the cells in the region, those boundary points are used to perform a least square plane fit to calculate the best fit plane. That is, given a set of points, determine A, B, C and D, so that the plane Ax+By+Cz=D best fits the boundary points in the sense that the sum of squared errors between the points and the plane is minimized.[25]

Given a set of m boundary points P_i with position of (x_i, y_i, z_i), the sum of squared error Q is: [26-28]

$$Q = \sum_{i=1}^{m} (Ax_i + By_i + Cz_i - D)^2 .$$

(3. 18)

Therefore,

$$\frac{dQ}{dA} = \sum_{i=1}^{m} [2x_i(Ax_i + By_i + Cz_i - D)] = 0$$

$$\frac{dQ}{dB} = \sum_{i=1}^{m} [2y_i(Ax_i + By_i + Cz_i - D)] = 0 \quad ,$$

(3. 19)

$$\frac{dQ}{dC} = \sum_{i=1}^{m} [2z_i(Ax_i + By_i + Cz_i - D)] = 0$$

and

$$D = \frac{\sum_{i=1}^{m} (Ax_i + By_i + Cz_i)}{m} = A\frac{\sum_{i=1}^{m} x_i}{m} + B\frac{\sum_{i=1}^{m} y_i}{m} + C\frac{\sum_{i=1}^{m} z_i}{m} = A\bar{x} + B\bar{y} + C\bar{z} .$$

(3.20)

Subtracting Eq. (3.19) back to Eq. (3.18) produces a set of simultaneous equations:

$$
\begin{bmatrix}
\sum_{i=1}^{m}(x_i - \bar{x})^2 & \sum_{i=1}^{m}(x_i - \bar{x})(y_i - \bar{y}) & \sum_{i=1}^{m}(x_i - \bar{x})(z_i - \bar{z}) \\
\sum_{i=1}^{m}(x_i - \bar{x})(y_i - \bar{y}) & \sum_{i=1}^{m}(y_i - \bar{y})^2 & \sum_{i=1}^{m}(y_i - \bar{y})(z_i - \bar{z}) \\
\sum_{i=1}^{m}(x_i - \bar{x})(z_i - \bar{z}) & \sum_{i=1}^{m}(y_i - \bar{y})(z_i - \bar{z}) & \sum_{i=1}^{m}(z_i - \bar{z})^2
\end{bmatrix}
\begin{bmatrix} A \\ B \\ C \end{bmatrix}
=
\begin{bmatrix} 0 \\ 0 \\ 0 \end{bmatrix}
\quad (3.21)
$$

In order to avoid a trivial solution, the imposed condition on the coefficients of the plane is assumed as $A^2 + B^2 + C^2 = 1$. Solving Eq. (3.21) becomes an eigenvalue problem which can be solved through Jacobi algorithm.[29] The Jacobi method will return three sets of eigenvector [A, B, C] representing the best, intermediate and worst planes. The best plane is recognized by containing the smallest eigenvalue, and its eigenvector is a surface normal vector, which is orthogonal to the best fit plane.

With the surface normal vector and the particle velocity vector, the direction of the specular reflection is first calculated with respect to the surface normal and then converted back to the Cartesian coordinate system. The conversion is performed by matrix in Eq. (3.6), where α and β are the polar and azimuthal Euler angles of the incident velocity (illustrated and marked in Fig. 3.6); θ is the polar angle of the scatting, ϕ is the azimuthal scattering angles which is randomly chosen in the interval $[0, 2\pi)$ and v is the particle incident velocity.

The diffusive reflection on the surface contains a Lambertian angular distribution with respect to the surface normal as illustrated in Fig. 3. 8 a. This diffusive velocity also needs to be converted in Cartesian coordinate system and summed up with the specular reflection velocity. According to Euler's rotation theorem, any plane (X, Y, Z) rotation from Cartesian coordinate (x, y, z) may be described using three angles α, β and γ as illustrated in Fig. 3.7.[30,31]. The angle α represents a rotation around the z axis, β represents a rotation around the line of nodes

(intersection of the x-y and the X-Y coordinate planes) and γ represents a rotation around the Z axis.

In MCFPM 3-d, the surface plane and its normal vector can be assumed as a new coordinate system, where the surface normal vector is a rotated Z axis from z axis. The surface plane as a rotation result of x-y plane as shown in Fig. 3.8 b. By assuming the new X axis overlaps on the interaction line (N) of the x-y and the X-Y coordinate plane, the Euler angle γ can be neglected, and the diffusive velocity in x-y-z coordinate can be converted from the following equation:

$$\vec{v}_{dif} = z(\alpha)x(\beta)\vec{V}_{dif}$$

and   (3.22)

$$z(\alpha) = \begin{bmatrix} \cos\alpha & -\sin\alpha & 0 \\ \sin\alpha & \cos\alpha & 0 \\ 0 & 0 & 1 \end{bmatrix}, x(\beta) = \begin{bmatrix} 1 & 0 & 0 \\ 0 & \cos\beta & -\sin\beta \\ 0 & \sin\beta & \cos\beta \end{bmatrix}$$

The final particle reflection velocity is a sum of the diffusive and the specular reflection. With the above described algorithm, 3-d particle bombardment can be properly addressed and a flowchart of the newly developed 3-d particle bombardment is listed in Fig. 3.3 b.

Fig. 3.1. Examples of profile meshes with different material identities marked with various colors. a) An example of a profile with 2-d mesh to resolve trench, b) an example of a profile with 3-d mesh to resolve circular via.
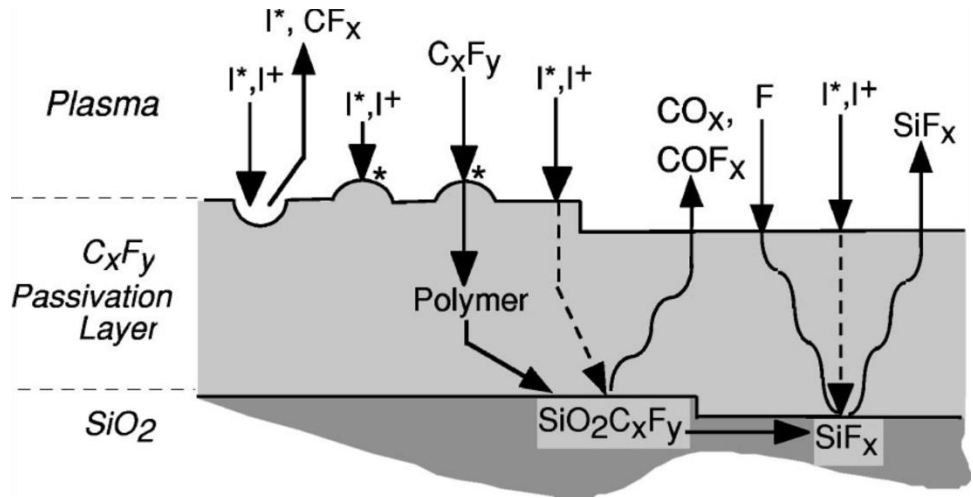
Fig. 3.2. Schematic of surface reaction mechanism for fluorocarbon etching of SiO_2/Si with I^+ referring to an ion and I^* referring to a hot neutral. The dashed line represents energy transfer through the polymer layer and the curved solid lines represent species diffusion through the polymer.[22]
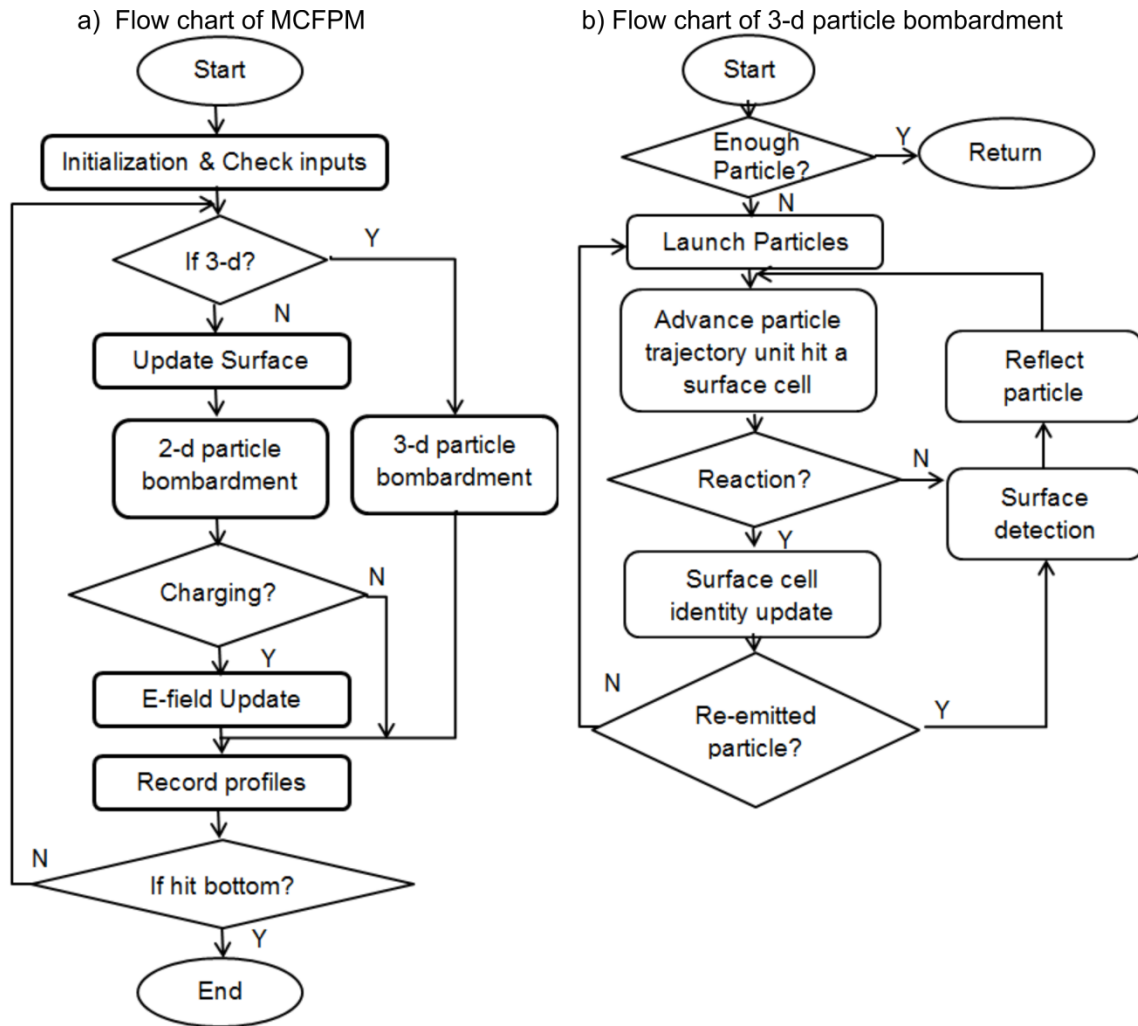
Fig. 3.3.a) A flow chart of the main program of MCFPM. b) A flow chart of the 3-d particle bombardment routine which is called by the main program.
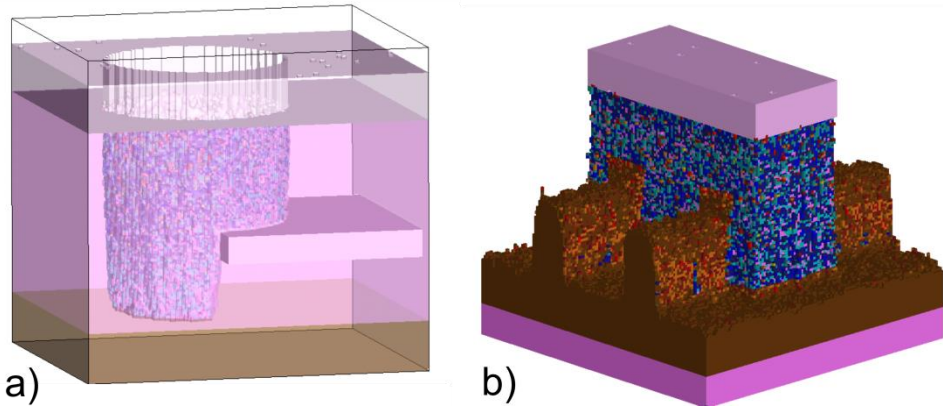
Fig. 3.4. Example of results from MCFPM 3-d. a) Self-aligned contact, and b) FinFET.
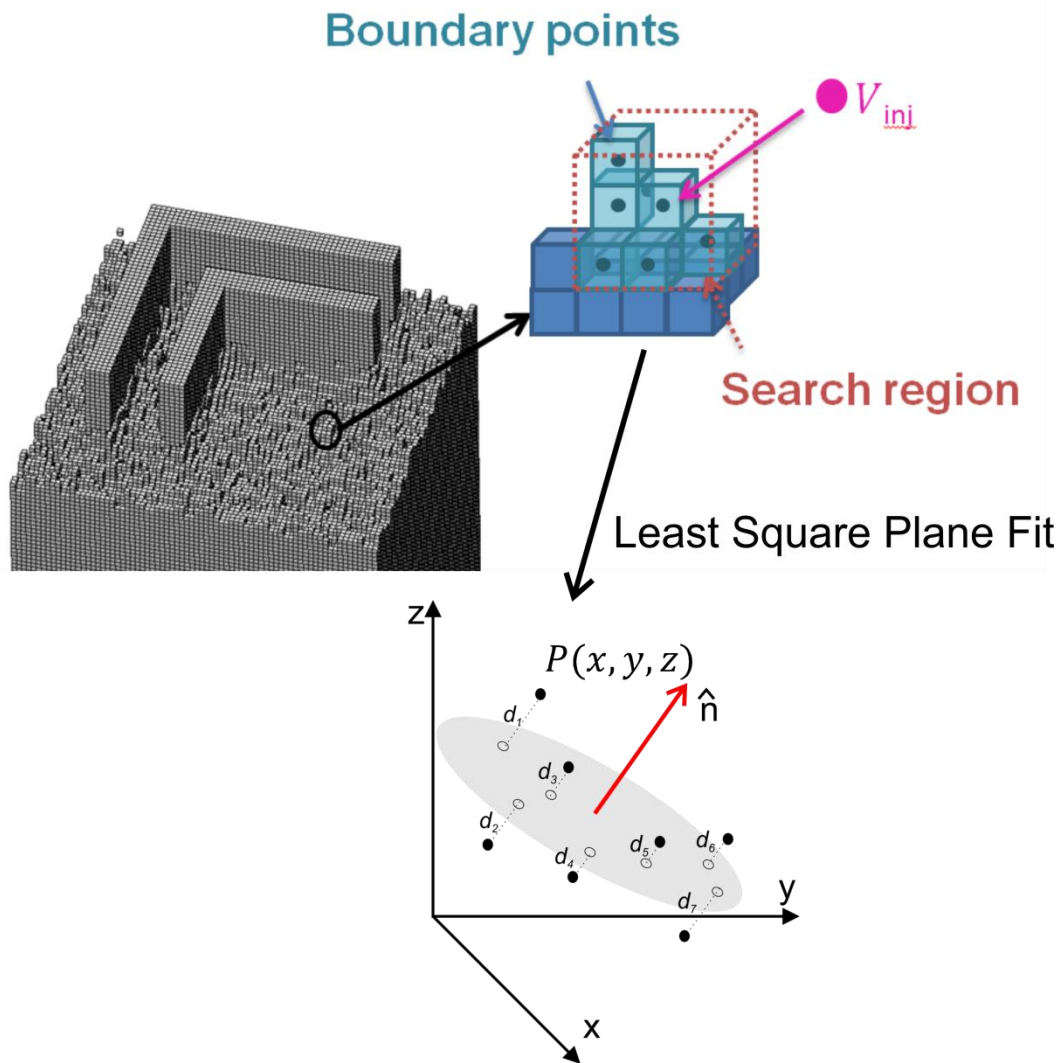
Fig. 3.5. Illustration of the 3-d surface advance algorithm. When a particle hits a solid cell, its neighboring cells will be checked to record the position of the boundary cells within the search region. Those positons are sent to perform a least square plane fit and return a normal vector of the best fit plane.
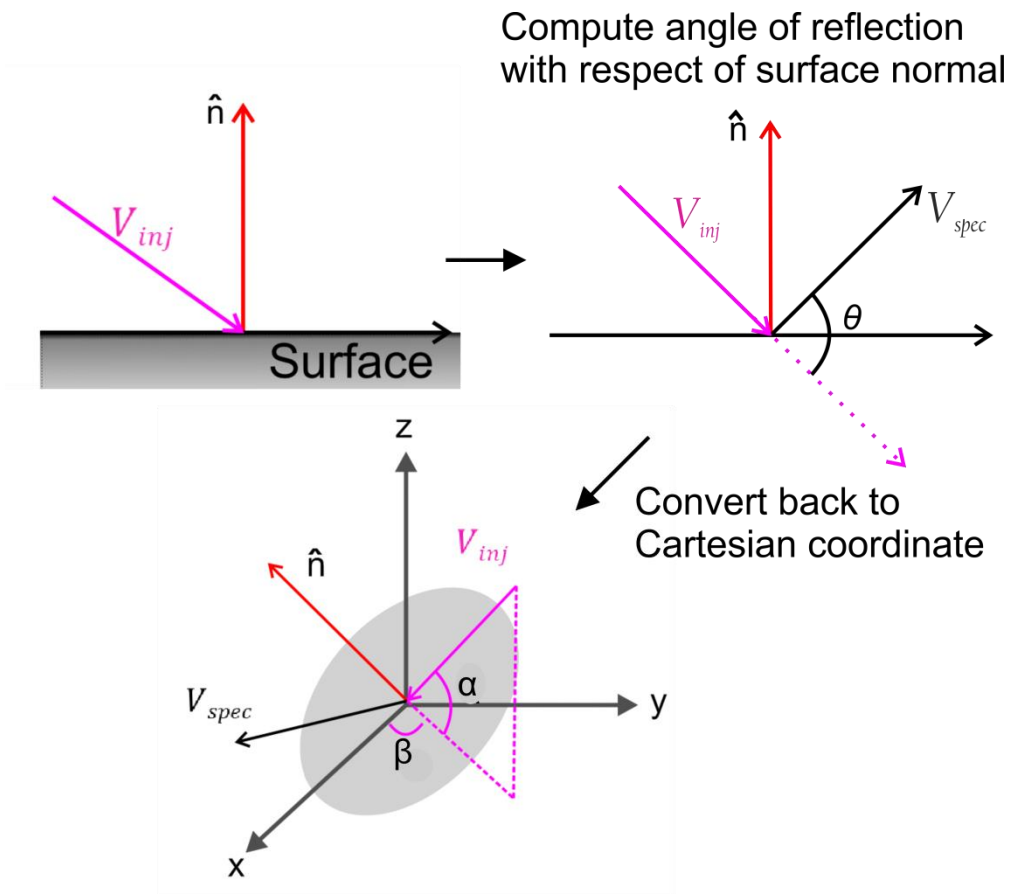
Fig. 3.6. Illustration of computing the specular reflection. The specular reflection angle is initially computed with respect to the surface normal and then converted back to the Cartesian coordinate system.
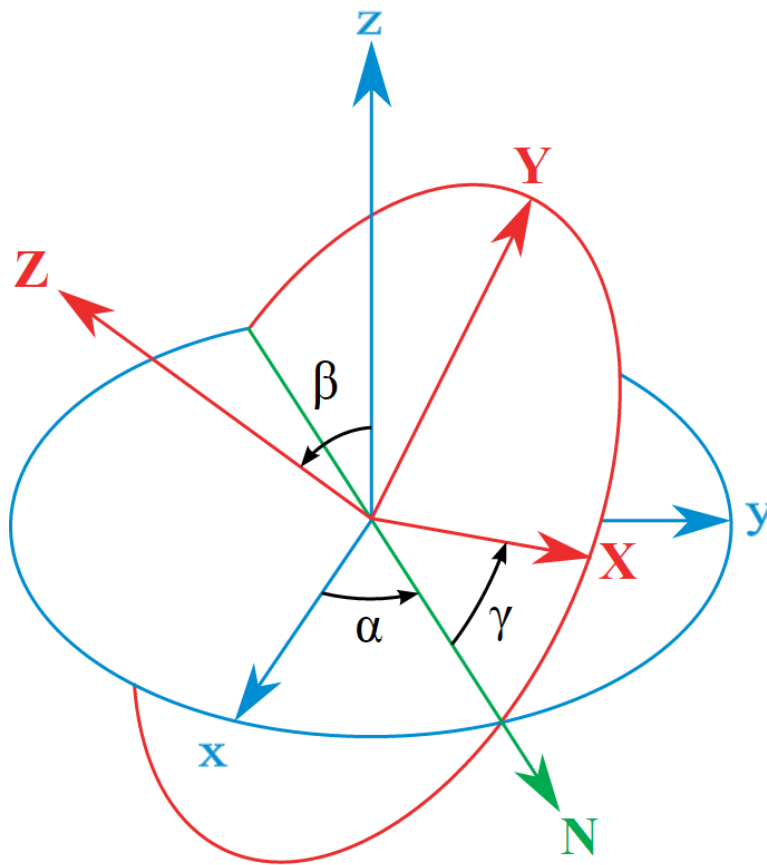
Fig. 3.7. Three Euler angles representing relationship between the rotated system (X-Y-Z, shown in red) and the original system (x-y-z, shown in blue). The line of nodes (N) is shown in green.[31]
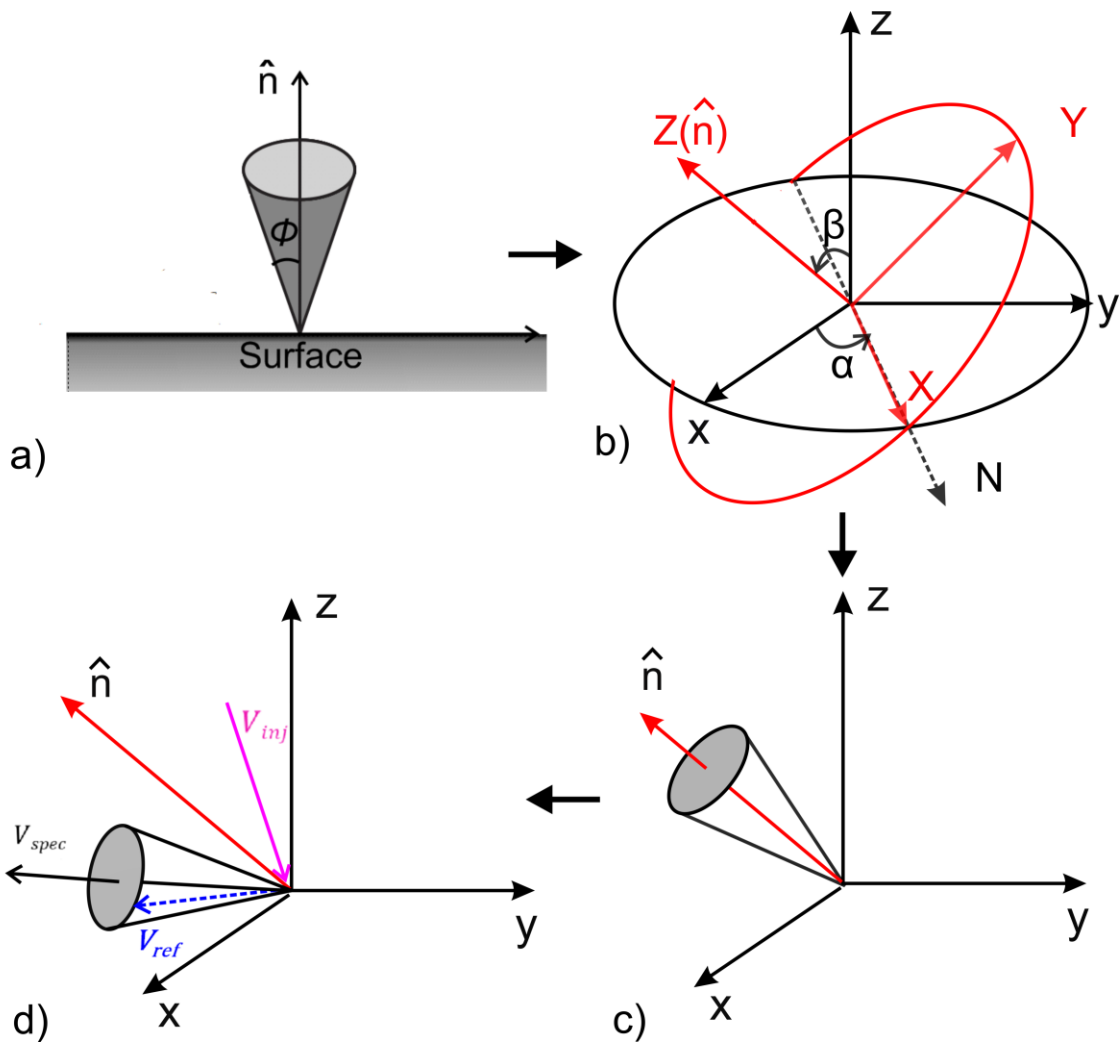
Fig. 3.8. Illustration of computing the diffusive reflection angle. a)The diffusive reflection of a particle will have a Lambertian-like distribution with respect to the surface normal. b) By assuming the surface normal as a rotated Z axis from the Cartesian z axis and rotated X axis overlay on the intercross line of the X-Y and x-y lane, only two Euler angles are needed. c) With the Euler angles, the diffusive reflection is calculated back to the master coordinate system. d) Final particle reflection is a sum of both specular and diffusive reflection.

3.6 References

1. R. J. Hoekstra, M. J. Grapperhaus, and M. J. Kushner, J. Vac. Sci. Technol. A **15**, 1913 (1997).
2. R. J. Hoekstra and M. J. Kushner, J. Vac. Sci. Technol. B. **16**, 2102 (1998).
3. L. Lu and M. J. Kushner, J. Vac. Sci. Technol. A **19**, 2652 (2001).
4. A. Sankaran and M. J. Kushner, J. Vac. Sci. Technol. A **22**, 1242 (2004).
5. A. Sankaran and M. J. Kushner, J. Vac. Sci. Technol. A **22**, 1260 (2004).
6. P. L. G. Ventzek, M. J. Grapperhaus, and M. J. Kushner, J. Vac. Sci. Technol. B **16**, 3118 (1994).
7. A. Agarwal and M. J. Kushner, J. Vac. Sci. Technol. A **27**, 37 (2009).
8. M. Wang and M. J. Kushner, J. Vac. Sci. Technol. A **29**, 051306 (2011).
9. J. Shoeb, M. M. Wang and M. J. Kushner, J. Vac. Sci. Technol. A **30**, 041303 (2012).
10. G. Wang and H. H. Sawin, J. Phys. D: Appl. Phys. **42**, 194014(2009).
11. H. Tsuda, N. Nakazaki, Y. Takao, K. Eriguchi, and K. Ono, J. Vac. Sci. Technol. B. 32, 031212 (2014).
12. N. Nakazaki, H. Tsuda, Y. Takao, K. Eriguchi, and K. Ono, J. Appl. Phys. 116, 223302 (2014).
13. L. H. A. Leunissen, R. Jonckheere, K. Ronse, and G. B. Derksen, J. Vac. Sci. Technol. B. **21**, 3140 (2003).
14. B. Radjenović and M. Radmilović- Radjenović, World Journal of Nano Science and Engineering. **4**, 84-89 (2014).
15. P. Moroz and D. J. Moroz, ECS Transactions, 50, 61 (2013).
16. T. Nozawa, T. Kinoshita, T. Nishizuka, A. Narai, T. Inoue and A. Nakaue, Jpn. J. Appl. Phys. **34** 2107 (1995).
17. O. Axelsson, *Iteractive Solution Methods*, (Cambridge University Press, New York, 1994).
18. A. Cheng and D. T. Cheng, Engineering Analysis with Boundary Elements. 29, 268 (2005).
19. C. C. Cheng, K. V. Guinn, V. M. Donnelly, and I. P. Herman, J. Vac. Sci. Technol. A **12**, 2630 (1994).
20. C. F. Abrams and D. B. Graves, J. Appl. Phys. **86**, 2263 (1999).
21. D. J. Cooperberg, V. Vahedi and R. A. Gottscho, J. Vac. Sci. Technol. A **20**, 1536 (2002).
22. A. Sankaran and M. J. Kushner, Appl. Phys. Lett, **82**, 1824 (2003).
23. E. Meeks, Sandia National Laboratory, private communication, 1995.
24. CFD-GEOM introduction webpage, online at https://www.esi-group.com/software-services/virtual-environment/cfd-multiphysics/ace-suite/cfd-geom.
25. D. Eberly, *Least squares fitting of data*, online at http://www.magic-software.com
26. S. A Islam, *Math Notes—Least Squares Plane*, online at http://www.sbg.bio.ic.ac.uk/~islam/plane.html
27. V. Schomaker, J. Waser, R. E. Marsh, and G. Bergman, Acta Cryst **12**, 600 (1959).
28. D. M. Blow, Acta Cryst **13**, 168(1960).
29. L. N. Treffethen and D. Bau, *Numerical Linear Algebra*, (the Society for Industrial and Applied Mathematics. 1997) p. 225-227.
30. G. Arfken, *Mathematical Methods for Physicists,* (3rd ed. Orlando, FL: Academic Press, 1985) p. 198-200.
31. Euler angles, Wikipedia page, online: https://en.wikipedia.org/wiki/Euler_angles

Chapter 4 SPACE AND PHASE RESOLVED ION ENERGY AND ANGULAR DISTRIBUTIONS IN SINGLE- AND DUAL-FREQUENCY CAPACITIVELY COUPLED PLASMAS

4.1   Introduction

Acknowledging the complexity of rf sheath dynamics in dual frequency Capacitively Coupled Plasmas (CCPs), many analytical, computational and experimental efforts have addressed the shape of the ion energy angular distributions (IEADs) delivered to the substrate.[1-5].

Georgieva *et al.* [6] performed one-dimensional particle-in-cell (PIC) modeling of both single and dual-frequency CCPs discharges in Ar, CF_4 and N_2 mixtures at a pressure of 30 mTorr. The ion energy distribution (IED) was narrow with one outstanding peak in the single frequency (13.56 MHz) case, whereas the IED became wide and bimodal in the dual-frequency (2 MHz + 27.12 MHz) case. When the high frequency is applied, the electron density and consequently the sheath width oscillate at the high frequency (*HF*) within the low frequency (*LF*) cycle. This oscillation in sheath width, in addition to the additional *HF* voltage, is reflected in the IEDs. There is also evidence of electron and negative ion accumulation in the sheath during the anodic portion of the *LF* cycle, which additionally thins the sheath. In experiments performed by Gans *et al* [7,8] rapid oscillations of the sheath thickness was also observed in a dual-frequency (2 and

27.12 MHz) CCP using a He/O$_2$ gas mixture at 490 mTorr. During this oscillation, the maximum electron energy gain from stochastic heating can be expected around the minimum voltage of the *LF* component when the sheath edge is close to the electrode. An additional energy gain and increased excitation can be observed at the maximum sheath extension. The strong dual-frequency coupling brings about these complex electron dynamics within the sheath.

One conclusion of these works is that the *HF* has an important (or at least non-negligible) effect on the IEAD delivered to the substrate. An implied conclusion of these works is that as long as the *HF* is used to produce the plasma, the shape of the IEAD cannot be truly independent of plasma production.[9] Since the sheath thickness is then a function of power deposition, there are second order effects that shape the IEAD, particularly at higher pressures where the sheath may become collisional.

These interdependencies motivate examining low pressure (a few mTorr) inductively coupled plasmas (ICPs) having multiple frequencies applied to the substrate.[10] In these systems, the plasma production is more nearly a unique function of the ICP power and the sheath is essentially collisionless. The *LF* and *HF* biases can be independently varied without significantly affecting ion or radical production.

The majority of studies to date have emphasized the shape of the IEADs when the ions strike the substrate since this is the quantity that directly affects the feature in microelectronics fabrication. The final shape of the IEAD is the end result of the transit of ions from the bulk plasma, through the presheath and through the sheath. To better understand the dynamics of IEADs as they strike the substrate, it is instructive to track the formation of the IEAD as ions transit from the bulk plasma to the wafer. Experimentally, this investigation may be conducted using laser-induced fluorescence (LIF) which is capable of measuring components of the ion

velocity distributions (IVD) as a function of position in the sheath and phase during the rf cycle.[11-15] For example, Jacobs *et al*. have used LIF to measure IVDs in a pulsed ICP reactor.[16] They observed ions approaching the Bohm velocity entering the sheath. They also applied this technique to tracking ions transiting a 2.2 MHz rf biased sheath as a function of phase. The phase resolved IVDs vary dramatically throughout the cycle, in accordance with theory.[17]

This chapter reports a computational investigation of the time and spatial development of IEADs in low pressure ICPs having single and multi-frequency substrate biases as the ions transitions from the bulk plasma, through the presheath and sheath, and are incident onto the substrate. The choices of geometry, biasing pressure and gas mixture were made to enable comparison to a companion experimental investigation of IVDs in the sheath as a function of phase using LIF. The simulations were performed with an ion Monte Carlo Simulation embedded within the HPEM, which is discussed in detail in Chapter 2 and briefly described in Sec. 4.2. IEADs for single frequencies applied on the substrate while varying frequency and pressure, and comparison to experiment, are discussed in Sec. 4.3. IEADs for dual frequency excitation are discussed in Sec. 4.4. The concluding remarks are in Sec. 4.5.

4.2   Description of the Model

The model (HPEM) used in this study is a two-dimensional fluid-hybrid plasma equipment model, which has been previously discussed in detail in Chapter 2.[18] The intent of the experimental and computational investigation was to study the transport of argon ions which have accessible transitions for LIF. Due to details having to do with the design of the reactor and substrate, a Si wafer had to be in place while the LIF measurements were made. The resulting sputtering of the Si wafer eventually coated optical access windows. So O_2 was added to the

argon in order to prevent the buildup of Si on the reactor windows. Simulations were conducted in Ar/O$_2$ gas mixtures. The reaction mechanism for Ar/O$_2$ plasma used in the model is discussed in Ref. [19]. The species in the mechanism were Ar, Ar* [representing four sublevels of Ar(4s)], Ar$^+$, O$_2$, O$_2^+$, O$_2^*$[O$_2$(1Δ)], O, O*[O(1D)], O$^+$, O$^-$ and e. The mechanism included major reactions which directly affect the species density such as ionization, oxygen dissociation, charge exchange, electron attachment and electron impact collisions.

4.3 Plasma Properties in an ICP Reactor with a Single Frequency rf Biased Substrate

The model representation of the ICP reactor used in this study is schematically shown in Fig. 4.1. The upper portion of the plasma chamber consists of an alumina dome ($\varepsilon/\varepsilon_0 = 9.0$), 18 cm in radius and 13.5 cm above the wafer, flaring out to an alumina ring having radius of 24 cm. Ten turns of the ICP coil sit on top of the ring and on the vertical surface of the dome. This antenna is driven at 400 kHz. Gas is injected through several nozzles on the top of chamber.

The substrate consists of a dielectric chuck with a center electrical feed to a biased substrate in contact with the wafer. The outer wall of the chamber is grounded. A conductive Si wafer ($\varepsilon/\varepsilon_0 = 12.5$, $\sigma = 0.01$ Ω^{-1}cm^{-1}), 30 cm in diameter, sits in electrical contact with the substrate which is surrounded with a dielectric focus ring ($\varepsilon/\varepsilon_0 = 8$, $\sigma = 10^{-6}$ Ω^{-1}cm^{-1}). The annular pump port is at the bottom of the computational domain coaxially surrounding the substrate. During execution of the code, the flow rate through the pump port is adjusted to keep the pressure inside the plasma chamber constant.

The base operating conditions are Ar/O$_2$ = 80/20 with a flow rate of 50 sccm at a pressure of 2 mTorr. The ICP coils delivered 480 W. The substrate bias is 2 MHz. with a fixed 500 V rf bias with -400 V dc self-bias. All voltages in this article refer to voltage amplitude. I chose to

specify the voltages and biases on the substrate instead of setting a power, allowing the system to seek its own voltage to deliver the desired power. This allows a more straight forward comparison of IEADs when other parameters are changed. In later cases, a *HF* bias (10 – 60 MHz) is additionally applied to the substrate.

4.3.1   IEADs with a Single LF

The reactor scale plasma properties are shown in Fig. 4.2 for the base case conditions. The peak plasma density is 1.8×10^{11} cm^{-3} which is sustained by a bulk electron temperature of $T_e = 4.2$ - 4.3 eV. The total positive ion density is 2.5×10^{11} cm^{-3}, yielding a peak electronegativity of 0.28, which is calculated from $1 - \frac{\Sigma[n^+]}{[e]}$. The maximum gas temperature is 462 K. The inductively coupled coils provide the majority of power deposition to maintain the high-bulk plasma density. The contributions to ionization by the rf bias, either in terms of heating the bulk electrons or producing ionization by secondary electrons, is small. The computed bulk ionization rate is calculated to be one order larger than the secondary ionization rate.   In the middle of the plasma, the ion temperature $T_{ion} = 0.15$ eV whereas in the near presheath, T_{ion} is at most a few eV due to collisions. So in general, $T_{ion} < T_e$ is assumed in the following discussion.

For the base conditions where only a single *LF* rf bias is applied, τ_{ion}/τ_{rf} is not small for Ar$^+$.[3,22] The ion transit time τ_{ion} can be estimated by [20]

$$\tau_{ion} = 2(\frac{s^2 M_i}{2q<V_s>})^{\frac{1}{2}}[(1+\frac{k_B T_e}{2q<V_s>})^{\frac{1}{2}} - (\frac{k_B T_e}{2q<V_s>})^{\frac{1}{2}}] \tag{4.1}$$

where *s* is the sheath thickness, M_i is the ion mass and $<V_s>$ is the time-average sheath potential. The electron density n_e at the edge of the sheath is 9.8×10^{10} cm^{-3} and so the ratio τ_{ion}/τ_{rf} in this case is estimated to be 0.45.

76

For rare gas in low pressure, the charge exchange collision is the dominant ion-neutral collision. Therefore, the momentum transfer collision is neglected for this study. At 2 mTorr, the mean free path of Ar^+ for charge exchange with Ar and O_2 is ≈ 1.5 cm, which is much larger than the sheath thickness and the vast majority negative ions are confined to the bulk plasma. Therefore, the sheath is essentially collisionless. The time averaged IED for Ar^+ at the mid-radius of the wafer [location labeled *middle* in Fig. 4 .1(b)] as a function of height above the wafer from the bulk plasma through the presheath and sheath is shown in Fig. 4.3 a. The discontinuities with increase in energy are caused by the discreteness of the mesh used in collecting statistics. All IEDs are separately normalized to unity for clearly illustrating statistics and easily comparing at different spatial and time points. The boundary between the presheath and sheath is approximately where the ion energy begins to increase from its nearly constant value in the presheath, and is approximately 4 mm. The Bohm velocity is not used for defined the sheath boundary here as the argon and oxygen have different masses. The sheath is composed from different ion species. At a height of 4.5 mm, ions are already well into the presheath, having an average energy of near 10 eV as shown in Fig. 4.3. In the bulk plasma and near-presheath, the IED is essentially thermal. When ions enter the sheath, the electrical field in the vertical direction accelerates the ions to higher energy during the cathodic portion of the cycle and forms a bimodal distribution, which can be seen to form starting at about 2 mm above the wafer.

IEADs as a function of height from the bulk plasma (7 cm above the wafer) to the wafer averaged over the rf cycle are shown in Fig. 4.4. (Similar as the IEDs, all IEADs are separately normalized to unity.) The IEADs from sheath the boundary (4.5 mm height) to the wafer are shown within 15 degrees of the vertical on an energy scale extending to 900 eV. IEADs at

greater heights are shown within 90 degrees of the vertical on an energy scale extending to 10 eV. In the bulk plasma, the average ion energy is about 0.15 - 0.3 eV and the IEAD has essentially an isotropic distribution. The narrowing of the angular distribution due to the anisotropic ambipolar electric field begins at about 4 cm above the wafer, where the axial component of ambipolar electric field, E_z = -0.29 V/cm (or E/N = 725 Td). At 1 cm above the wafer, the average energy is about 3 eV and the distribution has narrowed to 30 degrees, with E_z = -1.74 V/cm (or E/N = 4,350 Td). Entering the sheath proper is in part indicated by the elevation of the low energy component of the IEAD above thermal, which occurs at about 2 mm. It is at this point that the IEAD splits into a bimodal distribution. The formation of bimodal double peak distribution was explained in Sec. 1.3.

As ions transit through the presheath and enter the sheath (between 3.5 mm and 4.5 mm), the IEDs first uniformly accelerate a few eV before separating into two bimodal peaks, low and high energy. The initial uniform acceleration occurs in that part of the presheath where charge separation is small and there are few cyclic dynamics in the electric field. The fields at this point are still largely ambipolar. Between 3.5 and 2.6 mm, the sheath proper begins with cyclic variation in the electric field, which then produces the bimodal structure which narrows in angle as the vertical component of the IED begins to dominate. For these conditions, the sheath is essentially collisionless, and so once the ions enter the sheath, their trajectories are ballistic. The width of the IED, ΔE, continues to increase as ions transit through the sheath with the final width being 700 eV prior to striking the wafer. This width can be approximated analytically by [21,22]

$$\Delta E = \frac{V_{so}\tau_{rf}}{\pi\tau_{ion}} \quad , \tag{4.2}$$

where V_{so} is the amplitude of the rf sheath voltage drop, which is about 900 V here. Based on our estimate of $\tau_{rf}/\tau_{ion} = 2.2$-$2.3$, the analytical estimate of ΔE is 630 eV. The differences are largely due to defining where the edge of the sheath precisely sits. Because the sheath edge oscillates with the rf cycle, the sheath thickness used for calculating ion transit time is estimated from a time averaged result.

In microelectronics fabrication, it is highly desirable to have both a uniform ion flux and a uniform IEAD to the edge of the wafer so that devices can utilize the entire area of the wafer. (This is termed minimizing *edge exclusion.*) IEADs were separately collected over the center of the wafer (averaging from r = 1-3 cm), the middle of the wafer (r = 7-9 cm) the outer portion of the wafer and above the focus ring (r = 15-16 cm). These IEADs are shown in Fig. 4.5 a. The decrease in energy over the focus ring is a consequence of the capacitance of the focus ring being smaller than that of the wafer and smaller than that of the sheath. The voltage across the sheath results from voltage division between the capacitance of the sheath, the capacitance of the substrate and the resistance of the bulk plasma. Since the capacitance of the focus ring is smaller than the wafer, the focus ring charges more rapidly and so removes voltage from the sheath, producing a lower energy IEAD. A decrease in peak energy of 30-40 eV and a broadening in angle of the IEAD are found in the transition region. This broadening is surprisingly large at higher energy, which is the result of cyclic generation of radial components of the electric field.

Electric field unit vectors as a function of height are shown in Fig. 4.5 b averaged over the rf cycle. The electric field transitions from essentially perpendicular to the wafer to having radial components 3-4 mm from the edge of the wafer. Due to current being collected asymmetrically during the rf period, there are time averaged radial components that point both inwards and outwards as a function of height, which contributes to broadening of the IEAD.

Having electric field components that point in only one direction would shift the IEAD to one side. For example, during the anodic portion of the rf cycle, the capacitance of the dielectric focus ring close to the edge of the wafer more rapidly changes than the capacitance of the sheath. Electron current is therefore directed towards the focus ring for only a portion of the cycle.

The development of the IEAD as ions transition from the bulk plasma to the wafer is shown in Fig. 4.6 for an rf frequency of 2 MHz as a function of height and phase during the period. For these conditions, $\tau_{ion}/\tau_{rf} \approx 0.45$. IEADs are shown at 8 phases during the rf cycle along each row in the figure, with each row corresponding to a different height above the wafer. The IEADs shown are averaged over that 1/8 of the period. The applied voltage crosses zero from negative to positive at $\phi = 0$, and from positive to negative at $\phi = \pi$. In the right four columns, the rf bias is negative. During this cathodic portion of the cycle, the sheath potential is positive and ions are strongly accelerated during these phases. During this cathodic portion of the cycle, the ions progressively extend to higher energies while narrowing in angle as the wafer is approached.

In the left columns of Fig. 4.6, the rf bias is positive. During this anodic portion of the cycle, the sheath potential reduces to nearly the floating potential. During this portion of the period, ions retain energies and angular widths akin to that at the edge of the presheath until about 1.5 mm above the wafer. Even with the acceleration that occurs in the last 1 mm above the wafer, the wafer receives predominantly low energy ions of broader spatial extent during the anodic portion of the cycle. IEADs at 3.5 mm above wafer (about 0.5 mm beyond the edge of the presheath) are broad in angle at all phases with only significant acceleration (to about 50 eV) at the peak of the cathodic portion of the cycle. At the peak of the anodic portion of the cycle, the IEADs are nearly unchanged from their shapes in the presheath. Approaching the wafer, the

80

IEADs in the cathodic portion of the cycle extend higher energy and narrow in angle as the vertical velocity component increases while the horizontal component remains nearly constant.

The width in energy of the IEADs at any given phase is a function of the averaging time, here 1/8 of the cycle – the shorter the averaging time the narrower will be the energy spread. The IEADs during the first and last quarter of the cathodic portion of the cycle appear to be broader in energy since the dV/dt is larger during this averaging period. At the peak of the anodic portion of the cycle, the ions remain at nearly their presheath energies until approaching within 1 mm of the wafer. This implies that the presheath may extend nearly all way to the wafer during certain phases of the rf cycle. The bimodal character of the IEAD obtained for $\tau_{ion}/\tau_{rf} \approx 0.45$, is clearly composed of ions that arrive at the substrate at different phases of the rf cycle.

The IEADs for 2 MHz from 2 to 20 mTorr are shown in Fig. 4.7. With increasing pressure, the mean free path of the Ar^+ ion decreases, though even at 20 mTorr (mean free path $\approx$ 1.5 mm) there are few collisions in the sheath. The plasma density usually increases with pressure. However, the density kept dropping as the pressure increased upon 20 mTorr with fixed flow rate 150 sccm. The dominant effect is a reduction in the plasma density with increasing pressure, which increases the sheath thickness since the bias voltage is constant. With the thicker sheath, the transit time of the ion increases which narrows the ΔE of the IEAD.

4.3.2   IEADs with a Single HF

As the substrate bias frequency increases significantly above a few MHz, τ_{ion}/τ_{rf} increases above unity, and so the ions sample the oscillations of the sheath over multiple cycles. For sufficiently high frequencies, electron heating from the bias may begin to make a contribution to the plasma density. For example, the electron density is shown in Fig. 4.8 for rf bias frequencies

of 10-60 MHz. (See Fig. 4.2 for the values at 2 MHz.) For purposes of comparison, the rf bias voltage amplitude (500 V) and dc self-bias (-400 V) are constant and the same values as for 2 MHz. With electron heating scaling as ω^2,[23] the power deposition from the rf bias increases from 508 W at 2 MHz (dominantly ion acceleration) to 2370 W at 60 MHz, the latter having electron heating exceeding that due to the inductive coils. As a result, the peak electron density increases with increasing bias frequency from 2.3×10^{11} cm^{-3} at 10 MHz to 4.8×10^{11} cm^{-3} at 60 MHz. Because 60 MHz largely modifies plasma densities, which interferes the independent control of ion flux, it would be unusual to use a single 60 MHz frequency at these voltages as the substrate bias in an ICP reactor. This parameterization over frequency using a fixed voltage is for the purpose of investigating scaling laws.

The IEADs and IEDs of Ar$^+$ onto wafer are shown in Fig. 4.9 for frequencies of $2 - 60$ MHz. The ΔE of the IEDs progressively decrease and converge on the average sheath potential as the frequency increases due to the increase in τ_{ion}/τ_{rf}. Tsui [24] first demonstrated these trends using PIC simulations of a current-driven collisionless rf plasma sheath. The IEDs from the bulk plasma to and through the sheath for frequencies of 10-60 MHz for otherwise the base-case conditions are shown in Fig. 4.10. (Note the difference in energy scales for the near-wafer region, 0-4 mm and the presheath, 4-9 mm) The IEDs in the presheath are not particularly sensitive to frequency. Since the sheath thickness does not appreciably change with frequency (the voltage is fixed and the plasma density changes by less than a factor of 2), the penetration of electric fields from the sheath into the bulk plasma does significantly change. As a result, there is not a large change in the electric fields in the presheath and the IEDs remain thermal for all frequencies to a height of about 4.5 mm. The structure of the IED suggests that as the frequency increases, the high energy component of the IED converges toward the average sheath potential

while the low energy component dissipates. Once the transit time exceeds one rf period as frequency increases, the all of the ions experience high electric fields at some point during the cathodic portion of the cycle. As a result, the low energy component of the IED dissipates.

The IEADs as a function of phase for frequencies of 10 – 60 MHz at a height of 0.5 mm above the wafer are shown in Fig. 4.11. The phases, ϕ, refer separately to each frequency with the voltage crossing zero (negative to positive) at $\phi = 0$ and the peak of the cathodic portion of the cycle occurring at $\phi = 3\pi/2$. As the frequency and τ_{ion}/τ_{rf} increase, the phase variation in the IEADs and so the phase variation in ion fluxes to the substrate dissipate. However, even at 30 MHz there is significant phase modulation – the average ion energy varies by 95 eV over the rf cycle. At 60 MHz, this variation decreases to 50 eV.

4.3.3   Comparison to Experiment

Laser induced fluorescence measurements of IVDs were conducted using the experimental setup, techniques and chamber described in detail in Refs. [16,17].   The LIF measurements produce IVDs (which are converted to IEDs) as a function of height above the wafer, radial position across the wafer, and phase during the rf cycle. The ICP reactor was run continuously at 480 W at a fill pressure of 0.5 mTorr. This lower pressure was necessary to avoid quenching of the fluorescence by collisions with neutrals. A 2.2 MHz bias was pulsed at 10 Hz and run at an 11% duty cycle. This produces a sufficiently long pulse length that the IEDs are in a quasi-steady state. The amplitude of the applied bias was 300 V, with a dc self-bias of approximately -300 V.

IVD measurements were phase locked and taken during 8 phases of the rf cycle. IEDs for these 8 phases at a radius of 11 cm (4 cm from the edge of the wafer) are shown in Fig. 4.12 as a function of height above the wafer, 5.2 mm to 2 mm. (IVDs were not obtained at lower

heights due to the low LIF signal.) Ions are shown accelerating from the bulk plasma through the presheath and into the sheath. During the cathodic portion of the cycle (phases π - 2π) ions begin accelerating towards the wafer at larger heights above the wafer, a consequence of the thickening of the sheath during the cathodic cycle. During the anodic cycle (phases 0 - π) the sheath thins and ions drift towards the wafer to lower heights with IEDs resembling that of the presheath. For $\phi = \pi/2$ - $3\pi/4$, the presheath IED is retained to a height of 3.6 mm, and significant acceleration does not occur until at height of 2 mm. These trends are essentially the same as the computed IEADs shown in Fig. 4.6.

The narrowing of the IEADs when transitioning from the presheath to the sheath are experimentally demonstrated by the results shown in Fig. 4.13 where time averaged IEADs are shown at several heights above the wafer at a radius of 12.4 cm. Since the LIF measurement of the thermal ion distribution function was power broadened, the perpendicular distribution function widths were scaled so that ions in the bulk plasma bulk are at ambient temperature. The angular distribution narrows as ions traverse the sheath and approach the wafer. The ions at the edge of the presheath may have an angular skew that is straightened traversing the sheath. Similar trends are also observed and discussed in detail in our 2 MHz single frequency IEADs results as shown in Fig. 4.4.

Predictions for the IEDs extend from the bulk plasma through the sheath to the wafer at phases of $\phi = \pi$ (most cathodic) and $\phi = 0$ (most anodic) are shown in Figs. 4.14 and 4.15 for an inner radius (112 mm) and at the wafer edge (148 mm). Comparing to the experimental results (Figs. 4.16 and 4.17), the model predicts a similar range of energies ($350 - 400$ eV) at 1.2 mm above the wafer at phase $\phi = \pi$. For the least negative bias, $\phi = 0$, the maximum energy is about 50 eV at 1.2 mm above and reach the wafer at $50 - 100$ eV. The double-peaked nature of

the IED begins at the sheath edge at about 4 mm. At this low frequency of 2 MHz, there is a clear separation in phase of the low and high energy components of the IEDs regardless of radial position above the wafer. The details of IEDs near the edge of the wafer are sensitive to the charging of the focus ring, its dielectric constant and subtleties of its geometrical relationship to the edge of the wafer. The simulation predicts an edge effect of only 10 eV difference in the maximum of the IED since the sheath is fairly uniform in this reactor. The experimental results (Figs. 4.16 and 4.17) confirmed this trend. The maximum energy at the surface of the wafer extends to 720–730 eV at the inner radius and 690–700 eV at the edge of the wafer, somewhat higher than that implied by experiments, 650 eV.

4.3.4   Dual Frequency IEADs

With single frequency excitation, the IEADs, at least for Ar^+, at high frequencies diminish their dependence on phase during the rf cycle beginning at about 30 MHz. Therefore, to investigate dual-frequency excitation, the combinations of 2 MHz with 10, 20 and 30 MHz are focused in this part of study. This is also convenient from a computational standpoint since the periods are integral multiples of each other. Firstly, the IEADs were investigated as a function of phases with equal amplitudes of the *LF* and *HF* biases, 400 V. IEADs for a *HF* of 10 MHz, 20 MHz and 30 MHz are in Figs. 4.18, 4.19 and 4.20 for 0.5 mm above the wafer. The approximate sheath potential is shown in part (a) of each figure. Rows in part (b) of each figure corresponds to 1/5 of the *LF* cycle (200 ns), matching the columns shown by dotted lines in part (a). The first two and half rows correspond to the anodic part of the *LF* cycle (minimum *LF* sheath potential). The second two and half rows correspond to the cathodic part of the *LF* cycle (maximum *LF* sheath potential). For the 10 MHz case, this results in one *HF* cycle for each row of part (b). For 20 and 30 MHz, each row corresponds to 2 and 3 *HF* cycles.

The IEADs for 2+10 MHz shown in Fig. 4.18 reflect the variation previously observed for single frequency biases. However, there is a phase delay compared with the instantaneous sheath potential, which can be seen when comparing to the IEADs for single 2 MHz and 10 MHz (Figs. 4.6 and 4.11). For the most anodic phases of the *LF*, there is little phase variation of the IEADs attributable to the *HF*. There is more phase variation during the cathodic portion of the *LF* cycle. The maximum variation in the sheath potential by the *HF* during the anodic phase is the *HF* amplitude. With only the *LF*, the sheath potential would be essentially constant during the anodic phase due to the electropositive nature of the plasma. With the amplitudes of the *LF* and *HF* being equal, portions of the *LF* anodic cycle appear to be cathodic due to the *HF* oscillation of the sheath. The oscillation is at most the *HF* amplitude. In the cathodic phase of the *LF*, the sheath potential varies by twice the amplitude of the *HF*. The phase variation resulting from single frequency 10 MHz excitation (see Fig. 4.11) is significantly larger than phase variation during a 10 MHz cycle for the dual frequency excitation. The maximum energy of IEADs is lower than the maximum instantaneous sheath potential 1200 V (sum of the *LF* and *HF* amplitudes plus dc self-bias), which occurs during the last two 10 MHz cycles. This is likely a consequence of the ion transit time being longer during the short overlap of the cathodic portions of both *LF* and *HF* cycles.

IEADs for 2+20 MHz are shown in Fig. 4.19 where each row in the figure corresponds to 2 *HF* cycles. The phase modulation of the IEADs, even on the *LF* cycle, is suppressed compared to the 2 MHz and 2+10 MHz cases. There is certainly modulation corresponding to the *HF* but even this modulation is suppressed compared to the single frequency 20 MHz case. This modulation is further suppressed during the anodic portion of the *LF* cycle. These trends are reinforced by the IEADs for 2+30 MHz shown in Fig. 4.20. With increasing frequency, the

modulation in energy of the IEAD decreases. The oscillation is about 200 eV at 20 MHz and 100 eV at 30 MHz. Assuming the sheath thickness does not change with the change in *HF*, the ions experience more *HF* cycles during one *LF* cycle at 30 MHz, which results in more averaging over the *HF* cycle. Therefore, the IEADs for 2+30 MHz mainly follow the *LF* sinusoidal waveform with small a small modulation due to the *HF*. During the anodic portion of *LF*, both 2+20 MHz and 2+30 MHz have similar IEADs with a minimum energy of 200 eV, which is about the average of *HF* amplitude. For the cathodic portion of *LF*, IEADs for both 2+20 MHz and 2+30 MH reach maximum energies of 900 eV, which is less than the sum of maximum *LF*, average *HF* amplitude and dc self-bias. This is likely a consequence of the ions not being able to respond to the *HF*.

The ion transit time is partially dependent on the sheath thickness, and so the modulation of the IEADs and the apparent phase delays with respect to the maximum sheath potentials may be a consequence of variations in sheath thickness. Wang and Wendt [25] found that the sheath thickness is sensitive to the electric field and space charge density at the sheath edge in low pressure high density plasma tools. Experiments performed by Gans *el at* [7,8] also obtained rapid oscillation of the sheath edge due to coupling of both high and low frequencies. The relative oscillation in the sheath thickness was investigated by examining the modulation in plasma density at the sheath edge, assuming that the sheath thickness will scale with $n_e^{-1/2}$.

The electron density and implied sheath thickness for dual frequency excitation over one *LF* cycle are shown in Fig. 4.21. The relative sheath thickness is larger during the last several *HF* periods in all cases, which corresponds to the cathodic portion of the *LF* period. The thicker sheath implies a longer ion cross time and perhaps explains the phase delay in the IEADs discussed above. The large sheath thickness for 10 MHz at the end of fourth *HF* cycle is at the

coincidence of the peak of the cathodic *LF* and *HF* cycles. This thicker sheath may explain why the IEAD fails to reach the maximum sheath potential at this phase. (See Fig. 4.18.) The fact that the sheath is thicker during the cathodic portion of the *LF* for all *HF* contributes systematically to the phase delay. For 20 and 30 MHz, the variation in sheath thickness is small, and so the phase delay is smaller than at 10 MHz. During the anodic portion of the *LF* cycle, the sheath thickness has less variation and so the ion transit time has less variation.

The just discussed results were for equal amplitudes of the *LF* and *HF* voltages. The IEADs are sensitive functions of the ratio of these amplitudes.[4,26] For example, time averaged IEADs onto the wafer are shown in Fig. 4.22 for 2+30 MHz having V_{HF}/V_{LF} = 0.5, 1.0 and 2.0. The time averaged IEADs in all cases show multi-peaks with the addition of the *HF* bias. The low ratio of V_{HF}/V_{LF} produces an IEAD similar to that for a single frequency 2 MHz as the *LF* voltage dominates the sheath potential, and the ions have difficulty responding to the *HF*. Nevertheless, adding *HF* does enable the ions to experience higher electric fields and so does narrow the angular spread compared with single frequency case. In all cases, the average energy of the IEAD corresponds to the average sheath potential over the *LF* cycles.

The multiple peaks observed in the time averaged IEADs onto the wafer come from ion dynamics occurring at different phases. These trends are shown in Figs. 4.23 and 4.24, where IEADs are plotted at 0.5 mm above the wafer for 2+30 MHz with V_{HF}/V_{LF} = 0.5 (Fig. 4.23) and V_{HF}/V_{LF} = 2.0 (Fig. 4.24). IEADs follow the instantaneous 2 MHz sheath potential with the addition of the average 30 MHz contribution to the sheath potential. In the V_{HF}/V_{LF} = 2.0 case (Fig. 4.24), the average sheath potential is larger during the anodic portion of the *LF* cycle, thereby elevating the IEADs to higher energy though in a phase dependent manner. This produces modulation in the IEAD during the anodic portion of the cycle that is preserved as

peaks in the on-wafer IEADs. There is more modulation during the anodic *LF* cycle as the *HF* dominates the sheath dynamics. For the $V_{HF}/V_{LF} = 0.5$ case, the sheath potential is lower in the anodic phases of *LF* cycle, which results in a broader IEAD.

4.4 Concluding Remarks

The properties of IEADs as ions transit from the bulk plasma through the presheath and sheath in an industrial ICP reactor with a capacitively coupled substrate bias were computationally investigated for single and dual frequency excitation. There is significant phase variation in the IEADs as a function of height up to frequencies as high as 30 MHz for Ar^+ ions. At low frequencies, the presheath extends nearly to within 1 mm of the wafer during the anodic portion of the cycle and so the IEADs remain low energy and broad in angle during this portion of the cycle. As a result, the bimodal IEAD contains a low energy, broad angular component arriving during the anodic portion of the cycle and a high energy, narrow angular component arriving during the cathodic portion of the phases. When increasing frequency, the bimodal distribution is known to transit into a single peak. The transition appears to occur by first losing the low energy component. This is due to the presheath no longer extending as close to the wafer during the anodic portion of the cycle. These trends are corroborated by LIF measurements of IVDs as ions transit the sheath. With dual-frequency excitation, time averaged IEADs incident onto the wafer have multiple peaks. These peaks can be correlated with phase dependent energy oscillations and phase delays due to the interference between the *LF* and *HF*, and perhaps some phase dependent thickening of the sheath. The ratio of the voltage amplitudes of the *LF* and *HF* sources is an important parameter to control these phase variations.

Although this chapter investigated the fundamental plasma physics issue, it is advisable for real industrial application. The results of ion kinetics represent a fundamental advance in the

application of diagnostics for materials processing plasma. Understanding the tendency of ion kinetics under complex sheath dynamics provides insights for process engineers when they want to optimize certain processes which depend on ion energy and angular distributions.
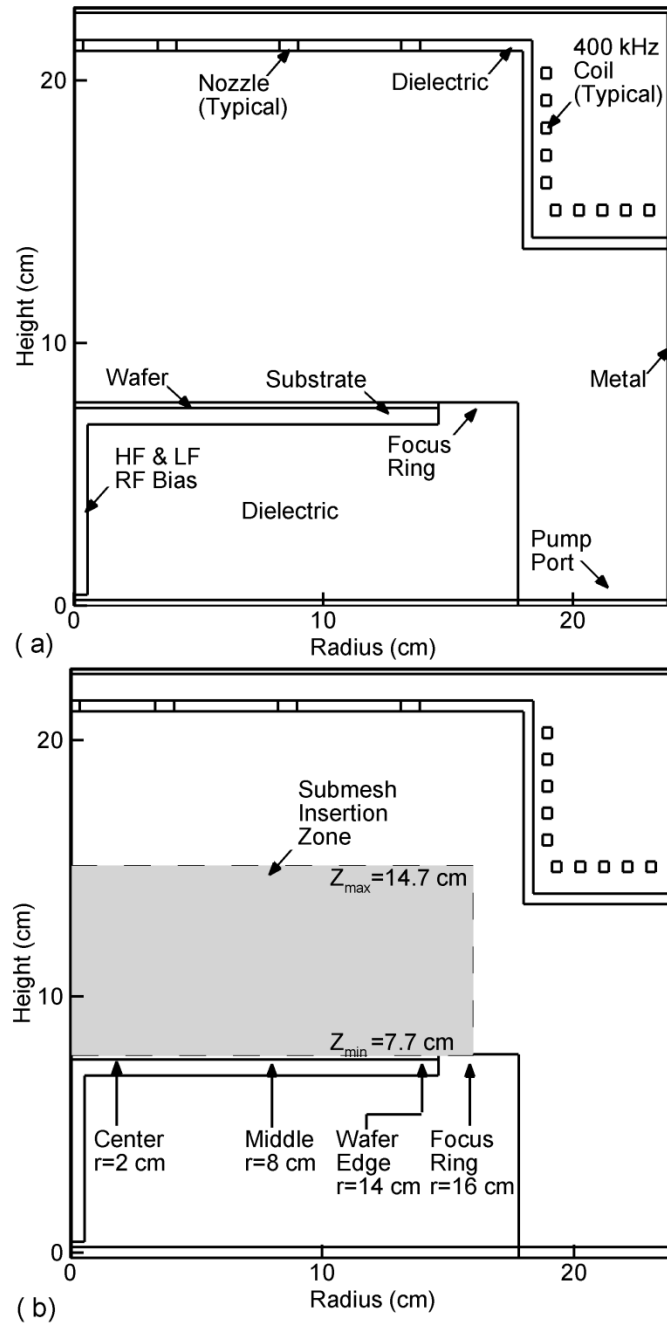
Fig. 4.1. Properties of the ICP reactor. a) Schematic showing the wafer on a substrate capacitively powered at *LF* and *HF* surrounded by dielectric focus rings. The 10-turn ICP coil surrounds the top of the reactor and is operated at 400 KHz. b) The submesh insertion zone where IEAD will be analyzed. The radial positions where IEADs will be plotted are labeled.
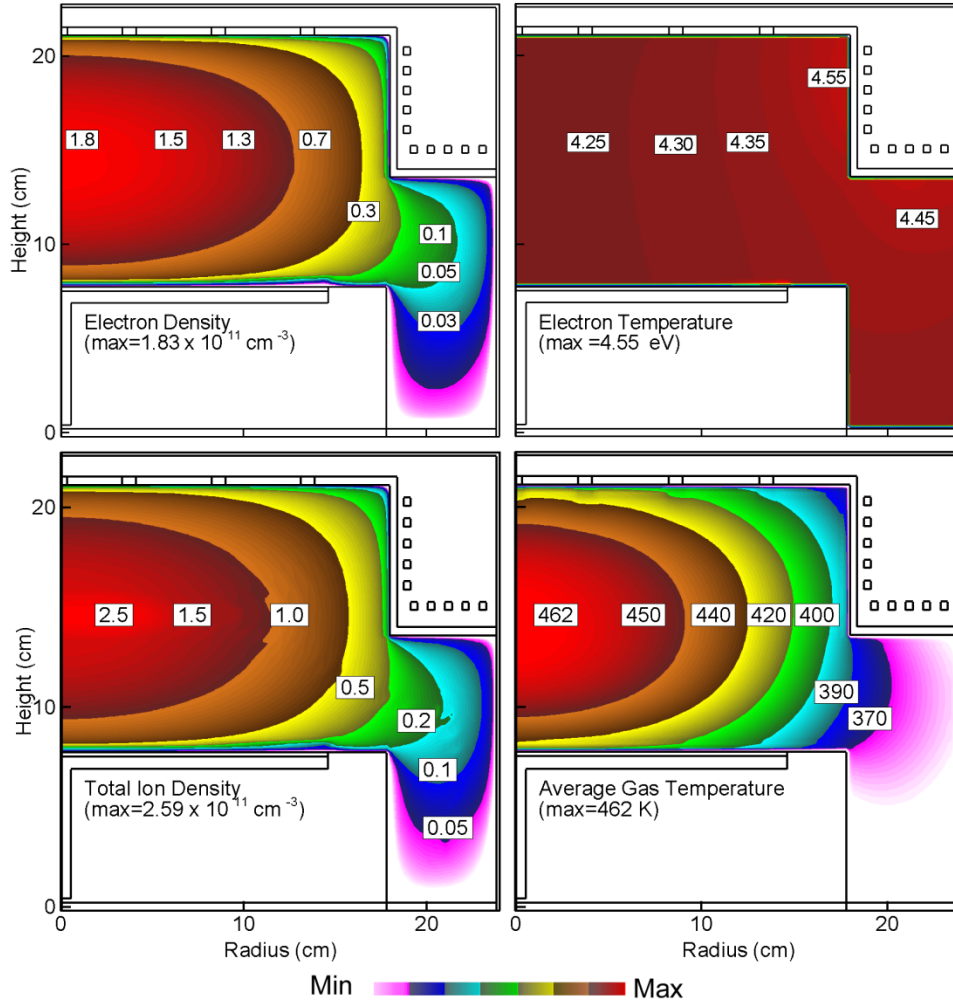
Fig. 4.2. Time averaged plasma properties for the base case conditions (Ar/O$_2$=80/20, 2 mTorr, 50 sccm, coils are powered at 480 W 400 kHz. *LF*=2 MHz, V$_{LF}$ =500 V and dc self-bias=-400 V). a) Electron density, b) electron temperature, c) total positive ion density and d) average gas temperatures. The electron and ion densities are log-scales with contour labels having units of 10^{11} cm^{-3}. The electron temperature and average gas temperature are in linear-scales.
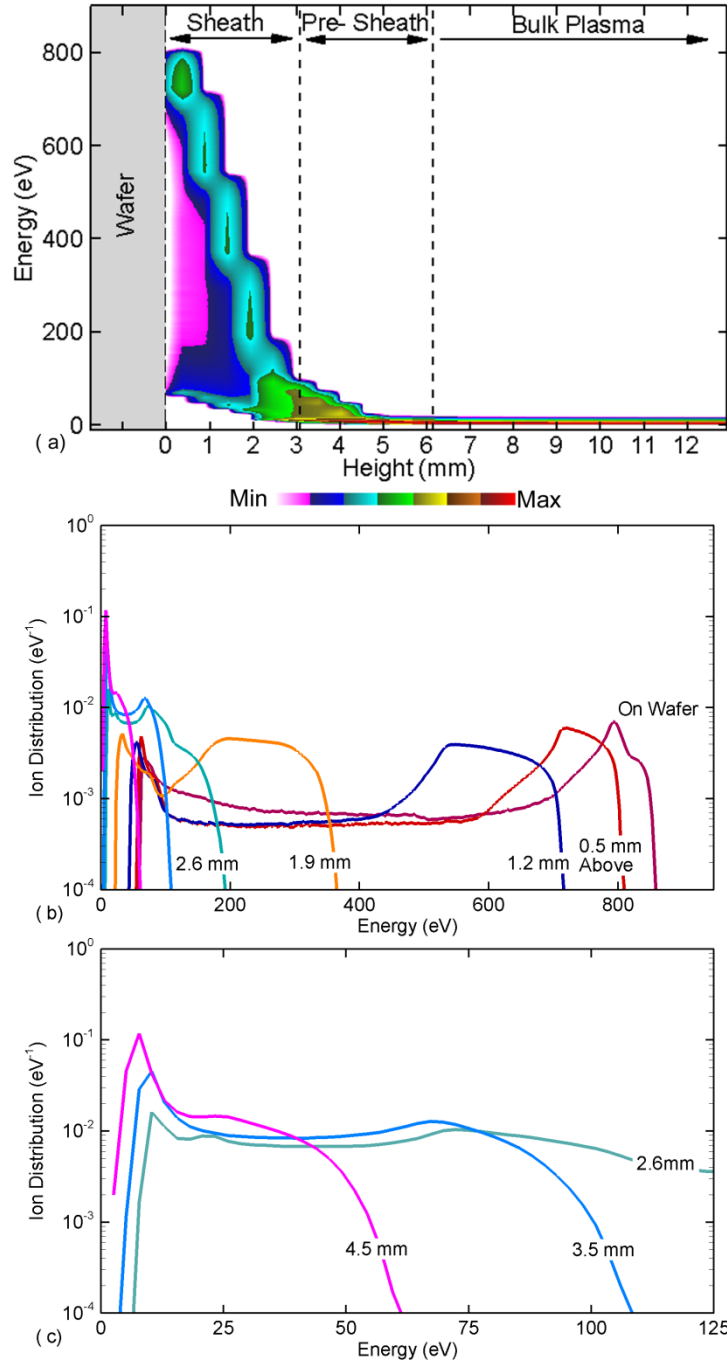
Fig. 4.3. Time averaged IEDs for Ar$^+$ at the middle of the from the bulk plasma to sheath region for the base case conditions (Ar/O$_2$=80/20, 2 mTorr, LF=2 MHz, V$_{LF}$ = 500 V, dc self-bias= -400 V). a) IED from bulk plasma to wafer. The approximate sheath and presheath boundaries are labeled in frame. Discontinuities in energy are caused by the mesh resolution in collecting statistics. b) IEDs at selected positions over the full energy range. c) IEDs at 4.5 mm, 3.5 mm and 2.6 mm above the wafer over a lower range in energy.

93
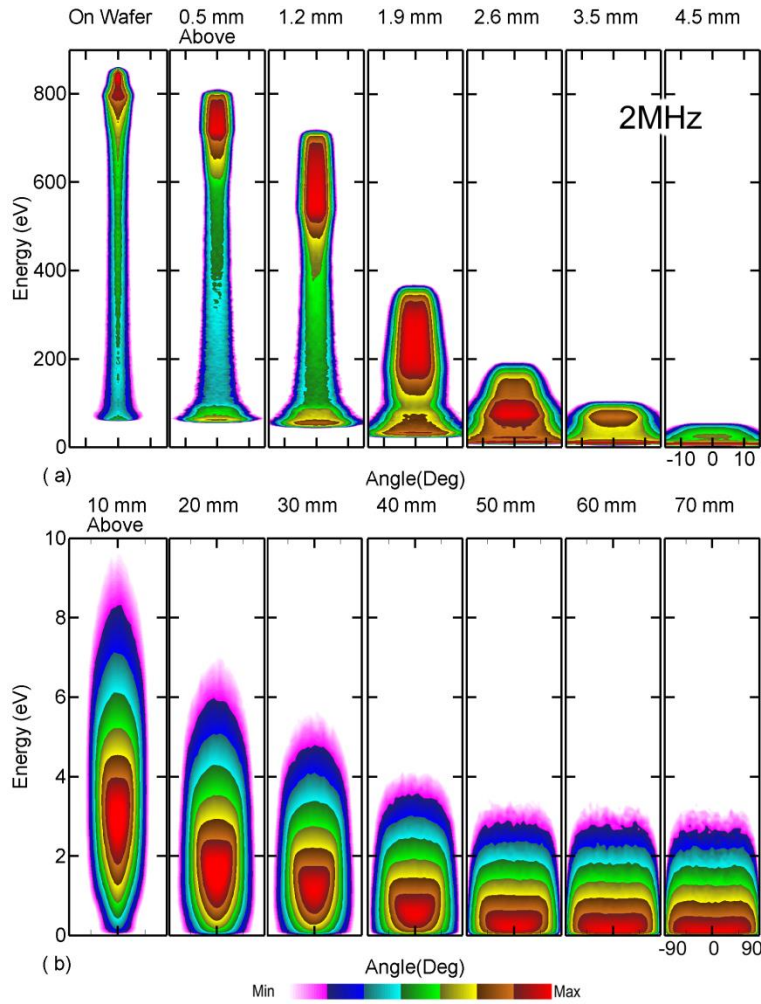
Fig. 4.4. Time averaged IEADs for Ar$^+$ as a function of height above the wafer. IEADs are plotted on a log scale over 2 decades. a) IEADs from on wafer to the edge of the presheath for energies up to 900 eV and angles -15 to 15 degree. b) IEADs from the presheath into the bulk plasma for energies up to 10 eV and angles -90 to 90 degree. The operating parameters are the base case (Ar/O$_2$=80/20, 2 mTorr, LF=2 MHz, V$_{LF}$ = 500 V, dc bias=-400 V).
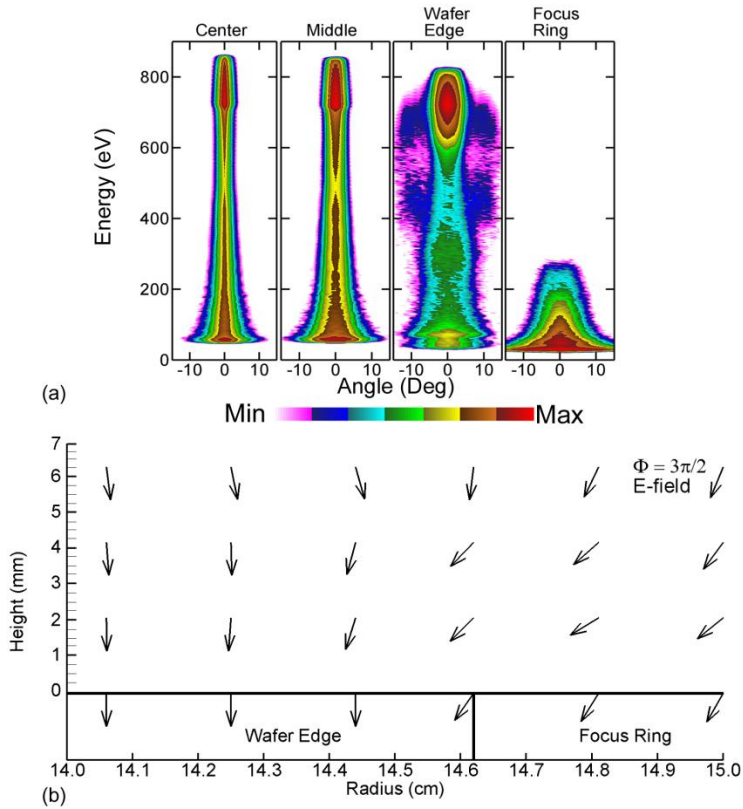
Fig. 4.5. IEADs and electric field vectors as a function of radial position. a) IEADs Ar^+ 0.5 mm above wafer for the base condition (Ar/O_2=80/20, 2 mTorr, LF=2 MHz, V_{LF} = 500 V, dc bias = -400 V). The IEADs are separately collected over the center of the wafer (r = 1-3 cm), the middle of the wafer (r = 7-9 cm), the edge of the wafer (r = 13-15 cm) and the focus ring (r = 15-16 cm). The contours span two decades using a log scale. b) Unit electric field vectors at the edge of the sheath and focus ring at the peak of the cathodic portion of the cycle.
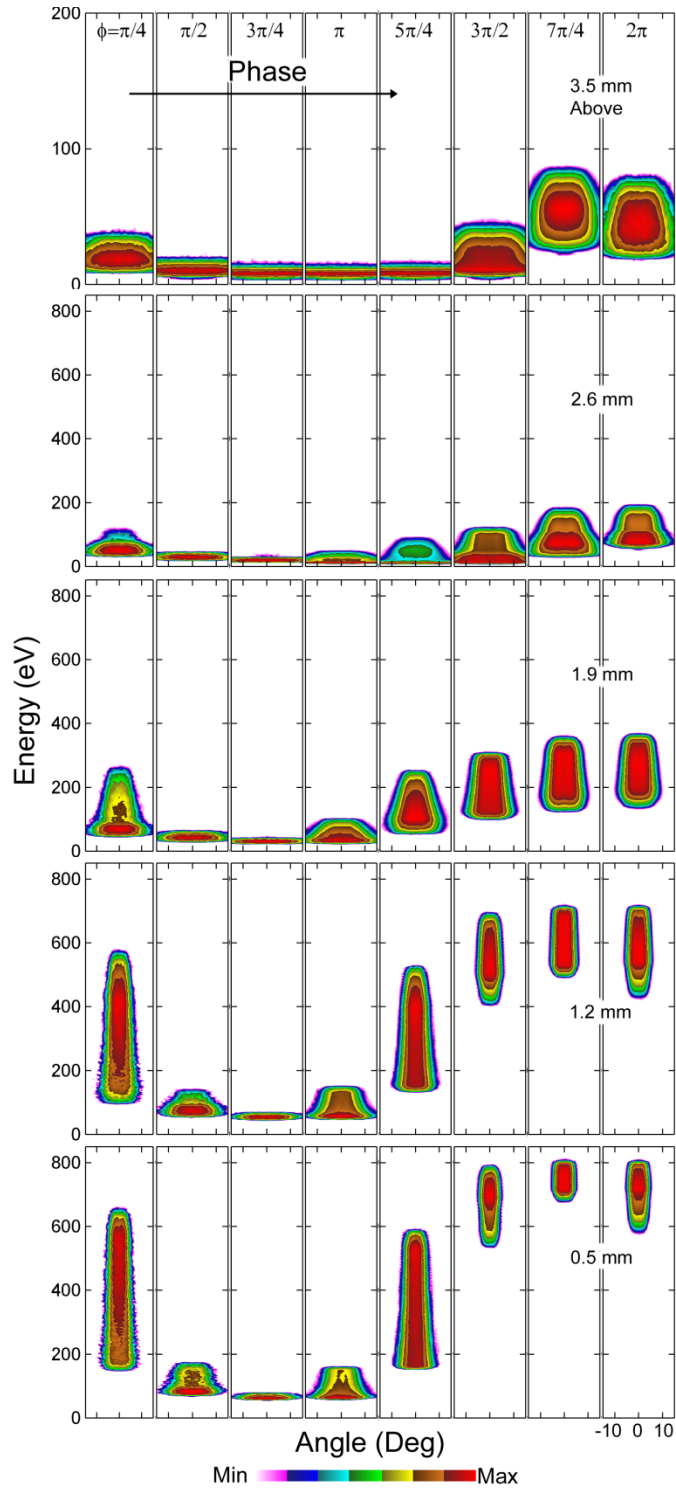
Fig. 4.6 IEADs of Ar$^+$ at the middle of the wafer (r = 8 cm) for base condition (Ar/O$_2$=80/20, 2 mTorr, *LF*=2 MHz, V$_{LF}$ = 500 V, dc bias=-400 V) at different heights above the wafer (top to bottom 3.5 mm, 2.6 mm, 1.9 mm, 1.2 mm and 0.5 mm). IEADs are shown averaged over 1/8 of the rf cycle for phases ending at $\phi = \pi/4$ to 2π along each row. The rf bias cross zero (negative to positive) at $\phi = \pi$.

96
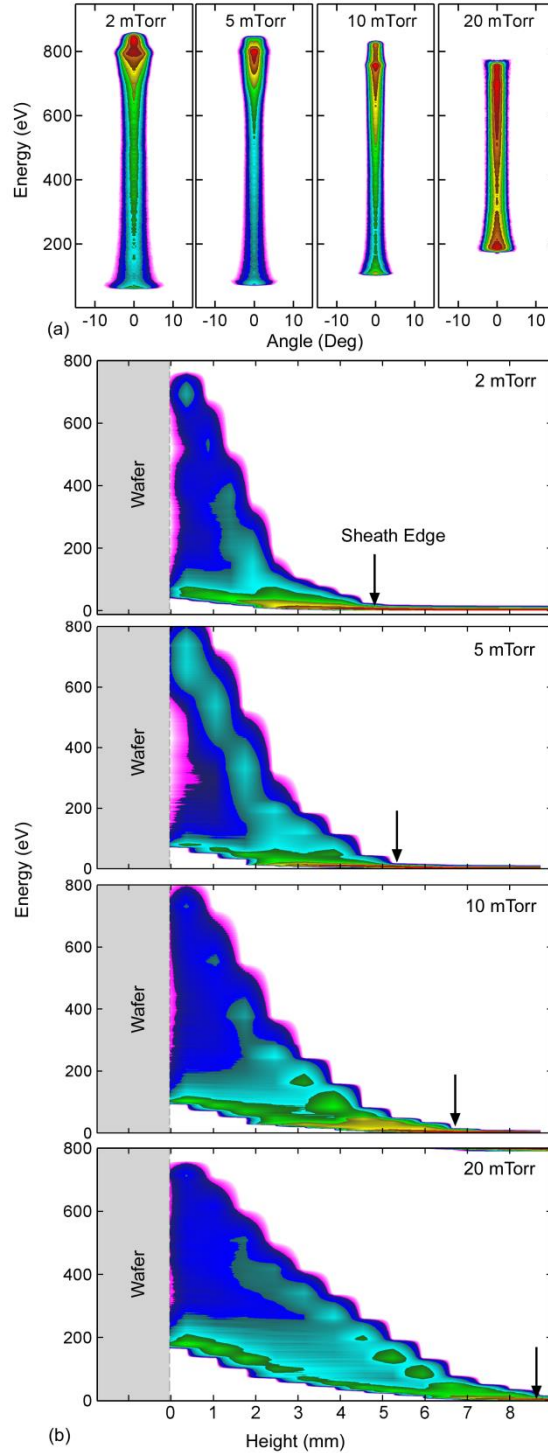
Fig. 4.7. Properties of Ar$^+$ ion transport at the middle of the wafer (r = 8 cm) for different pressures for otherwise the base case conditions. (Ar/O$_2$=80/20, *LF*=2 MHz, V$_{LF}$ = 500 V, dc bias=-400 V). a) IEADs as a function of pressure (2 mTorr to 20 mTorr). Flow rates for 2mTorr is 50 sccm, and for 5, 10 and 20 mTorr is 150 sccm. b) IEDs at the middle of the wafer as a function of height from the bulk plasma to the wafer.

97
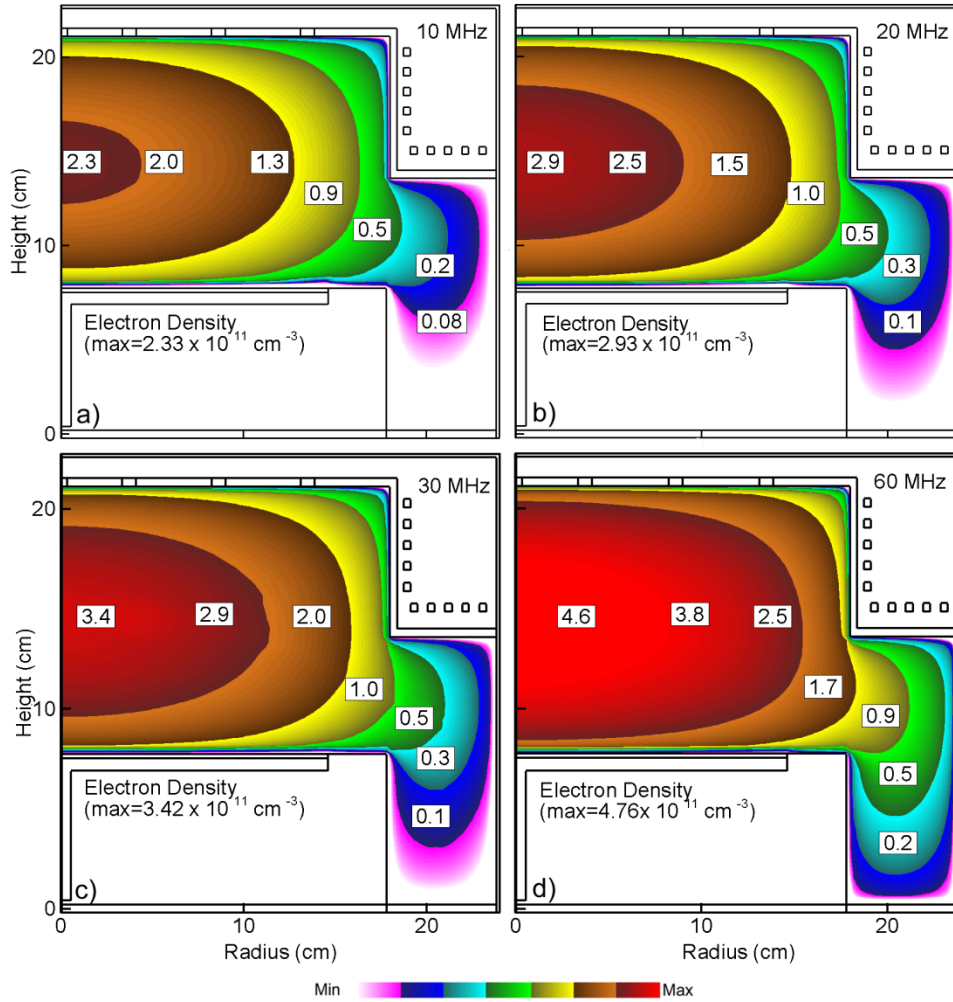
Fig. 4.8. Time averaged electron density for Ar/ O_2=80/20, 2 mTorr, when the *HF* is varied from a) 10, b) 20, c) 30 and d) 60 MHz. V_{HF} = 500 V, dc bias = -400 V. The maximum electron density, which increases with increasing *HF*, is noted in each frame with contour labels having units of 10^{11} cm^{-3}.
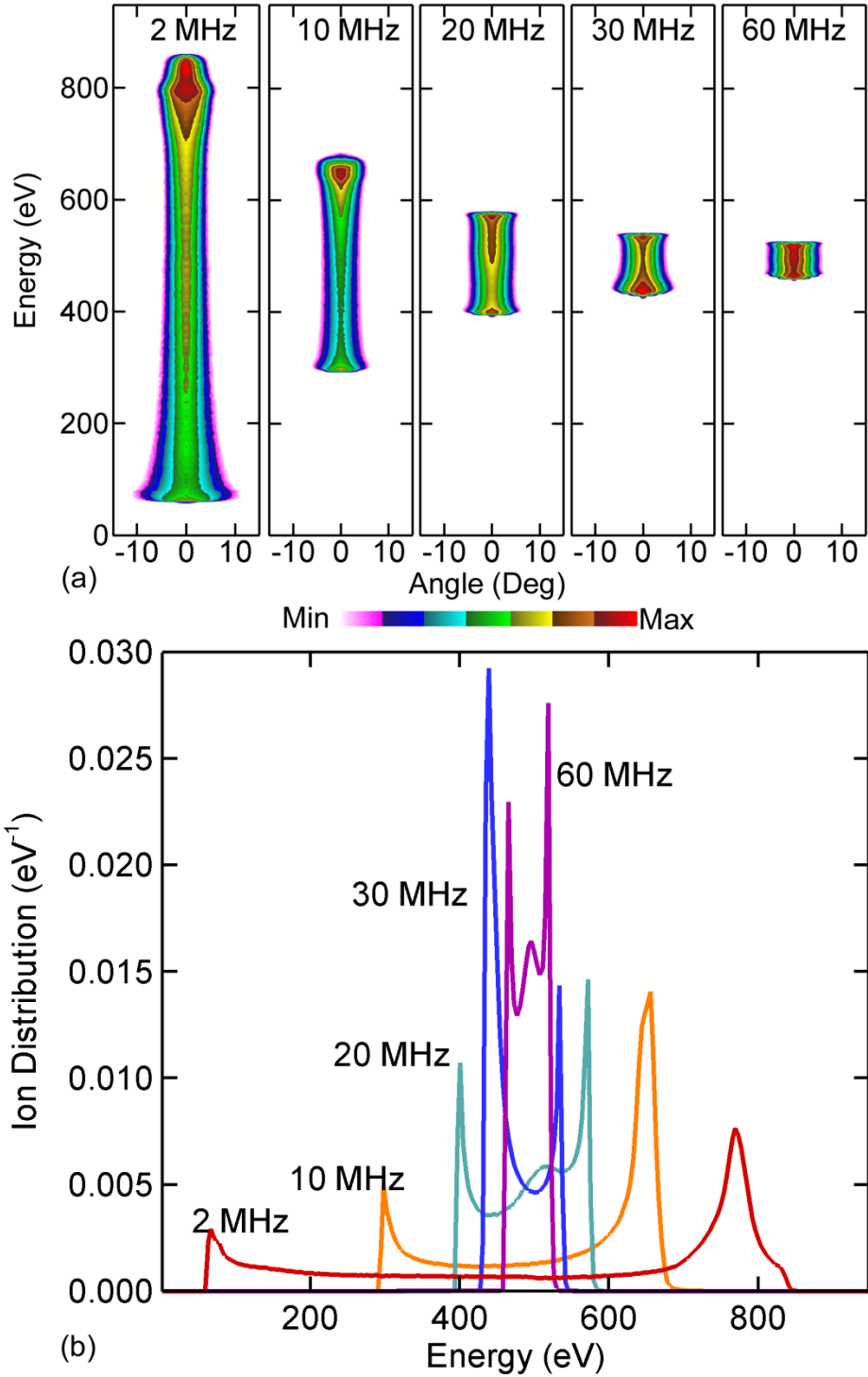
Fig. 4.9. Ar$^+$ ion properties incident onto the wafer for single frequency biases from 2 to 60 MHz for otherwise the base case conditions (Ar/O$_2$=80/20, 2 mTorr, V$_{HF}$ = 500 V, dc bias= -400 V). a) IEADs and b) IEDs.
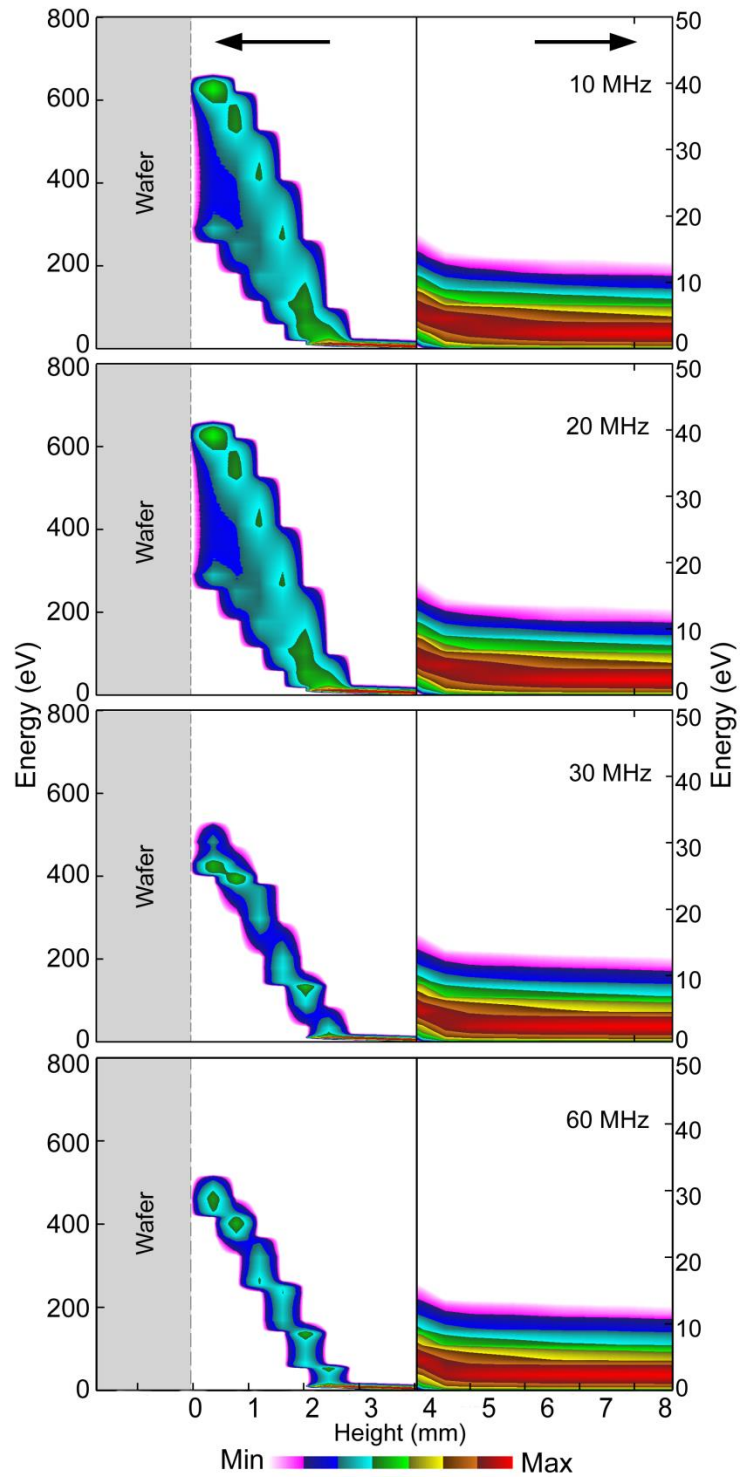
Fig. 4.10. IEDs for Ar$^+$ as a function of height above the wafer at the middle of the wafer for single frequency biases from 10 to 60 MHz for otherwise the base case conditions (Ar/O$_2$=80/20, 2 mTorr, V$_{HF}$ = 500 V, dc bias= -400 V). The left side of each figure is an energy scale up to 800 eV and on the right side on a scale up to 50 eV.

100
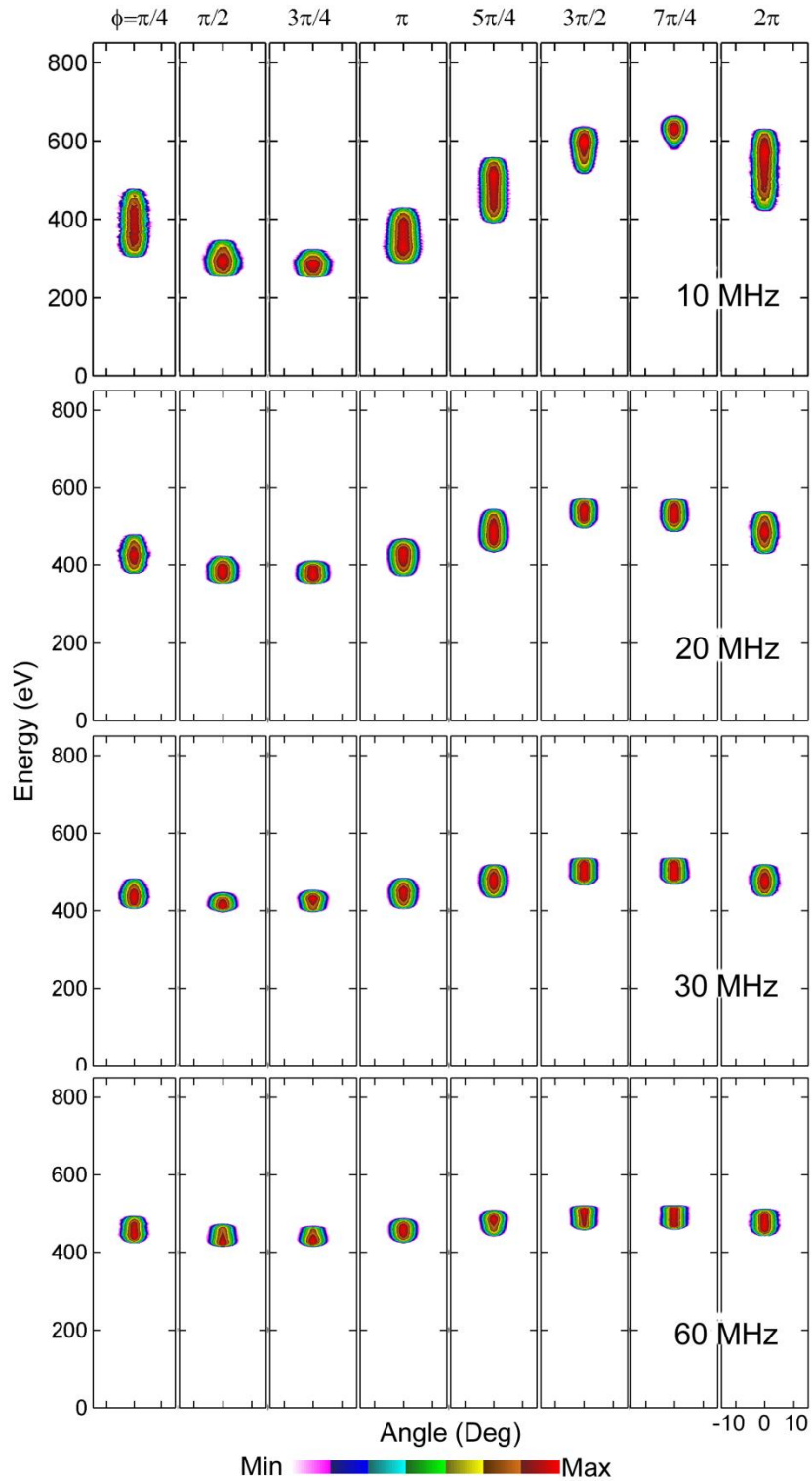
Fig. 4.11. IEADs of Ar$^+$ at the middle of the wafer (r = 8 cm) for frequencies (top to bottom) of 10, 20, 30 and 60 MHz for otherwise the base case condition (Ar/O$_2$=80/20, 2 mTorr, V$_{HF}$ = 500 V, dc bias= -400 V). The IEADs are shown 0.5 mm above the wafer averaged over 1/8 of the rf cycle for phases ending at ϕ = π/4 to 2π along each row. The rf bias cross zero (negative to positive) at ϕ = 0. With increasing frequency, IEADs become independent of phase.

101
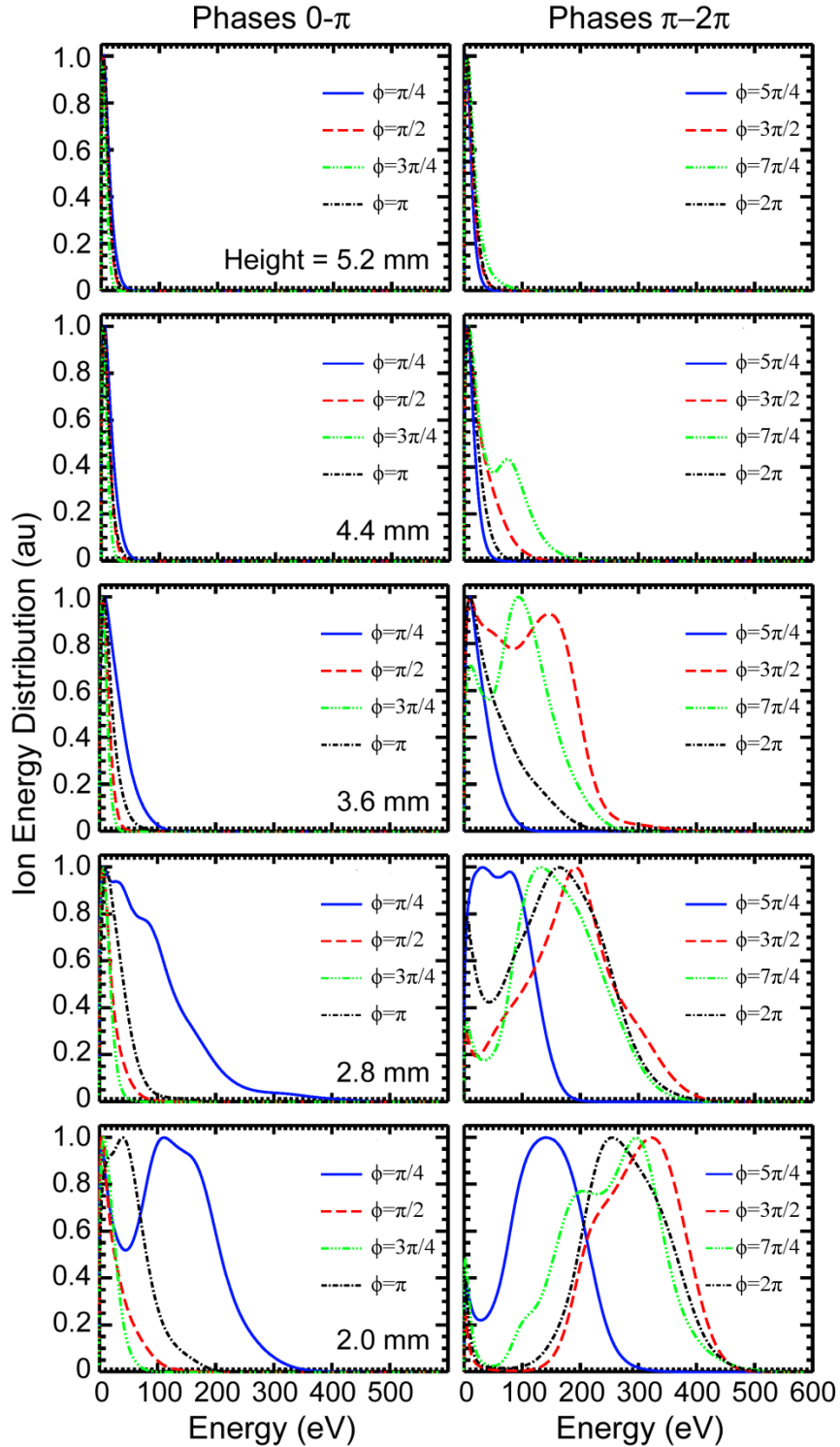
Fig. 4.12. Experimentally measured IEDs using LIF for a 2.2 MHz bias at a radius of 11 cm (Ar/O_2 = 80/20, 0.5 mTorr, V_{LF} = 300 V, V_{dc} = -300 V). The IEDs are shown at heights above the wafer from 5.2 mm to 2 mm (top to bottom). The development of the IEDs through the presheath and sheath are shown.
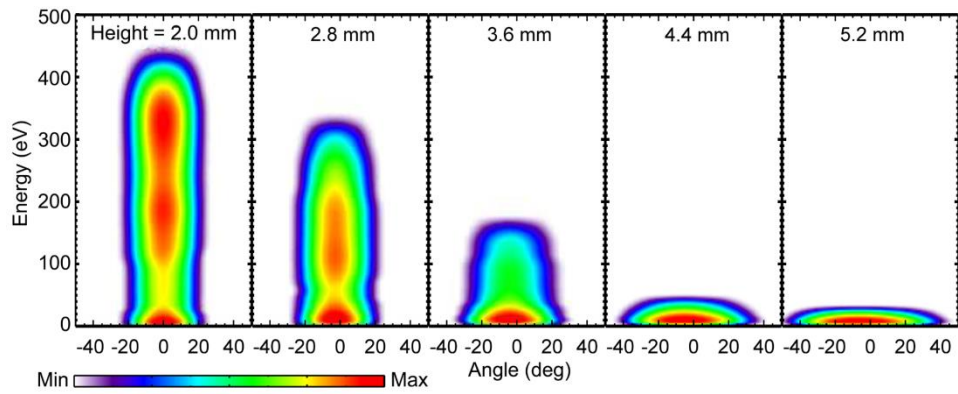
Fig. 4.13. Experimentally measured IEADs using LIF for a 2.2 MHz bias at a radius of 12.4 cm. The IEDs are shown at heights above the wafer from 2 mm to 5.2 mm (right to left). The narrowing of the IEADs is shown as the ions traverse the presheath and sheath. (Contours are on a log scale over 2 decades.)
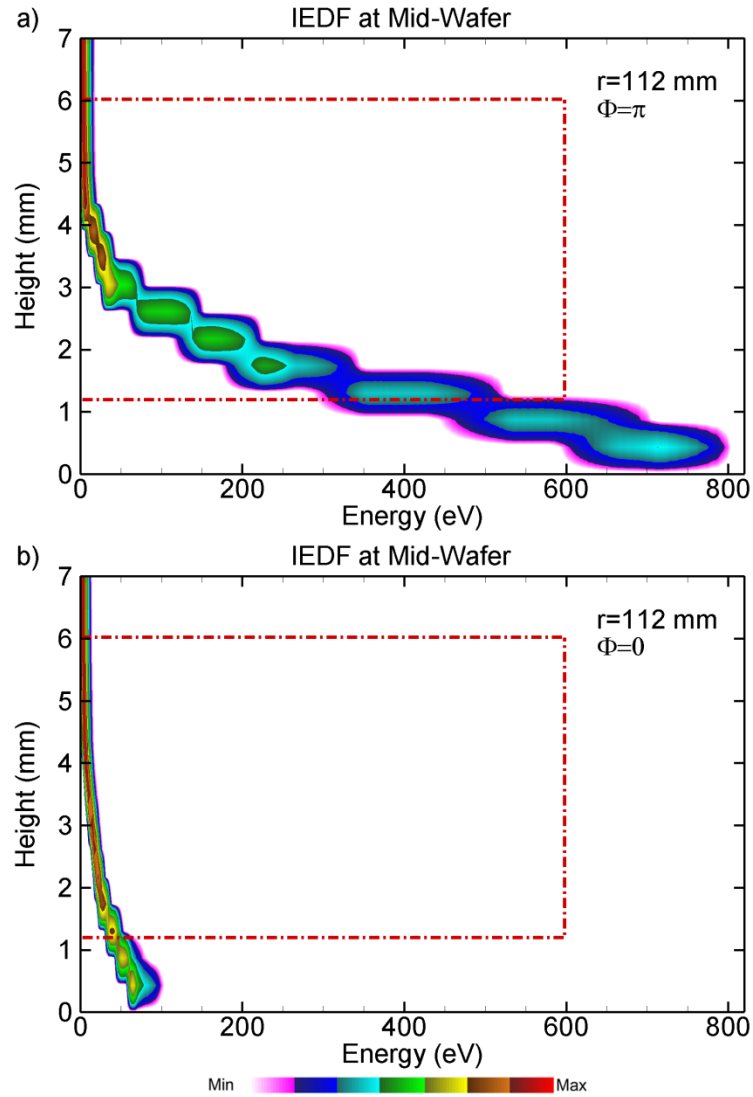
Fig. 4.14. Computed IEDs from bulk plasma through the sheath to the wafer at 112 mm for Ar/O$_2$= 80/20, 0.5 mTorr for 2 MHz, 400 V amplitude and dc bias of -360 V. a) Phase $\phi = 0$ and b) Phase $\phi = \pi$. The stair-step appearance is due to the discreteness of the mesh upon which the IEDs are collected. The plot is in log scale.
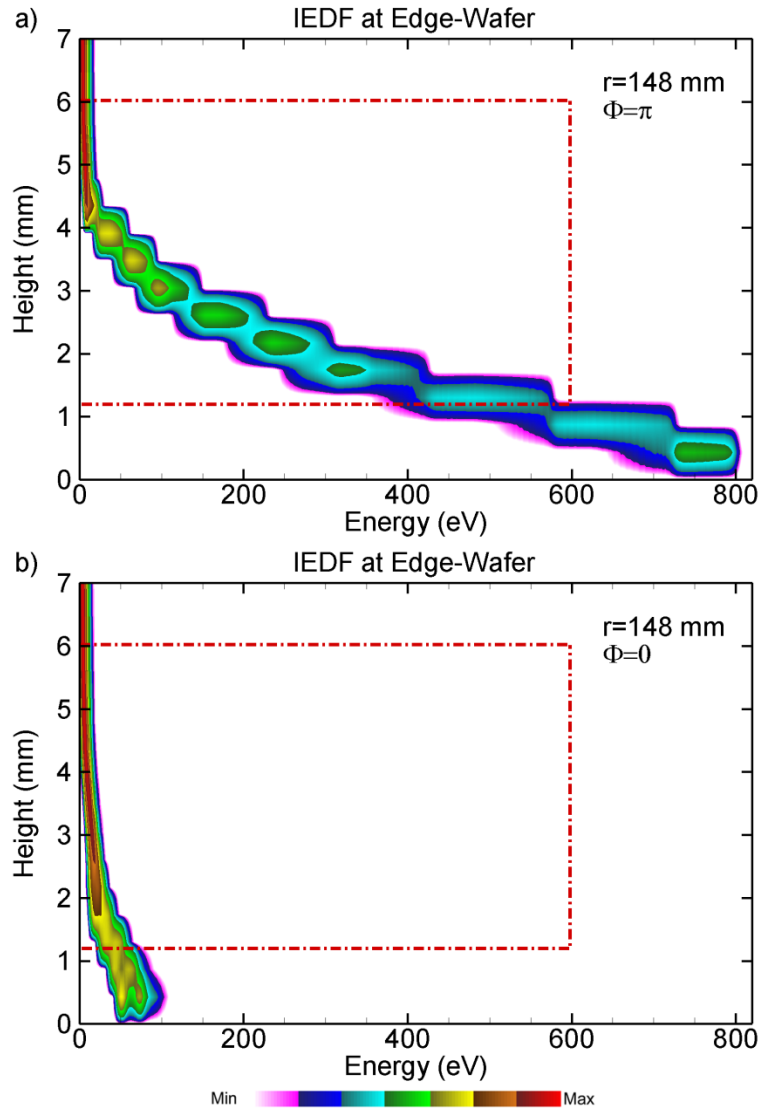
Fig. 4.15. Computed IEDs from bulk plasma through the sheath to the wafer at 148 mm for Ar/O$_2$= 80/20, 0.5 mTorr for 2 MHz, 400 V amplitude and dc bias of -360 V. a) Phase $\phi = 0$ and b) Phase $\phi = \pi$. The stair-step appearance is due to the discreteness of the mesh upon which the IEDs are collected. The plot is in log scale.
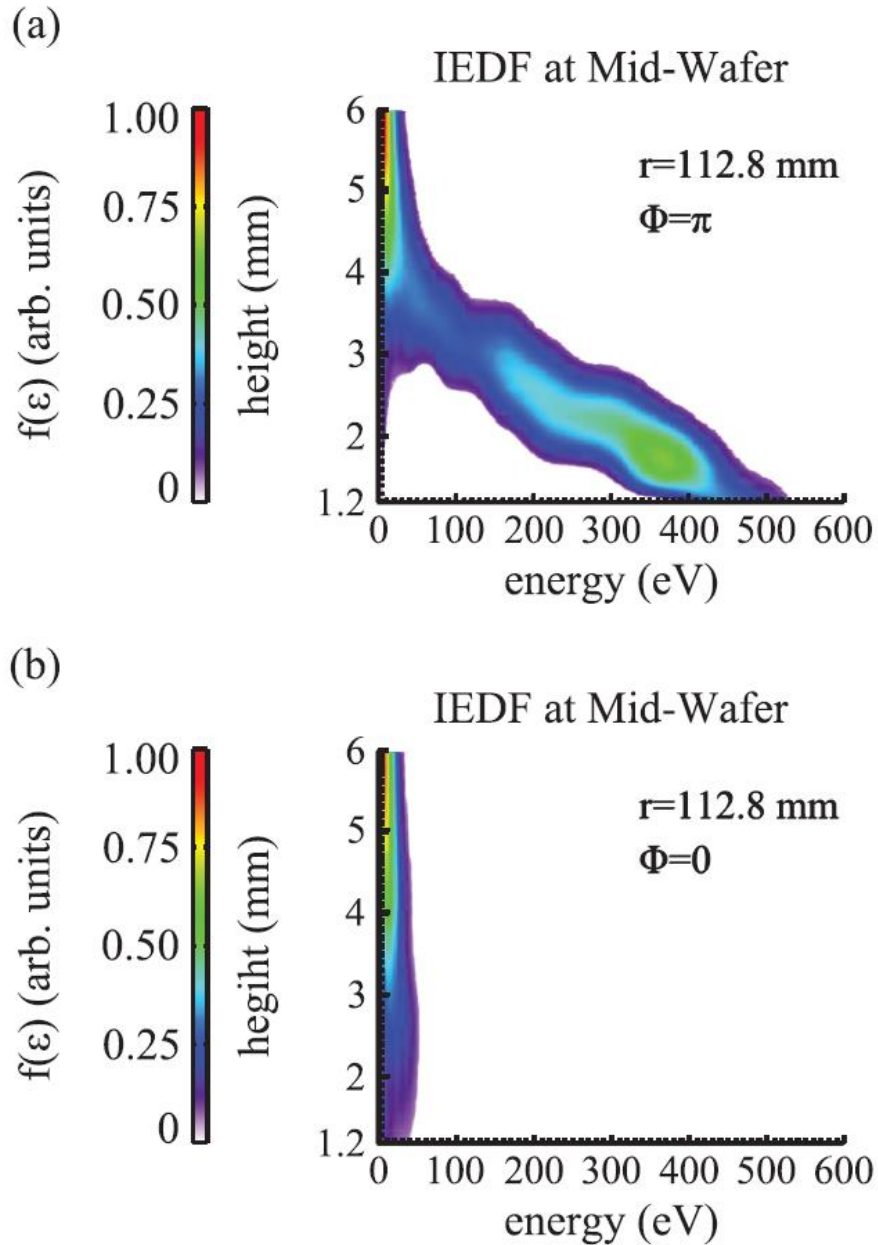
Fig. 4.16. Vertical IEDs at the edge of the wafer (r=112.8 mm) for two different phases. a) IED for $\phi = \pi$. Ions are accelerated from the thermal distribution prior to the presheath as the ions enter the sheath. The maximum energy reached by these ions at 1.2 mm, the lowest observation height, is approximately 500 eV. b) IED for $\phi = 0$. For this phase, the distribution remains primarily Maxwellian through as the ion transit time is short compared to the rf cycle.

(a)

IEDF at Wafer Edge

r=148.8 mm

Φ=π

(b)

IEDF at Wafer Edge

r=148.8 mm

Φ=0
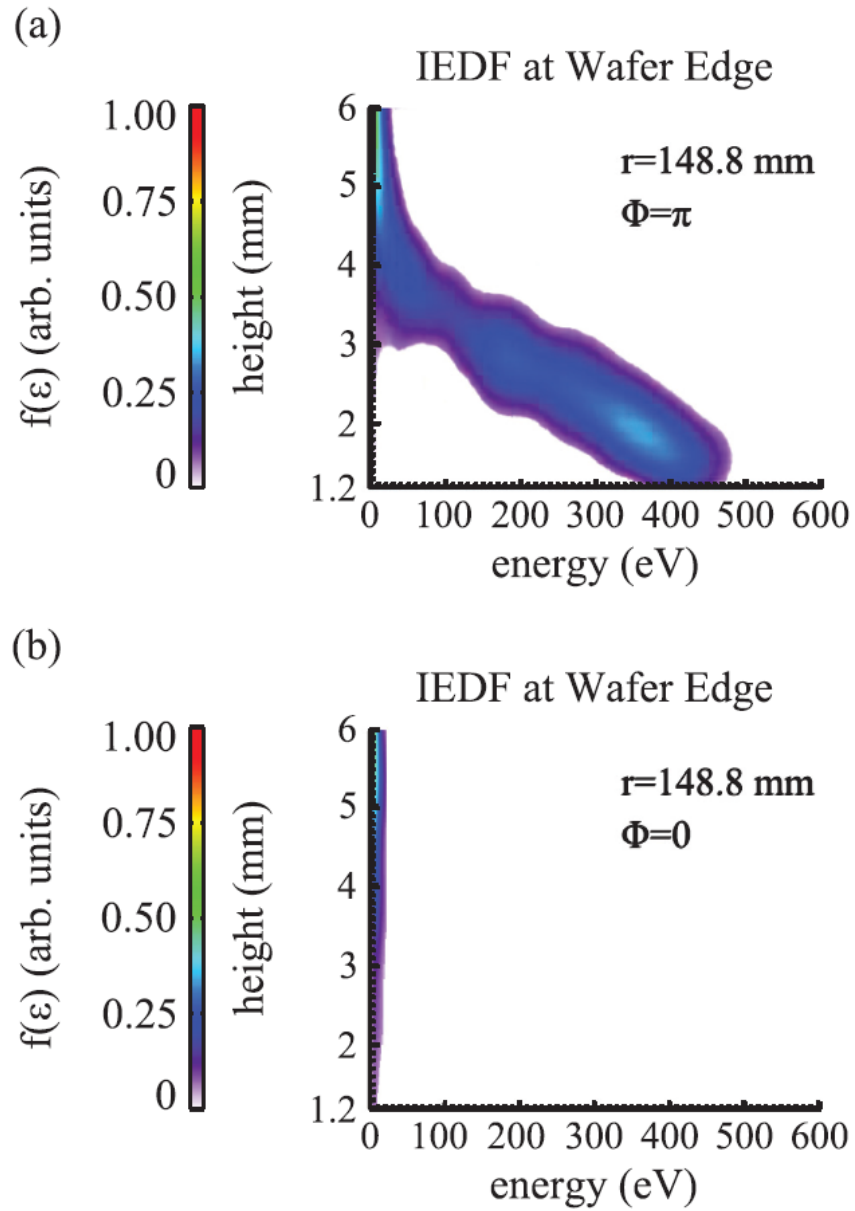
Fig. 4.17. Vertical IEDs at the edge of the wafer (r=148.8 mm) for two different phases. a) IED for $\phi = \pi$. Ions accelerate to energies comparable to those reached at mid-wafer. b) IED for $\phi = 0$. The distribution remains essentially Maxwellian through the sheath.
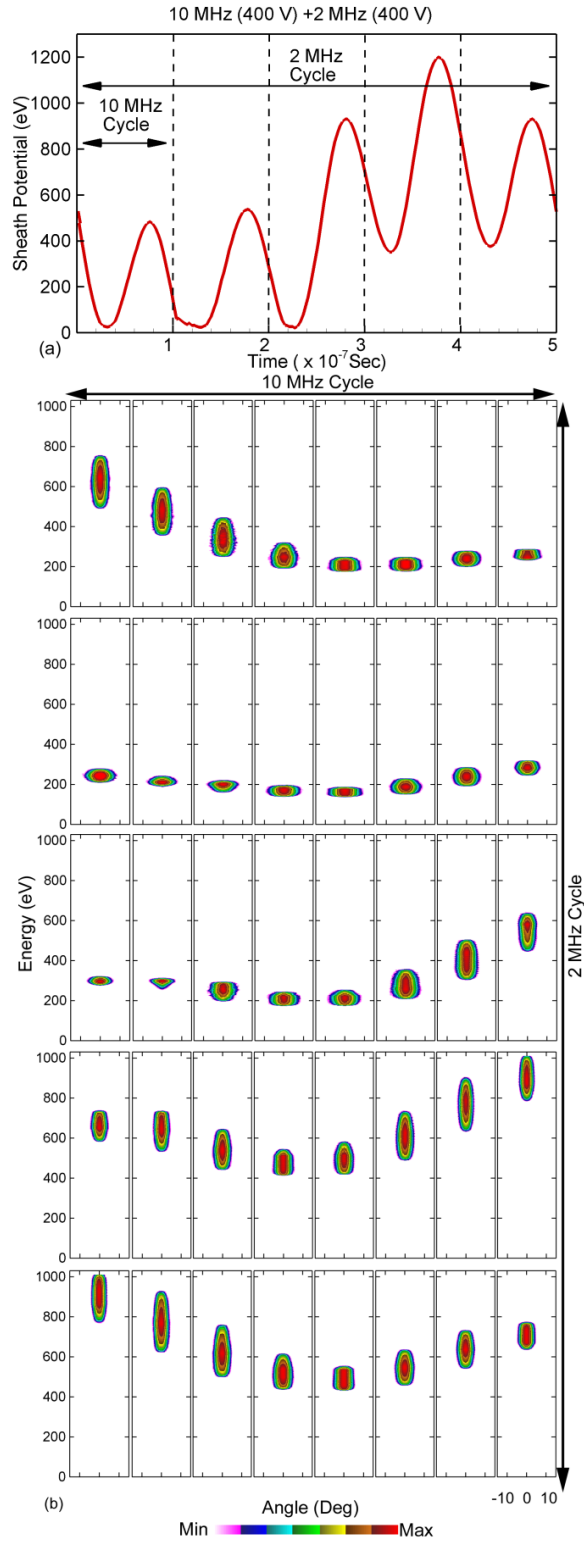
Fig. 4.18. IEADs for a 2 frequency rf bias having *LF* = 2 MHz (V_{LF} = 400 V) and *HF* = 10 MHz (V_{HF} = 400 V), with the dc self-bias = -400 V, a) Amplitude of the sheath potential during one 2 MHz period. b) IEADs for Ar^+ at the middle of the wafer for the entire 2 MHz cycle at a height of 0.5 mm.
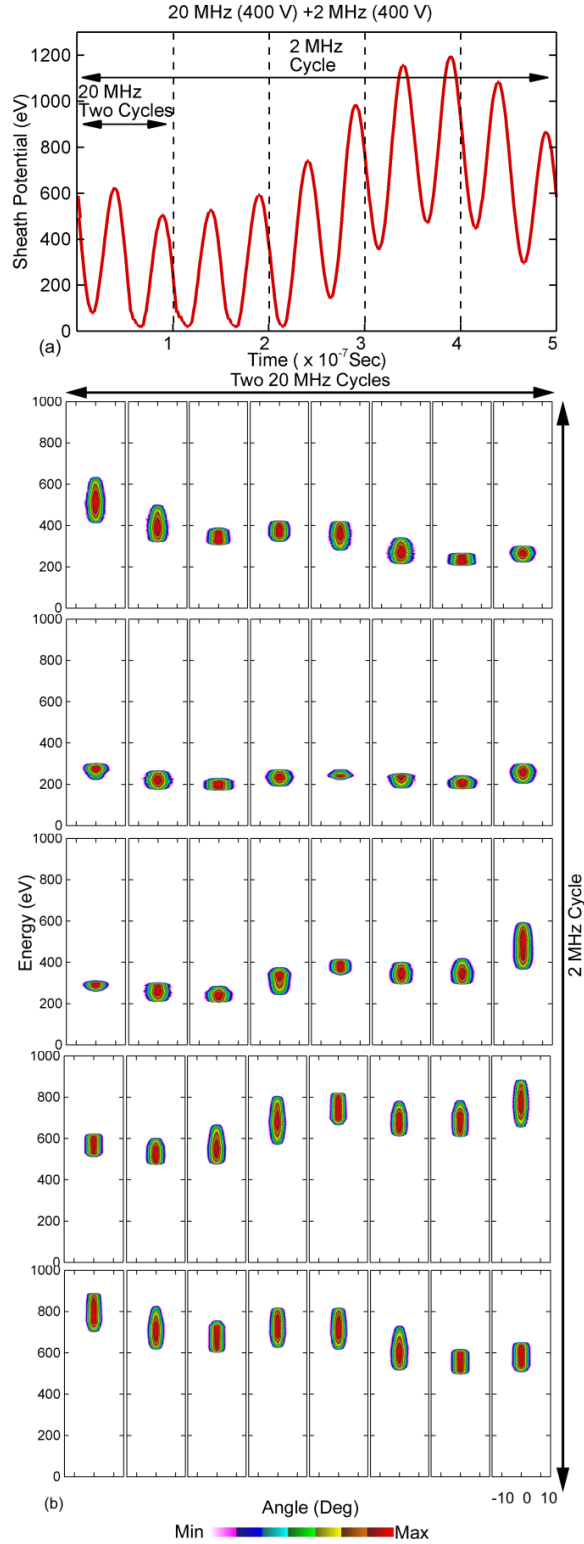
Fig. 4.19. IEADs for a 2 frequency rf bias having LF = 2 MHz (V_{LF} = 400 V) and HF = 20 MHz (V_{HF} = 400 V), with the dc self-bias = -400 V, a) Amplitude of the sheath potential during one 2 MHz period. b) IEADs for Ar$^+$ at the middle of the wafer for the entire 2 MHz cycle at a height of 0.5 mm.
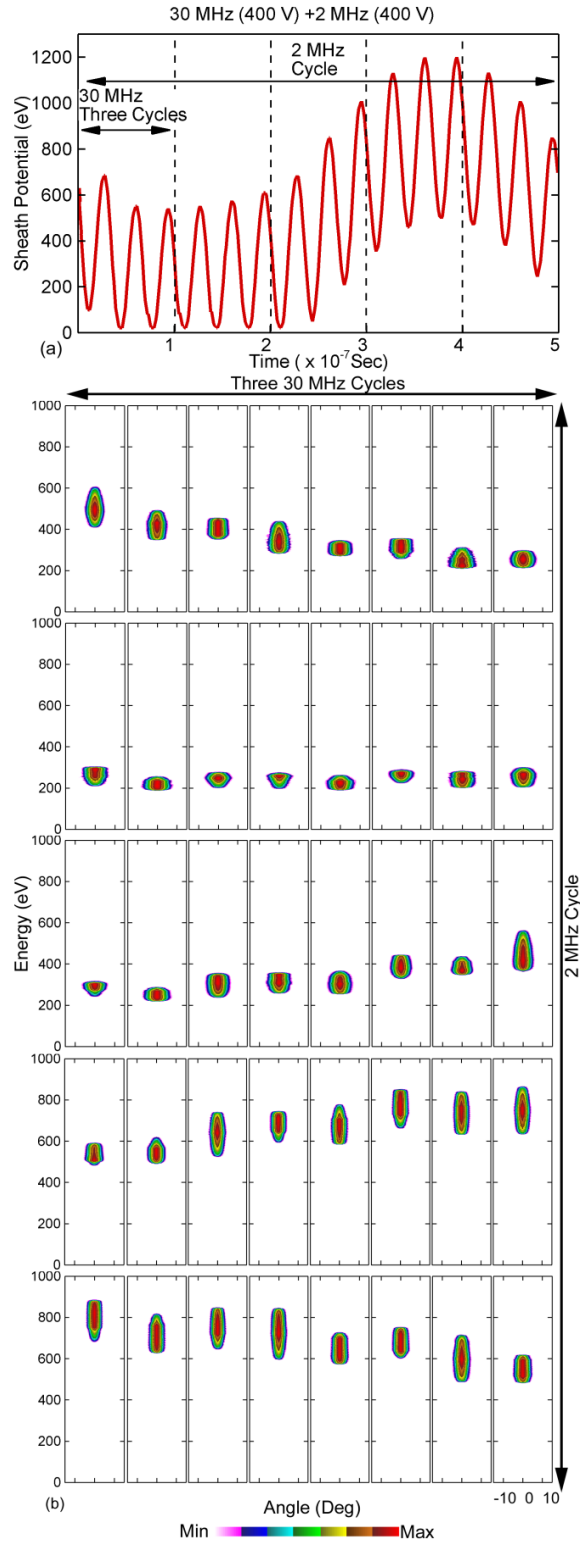
Fig. 4.20. IEADs for a 2 frequency rf bias having LF = 2 MHz (V_{LF} = 400 V) and HF=30 MHz (V_{HF} = 400 V), with the dc self-bias = -400 V, a) Amplitude of the sheath potential during one 2 MHz period. b) IEADs for Ar^+ at the middle of the wafer for the entire 2 MHz cycle at a height of 0.5 mm.
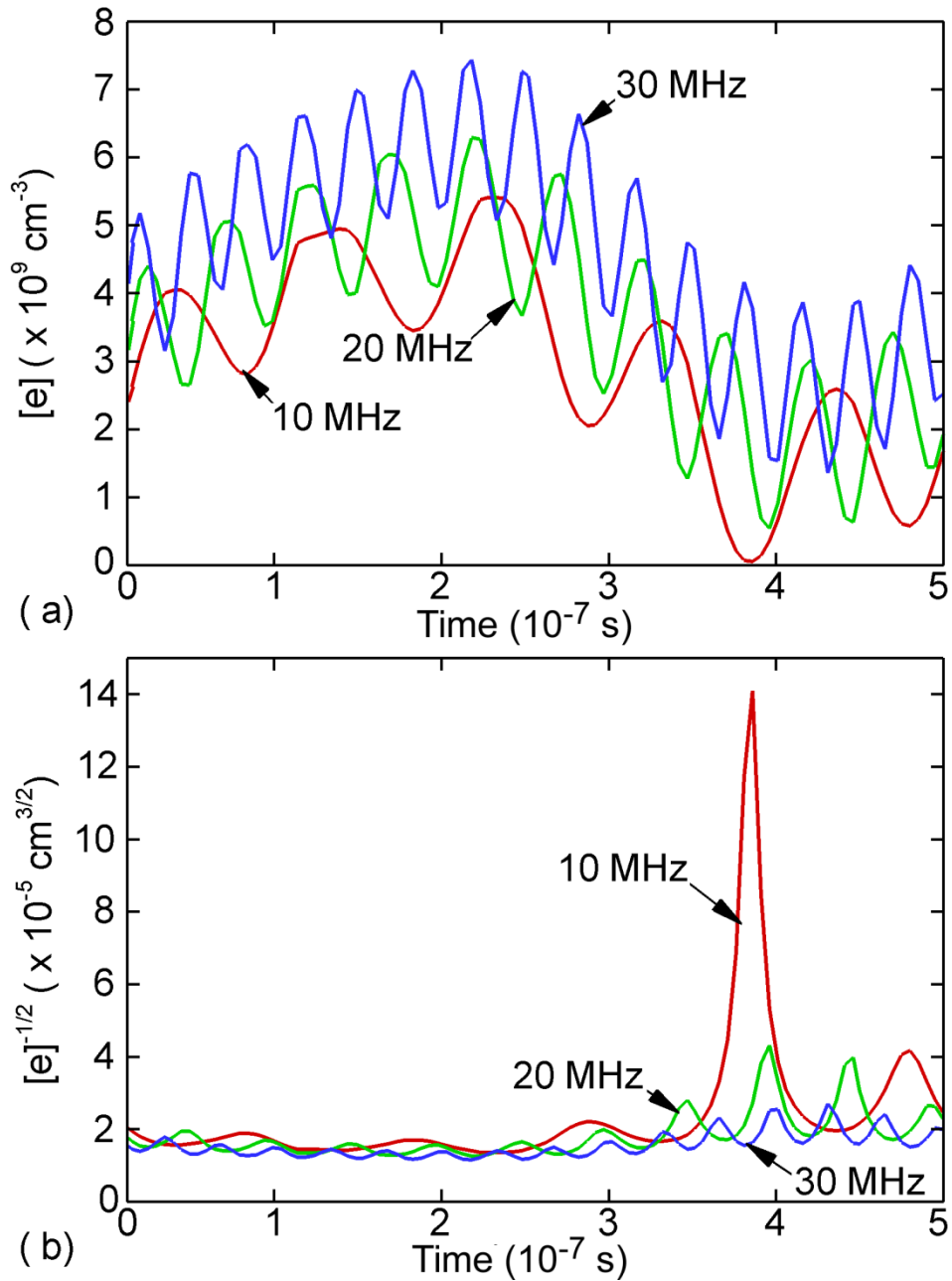
Fig. 4.21. Sheath properties for *LF*=2 MHz (V_{LF} = 400 V and *HF*=10, 20 and 30 MHz (V_{HF} = 400 V) with the dc self-bias = -400 V, a) Electron density at 1 mm above the middle of the wafer during one *LF* period. The increase of the *HF* produces a higher electron density. b) Implied change in sheath thickness assuming a scaling of $[e]^{-0.5}$. The sheath thickness varies within the rf period.
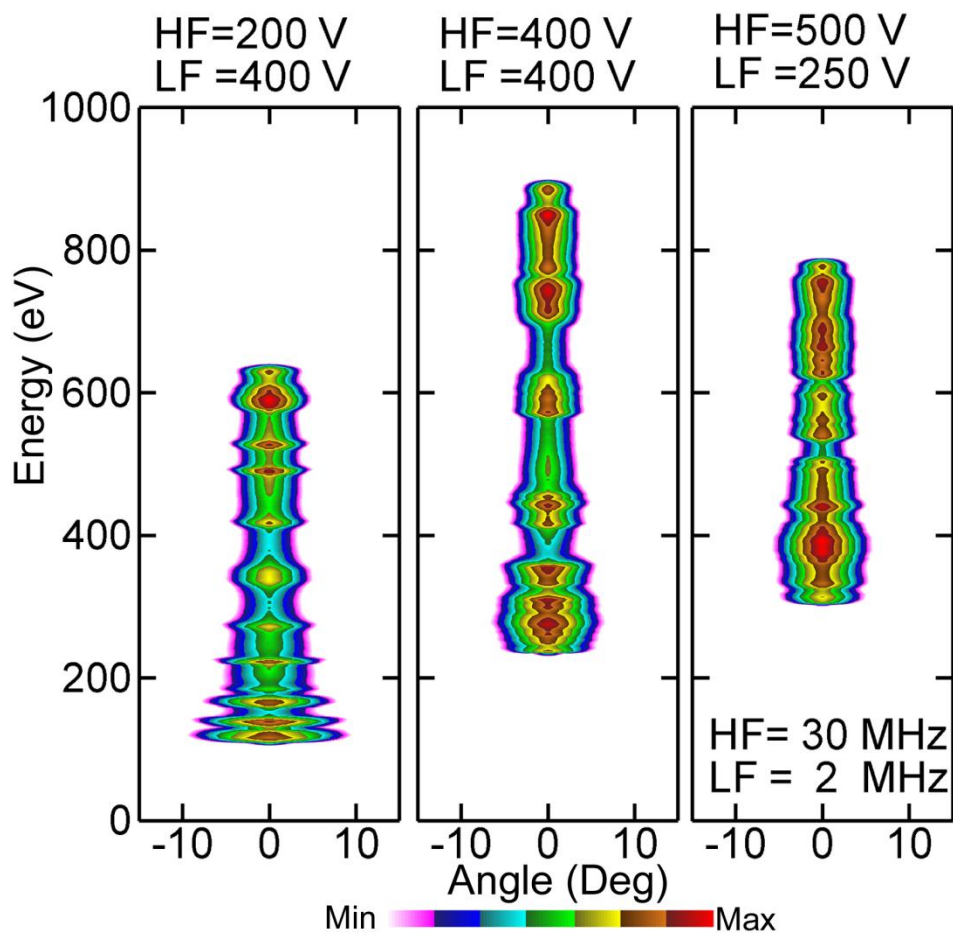
Fig. 4.22. IEADs of Ar$^+$ onto wafer for dual frequency excitation with *LF* = 2 MHz and *HF* = 30 MHz. The ratio of V$_{HF}$/V$_{LF}$= 0.5, 1.0 and 2.0 from left to right.
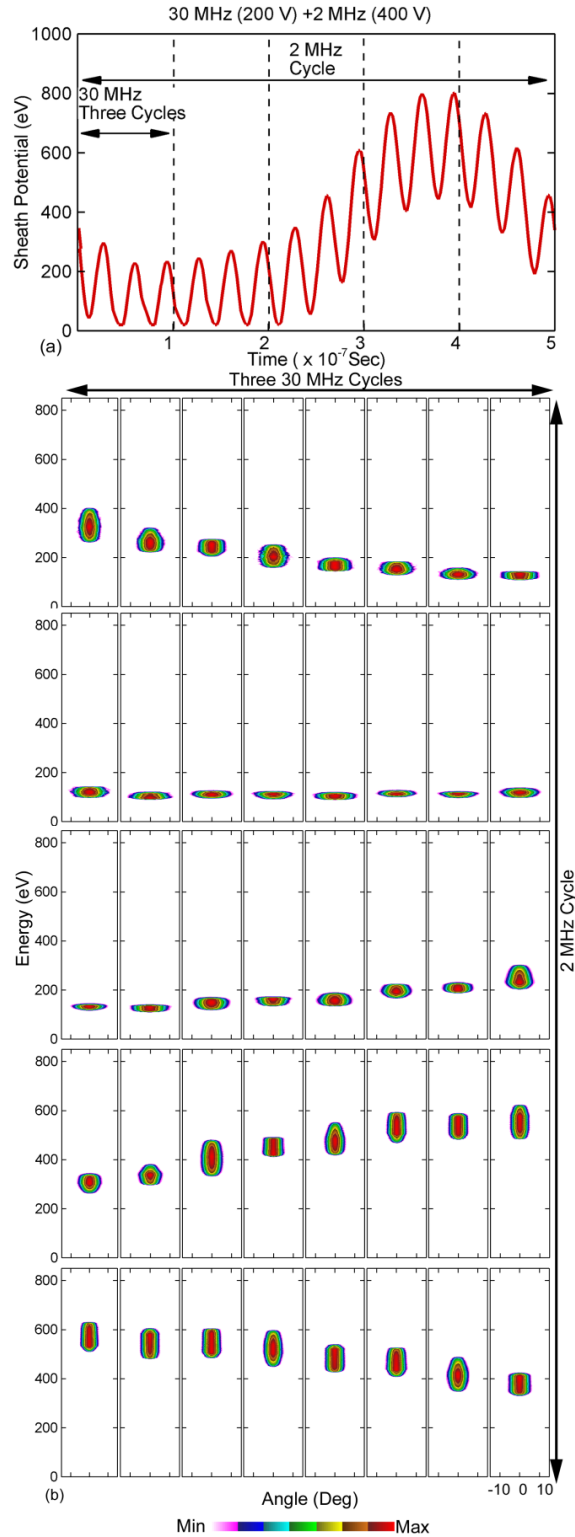
Fig. 4.23. IEADs for a 2 frequency rf bias having $LF = 2$ MHz ($V_{LF} = 400$ V) and HF=30 MHz ($V_{HF} = 200$ V), V_{HF}/V_{LF}= 2.0 a) Amplitude of the sheath potential during one 2 MHz period. b) IEADs for Ar^+ at the middle of the wafer for the entire 2 MHz cycle at a height of 0.5 mm.

113
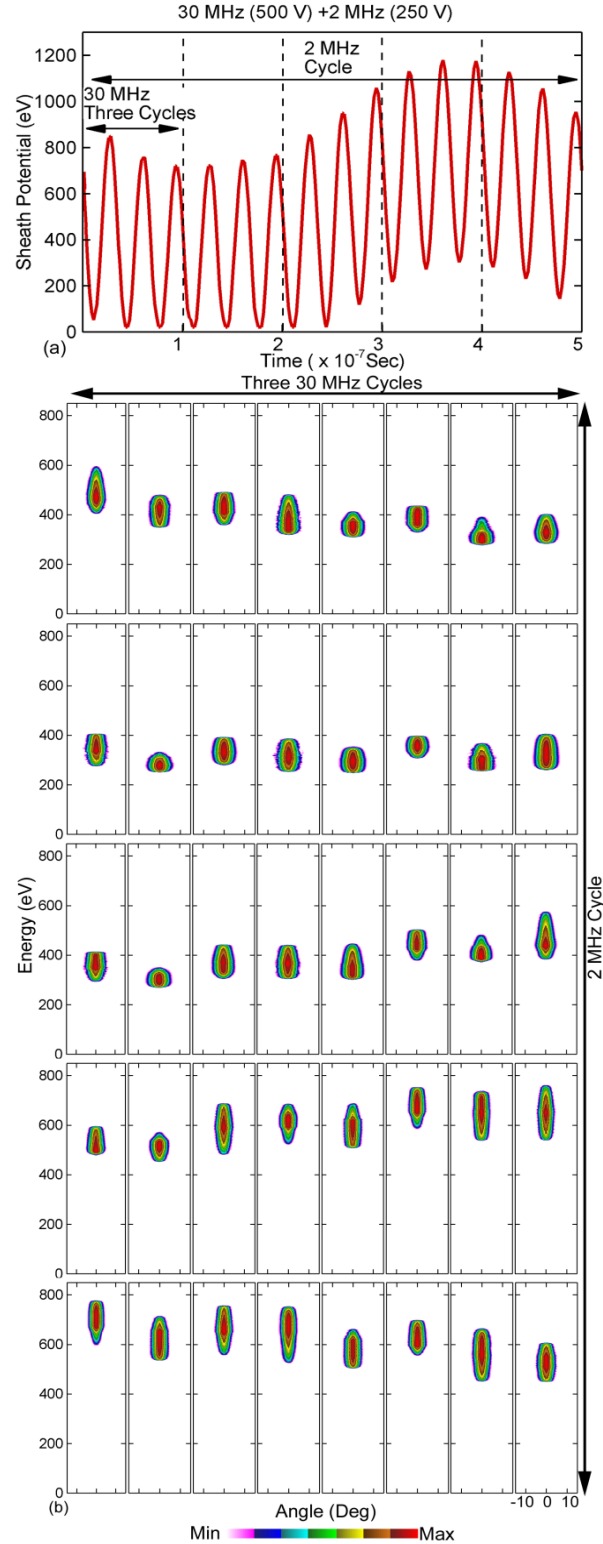
Fig. 4.24. IEADs for a 2 frequency rf bias having LF = 2 MHz (V_{LF} = 250 V) and HF=30 MHz (V_{HF} = 500 V), V_{HF}/V_{LF}= 2.0 a) Amplitude of the sheath potential during one 2 MHz period. b) IEADs for Ar^+ at the middle of the wafer for the entire 2 MHz cycle at a height of 0.5 mm.

4.6   References

1. M. Olevanov, O. Proshina, T. Rakhimova and D.Voloshin, Phys. Rev. E **78**, 026404 (2008).
2. S.-B. Wang and A. E. Wendt, J. Appl. Phys. **88**, 643 (2000).
3. Y. Zhang, J. Liu, Y. Liu and X. Wang, Phys. Plasmas **11**, 3840 (2004).
4. J. K. Lee, O. V. Manuilenko, N.Y. Babaeva, H. C. Kim and J. W. Shon, Plasma Sources Sci. Technol. **14**, 89 (2005).
5. T. Yagisawa, K. Maeshiga, T. Shimada and T. Makabe, IEEE. Trans. Plasma Sci. **32**, 90 (2004).
6. V. Georgieva, A. Bogaerts and R. Gijbels, J. Appl. Phys. **94**, 3748 (2003).
7. T. Gans, J. Schulze, D. O'Connell, U. Czarnetzki, R. Faulkner, A. R. Ellingboe and M. M. Turner, Appl. Phys. Lett. **89**, 261502 (2006).
8. J. Schulze, T. Gans, D. O'Connell, U. Czarnetzki, A. R. Ellingboe and M. M. Turner, J. Phys. D: Appl. Phys. **40**, 7008 (2007).
9. J. P Booth, G. Curley, D. Marić and P Chabert, Plasma Source Sci. Technol. **19**, 015005 (2010).
10. M. A. Sobolewski, J. K. Olthoff and Y. Wang, J. Appl. Phys. **85**, 3966 (1999).
11. S. Banna, A. Agarwal, K. Tokashiki, H. Cho, Sh. Rauf, V. Todorow, K. Ramaswamy, K. Collins, P. Stout, J.-Y. Lee, J. Yoon, K. Shin, S.-J. Choi, H.-S. Cho, H.-J. Kim, C. Lee, and D. Lymberopoulos, Trans. Plasma Sci. **37**, 1730 (2009).
12. B. K. Woodcock, J. R. Busby, T. G. M. Freegarde, and G. Hancock, J. Appl. Phys. **81**, 5945 (1996).
13. X. Wang and N. Hershkowitz, Phys. Plasmas **13**, 053503 (2006).
14. G. A. Hebner, J. Appl. Phys. **80**, 2624 (1996).
15. I. A. Biloiu, X. Sun and E. Scime, Rev. Sci. Instrum. **77**, 10F301 (2006).
16. B. Jacobs, W. Gekelman and P. Pribyl, Appl. Phys. Lett. **91**, 161505 (2007).
17. B. Jacobs, W. Gekelman, P. Pribyl and M. Barnes, Phys. Plasmas **18**, 053503 (2011).
18. M. J. Kushner, J. Phys. D: Appl. Phys. **42**, 194013 (2009).
19. S. Rauf and M. J. Kushner, J. Appl. Phys. **82**, 2805 (1997).
20. M. S. Barnes, J. C. Forster and J. H. Keller, IEEE Trans. Plasma Sci. **19**, 240 (1991).
21. B. Jacobs, Doctor of Philosophy in Physics Dissertation, UCLA (2010).
22. T. Panagopoulos, D.J. Economou, J. Appl. Phys. **85**, 3435 (1999).
23. H. C. Kim, F. Iza, S. S. Yang, M. Radmilović-Radjenović and J. K. Lee, J. Phys.D: Appl. Phys. **38**, R283 (2005).
24. R. T. C. Tsui, Phys. Rev. **168**, 107 (1968).
25. S.-B. Wang and A. E. Wendt, IEEE Trans. Plasma Sci. **27**, 1358 (1999).
26. G. Wakayama and K. Nanbu, IEEE Trans. Plasma Sci. **31**, 638 (2003).

Chapter 5 CONTROL OF ION ENERGY AND ANGULAR DISTRIBUTIONS IN DUAL- FREQUENCY CAPACITVIELY COUPLED PLASMAS THROUGH POWER RATIOS AND PHASES

5.1   Introduction

Capacitively coupled plasmas (CCPs) utilizing two radio frequency (rf) power supplies are widely used for anisotropic etching and deposition of materials for microelectronics fabrication where there is a continuing need to maintain critical dimensions (CDs).[1-3] Maintaining CDs is in part achieved by controlling energetic ion bombardment onto the wafer, which is the primary advantage of plasma-assisted processing. With the introduction of dual-frequency CCPs, additional control can be realized. However, the use of two frequencies produces complex sheath and ion transport dynamics. In an effort towards to improve the current understanding dual-frequency (DF) sheath dynamics and optimizing etching processes using DF-CCPs, several studies have investigated methods to overcome interference effects of DF-CCPs and to regain independent control of plasma parameters.

One such method is the electrical asymmetry effect (EAE). Schulze *et al*. demonstrated that the dc self-bias can be controlled in a symmetric CCP by the phase difference between the low frequency (*LF*) and high frequency (*HF*) when the *HF* is the second harmonic of the *LF*.[4] Control of the self-bias provides some control of the ion energy distributions (IEDs). Their

investigation focused on a geometrically symmetric DF-CCP operated at 13.56 MHz and 27.12 MHz with a variable phase shift. They found that the dc bias could be toggled between positive and negative by choice of the phase difference, and a stable process can be produced with an optimum voltage ratio between the harmonic rf frequencies.[4]

Over a range of applied voltages, modulation of the dc bias shifts the entire ion energy distribution, while keeping the width and shape of ion energy angular distribution (IEAD) relatively constant. In order to achieve high selectivity in plasma etching, it may be desirable reshape the IEAD and control the position of its peaks. To accomplish this, Maeshige *et al.*[5] suggested time modulating the DF-CCP using pulsed-power, which can control the incident fluxes as well as the IEAD. They numerically investigated the structure of the IEADs due to pulsing one of the frequencies. They predicted that pulsing a very high frequency (100 MHz) plasma source provided the potential to control high-energy negative ions and generate charge-free plasma processes in electronegative plasmas.

In this chapter, we report on results from a computational investigation of customizing and controlling IEADs in a DF-CCP sustained in Ar and Ar/CF_4/O_2 gas mixtures having a *LF* 2 MHz and *HF* up to 60 MHz biases applied to the substrate. The geometry is patterned after an industry standard configuration. By adjusting the ratio of power and the phase difference between frequencies, the character of the IEAD can be controlled. This control can be transferred to control of the CD of features, demonstrated here by simulations of etching of high aspect ratio features in SiO_2. A description of the computational models and reaction mechanisms used for this study are in Sec. 5.2. Simulation and experimental results for ion densities, and computed IEADs and profiles are discussed in Sec. 5.3. A control method using phase shifting between dual frequencies is discussed in Sec. 5.4. Concluding remarks are

presented in Sec. 5.5.

5.2   Description of the model

The Hybrid Plasma Equipment Model (HPEM) used in this study is described in Chapter 2. The evolution of surface features using energy and angular distributions for neutrals and ions produced by the HPEM is predicted by the Monte Carlo Feature Profile Model (MCFPM), which is discussed in detail in Chapter 3. In this study, the 2d mesh had dimensions of $\Delta x = \Delta y = 1.5$ nm. The time interval between launching particles Δt_p can be computed based on the total fluxes and the resolution of the mesh,

$$\Delta t_p = \frac{\Delta x \Delta y \rho}{\Gamma D},\tag{5.1}$$

where ρ is the density of the surface material, Γ is the total flux provided by the IEADs, and D is the width of total computational domain. For this investigation with SiO_2 etching, $\rho \approx 2.5 \times 10^{22}$ cm^{-3}, D is 112.5 nm and the total flux of plasma species, Γ, is $\approx 1\text{-}10 \times 10^{16}$ $cm^{-2}s^{-1}$. Using these values, the particle launch interval time is $\approx 10^{-3}$ s.

5.3   Plasma Properties in DF-CCP

The two-dimensional, cylindrically symmetric reactor used in this study is shown in Fig. 5.1. The gap between the electrodes is 3 cm. Gas is injected through several nozzles in the upper electrode. The top chamber and the metal wall are grounded. Both rf biases are applied to the bottom electrode through a blocking capacitor (1 μF). We chose to use a large capacitance to avoid the dc bias variation during the rf cycles. A conductive Si wafer ($\sigma = 0.01$ $\Omega^{-1}cm^{-1}$), 30 cm in diameter, sits in electrical contact with the substrate which is surrounded by a dielectric focus ring. The annular pump port is at the bottom of the computational domain coaxially surrounding

the substrate. During execution of the code, the flow rate through the pump is adjusted to keep the pressure inside the plasma chamber constant.

The base case operating conditions are 30 mTorr of Ar with both the *LF* (2 MHz) and *HF* (60 MHz) delivering the same power, 300 W. The species in the simulation are Ar, $Ar(1s_2)$, $Ar(1s_3)$, $Ar(1s_4)$, $Ar(1s_5)$, $Ar(4p,5d)$, Ar^+ and e. The reaction mechanism for Ar is essentially the same as described in Ref. [6] with the exception that the $Ar(3p^54s)$ multiplet is resolved into its four individual states. To investigate the relationship between IEAD and etching profiles, a SiO_2 film over a Si substrate was etched using an $Ar/CF_4/O_2 = 75/20/5$ gas mixture at 30 mTorr. The species in the mechanism were Ar, $Ar(1s_5, 1s_3)$ metastable, $Ar(1s_2, 1s_4)$ radiative, $Ar(4p,5d)$, Ar^+, CF_4, CF_3, CF_2, CF, C, F, F_2, C_2F_4, C_2F_6, C_2F_6, SiF_4, SiF_3, SiF_2, CF_3^+, CF_2^+, CF^+, C^+, F^+, F_2^+, CF_3^-, F^-, O_2, $O_2(^1\Delta)$, O_2^+, O, $O(^1D)$, O^+, O^-, COF, COF_2, CO_2, FO and e. The gas phase and surface reaction mechanisms are discussed in Refs. [6,7]. The injecting CF_4 experiences electron impact dissociation reactions and branches into CF_3, CF_3^+, CF_3^-, CF_2, CF_2^+, CF, F and F^-. The major negative ion formed by dissociate attachment to CF_4 is F^-. The mechanism also contained further election impact dissociation reactions with the new generated CF_x radicals. Collisions with Ar^+ or Ar* (excited states) can also produce sufficient energy for dissociative ionization of CF_x. All ion-neutral reactions were assumed as exothermic reactions, which occur independent of ion energy. Electron-ion and ion-ion reactions were estimated with typical rate constants in the range: $10^{-8} \sim 10^{-7}$ cm^3s^{-1}. Energy and angular distributions incident onto the substrate for all positive ions except for C^+ (having a negligible concentration) and major neutral particles produced by the PCMCM are used to predict profile evolution during etching of SiO_2 over Si.

For validation, the results from the computational model were compared to Langmuir probe measurements of ion saturation current in a commercial plasma etching reactor having

119

similar dimensions as shown in Fig. 5.1. The double probe contains two cylindrical tungsten wires 6 mm long and 0.5 mm in diameter. The measured ion saturation current density J_{is} is calculated from

$$J_{is} = I_s / A_p, \tag{5.2}$$

where I_s is the current collected by the probe with large negative biasing, and A_p is the probe area. Instead of deriving the ion density from the probe data to compare with the model, we simulated the probe data from the plasma properties predicted by the model. In the absence of a magnetic field, the ion density, n_i, is related to the saturation current as, [8]

$$n_i = \frac{4I_s}{q v_{th} A_p}, \tag{5.3}$$

where v_{th} is the ion thermal speed entering the sheath of the probe from the presheath. Since $T_e \gg T_i$ (T_e is the electron temperature, T_i is the ion temperature), we can approximate $v_{th} = \sqrt{\frac{2k_B T_e}{m_{ion}}}$. The simulated ion saturation current density in the center of bulk plasma is then

$$J_{is} = \frac{q n_i}{4} \sqrt{\frac{2k_B T_e}{m_{ion}}}, \tag{5.4}$$

where n_i and T_e are the local values of ion density and electron temperature predicted by the model.

Both single- and dual- frequencies CCPs were investigated. The single-frequency operating conditions were Ar at 70 mTorr with an 800 sccm flow rate. A 60 MHz rf bias with power varying from 50 to 200 W was supplied on the bottom electrode. The gap between the two electrodes was 24 mm. A 300 mm Si wafer was placed on the substrate. The temperatures of the top and bottom electrode were controlled at 80 and 20 °C. These temperatures are

accounted for in the model which affects the final results due to rarefaction of the gas. Accounting for the material temperatures was important in comparing computed results to experiments. The simulated and measured values of J_{is} as a function of radius for different powers (5-200 W) are shown in Fig. 5.2. Results from the simulations match well with the experiment, agreeing to within 10-15% in magnitude and capturing the major trends in radial dependence. There is a small increase in J_{is} towards the edge of the wafer due to electric field enhancement.

Similar results are shown in Fig. 5.2c for a DF-CCP sustained in $Ar/O_2 = 90/10$ at a pressure of 20 mTorr. The 2 MHz *LF* delivers 2500 W and the 60 MHz *HF* delivers 600 W. The agreement is qualitatively good – to within 10% at large radius and 50% on axis. The higher current density on axis may be a consequence of a finite wavelength effect at the higher frequency. Upadhyay *et al.* found that the presence of higher harmonics causes a center-peaked electron density in both simulations and experiments of a 60 MHz CCP with powers greater than 500 W.[9]

As a point of reference, the electron density (n_e), electron temperature (T_e) and two electron-impact ionization sources (by bulk and secondary electrons) are shown in Fig. 5.3 to illustrate the base case operating conditions in argon at 30 mTorr. With equal powers (300 W) at the *LF* and *HF*, the plasma density is about 10^{11} cm^3, which is sustained by a bulk electron temperature of $T_e = 2.5$ eV. The *HF* and *LF* voltages are 110 V and 257 V to deliver the specified power. T_e is fairly uniform in the reactor due to the high thermal conductivity produced by electron-electron collisions. The electrons have two sources of ionization, by bulk ionization and sheath accelerated secondary electron emission produced by ion bombardment (secondary emission coefficient $\gamma = 0.15$).[10] Since the efficiency of ionization by bulk

electrons scales with frequency, the *HF* dominates the bulk ionization which exceeds that by secondary electron emission by a factor of 10.

The properties of Ar^+ transporting through the sheath and onto the substrate are summarized in Fig. 5.4. IEDs are shown in Fig. 5.4 a averaged over the rf cycle as a function of height from the bulk plasma, 4.6 mm above the wafer, through the presheath and sheath. The IEDs are separately normalized to unity at each height. The boundary between the presheath and sheath is approximately where the ion energy begins to increase from its nearly constant value in the presheath. The sheath thickness is $\approx$2.7 mm. This is in the thin sheath limit for the 2 MHz bias (ion transit time is short compared to the rf period) and in the thick sheath limit for the 60 MHz bias (ion transit time is long compared to the rf period). The end result is a modulation in the IEDs, as shown in Fig. 5.4 b and c. These conditions also produce an IED that is time dependent during the 2 MHz cycle.

The shape of IED illustrates the coupling between the two frequencies. The 2 MHz contributes to the bi-modal structure of the IED, which results from the Ar^+ transit time being commensurate to the 2 MHz period. In this limit, the energy of individual ions striking the surface depends on the phase in the 2 MHz cycle that the ion enters the sheath.[11] On the other hand, the modulation of the IED is largely caused by the addition of the 60 MHz power. The depth of this modulation is a measure of the thickness of the sheath. For a sheath that appears thin at 60 MHz and for equal amplitudes of the *LF* and *HF*, the modulation would be nearly 100%. For a thick sheath at 60 MHz, there should be little modulation. The *HF* modulation of the IEDs compromise independent control by the *LF*.[10,12] These trends are in agreement with the experiments by Liu *et al*. that showed that as the amplitude of the *HF* approaches that of the *LF* voltage, independent control of the IED by the *LF* is compromised.[13]

5.3.1   Control of IEDs with Ratio of the HF/LF Power

The IEDs for the base case suggest that independent control of IEDs in DF-CCPs may be compromised with a high plasma density and a thin sheath. This finding emphasizes the challenge of controlling IEDs in high plasma density DF-CCPs and the necessity to consider the influence on IEDs of not only the *LF* but also the *HF*. One possible method for tuning the time averaged IEDs onto the wafer is adjusting the ratio of power between the *HF* and *LF*. For example, electron densities are shown in Fig. 5.5 and IEADs are shown in in Fig. 5.6 for argon plasmas having the *LF* power fixed at 300 W and the *HF* power varied from 300 W to 1200 W. The voltage amplitude of the *HF* increases from 110 V to 185 V. The plasma density increases from 1.3×10^{11} cm^{-3} at 300 W to 3.6×10^{11} cm^{-3} at 1200 W, somewhat less than linearly due to there also being power deposition into ions by the *HF* power. Since the electron heating scales with ω^2, the higher *HF* power correlates with higher rates of ionization and, for this geometry, better uniformity. The *LF* voltage drops from 256 V to 113 V while keeping the *LF* power constant. As the plasma density increases with increasing *HF* power, the ion current will also increase, and therefore a lower *LF* voltage is needed to sustain the same power. This decrease in *LF* voltage with increasing *HF* power replicates the trends observed by Booth *et al*. for DF-CCPs sustained in Ar/C$_4$F$_8$/O$_2$ and Ar/O$_2$ mixtures (frequencies of 2 MHz and 27 MHz).[14]

By design, the IEDs should be relatively insensitive to the *HF* power deposition. The general trend shown in Fig. 5.6 is that the width in energy of the IEDs decreases while the width in angle increases with increasing *HF* power deposition. This is counter-intuitive since with the increase in plasma density that occurs with increasing *HF* power, the sheath becomes thinner. For otherwise constant conditions, the width of the IED should then increase. However, with higher *HF* power, the plasma density increases, enabling a larger current. In order to keep the

LF power constant, the amplitude of the *LF* voltage and magnitude of the dc bias decrease. Since the characteristics of the IEDs are, in fact, dominated by the *LF*, the width of the IED decreases to reflect this decrease in *LF* amplitude and dc bias. These findings are consistent with the observations of Liu *et al*.[12]

If the *HF* power is fixed and produces a sufficiently high plasma density to be in the thin sheath limit, then varying the *LF* power should have little effect on bulk plasma properties, since electron heating is dominated by the *HF*. Electron densities for *LF* powers from 300 W to 1200 W are shown in Fig. 5.7. The peak electron density only nominally increases with power, from 1.3×10^{11} cm^{-3} at 300 W to 1.4×10^{11} cm^{-3} at 1200 W about 4% with every 300 W increase in *LF* power. Since the ion density and so ion current do not appreciably change, an increase in *LF* power results in a nearly linear increase in *LF* voltage. As the *LF* voltage increases, the contribution by secondary electrons to ionization increases, which is in part responsible for the increase in ion density.

IEADs for *LF* powers from 300 W to 1200 W are shown in Fig. 5.8 while keeping the *HF* power constant at 300 W. The increase in average ion energy and small increase in plasma density with increasing *LF* power indicates that the majority of additional *LF* power contributes to ion acceleration in the sheath. The average ion energy scales with dc bias, which increases in magnitude from -133 V to -380 V, producing an increase in the spread of the IED from $\Delta E = 290$ eV to 910 eV.

The plasma density increases by less than 10% with while increasing the *LF* power from 300 W to 1200 W, and so the *LF* voltage amplitude linearly increases from 122 V to 772 V to deliver the specified power. The large increment in *LF* voltage and corresponding increase in dc bias increases the sheath potential during the cathodic portion of the *LF* cycle while having a

nominal effect on the anodic portion of the *LF* cycle. These trends extend the high energy of the IED while not significantly affecting the low energy portion of the IED. The greater extent of the high energy portion of the IED narrows the angular distribution from 9° at 300 W to 6° at 1200 W. The *HF* voltage amplitude also increases by 26 V as the *LF* power is increased (110 V to 136 V). This increase in *HF* voltage results from a thickening of the sheath with increasing *LF* power. The sheath thickness increases from 2.7 mm at a *LF* power of 300 W to 4.1 mm for 1200 W. The modulation of the sheath by the *HF* therefore decreases on a proportional basis, particularly at the peak of the cathodic portion of the cycle. The *HF* voltage amplitude therefore increases to increase the proportional modulation of the sheath.

The modulation of the IEDs due to the 60 MHz lessens as the *LF* power increases. This is due in part to the sheath thickening as the *LF* voltage increases, which results in ion transport being more in the thick-sheath limit at 60 MHz. The position of the lower energy peak increases from 77 eV to 122 eV with increasing *LF* power. This increment in the low energy extent is mainly due to the increase in the *HF* voltage. During the anodic portion of the *LF* cycle, the *LF* sheath is at its minimum. The sheath potential is then dominated by the *HF* whose amplitude increases with *LF* power.

Extrapolation of the just discussed trends for IEDs as a function of *LF* and *HF* power to more complex gas mixtures should be done with caution. Plasma etching processes typically involve gas mixtures that have several molecular constituents, one or more of which are often electronegative. The bulk plasma sustained in these gas mixtures is more resistive than noble gas and non-attaching gas mixtures due to the attachment that occurs in the bulk plasma. At the same time, the electron impact ionization cross sections in these mixtures at energies of hundreds of eV are typically larger than for the noble gases. The end result is that the plasma density and

125

ion current are both more sensitive functions of the *LF* power in DF-CCPs than in noble gases. For example, Booth *et al.* [14] measured electron densities and ion currents in DF-CCPs sustained in $Ar/C_4F_8/O_2$ mixtures (50 mTorr, 2 MHz + 27.12 MHz) while varying both the *LF* and *HF* power. They found that both electron density and ion current increased nearly linearly with increasing *HF* power with constant *LF* power. The resulting increase in ion current reduced the *LF* voltage. For constant *HF* power, both the electron density and ion current also increased with *LF* power. For example, for a *HF* power of 600 W, the electron density nearly doubled when increasing the *LF* power from 0 to 700 W.

Similar trends for gas mixtures as found by Booth *et al.* [14] result from our computations. For example, DF-CCPs sustained in an $Ar/CF_4/O_2 = 90/9/1$ mixture at 50 mTorr were simulated as a function of 2 MHz and 30 MHz power. The resulting electron densities and *LF* voltage are shown in Fig. 5.9 a. Unlike the Ar discharges, electron density increases with increasing *LF* power. For a constant 550 W *HF*, n_e increases from 1.4×10^{11} cm^{-3} to 2.0×10^{11} cm^{-3} when increasing the *LF* power from 100 W to 700 W. This sensitivity of electron density to the *LF* power is due to the increase in joule heating in the bulk plasma in the molecular gas mixture due to its higher resistivity. There is also a larger contribution to ionization by secondary electron emission than in the noble gas discharges. The *LF* voltage decreases with increasing *HF* power, as shown in Fig. 5.9 b. The amount of decrease is smaller than in the noble gases as both the *HF* and *LF* power increase. As the *LF* power increases and its contribution to ionization increases, the ion current becomes a more sensitive function of the *LF* power and less sensitive to the *HF* power. These findings also align with those of Liu *et al.* [13]

5.3.2   Etching SiO₂ with Power Adjusted Ar/CF₄/O₂ Gas Mixture in DF-CCPs

In order to assess control of the *LF* and *HF* components of the IEADs on etching of SiO_2,

an Ar/CF$_4$/O$_2$ =75/20/5 mixture was used in the model. The resulting IEADs were then used in the MCFPM to address etching of SiO$_2$ over Si. Although the IEADs of all ions are computed, to illustrate the trends of IEDs with different *HF* or *LF* power, we only plot the total IEDs, and the IEDs for the heaviest (CF$_3^+$) and lightest (O$^+$) ions that have significant fluxes. For example, the total IED for Ar/CF$_4$/O$_2$ is shown in Fig. 5.10 for a *LF* of 2 MHz and powers of 300 W and 600 W. The 60 MHz, *HF* power was varied from 300 to 1200 W. For 300 W at 2 MHz, the 60 MHz voltage amplitude increases from 76 V to 172 V over the range of 300 W to 1200 W. The voltage at 2 MHz decreases from 122 V to 103 V. When the 2 MHz power increases to 600 W, similar changes of voltages are observed. The *HF* voltage increases from 70 V to 162 V while the *LF* voltage drops from 166 V to 145 V. Both cases show the same trends as observed for the pure Ar cases, but with much smaller amplitude modulation due to the larger plasma density and current in the Ar/CF$_4$/O$_2$ mixture.

The smaller change in voltage amplitude also leads to a smaller variation in dc bias, from -32 V to -63 V in the 300 W case and -36 V to -68 V in the 600 W case. Comparing these IEDs with those for pure Ar (Fig. 5.6), a different trend in the dc biases is found. In the pure Ar case, when increasing *HF* power, the dc bias becomes less negative. The differences in these trends may be explained by the spatial distribution of the plasma. In Ar/CF$_4$/O$_2$ the plasma is more edge peaked with a maximum density at a radius of about 12.5 cm. In the pure Ar case, the density has a peak near a radius of 10 cm and is more radially uniform. These differences influence the balance between displacement and conduction current collected on the substrate. The end result is that a less negative self dc bias is needed to balance the current for the Ar/CF$_4$/O$_2$ cases.

The modulation of the *LF* sheath by the *HF* voltage is smaller in the Ar/CF$_4$/O$_2$ mixture

compared to the Ar cases, and so the IED maintains its double peaked shape for all of the *HF*

powers. At the dc bias becomes more negative, the entire IED shifts to higher energy.[15] The

modulation in the total IED due to the 60 MHz power is less significant for the total IED

compared to that of the individual ions. For example, IEDs for CF_3^+ (the heaviest ion) and O^+

(the lightest ion) for a *LF* power of 600 W and *HF* power of 300 to 1200 W are shown in Fig.

5.11. The energies at which the peaks of the modulation occur are a function of mass, and so

there is some smoothing of the total IED, that results from the summation of the peaks of the

IEDs from different ions. For the same conditions, the width in energy of the IED for the heavier

CF_3^+ is smaller than for the lighter O^+. The IED for O^+ extends to a 20 eV higher energy than

the IED for CF_3^+. The energy width, ΔE, of the IED in a DF-CCF scales with ion mass M_i

[2,16] as

$$\Delta E \sim \frac{\overline{V}_s}{\overline{s}\,\omega_{LF}}(\frac{2q\overline{V}_s}{M_i})^{1/2},\qquad\qquad\qquad(5.5)$$

where $\overline{V}_s$ and $\overline{s}$ are the average sheath potential and sheath width, ω_{LF} is the value of *LF* and, q is

the electron charge. With 600 W at 2 MHz and 300 W at 60 MHz, the ΔE for CF_3^+ is 170 eV

and that for ΔE of O^+ is 180 eV. According to Eq. (5.5), the ratio of the widths should scale as

$\Delta E_{CF_3^+}/\Delta E_{O^+}=0.49$. The disagreement may come from the addition of the large power at 60

MHz at whose frequency both ions see the sheath as being thick.

The ion and neutral energy and angular distributions, and fluxes computed for $Ar/CF_4/O_2$

mixtures were used to investigate the sensitivity of etch profiles to the ratio of powers of the *LF*

and *HF*. The system we investigated is etching a trench through SiO_2 over Si with a hardmask.

The width of the mask opening is 37 nm and the aspect ratio is 15. The over-etch was 20%.

(That is, the etch continued for an additional 20% of the time required to reach the bottom of the

feature.) Profiles, etch rates and the width of the center of the feature compared to mask opening

(called CDR – critical dimension ratio) are shown in Fig. 5.12 while varying the *HF* power. The

desired value of CDR is 1.0 – tapered profiles have CDR < 1 and bowing profiles have CDR > 1.

With only 300 W at both the *HF* and *LF*, the large flux of low energy ions results in excessive

polymer deposition on sidewalls. With this polymer build up, an etch stop occurs before

reaching the underlying Si.

Increasing *HF* power produces a nearly linear increase in etch rate for a given *LF* power

due to the higher ion and radical flux. The etch rates for low *LF* power (300 W) and high *LF*

power (600 W) converge at high *HF* power. This convergence likely results from the similar

values of dc biases, which determine average ion energy, with increasing *HF* power deposition.

Although the cases for 600 W at *LF* have more ions in the high energy peaks, they also have

more ions in the low energy peaks, which will promote polymer deposition and restrain etching.

CDR also improves with increasing *HF* power, from a low of 0.38 (low *LF* and low *HF* power)

to 0.72 (high *LF* and high *HF* power). A portion of the increase in etch rate is due to a

moderately higher F/CF_x ratio in the flux incident onto the wafer – higher values of F/CF_x

usually produce higher etch rates.[17] The F/CF_x ratio increases from 2.07 (low *LF* and low *HF*

power) to 2.27 (high *LF* and high *HF* power). Etch profiles for these conditions are sensitive to

HF power beyond simply the rate of etching due to the change in CDR.

The total ion IEDs for $Ar/CF_4/O_2$ are shown in Fig. 5.13 for *HF* powers of 300 W and

600 W, while varying the 2 MHz power from 300 to 1200 W. For a 300 W *HF* power, the *LF*

voltage amplitude increases from 122 V to 216 V for 300 W to 1200 W. The voltage amplitude

of the *HF* decreases from 76 V to 63 V. The dc bias becomes more negative, from -32 V to -46

V. For a *HF* power of 600 W, similar changes of voltages are observed. The *LF* voltage

increases from 111 V to 214 V, the *HF* voltage decreases from 113 V to 96 V while the dc bias increases (becomes more negative) from -42 V to -60 V. The IEDs for CF_3^+ and O^+ for a *HF* power of 600 W and *LF* power of 300 to 1200 W are shown in Fig. 5.14. As in the case of varying the *HF* power, when varying the *LF* the modulation of the total IEDs by the *HF* is not particularly severe. The contributions of different ions having peaks at complementary energies tend to smooth the IEDs. However the modulation of IEDs of individual species is significant, reaching nearly 100% for O^+.

As the properties of the bulk plasma are less influenced by the *LF* power than the *HF* power, the plasma impendence does not significantly change with changes in *LF* power. Therefore, changing the *LF* power will produce changes in the IED similar to changing the *LF* voltage amplitude. Georgieva *et al.* performed PIC simulations to investigate the influence on IEDs of changing the voltage in DF-CCPs. They found that when keeping the *HF* voltage constant, increasing the *LF* voltage monotonically shifted the high energy extent of the IEDs to higher energy.[2] In comparing with their results, our keeping the *HF* power constant results in the *HF* voltage dropping by about 16% over the range of *LF* powers of 300 W to 1200 W. This decrease in *HF* voltage will decrease the sheath potential during the anodic portion of the *LF* cycle. Therefore, the low energy peaks shift to lower energy as the *LF* power increases.

Profiles, etch rates and CDRs are shown in Fig. 5.15 while varying the *LF* power. Etch rates increase nearly linearly with increasing *LF* power at the lower *HF* power (300 W) and somewhat sub-linearly for the higher *HF* power (600 W). Since the ion fluxes are constant to within 8-9 % over this range of *LF* powers, this increase in etch rate is due primarily to the increase in ion energy. The maximum ion energy increases about 64% with *LF* power from 300 to 1200 W. On this basis alone, one would expect only a 30% increase in etch rate since

chemical sputtering rates scale with $\varepsilon^{1/2}$. The significantly greater increase in etch rate is due, in part, to a depletion of the low energy portion of the IEDs, an energy regime which more efficiently promotes polymerization. With a more moderate amount of polymerization on the sidewalls, the CDR improves from 0.38 to 0.72.

5.4 Control of IEDs in DF-CCP with Phase Shifting

The influence of changing the phase between the *LF* and its second harmonic *HF* (n = 2) in CCPs has been well studied.[4] The influence of the phase relationship between the fundamental and higher harmonic frequencies (n > 10) is usually not emphasized as the ion transit time for these harmonics is long enough compared to the period to only affect the average ion energy. However, the just discussed results suggest that the modulation of the IED by the *HF* may be significant when the plasma density is high and the average sheath thickness is small.

Here, we investigate possible methods to control IEDs in a DF-CCP based on the phase difference between the *HF* and the *LF* where the *HF* is the 10th, 20th and 30th harmonic (n = 10, 20, 30) of the fundamental. In this part of study, both pure Ar and $Ar/CF_4/O_2=75/20/5$ mixtures were investigated. All operating conditions are the same as in the previous section except that the *HF* is 20, 40 or 60 MHz. Phase differences of 0 and π were investigated for comparison to the electrical asymmetry effect theory.[4] Here, we keep the power constant at 300 W each for the *HF* and *LF*.

Electron densities in pure Ar are shown in Fig. 5.16 for phase differences of $\Delta\phi = 0$ and π, for *HF* of 20, 40 and 60 MHz. There is not a significant difference in peak plasma densities over this range of *HF*, though the highest frequency does produce more uniform plasmas. Although there are not significant differences in the time averaged plasma properties, the phase difference between the *LF* and *HF* does modulate the dynamics of the plasma potential which in

turn affects the IEDs.

For example, IEDs for pure Ar plasmas are shown in Fig. 5.17 for $\Delta\phi = 0$ and π for *HF* of 20, 40 and 60 MHz. The IEDs for 2 + 20 MHz show significant differences in the modulation by the *HF* between the $\Delta\phi = 0$ and π cases. In each case, the peaks in modulation are separated by either 37 eV or 74 eV. The modulation is most severe during the cathodic portion of the *LF* cycle when ions arrive with their highest energy. The modulation is smaller during the anodic portion of the *LF* cycle when ions arrive with their lowest energy. These differences in modulation may result from a resonance effect in which the simultaneous cathodic portions of the *LF* and *HF* cycles increase the ion energy in proportion to both amplitudes, while the simultaneous anodic portions of the *LF* and *HF* cycles do not increase the ion energy. When one frequency is anodic and other cathodic, only the cathodic amplitude significantly contributes to ion acceleration. Similar phenomena also occur for 2 + 40 and 2 + 60 MHz. The energy separation of the peaks in modulation decreases with increasing *HF*. The total number of peaks for both values of $\Delta\phi$ is given by ratio of the *HF* to the *LF*, while the amplitude of the modulation is inversely proportional to the *HF*.

From the cycle averaged perspective, we found the time averaged sheath thickness decreases as the *HF* increases as shown in Fig. 5.18. Here the IEDs are shown as a function of height above the wafer for $\Delta\phi = 0$ and π. The cycle averaged sheath properties, as reflected by the ion energies as a function of height, have a small sensitivity to $\Delta\phi$ at a *HF* of 20 MHz. With $\Delta\phi = 0$, the sheath is thinner by 1-2 mm, leading to asymmetries in the IEDs when changing phase. At a *HF* of 60 MHz, the cycle averaged sheath properties are nearly independent of $\Delta\phi$, resulting in less sensitivity to the phase difference

From the perspective of sheath dynamics, the electron density remaining in the sheath 1.5

mm above the wafer during one *LF* period is shown in Fig. 5.19. On the average, the electron density remaining in the sheath is higher with higher *HF*, which explains the thinner sheath at high *HF*. (Sheath thickness approximately scales with $n_e^{-1/2}$.) The electron density in the 2+20 MHz sheath is smaller for $\Delta\phi = \pi$ compared to $\Delta\phi = 0$, which explains the difference in sheath thickness with $\Delta\phi$. The sheath boundary oscillates more rapidly during the *LF* cycle with larger *HF*, which explains the smaller amplitude of the *HF* modulation in the IEDs. With the thinner sheath having less modulation during the anodic *LF* cycle, the ion transit time to cross the sheath is short for both the *LF* and *HF* and there is less modulation in the IEDs. Although there is a thicker sheath during the cathodic part of the cycle, the larger amplitude of the modulation in the sheath produces more modulation in the IEDs.

By dynamically changing the phase difference between the *HF* and *LF*, a smooth time averaged IED can be achieved that minimizes modulation. For example, IEDs for Ar$^+$ obtained by time averaging the IEDs produced by $\Delta\phi = 0$ and π are shown in Fig. 5.16. The IEDs produced by alternating between $\Delta\phi = 0$ and π are progressively freer of modulation as the *HF* increases.

The IEDs which result from phase control are in part a function of ion mass and so complex gas mixtures having ions of different masses will have more complex responses than observed for pure argon discharges. For example, IEDs from the Ar/CF$_4$/O$_2$ mixture for CF$_3^+$ (heaviest ion), O$^+$ (lightest ion) and averaged for all ions are shown in Fig. 5.20 for 2 + 20 MHz with $\Delta\phi = 0$ and π. IEDs are shown in Fig. 5.21 for 2 + 60 MHz. The IEDs for CF$_3^+$ for 2 + 20 MHz have *HF* modulation that is a sensitive function of $\Delta\phi$, whereas the modulation of the IEDs for O$^+$ is less sensitive to $\Delta\phi$. Since the heavier ions dominate the total ion flux to the wafer, the ion-averaged IEDs display the more severe modulation. When dynamically switching between

$\Delta\phi = 0$ and π, the IEDs lose much of their modulation. As in the IEDs for pure Ar plasmas, the modulation frequency is greater for 2 + 60 MHz however the modulation depth is smaller. Here the modulation for O^+ may be more severe compared to CF_3^+ as the heavier ion is clearly in the thick sheath limit. When dynamically switching between $\Delta\phi = 0$ and π, the majority of modulation is lost for the individual ions. The ion averaged IEDs for these conditions are nearly devoid of modulation.

5.5 Concluding Remarks

IEADs and plasma properties were computationally investigated for dual frequency capacitive plasmas in Ar and Ar/CF$_4$/O$_2$ gas mixtures for frequencies of 2 + 20/40/60 MHz. For DF-CCPs at low pressure, the electron heating and ionization rates scale with ω^2. The plasma density nearly linearly increases with *HF* power as well as shifting the total IEADs to higher energies. We observed different trends when increasing *LF* power depending on the gas mixture. Increasing low frequency power will mainly increase power dissipated within the sheath with little change in plasma density for electropositive gas mixtures such as Ar. However, in the Ar/CF$_4$/O$_2$ mixture, the plasma density increased about 60% with a *LF* power increase from 300 W to 1200 W. These trends are attributed to the more resistive plasma in the molecular, attaching gas mixture and larger contributions to ionization by high energy secondary electrons. When etching high aspect ratio features in SiO$_2$, CDR and etch rate both nearly linearly improve with increasing *LF* and *HF* power. These improvements with *LF* power are due to the shift in the IED to higher energies and the larger radical and ion fluxes produced by the increment in plasmas density. The increase in etch rate with increasing *HF* power in large part is a consequence of the increase in reactive fluxes. However, the improvement in CDR implies a favorable change in the IEAD as well. *HF* was also found to contribute to ion sheath dynamics

and shaping of the IEADs when the sheath is thin. This observation may not be generally true, especially when the sheath is thick.

Changing the phase between the *HF* and *LF* in high plasma density and thin sheath discharges will modify the sheath dynamics and so modify the IEDs incident onto the wafer. When controlling the phase between the *LF* and *HF* between 0 to π, the contribution of the *LF* to the IEDs persists while that of the *HF* modulation shifts in energy. This modification of the IEDs is more severe when the *HF* is a lower frequency. The natural modulation in the IEDs by the *HF* can be smoothed by averaging the IEDs produced by different phase shifts. For example, by continually sweeping the phase shift between 0 to π, a smooth IED free of *HF* modulation can be produced. As this study has focused on the influence of *HF* modulation on IEDs, conditions were chosen that would not significantly change the dc self-bias, which would in turn shift IEDs in energy, as in the electrical asymmetry effect (EAE). However, by combining *HF* modulation with the EAE effect using, for example, 3 frequencies, IEADs may be controlled over a large energy extent using this recently demonstrated phase lock control techniques .[18]

5.6   Figures
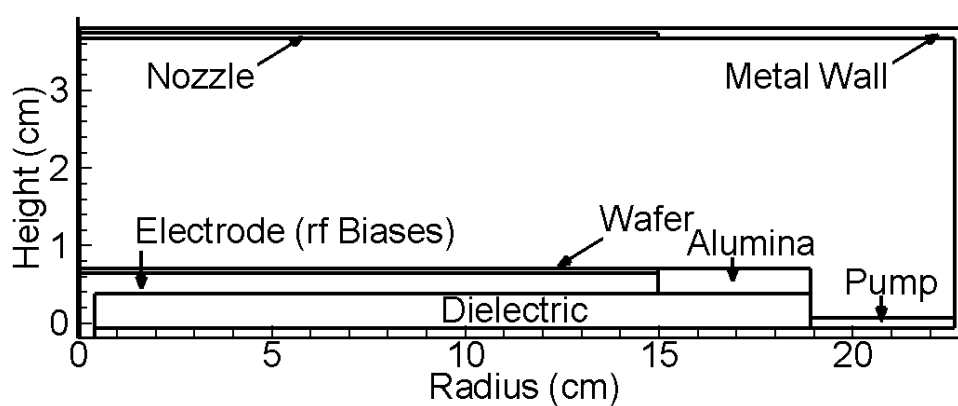
Fig. 5.1. Schematic of the 300 mm DF-CCP reactor. Capacitively coupled *LF* and *HF* power is applied to the substrate surrounded by dielectric focus rings. Both showerhead and chamber wall are grounded.
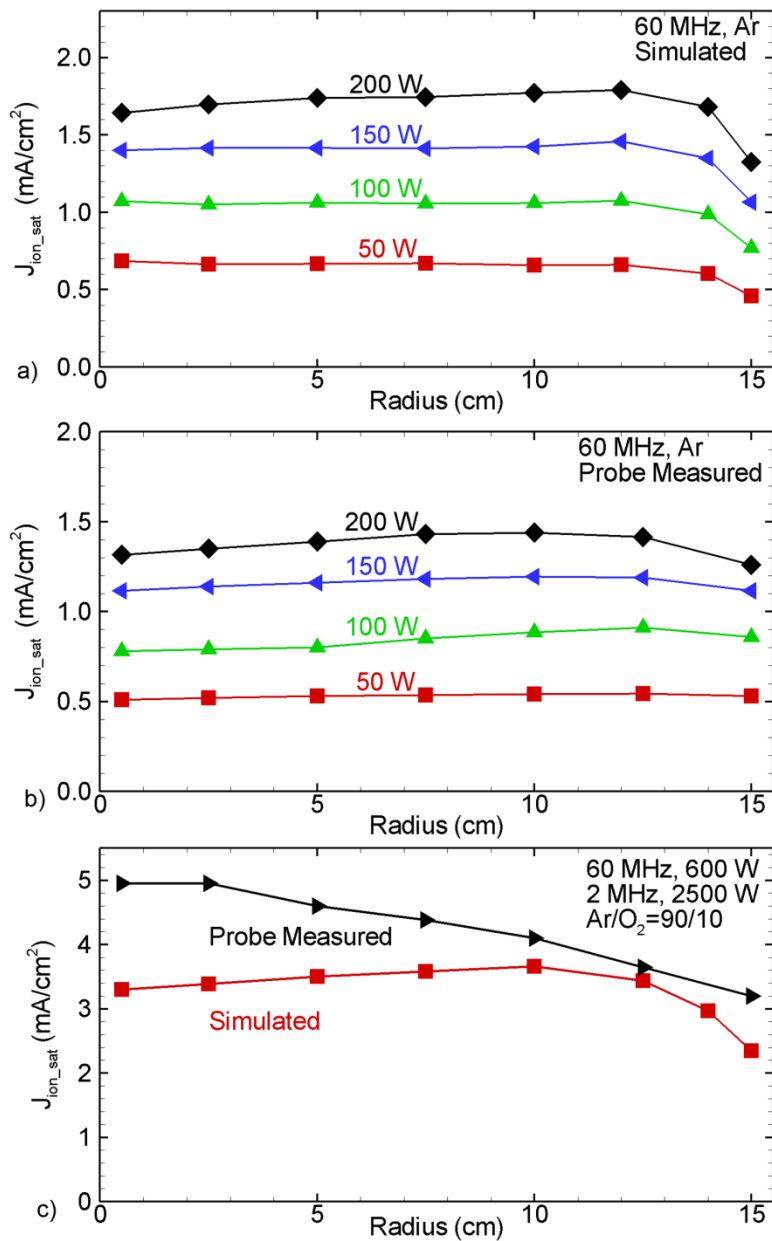
Fig. 5.2. Ion saturation current density as a function of radius at mid-gap. Results are for Ar, 70 mTorr, 800 sccm, 60 MHz for powers of 50 – 200 W. a) Simulation and b) experiments. c) Simulated and measured ion saturation current density at middle of a DF-CCP. The conditions are Ar/O$_2$= 90/10 at 20 mTorr, 300 sccm, LF = 2 MHz, 2500 W and HF = 60 MHz, 600 W.
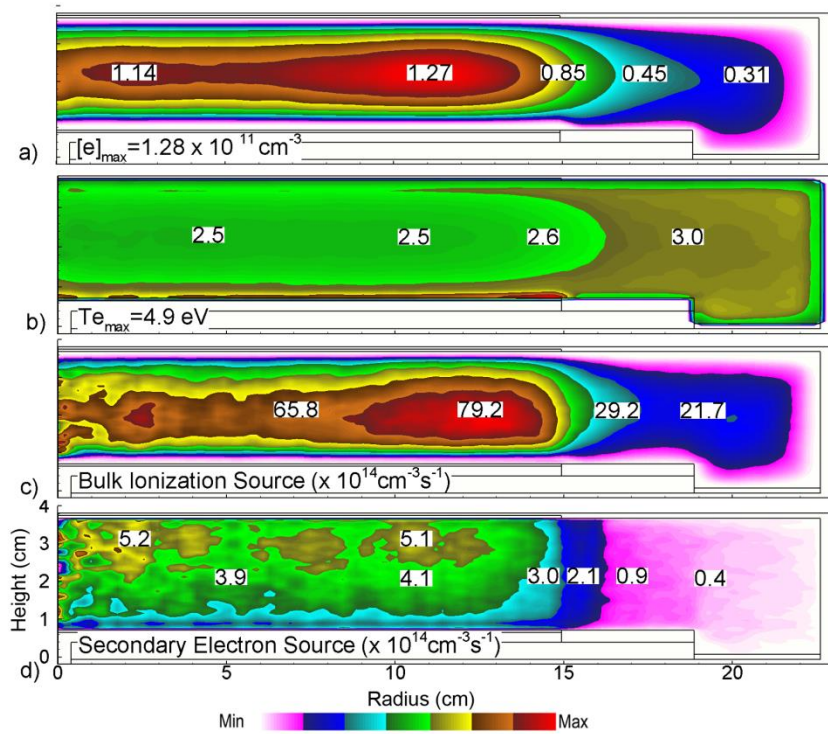
Fig. 5.3. Time averaged plasma properties for the base case conditions (Ar, 30 mTorr, 1000 sccm, LF = 2 MHz, 300 W, HF = 60 MHz, 300 W and dc self-bias = -132 V). a) Electron density, b) electron temperature, c) bulk electron ionization source and d) ionization by sheath accelerated secondary electrons. The plots are linear scales with contour labels having units of 10^{11} cm^{-3}, eV and 10^{14} cm^{-3}s^{-1}.
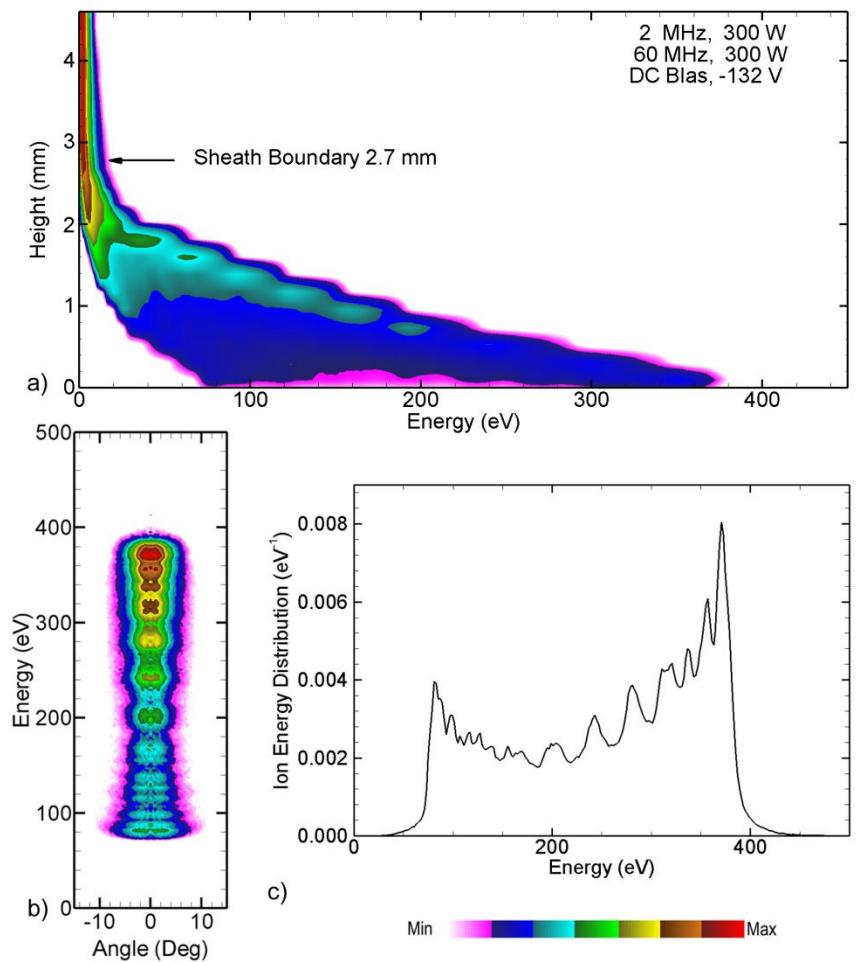
Fig. 5.4. Time averaged IEDs and IEADs for Ar$^+$ for the base case conditions (Ar, 30 mTorr, 1000 sccm, *LF* = 2 MHz, 300 W, *HF* = 60 MHz, 300 W and dc self-bias = -132 V), a) IED from the bulk plasma 4.6 mm above the wafer to the wafer surface with approximate sheath boundary labeled. Discontinuities in energy are caused by the mesh resolution in collecting statistics. b) IEAD collected on wafer. b) IED collected on wafer.
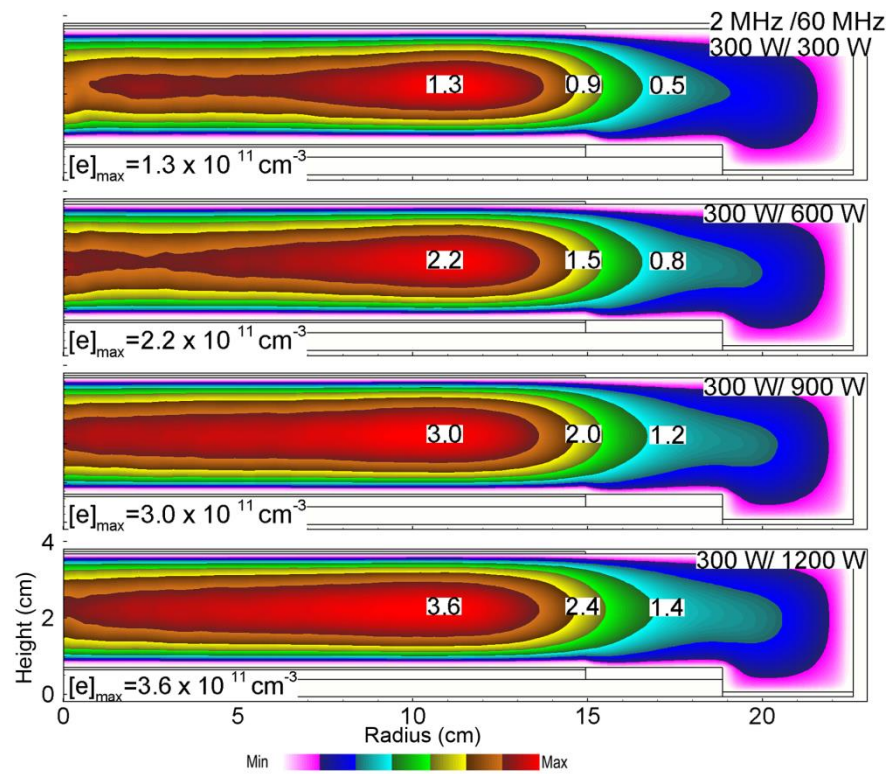
Fig. 5.5. Electron densities for 300 W at 2 MHz, and 60 MHz power of (top to bottom) 300 W, 600 W, 900 W and 1200 W. (Ar, 30 mTorr, 1000 sccm).
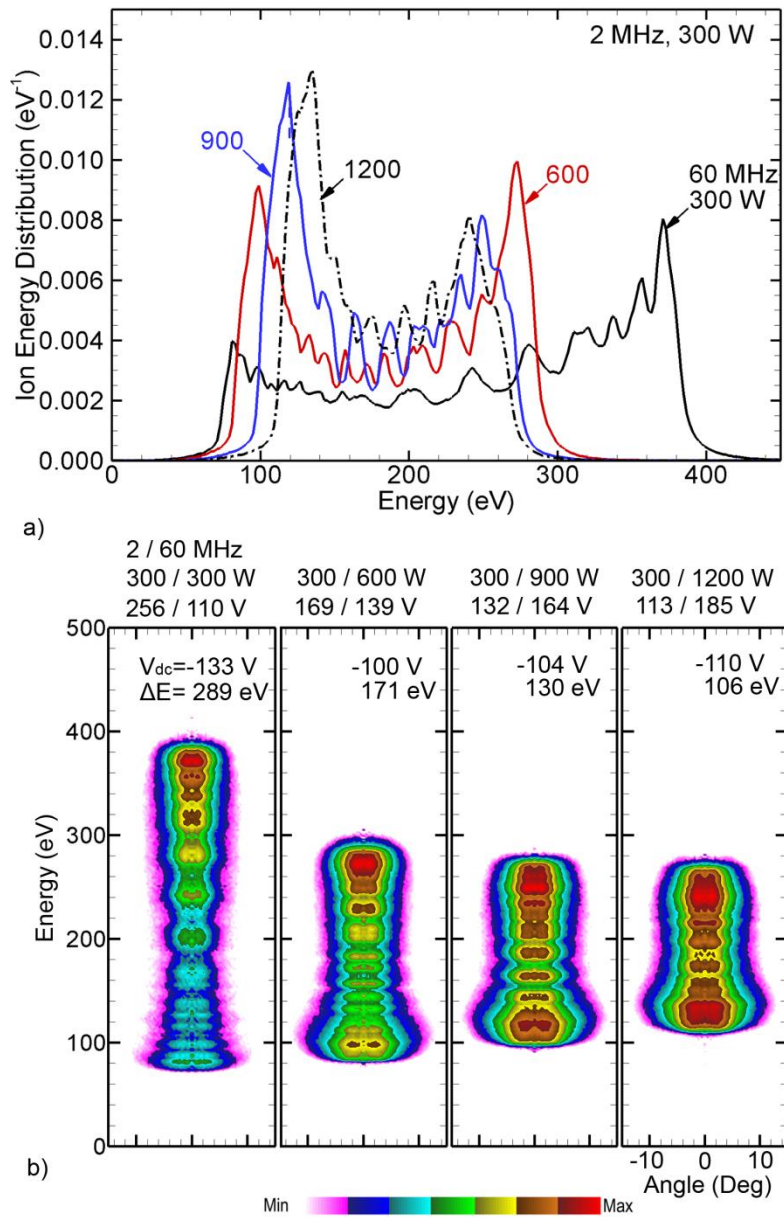
Fig. 5.6. Time averaged Ar$^+$ ion distributions onto the wafer for 300 W at 2 MHz power, and 60 MHz power of 300 W, 600 W, 900 W and 1200 W. a) IEDs and b) IEADs. The voltages at each frequency, dc bias and energy width of the IEADs are noted in each frame. (Ar, 30 mTorr, 1000 sccm).

141
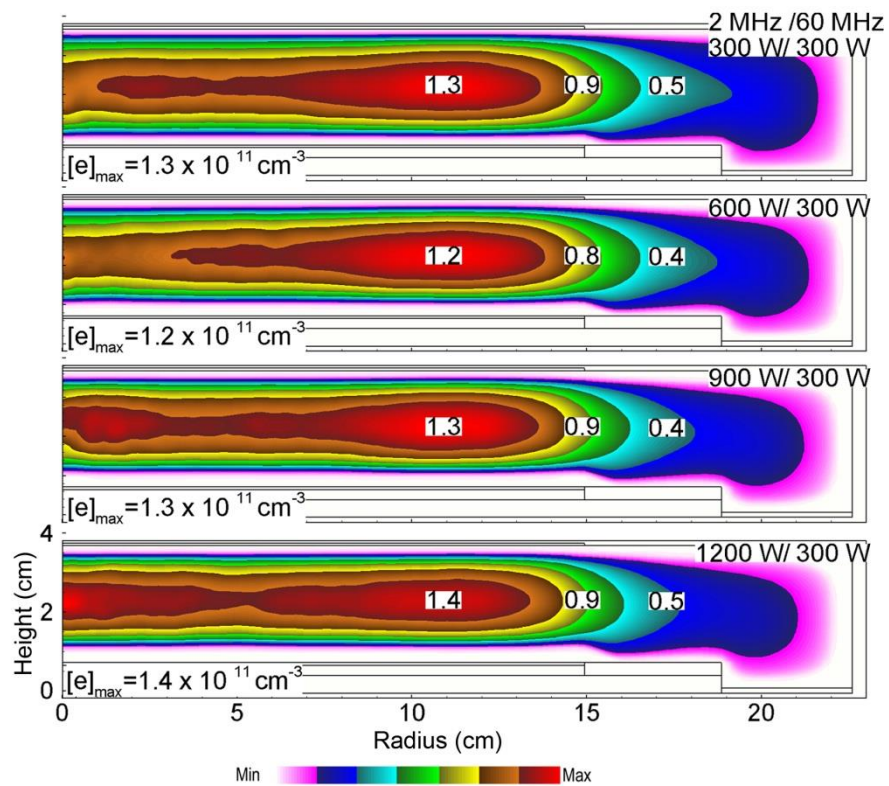
Fig. 5.7. Electron densities for 300 W at 60 MHz power and MHz power of (top to bottom) 300 W, 600 W, 900 W, and 1200 W. (Ar, 30 mTorr, 1000 sccm).
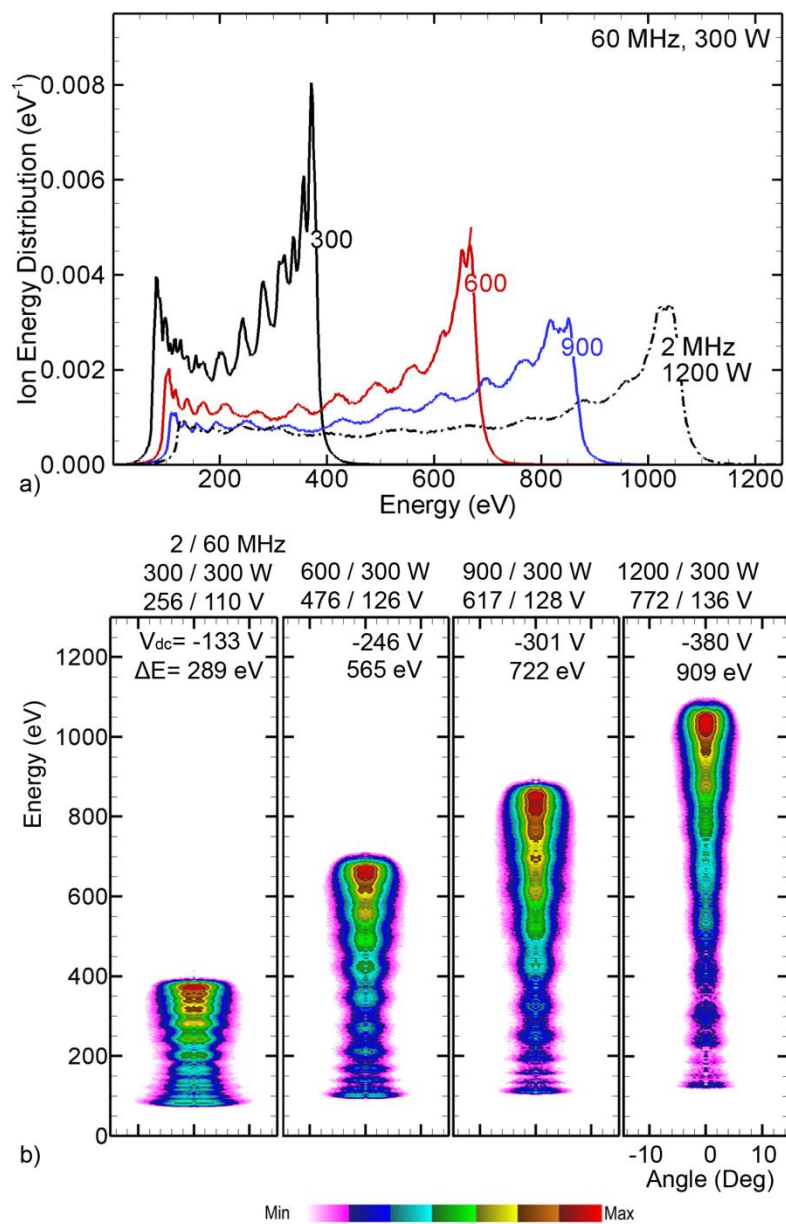
Fig. 5.8. Time averaged Ar$^+$ ion distributions onto the wafer for 300 W at 60 MHz power, and 2 MHz power of 300 W, 600 W, 900 W and 1200 W. a) IEDs and b) IEADs. The voltages at each frequency, dc bias and energy width of the IEADs are noted in each frame. (Ar, 30 mTorr, 1000 sccm).
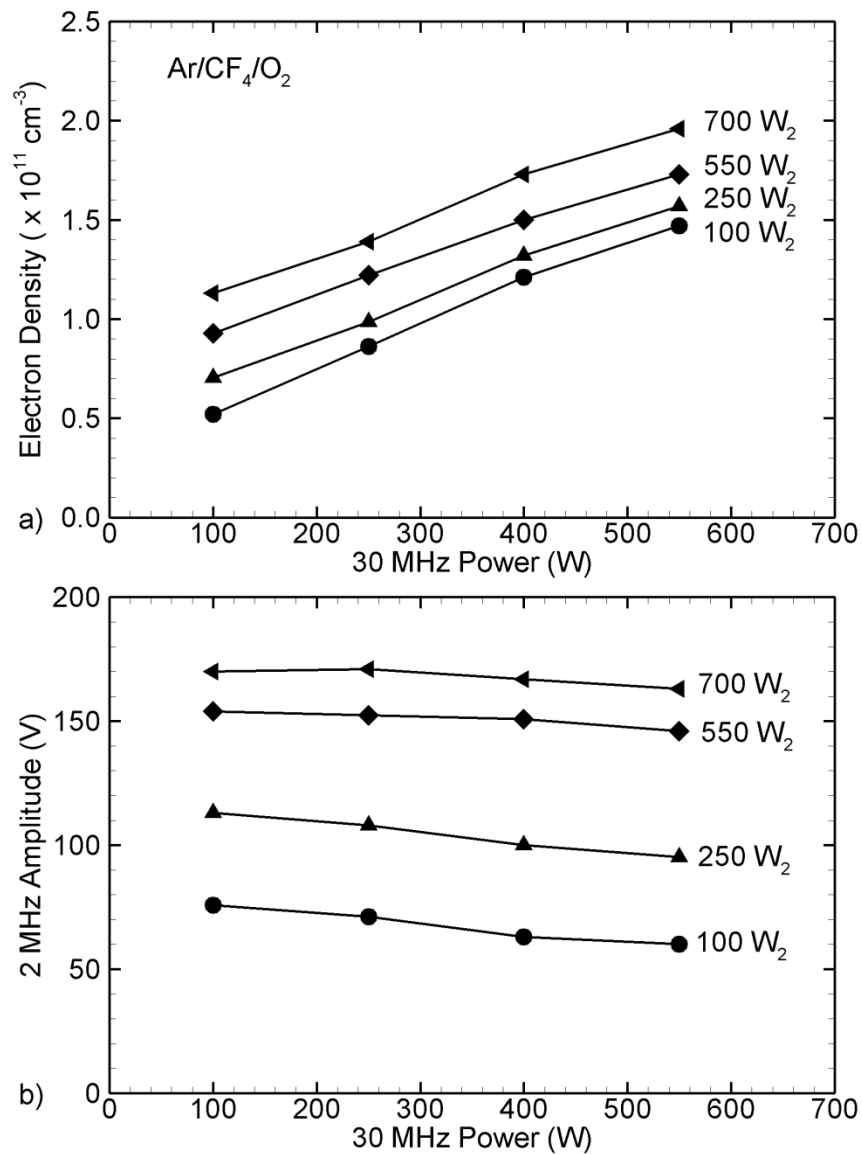
Fig. 5.9. Plasma properties as a function of 2 and 30 MHz power for $Ar/CF_4/O_2 = 90/9/1$ at 50 mTorr (184 sccm). a) Electron densities at mid-gap and radius of 3 cm. b) 2 MHz rf amplitude.
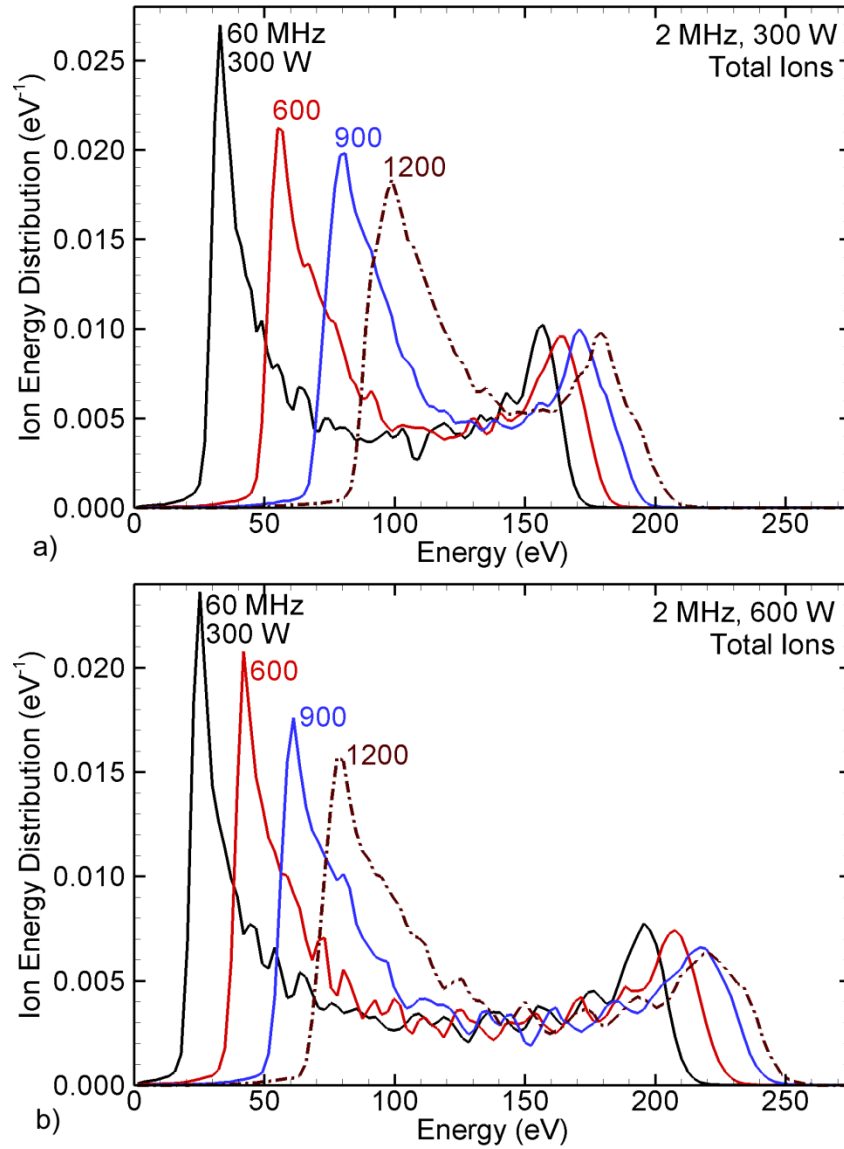
Fig. 5.10. Time averaged total ion IEDs onto the wafer for $Ar/CF_4/O_2 = 75/20/5$ at 30 mTorr (500 sccm) with for 60 MHz power of 300 W, 600 W, 900 W and 1200 W. Cases are shown for a 2 MHz power of a) 300 W and b) 600 W.
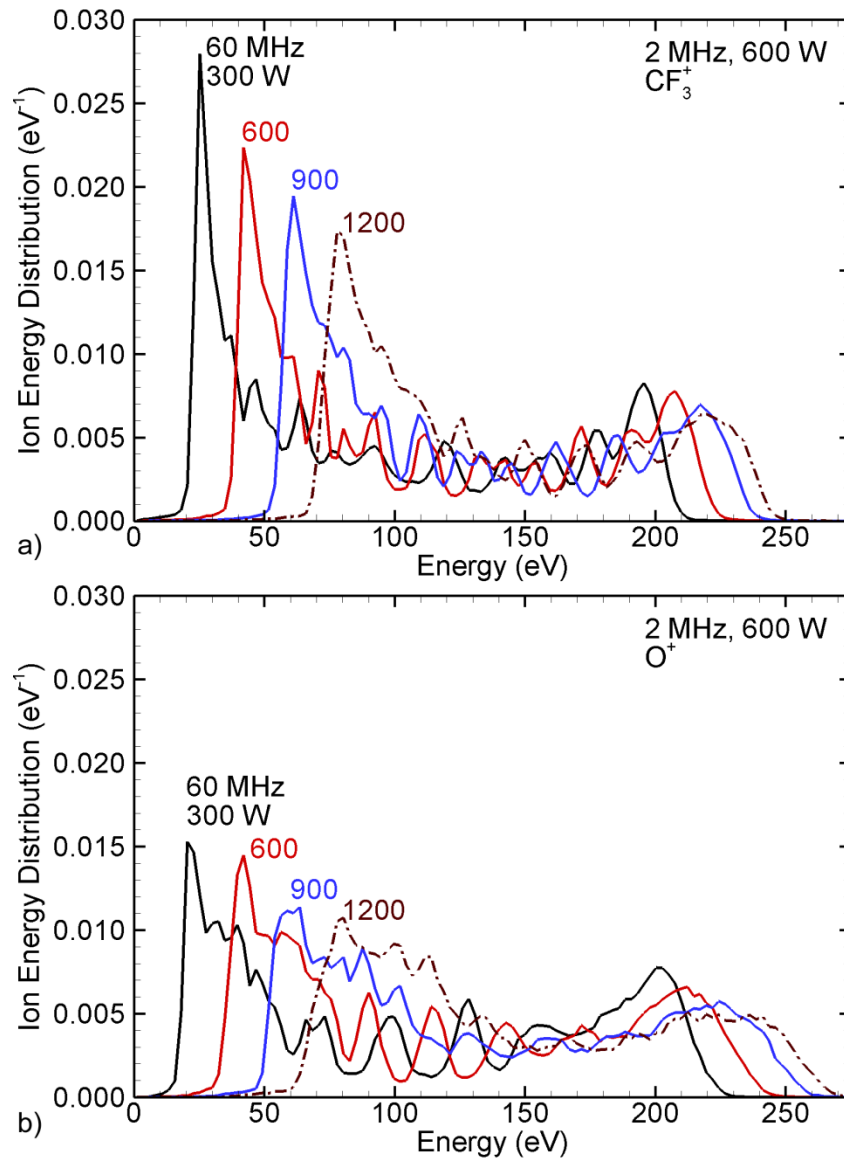
Fig. 5.11. Time averaged IEDs onto the wafer for $Ar/CF_4/O_2 = 75/20/5$ at 30 mTorr (500 sccm) for 600 W at 2 MHz and 60 MHz power of 300 W, 600 W, 900 W and 1200 W. a) CF_3^+ (heaviest ion) and b) O^+ (lightest ion).
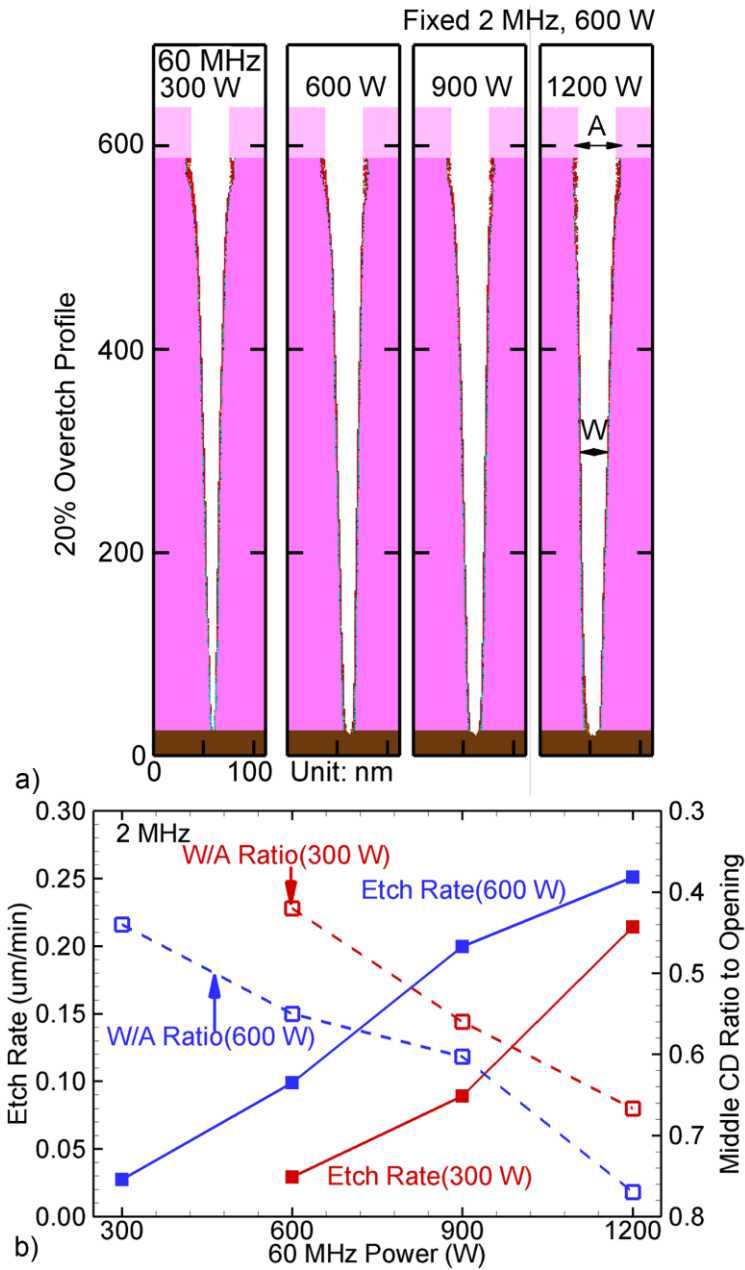
Fig. 5.12. SiO$_2$ etch (over Si) characteristics for 60 MHz power of 300 W, 600 W, 900 W and 1200 W. a) High aspect ratio features for 20% over-etch with 600 W at 2 MHz power. b) Etch rate (solid lines) and CDR (dotted lines) for 2 MHz power of 300 W and 600 W. (CDR is the width at the center of the feature to the mask opening.)

147
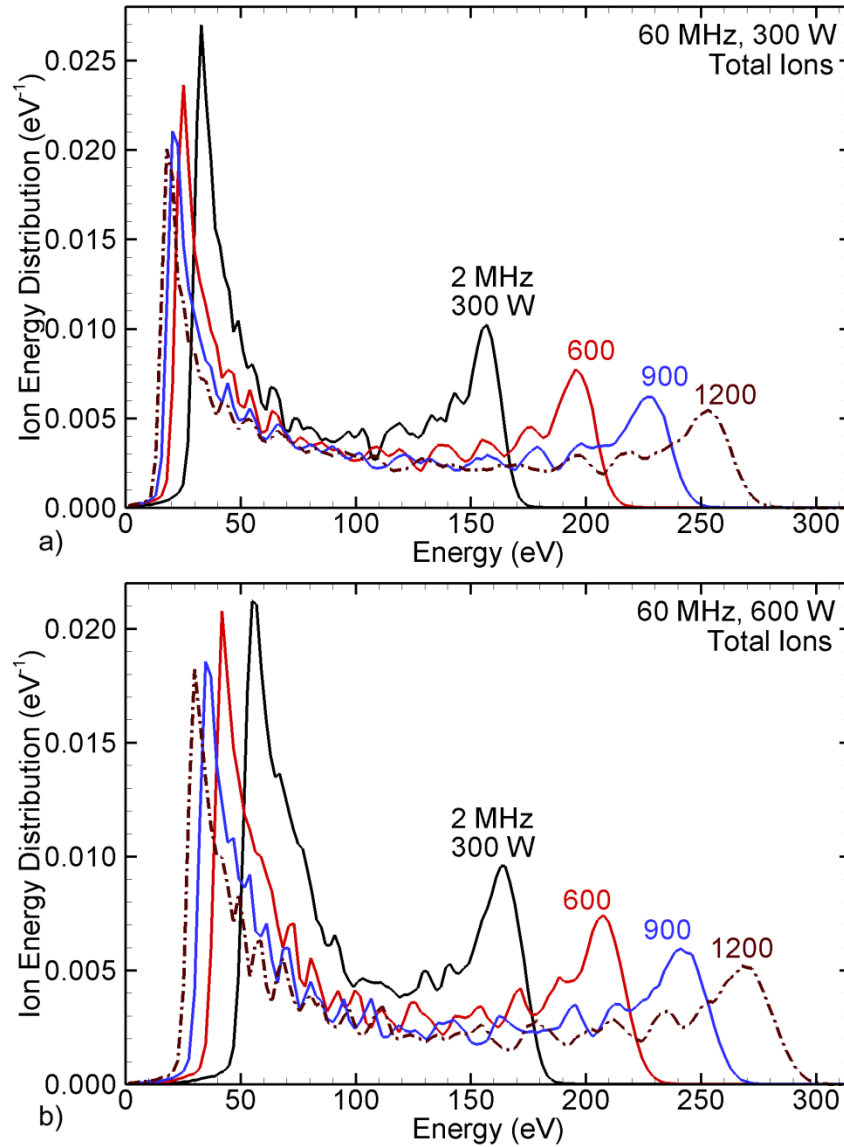
Fig. 5.13. Time averaged total ion IEDs onto the wafer for Ar/CF$_4$/O$_2$ = 75/20/5 at 30 mTorr (500 sccm) with for 2 MHz power of 300 W, 600 W, 900 W and 1200 W. Cases are shown for the 60 MHz power of a) 300 W and b) 600 W.
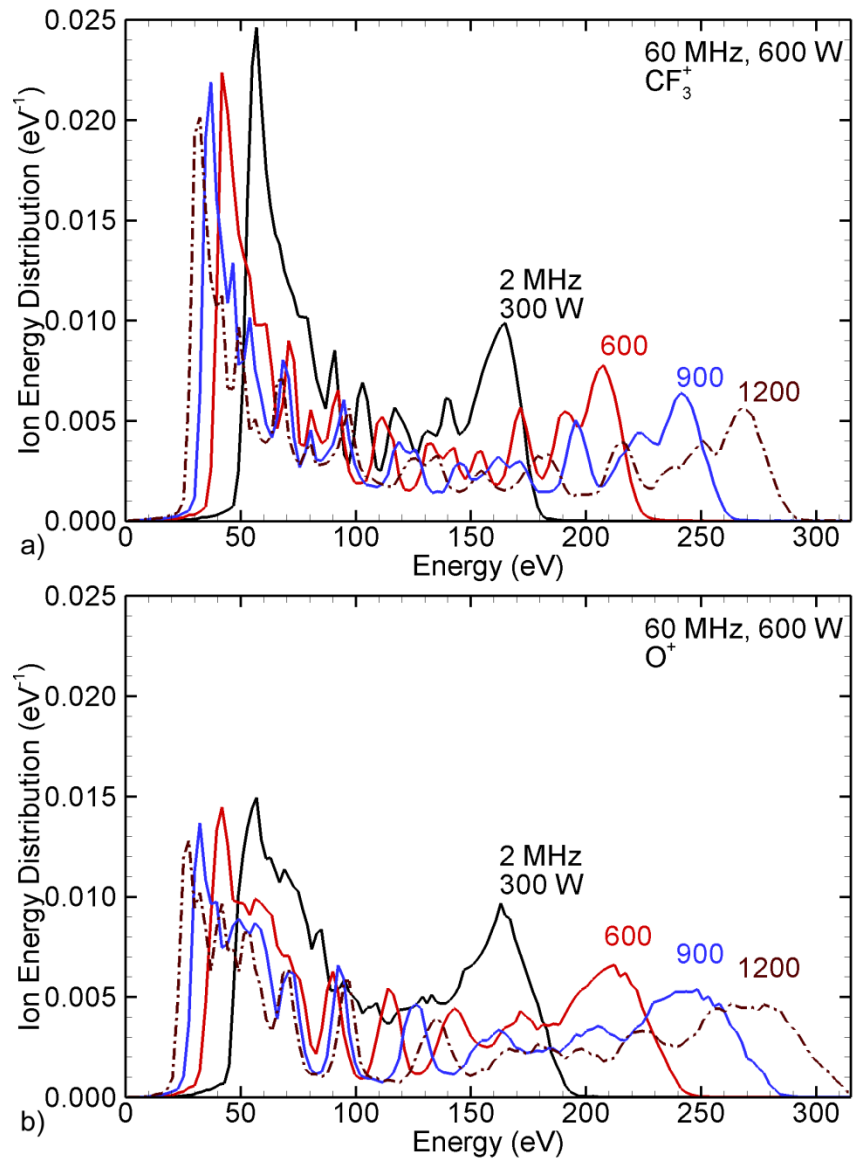
Fig. 5.14. Time averaged IEDs on wafer for Ar/CF$_4$/O$_2$ = 75/20/5 at 30 mTorr (500 sccm) for 600 W at 60 MHz and 2 MHz power of 300 W, 600 W, 900 W and 1200 W. a) CF$_3^+$ (heaviest ion) and b) O$^+$ (lightest ion).
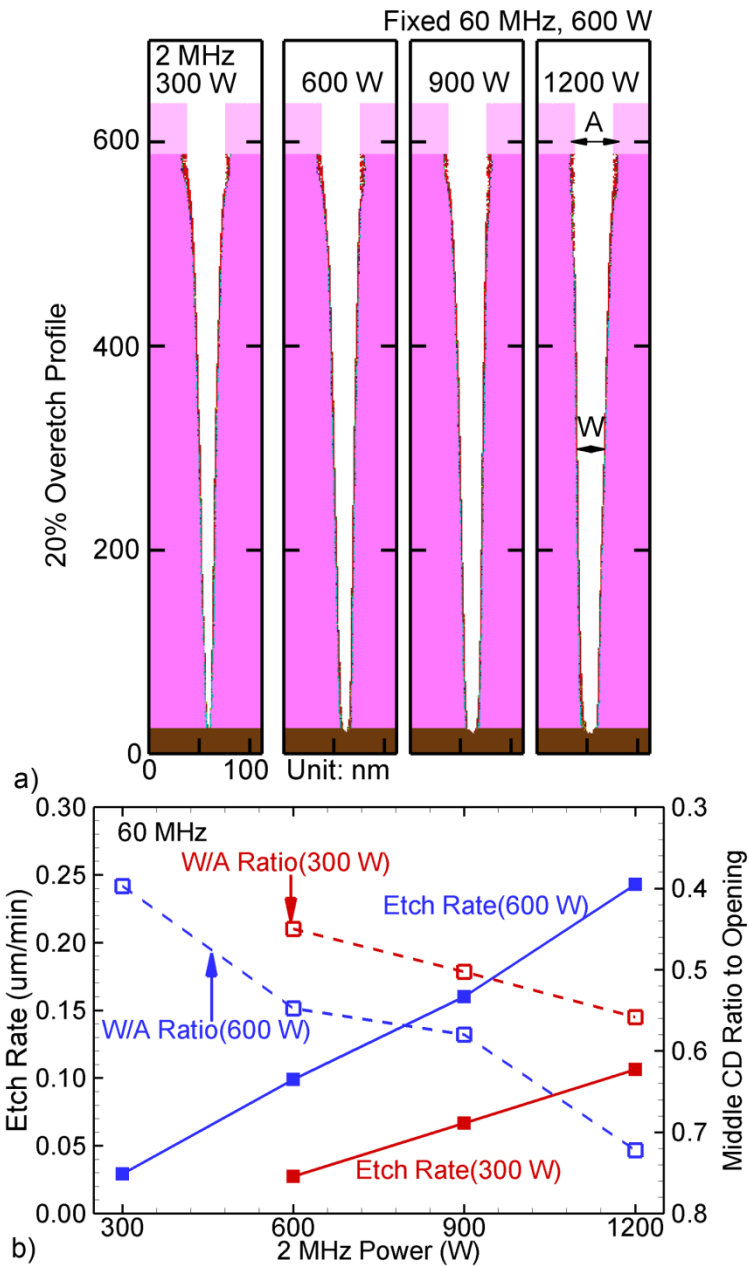
Fig. 5.15. SiO$_2$ etch (over Si) characteristics for 2 MHz power of 300 W, 600 W, 900 W and 1200 W. a) High aspect ratio features for 20% over-etch with 600 W at 60 MHz power. b) Etch rate (solid lines) and CDR (dotted lines) for 60 MHz power of 300 W and 600 W. (CDR is the width at the center of the feature to the mask opening.)

150
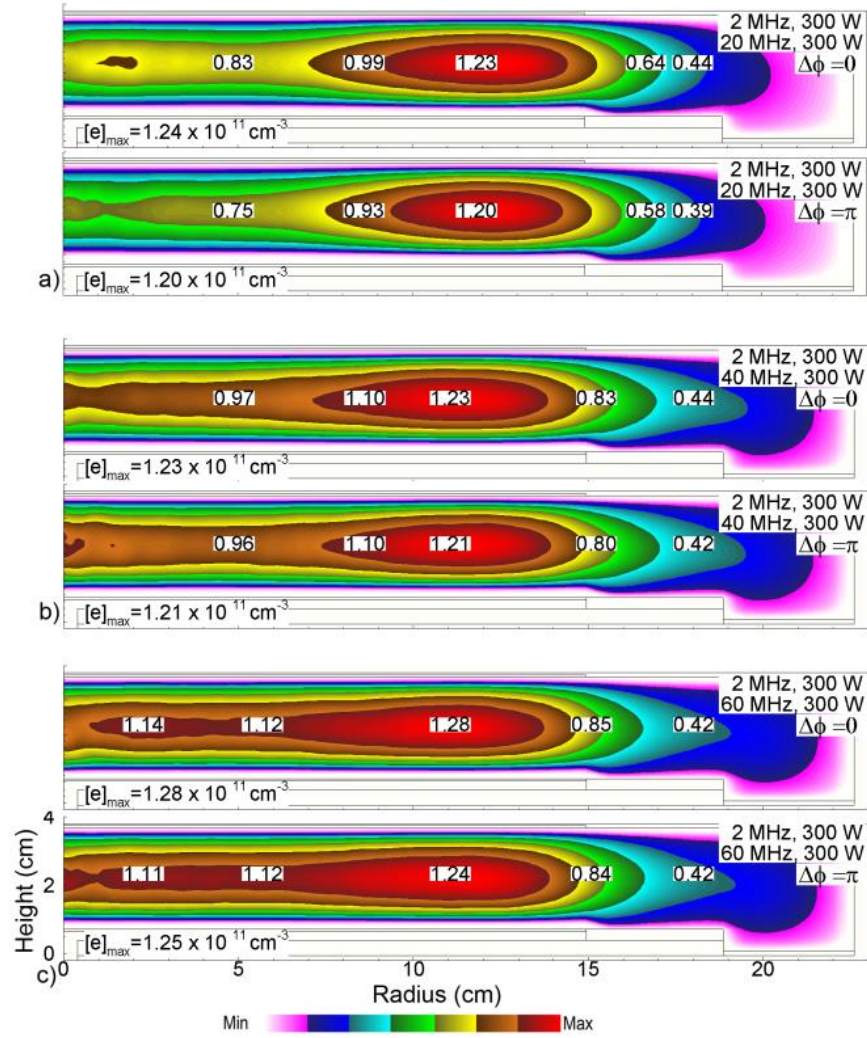
Fig. 5.16. Time averaged electron densities for phase difference between the *LF* and *HF* of *Δφ* = 0 or π, with *LF* = 2 MHz, 300 W, and 300 W *HF* [Ar, 30 mTorr, 1000 sccm]. *HF* = a) 20 MHz, b) 40 MHz and c) 60 MHz. The phase difference is with respect to *HF*.

151
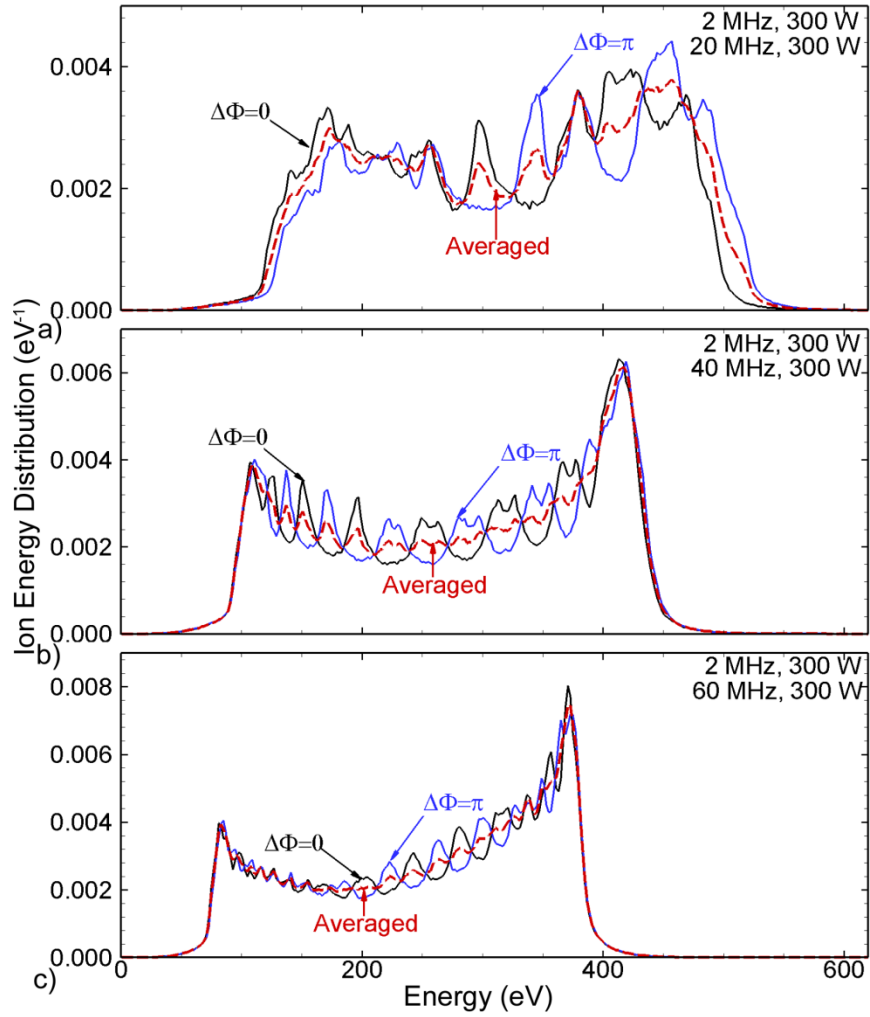
Fig. 5.17. Ar^{+} IEDs for *LF* = 2MHz, 300 W for different 300 W *HF* frequencies a) 20 MHz, b) 40 MHz and c) 60 MHz. Results are shown for *Δϕ* = 0 and π; and alternating between *Δϕ* = 0 and π. The time averaged IEDs of these two phase settings smooth out the *HF* modulations.

152
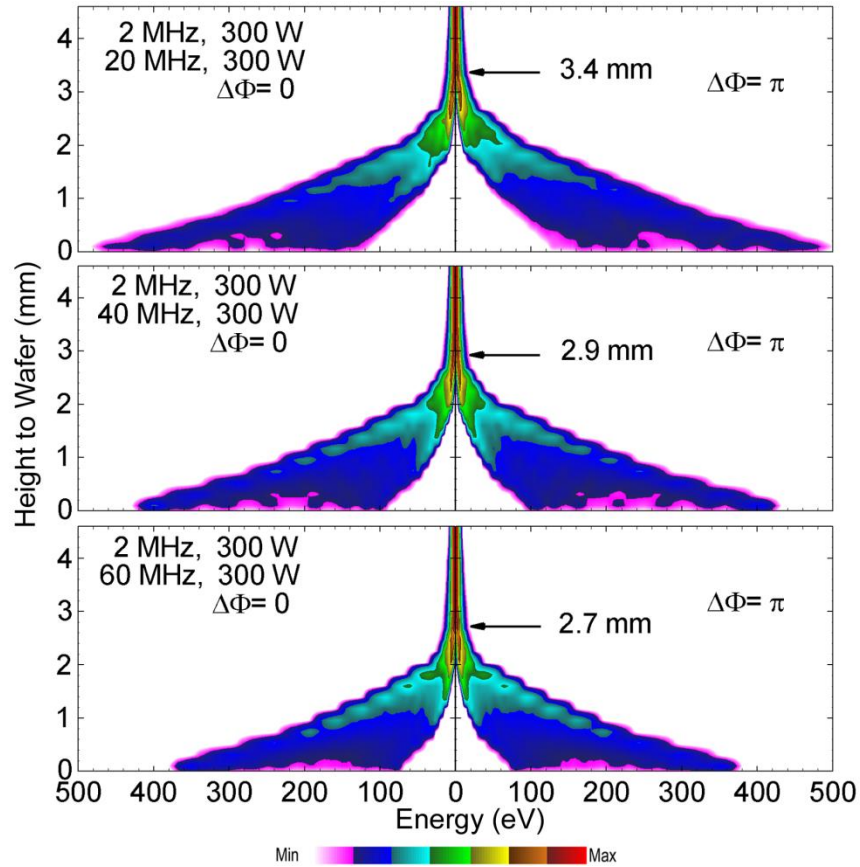
Fig. 5.18. IEDs for Ar$^+$ as a function of height above the wafer for *HF* = (top) 20, (middle) 40 and (bottom) 60 MHz for otherwise the base case conditions (Ar, 30 mTorr, *LF* = 2 MHz, 300 W, *HF* power = 300 W). The phase difference is $\Delta\phi$ = (left) 0 and (right) π. With an increase in *HF*, the electron heating becomes significant and the plasma density increases to produce reduced sheath thickness. Varying phases in lower *HF* frequency will modulate sheath dynamics and result in asymmetric time averaged sheath thickness. The sheath is asymmetric with respect to $\Delta\phi$ for *HF* = 20 MHz.
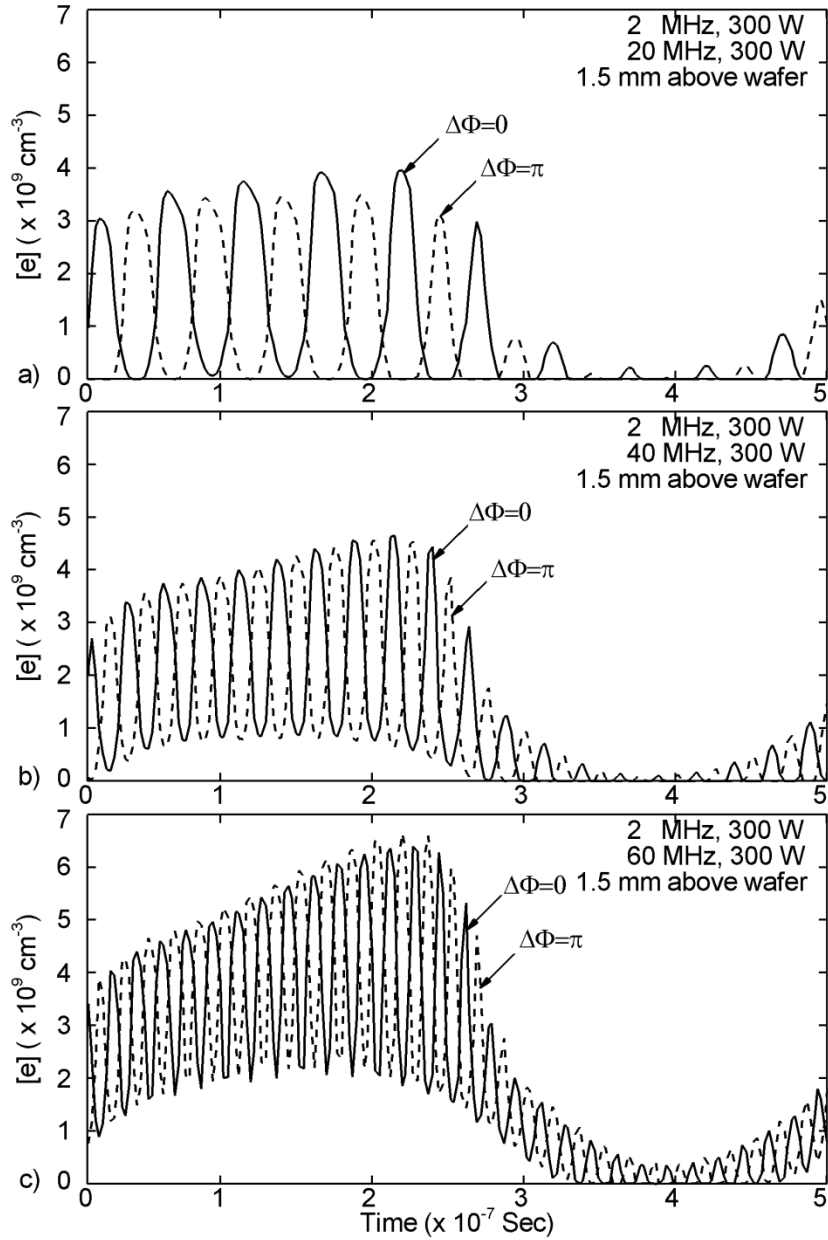
Fig. 5.19. Electron densities at 0.85 mm above the center of the wafer during one *LF* period for *LF* = 2 MHz, 300 W, and *HF* = 20, 40 and 60 MHz, 300 W. With constant power, the increase of the *HF* produces a higher electron density. Assuming a sheath thickness scaling of [e]$^{-0.5}$, the sheath thickness variation within the *LF* period can be estimated. With lower *HF*, the electron density is relatively low and sheath thickness changes more significantly during one *LF* cycle.
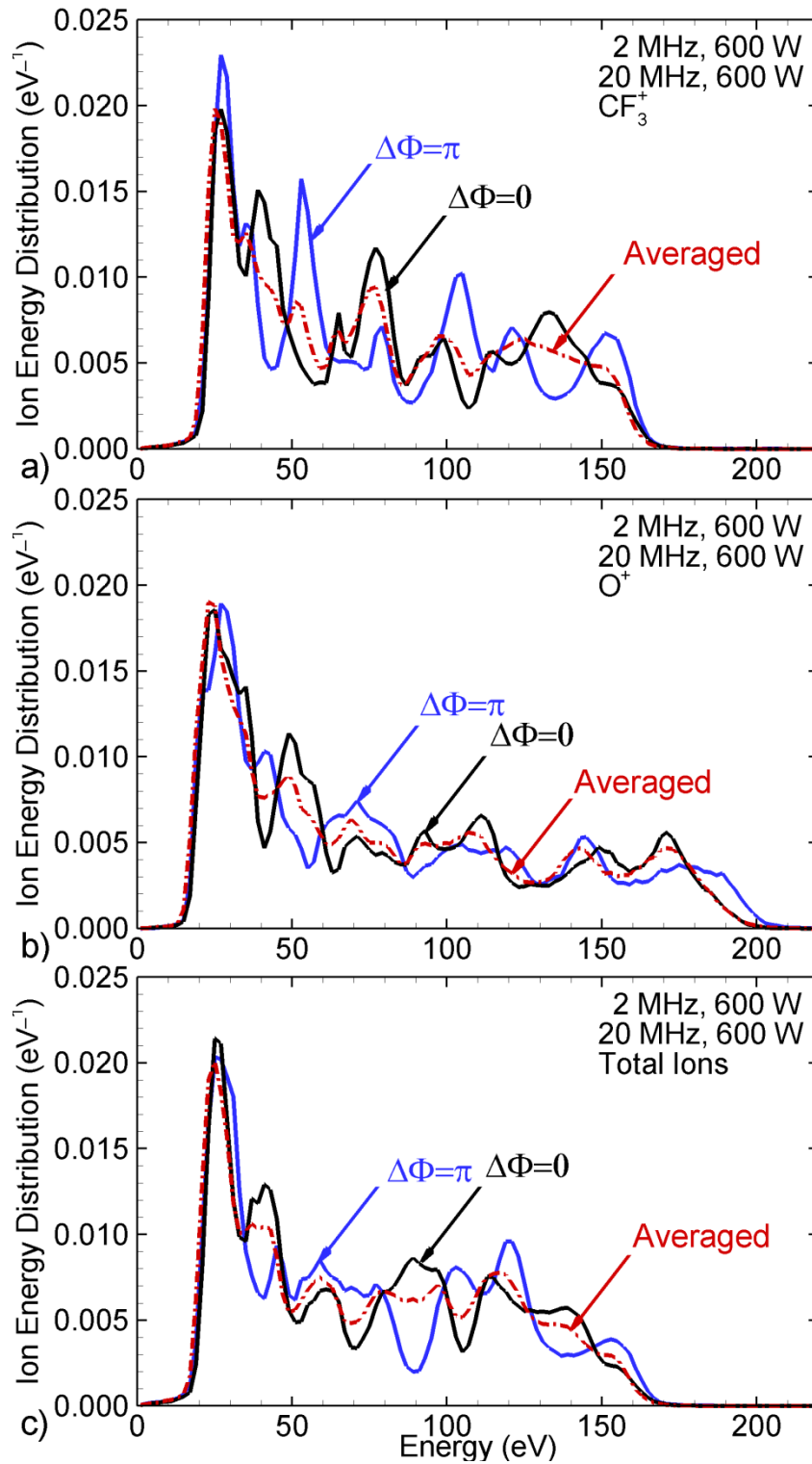
Fig. 5.20. Time averaged IEDs onto the wafer for Ar/CF_4/O_2 = 75/20/5 at 30 mTorr with LF = 2 MHz, 600 W, and HF = 20 MHz, 600 W. Results are shown for $\Delta\phi$ = 0 and π; and alternating between $\Delta\phi$ = 0 and π. a) CF_3^+ (heaviest ion, b) O^+ (lightest ion) and c) total ion.

155
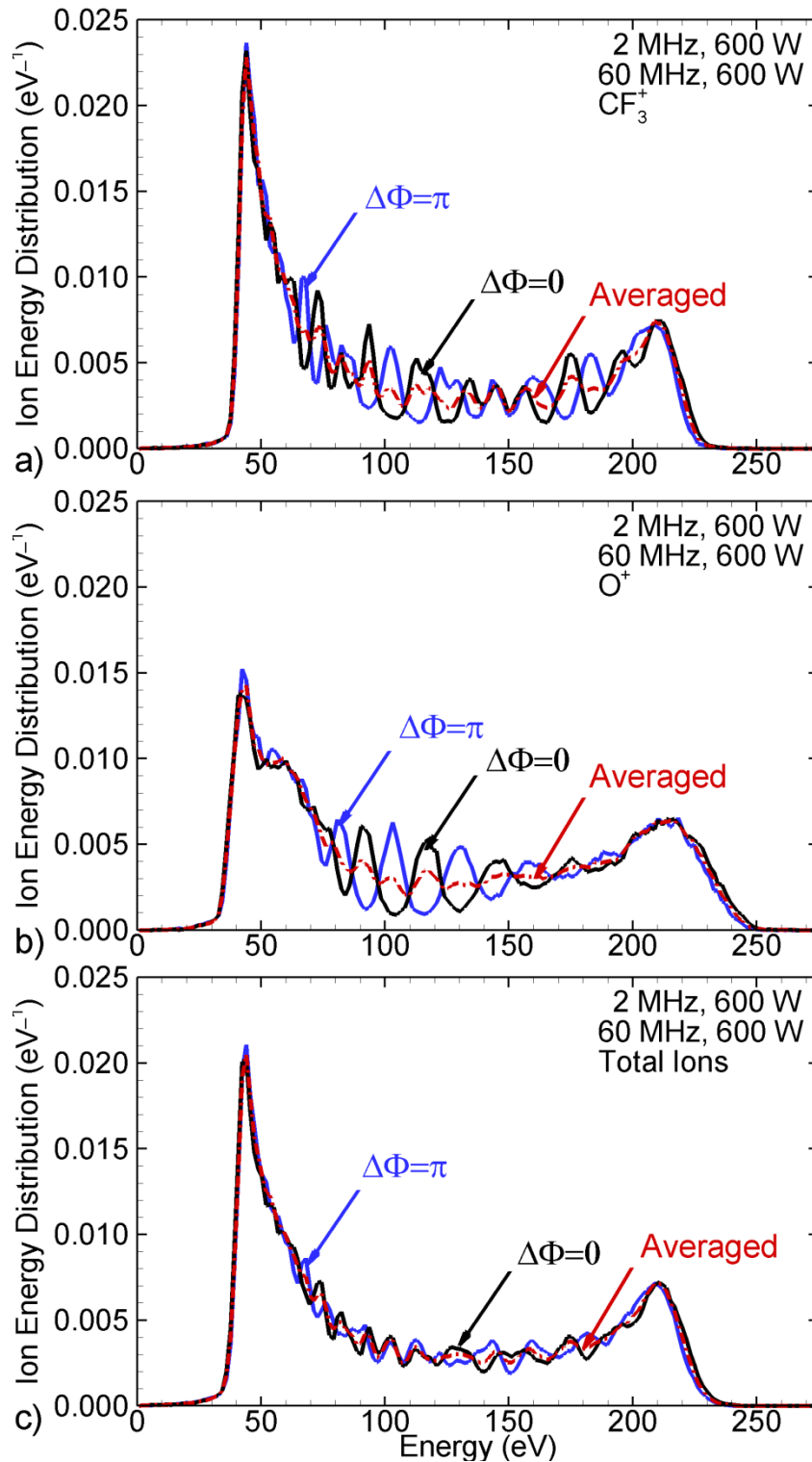
Fig. 5.21. Time averaged IEDs onto the wafer for $Ar/CF_4/O_2 = 75/20/5$ at 30 mTorr with $LF = 2$ MHz, 600 W, and $HF = 60$ MHz, 600 W. Results are shown for $\Delta\phi = 0$ and π; and alternating between $\Delta\phi = 0$ and π. a) CF_3^+ (heaviest ion, b) O^+ (lightest ion) and c) total ion.

5.7 References

1. T. Kitajima, Y. Takeo, and T. Makabe, J. Vac. Sci. Technol. A **17**, 2510 (1999).
2. V. Georgieva and A. Bogaerts, J. Appl. Phys. **98**, 023308 (2005).
3. T. Kitajima, Y. Takeo, Z. Lj. Petrović and T. Makabe, Appl. Phys. Lett. **77**, 489 (2000).
4. J. Schulze, E. Schüngel, U. Czarnetzki, and Z. Donkó , J. Appl. Phys. **106**, 063307 (2009).
5. K. Maeshige, G. Washio, T. Yagisawa and T. Makabe, J. Appl. Phys. **91**, 9494 (2002).
6. A. V. Vasenkov, X. Li, G. S. Oehrlein and M. J. Kushner, J. Vac. Sci. Technol. A **22,** 511 (2004).
7. A. Vasenkov and M. J. Kushner, J. Appl. Phys. **95**, 834 (2004).
8. F. F. Chen, Electric Probes, in "*Plasma diagnostics Technique"*, ed. by R. A. Huddlestone and S. L. Leonard, eds. (Academic Press, New York, 1965),Chap. 4, pp.113-200.
9. R. R. Upadhyay, I. Sawada, P. L. G. Ventzek and L. L. Raja, J. Phys. D: Appl. Phys. **46**, 472001 (2013).
10. C. Böhm and J. Perrin, Rev. Sci. Instrum. **64**, 31 (1993).
11. E. Kawamura, V. Vahedi, M. A. Lieberman and C. K. Birdsall, Plasma Sources Sci. Technol. **8**, R45 (1999).
12. D. Economou, J. Vac. Sci. Technol. A **31**, 050823 (2013).
13. J. Liu, Y-X. Liu, Z-H. Bi, F. Gao and Y-N Wang, J. Appl. Phys. **115**, 013301 (2014).
14. J. P. Booth, G. Curley, D. Marić and P. Chabert, Plasma Sources Sci. Technol. **19**, 015005 (2010).
15. A. J. van Roosmalen, W. G. M. van den Hoek and H. Kalter, J. Appl. Phys. **58**, 653 (1985).
16. A. Hallil, O. Zabeida, M. R. Wertheimer and L. Martinu, J. Vac. Sci. Technol. A.**18**, 882 (2000).
17. X. Li, X. Hua, L. Ling and G. Oehrlein, J. Vac. Sci. Technol. A. **20**, 2052 (2002).
18. D. Coumou, D. H. Clark, T. Kummerer, D. Sullivan and S. Shannon, IEEE Trans. Plasma Sci. **42**, 1880 (2014).

Chapter 6 CONTROL OF ION ENERGY DISTRIBUTION USING PHASE SHIFTING IN MULTI-FREQUENCY CAPACITIVELY COUPLED PLASMAS

6.1   Introduction

With the goal of having finer control of ion energy distributions (IEDs), as characterized by the self-generated dc bias in capacitively coupled plasmas (CCPs), the electrical asymmetry effect (EAE) was developed by Heil *et al*. – a dual-frequency (DF)-CCP in which the frequencies consist of the fundamental frequency and its second harmonic.[1]. With the rf waveform composed with the fundamental and its second harmonic, the dc self-bias was found a linear function of the phase angle between the two. Using this technique, the dc self-bias in geometrically symmetric, DF- CCPs can be controlled through control of the phase difference between the first and second harmonics. For example, the dc bias can be varied from positive-to-negative if the dual-frequencies are 13.56 and 27.12 MHz.[1-4] Heil *et al*. demonstrated that the EAE has the potential to separately control the magnitude of the ion flux and IEDs incident on to electrodes.[1]   Several other studies have also investigated, both numerically and experimentally, the fundamentals and applications of the EAE.[1-10]

The EAE was initially investigated with a fundamental frequency of 13.56 MHz in geometrically symmetric CCPs to produce an asymmetric plasma response. Korolov *et al*.

investigated the EAE by varying the fundamental frequency from 0.5 MHz to 60 MHz for CCPs sustained in argon at 375 mTorr with an electrode gap of 2.5 cm.[5] Their simulations showed that a reduction in the ability to control the range of mean ion energies at lower fundamental frequencies resulted from the contributions of the secondary electron emission. This reduced response at low frequencies was experimentally observed by Lafleur and Booth.[6] The EAE was also investigated in a geometrically asymmetric chamber by Schüngel *et al*.[7] In experiments performed in Ar plasmas at 30 mTorr, they found that the EAE can still control the mean ion energies through adjusting the dc self-bias in asymmetric systems, though this control was limited by the natural negative dc-bias that is produced on the smaller electrode.

The EAE was also found to have utility improving the uniformity of sputtering and thin film deposition. Bienholtz *et al*. investigated the EAE in a large area (500 mm diameter) multi-frequency CCP with an Ar/N_2 mixture at 22.5 mTorr, a chamber commonly used for sputter deposition processes.[8] Their system was operated with phase control between 13.56 MHz and 27.12 MHz. With Fourier analysis of the voltage waveforms for various phase angles, they found that not only the second harmonic, but also the amplitude and phase shift of higher harmonics had an influence on plasma density and dc self-bias. Although the electron density remained constant for a wide range of phase shifts, the plasma density increased by as much as 50% at specific phase shifts. Bienholtz *et al*. also reported on a challenge in controlling IEDs with the EAE due to the lack of control of currents produced at the higher harmonics. Hrunsk *et al*. reported favorable results for improved uniformity when applying the EAE to silicon thin film deposition. in large area (1100 × 1400 mm) reactors.[9,10] The uniformity with 13.56 MHz + 27.12 MHz excitation was better than that produced by a single frequency 27.12 MHz

discharge, an effect they attributed to a reduction in the standing wave effect found in high frequency, large area systems.

When controlling the phase between multiple frequencies, different varieties of non-sinusoidal waveforms can be generated for producing different plasma properties. Bruneau *et al*. reported producing an EAE-like effect when using up to 5 harmonics.[11,12] Their 1-d particle-in-cell simulation predicted 50% higher ion flux on one electrode in geometrically symmetric CCPs when the sum of the harmonic frequencies had a specified phase shift. This effect was attributed to differing rising and falling slopes in time of the voltage waveform. At low pressure, longer mean free paths produced more uniform ionization and so more uniform sheath properties. When increasing the pressure in Ar plasmas from 20 to 800 mTorr, ionization became more localized at both sheath edges and the asymmetry in ion flux became more pronounced. The asymmetry of the discharge decreased at lower fundamental frequencies as sheath heating no longer dominated the overall electron heating.

The prior investigations primarily focused on the influence of phase shifting on plasma properties with customized voltage waveforms over a large frequency range. [13-16] We follow those studies with an investigation of the consequences of the EAE on IEDs within the multiple rf frequencies of 15 + 30 MHz and 15 + 30 + 60 MHz.. With plasma reactors in industry moving from DF-CCPs to triple frequency CCPs (TF-CCPs), the extension of the EAE to those systems would be beneficial. We report on experimentally measured plasma properties and IEDs, and results from computational investigations in both DF- and TF-CCPs with the phase shift with respect to the harmonics ranging from 0° to 360°. We found that the dc self-bias varied with the modulation of the rf waveform as the EAE theory predicts in both DF- and TF-CCPs. The phase shifting of the harmonic frequencies also modulated the plasma densities and brought about a

160

change in the sheath thickness. With the sheath thickness varying, the shape of the IEDs changed due to there being different ion transit times of ions of different masses through the sheath. The consequences of these trends on etch profiles is discussed.

The computational methods and experimental setup of the collaborated group are described in Sec. 6.2. The results and discussion are presented in Sec. 6.3 (plasma properties in DF-CCPs) and Sec. 6.4 (plasma properties in TF-CCPs). The concluding remarks are discussed in Sec. 6.5.

6.2   Description of Models and Experiment

For this study, the HPEM was used as the reactor scale simulator. The Electron Monte Carlo Simulation (eMCS), the Fluid Kinetics Poisson Module (FKPM) and the Plasma Chemistry Monte Carlo Module (PCMCM) were used to investigate EAE phenomena and ion energy distributions onto the substrate. Time steps were chosen to be less than 1/300 of the highest applied frequency (1.11×10^{-10} s for 30 MHz in DF-CCPs and 5.5×10^{-11} s for 60 MHz in TF-CCPs).

When investigating the consequences of phase shift between the fundamental and second harmonic frequencies, the voltage waveform on the bottom electrode is expressed as

$$V_B(t) = V_{LF} \sin(\omega_{LF} t + \varphi_{LF}) + V_{HF} \sin(\omega_{HF} t + \varphi_{HF} + \Delta\phi_{HF}), \tag{6.1}$$

where *LF* refers to the low frequency and *HF* refers to the high frequency. φ_{LF} and φ_{HF} refer to the unknown phase offset from the signal generator to the electrode through the transmission line in the experiment for each frequency. Having no other information, these phase offsets are assumed to be the same. $\Delta\phi_{HF}$ refers to the shift in the phase of the *HF* with respect to the *LF*. Unless noted otherwise, in the computations *LF* = 15 MHz and *HF* = 30 MHz.

In the TF-CCP, a sinusoidal 60 MHz waveform was applied on the top electrode, which is expressed as

$$V_T(t) = V_{60}\sin(\omega_{60}t + \varphi_{60} + \Delta\phi_{60}),\qquad\qquad(6.2)$$

where φ_{60} refers to the phase offset from the 60 MHz signal generator and $\Delta\phi_{60}$ refers to the shift in the phase of the 60 MHz with respect to the 15 MHz voltage. In the experiment, installed phase locks were only used on the fundamental and second harmonic frequencies. Therefore the phase offset and phase shift of 60 MHz are unknown. The influence of the 60 MHz phase shift was investigated with the model and will be discussed in Sec. 6.4.

The majority of the simulations were performed in pure argon with species consisting of Ar, Ar($1s_2$), Ar($1s_3$), Ar($1s_4$), Ar($1s_5$), Ar(4p,5d), Ar$^+$ and e. The reaction mechanism for Ar is essentially the same as described in Ref. [17] with the exception that the Ar($3p^54s$) multiplet is resolved into its four individual states. In addition to the pure argon cases, an Ar/CF$_4$/O$_2$ gas mixture was also simulated to study the influence of the EAE on plasma etching process. The gas phase and surface reaction mechanisms are discussed in Refs. [18,19]. The species in the Ar/CF$_4$/O$_2$ mechanism were Ar, Ar($1s_5$, $1s_3$) metastable, Ar($1s_2$, $1s_4$) radiative, Ar(4p,5d), Ar$^+$, CF$_4$, CF$_3$, CF$_2$, CF, C, F, F$_2$, C$_2$F$_4$, C$_2$F$_6$, C$_2$F$_6$, SiF$_4$, SiF$_3$, SiF$_2$, CF$_3^+$, CF$_2^+$, CF$^+$, C$^+$, F$^+$,F$_2^+$, CF$_3^-$, F$^-$, O$_2$, O$_2$($^1\Delta$), O$_2^+$, O, O(^{1}D), O$^+$, O$^-$, COF, COF$_2$, CO$_2$, FO and e.

Energy and angular distributions incident onto the substrate for Ar$^+$, CF$_3^+$,CF$_2^+$,CF$^+$,F$^+$ and F$_2^+$ and major neutral particles produced by the PCMCM were transferred to the Monte Carlo Feature Profile Model (MCFPM) that is described in detail in Chapter 3. MCFPM 2-d was applied in this study to predict profile evolution for etching SiO$_2$ over Si. The reaction mechanism for etching of Si and SiO$_2$ in fluorocarbon plasma is described in detail in Ref. [16].

In order to eliminate the effect of mask erosion on etch profiles, a hardmask is assumed that does not change its shape during processing.

Computed results for IEDs are compared with rf phase locked harmonic experimental results measured by Prof. Steven Shannon's Fourth State Applications Research Group at North Carolina State University. Measurements of ion energy distributions incident onto the substrate and dc biases were made in a parallel plate, CCP. The apparatus could be powered by 3-separate voltage sources, typically a fundamental and its second harmonic, and a *HF*. Control algorithms were developed to enable phase locking of the fundamental and the second harmonic. The DF-CCP has been previously reported and described in detail in Ref. [20]. The TF experimental setup is shown in Fig. 6.1 and comprises the following subsystems: 1) plasma source with vacuum regulation and gas flow control; 2) very high frequency power supply and impedance matching network; 3) phase-locked, harmonic drive rf power supply and associated dual frequency matching network; and 4) metrology comprising an energy analyzer and rf sensors. An rf-compensated Langmuir probe, positioned at the center of the discharge, was used to measure electron density, electron temperature, and plasma potential. IEDs were measured with a Retarding Field Energy Analyzer (RFEA) from Impedans, Ltd, which was positioned on the bias electrode.

In order to control the phase difference between rf frequencies, the frequency and phase locking technology is installed in the experiment based on a digital phase-lock loop 1-17 (dPLL). The harmonic rf power delivery system is composed of two frequency agile rf supplies. The 13.56 MHz rf generator is designated as the master and the 27.12 MHz rf power supply is the slave. This rf excitation signal is sampled by the slave generator, converting it to a digital signal and processing it along with a digital representation of the local rf it generates. To create a

harmonic replica of the master frequency, the slave controller applies a digital phase-lock loop to synchronize and scale the local frequency to the excitation signal. In the slave controller, digital down-conversion is separately performed for the sampled excitation signal and the local frequency generated by the slave. This digital process down-samples the digital signals from the A/D conversion rate to an integer divisible sample rate. While lowering the data rate, a variable narrowband filter attenuates the spurious frequencies to retain a digital baseband signal. This digital process is followed for both the excitation signal and the local rf signal. The digital baseband signals are represented in a mathematically complex form and applied to the digital phase-lock loop. To determine the frequencies of each signal, the time derivative of the phasor of each digital baseband signal was computed. This provides a measure of the excitation signal frequency, $f_e = \frac{\partial \theta_e(t)}{2\pi \partial t}$, and the local slave frequency, $f_{rf} = \frac{\partial \theta_{rf}(t)}{2\pi \partial t}$. To adjust the local frequency of the slave output power to the excitation signal, a frequency error, $f_\Delta = f_e - f_{rf}$, was computed and applied to a proportional, integral, and derivative controller [22] that iteratively produces updates to a digital synthesizer generating the frequency of the slave power supply. As the frequency converges to the harmonic of the master frequency, the frequency error $f_\Delta \rightarrow 0$.

Once the slave frequency is locked, the dPLL transitions to phase control. The output phase of the rf is compared to the desired phase and maintains this set point through transient conditions and systematic effects. The dPLL generates the harmonic frequency and accurately maintains the target phase output relationship with the coupled excitation signal from the slave. The benefit is substantial enough to gain a higher degree of fidelity in generating the desired IED.

6.3   Plasma properties and IEDs in a dual- frequency CCP reactor

Schematics of the two-dimensional, cylindrically symmetric DF- and TF- CCPs used in the simulation are shown in Fig. 6.2. In the DF-CCP, the gap between the electrodes was 2.54

cm to match the experiments. Gas was injected through the top nozzle at 50 sccm near the chamber wall. The top chamber and the metal wall were grounded, and thus the CCP reactor is geometry highly asymmetric. Both rf biases were applied to the bottom electrode through a blocking capacitor (1 µF). The 15 cm in diameter substrate was surrounded by a dielectric focus ring ($\varepsilon/\varepsilon_0 = 2.53$, $\sigma = 10^{-9}$ $\Omega^{-1}cm^{-1}$). The annular pump port was at the bottom of the computational domain, coaxially surrounding the substrate. During execution of the code, the flow rate through the pump port, also nominally 50 sccm, was adjusted to keep the pressure inside the plasma chamber constant.

Operating conditions for the TF-CCP were the nearly same as for the DF- CCP, except that the gap was 1.90 cm and a 60 MHz rf source was applied to the top electrode. All results from the experiment were obtained with 13.56 MHz + 27.12 MHz power applied to the bottom electrode and an optional 60 MHz on the top electrode for TF-CCP. For reasons having to do with computational alignment of frequencies and minimizing numerical error, the lower two rf frequencies in the simulation were rounded to 15 MHz and 30 MHz. The phase shift between the harmonics was at 30° increments for both the simulation and experiments.

The experimental chamber is highly asymmetric- that is, the area ratio between the grounded surfaces and power electrodes greatly exceeds unity, and this naturally produces a dc bias. The entire volume of the reactor exceeds what can be realistically included in the numerical mesh of our model. This result the area of the grounded surfaces in the model is smaller than the actual experimental setup. Therefore, for a given applied voltage, the same amount of dc self-bias cannot be produced in the simulation. The primary objective of this study is the behavior of the IEDs which are most sensitive to the dc bias. Therefore, the voltage in the model is adjusted

to match that base case dc self-bias in the experiment. This difference in voltage amplitude has an effect on predicted plasma densities, as discussed below.

To validate the HPEM and, in particular, the PCMCM that produces IEDs, a set of single frequency simulations were performed with pressures ranging from 10 to 40 mTorr of Ar with a flow rate of 50 sccm. The power was 100 W at 30 MHz. The dc self-bias was kept at a constant value of -87V in the simulation. The simulated IEDs, shown in Fig. 6.3 a, agree favorably with previously published experimental results, shown in Fig. 6.3 b.[21] To better visually match the presentation of the experimental results, the simulated IEDs were normalized to 1.0 at their maximum values. For these single frequency IEDs, the bimodal distribution typically obtained at low frequencies has already started merging towards a single peak. For a dc bias of -87 V and the time averaged plasma potential of 35 V, the average ion energy should be near 122 V, which is about the location of the peak of the IED. With constant power at high pressure, ion–neutral collisions produce modulation in the IEDs at energies of < 70-80 eV.[23] With a decrease in pressure, the ion mean free path increases and exceeds the sheath thickness. The sheath on the powered substrate transitions from collisional to less-collisional and the low energy tail of IEDs is less modulated when the pressure is below 20 mTorr. Because the RFEA system requires a balance between minimizing collisional distortion and maximizing ion fluxes, all DF/TF phase-locked simulations and experiments were conducted between 10 and 20 mTorr.

The mismatch in the maximum energy between the simulation and experiment results from some inherent differences in the mode of operation in the experiment and the simulations. In the experiments, current is the independent variable and power the dependent variable. In the simulations, power is the independent variable and current is the dependent variable. (Changing the model of operation of the model to current being the independent variable was beyond the

scope of this study.) As such, it is sometimes difficult to exactly match the operating conditions of the experiment with the simulations.

To provide a perspective for our investigation of EAE characteristics, a base case simulation was performed for Ar at 20 mTorr and 50 sccm flow. The waveform for DF excitation was $V_B(t) = 100V \sin(\omega_{15}t + \varphi_{15}) + 100V \sin(\omega_{30}t + \varphi_{30} + \Delta\phi_{30})$, where the phase offset of the signal generator to the electrode, $\varphi_{15} = \varphi_{30} = 180^o$ and there is no phase shift $\Delta\phi_{30}$ between the 15 and 30 MHz signals. The electron density, n_e, electron temperature, T_e, ionization by bulk electrons, S_e, and ionization by secondary electrons, S_{sec}, with secondary emission coefficient $\gamma = 0.15$ for this base case are shown in Fig. 6.4. This estimation of the emission coefficient is based on Ref. [24]. With an equal voltage for each of the dual-frequencies, the plasma density was approximately 10^{11} cm^3 with an average bulk electron temperature of $T_e = 3.3$ eV. The bulk ionization source, maximum of 1×10^{16} cm^{3}s^{-1} is about two orders larger than the ionization by secondary electrons.

The electron density predicted by the model is larger than that measured using probes for similar conditions, which is 2×10^{10} cm^{-3}. The experimental voltage amplitude for each frequency is about 40 V for those measurements. When using 40 V amplitude in the model, the predicted electron density drops to 5×10^{10} cm^{-3}, which is within about a factor of 2 of the measurement. As mentioned about, the main object of this study is the IEDs which most sensitive to the value of the dc bias. Due to the differences in the area of the grounded surfaces is the reactor between the model and experiment (see prior discussion), we adjusted the voltage in the model for the base case to 100 V in the simulation in order to produce an initial dc self-bias similar to that of the experiment. This increase in voltage accounts for about a factor of two increase in plasma density above that of the experiment.

With $\Delta\phi_{30}$ varied from $0^{\,o}$ to $360^{\,o}$ with $\varphi_{15} = \varphi_{30} = 180^{o}$, the dc self-bias is shown in Fig. 6.5 a. Due to the reactor being highly asymmetric, a dc self-bias is naturally generated to balance currents on both electrodes even with no phase shift. The consequence of the EAE adds to our substrate from the zero-phase dc bias, which in this case is negative. Therefore, the dc-self bias is always negative in the simulations and measurements. As the EAE theory predicts, the dc self-bias linearly depends on the phase angle of the 15 MHz. However, we observed that the dc self-bias shows a sinusoidal-like variation with the phase angle of 30 MHz varying from 0° to 360°. We also performed simulations with a phase offset $\varphi_{15} = \varphi_{30} = 0^{o}$ and 90° (i.e. waveforms that are sine and cosine functions, which different amplitudes), as shown in Fig. 6.5 b. Although dc self-biases show linear modulation at certain phases, most simulated dc-self biases show sinusoidal-like variations, which can be expressed as a sine function with its phase offset equal to the rf phase offset φ.

The amplitude of the variation in dc self-bias depends on the voltage amplitude of the 15 MHz and 30 MHz biases. When both voltage amplitudes are increased to 150 V, the rf currents on the electrode are increased for all phases shifts. Thus, more negative dc self-biases are produced for all phase shifts for bias waveforms $V_B(t) = 150V\sin(\omega_{15}t) + 150V\sin(\omega_{30}t + \Delta\phi_{30})$. Ultimately the With the application of cosine function (i.e. $V_B(t) = 100V\sin(\omega_{15}t + 90^{o}) + 100V\sin(\omega_{30}t + 90^{o} + \Delta\phi_{30})$, the simulated dc self-bias modulation is closed to the measured and simulated results of Schulze *et al.* [25]. Ultimately, the dc bias of at zero-phase (or a reference phase) is determined by the area ratios of the powered and grounded surfaces. The change in dc bias as a function of $\Delta\phi$ from the reference value then depends on the shape of the voltage wave form (e.g., sine vs. cosine) and which phase is being varied (fundamental or second harmonic). The simulate results show that the dc self-bias varies linearly

for most phase angles and shows sinusoidal-like shapes at other phase angles. This result suggests the linear dependence between dc self-bias and phase does not strictly hold as the waveform and geometrical conditions (e.g., symmetric vs asymmetric) change.

For example, in many prior studies of EAE, the basic voltage waveforms have zero phase offset at the fundamental and second harmonic, and the phase variation is applied to the fundamental. With all other conditions kept the same, the we used this form of the bias waveform in the model – $V_B(t) = 100V\cos(\omega_{15}t + \Delta\phi_{15}) + 100V\cos(\omega_{30}t)$. The predicted variation in dc self-biases, shown in Fig. 5c, agree well with the theoretical prediction. When $\Delta\phi_{15}$ is shifted from 0° to 90°, the dc self-bias becomes 75 V-less negative, which shows a similar trend to the 1-D simulations of an asymmetric CCP.[26]

This part of study suggests that the value of dc-self bias is determined by two kinds of asymmetries: electrical and geometrical. By adjusting phases, the electrical asymmetry effect modulates dc self-bias. Many previous studies have investigated EAE in geometrically symmetric reactors which do not have an initial dc self-bias resulting from the geometrical asymmetry. With the initial dc self-bias equal to zero, the EAE can tailor the dc self-bias to either positive or negative values. On the other hand, the initial value of dc self-bias is determined by the amplitude of the rf current and the geometrical asymmetry. In this case, the EAD modulates the dc bias but does not necessarily provide a full dynamic range from negative to positive.

The unknown phase offset in the experiment can be estimated by the variation in the dc bias starting phase at $\Delta\phi_{30} = 0^o$ if the phase offsets of both frequencies are the same. Since current is controlled in the experiment, the amplitudes of both frequencies had about a 15% variation during the parameterization of $\Delta\phi_{30}$. This variation may explain why at certain values

of $\Delta\phi_{30}$ there is less good agreement between the model and experiment. Other differences include the geometry of the reactor which in part determines the dc bias ($|V_{dc}| \propto \frac{A_{ground}}{A_{power}}$). Due to computational limitations the surface area of the grounded chamber walls is smaller in the model than in the experiment.

For otherwise the same conditions, the computed plasma density and uniformity were affected by phase shifting, as shown in Fig. 6.6. The electron densities were recorded as a function of radius to the edge of the substrate in the middle of the electrode gap. The plasma densities remained constant for the majority of the values of $\Delta\phi_{30}$ between 0 and 180°, with a maximum value of 1.1×10^{11} cm^{-3} at a radius of about 5 cm. At larger phase differences, the plasma density increased by 40% to 1.35×10^{11} cm^{-3} with the maximum shifting to the center of the reactor. A similar phenomenon was measured and reported by Bienholz et al.[8]. Keeping the voltage constant while providing different rf voltage waveforms with different $\Delta\phi_{30}$ produces different power deposition and different spatial distributions of ionization that provide larger instantaneous ionization rates. The cycle averaged ionization rates for bulk electrons for $\Delta\phi_{30} =$ 90° and 270° are shown in Fig. 6.6. (Recall that the plasma density is mainly produced by bulk ionization.) The ionization rates for $\Delta\phi_{30} = 90^o$ have a maximum near 5 cm that corresponds to the maximum in electron density. In contrast, the time averaged bulk ionization source for $\Delta\phi_{30}$ $=270$ ^{o} has a maximum near the axis, which corresponds to the peak in electron density for that phase offset. These results align with changes in the spatial dependence of the electron energy distribution with phase offset.

The sheath dynamics for different $\Delta\phi_{30}$ were also investigated. The rf waveforms for $\Delta\phi_{30}$ = 90° and 270° are shown in Fig. 6.7 a. The electron densities in the near sheath region (0 - 4

mm above the substrate) at the bullet-marked times are shown in Fig. 6.7 b. The $\Delta\phi_{30} = 90$ ^{o} voltage waveform spends the majority of the cycle below zero. This produces a longer cathodic portion of the cycle and more sheath expansion from $t = 0$ to $0.63T_{15}$ (one 15 MHz period). At t $= 0.63T_{15}$, electrons start to re-enter the sheath and the sheath totally collapses at $t = 0.75T_{15}$, when the most positive bias is applied. After that time, the sheath starts to expand again and the sheath boundary moves back towards the bulk plasma. Unlike the $\Delta\phi_{30} = 90^o$ voltage waveform, the cathodic portion of the cycle is shorter for $\Delta\phi_{30} = 270$ ^{o}. As a result, the sheath is collapsed for the majority of the 15 MHz period. The sheath for $\Delta\phi_{30} = 90$ ^{o} is generally thicker than for $\Delta\phi_{30} = 270$ ^{o} due to a lower plasma density and much longer cathodic phase. Since the ion transition time through the sheath depends on the sheath thickness and when ions enter the sheath, these sheath dynamics produce significant variations of the IEDs. With the sheath oscillation at different moment, the electron flux is reflected back to bulk plasma at different kinetics. Thus, the bulk ionization in the reactor gets affected with different phases.

The IEDs corresponding to variation in $\Delta\phi_{30}$ are shown in Fig. 6.8. Three phenomena occur when $\Delta\phi_{30}$ is vary that can affect the IEDs. First, the variation in dc self-bias produces a change in the modulation of the sheath potential and therefore the mean ion energy. For example, the high energy tail of the IEDs shifts by about 70 eV which tracks the change in the dc self-bias with change in $\Delta\phi_{30}$. The increase in dc self-bias for $\Delta\phi_{30} = 90$ ^{o} to -150V correlates with the extension of the IED to 220 eV. Second, the IEDs are 10 to 20 eV wider in energy at phases $\Delta\phi_{30} = 0$ ^{o} $- 120$ ^{o}. The energy width $\Delta E \propto \sqrt{n_e \overline{V_s}}$. The plasma densities at those phases are lower and so the sheath is thicker, this can contribute to a narrower energy width. However, the average sheath voltage is higher at those phases and is the main determining parameter for our operating conditions. Thus, the energy width slightly modulates at certain phases. Third, the

171

shape of IEDs is not consistent across phase changes. The energy at which the IED is maximum shifts with $\Delta\phi_{30}$. This shift is mainly due to the high frequency modulation of the sheath potential by the 30 MHz voltage.

Selected results from the experiment for IEDs are compared with results from the simulation in Fig. 6.9 a,b for when the dc self-bias is at its minimum and maximum. There is good agreement in trends and shape. Differences between experiment and the model may result from the assumption of there being an equal phase offset for both frequencies in the simulation. When different phases have the same dc self-bias, the mean ion energies are the same, however the energy of the peak in the IED is different due to the different ion sheath dynamics caused by the 30 MHz. Referring to Fig. 6.5 a, the simulated dc self-biases for $\Delta\phi_{30} = 150^o$ and 30° have similar c bias as the 200° and 20° cases in the experiment. The corresponding IEDs are shown in Fig. 6.9 c,d and have similar mean energies with different energy peak positions. These results suggest that the EAE may be used not only to control the mean ion energy region, but also to help customize the shape of the IED for different process requirements. The optimization of an etch process can be roughly divided into the rate of processing and selectivity. Selectivity depends on parameters such as the thickness of an overlying passivating polymer but selectivity more critically depends on the different in threshold energies for ion activation between different materials.[27] So even with the same average ion energy, subtle changes in the IEDs (e.g., absence of a low-energy portion or enhance of a high-energy portion) can make significant changes in the selectivity between materials.

The potential influence of EAE on plasma etching was computationally investigated using an Ar/CF$_4$/O$_2$ = 75/20/5 gas mixture at 20 mTorr. A high aspect trench was etched in SiO$_2$ over Si with a hardmask. The phase difference $\Delta\phi_{30}$ was varied from 0° to 270°. The resulting

172

IEDs for CF_3^+, Ar^+ and O^+ are shown in Fig. 6.10. The control of IEDs by use of the EAE is complicated by the different masses of the ions. The response of ions to the change in phase and harmonic content of the sheath is a function of their mass. Although the general trends of the IEDs for CF_3^+, Ar^+ and O^+ scale similarly with changes in $\Delta\phi_{30}$, the details of the individual IEDs are sensitive functions of the ion mass. The ability to control the width and location of the maximum in the IEDs scales inversely with ion mass. Small changes in the value of $\Delta\phi_{30}$ can translate to significant changes in the etch profile as shown in Fig. 6.10 d. The profiles are plotted at the time that the profile for $\Delta\phi_{30} = 270^o$ reached 20% over-etch (etching continued for 20% more time than was required to reach the bottom of the feature). The etch rate of SiO_2 generally scales as $(\varepsilon_{ion}^{1/2} - \varepsilon_{th}^{1/2})$, where ε_{th} is a threshold energy that depends on the details of the chemical system.[28]. With this scaling, the $\Delta\phi_{30} = 90^o$ case has the lowest etch rate (lowest) and the $\Delta\phi_{30} = 270^o$ case has the highest etch rate (largest dc self-bias). With similar values of the mean ion energy (dc self-bias), the $\Delta\phi_{30} = 0^o$ and 180° cases have different etch profiles, a consequence of the shape of the IED. For example, the larger low energy peak of the IED for $\Delta\phi_{30} = 0^o$ case stimulates additional polymer deposition on the sidewall of the feature or sputters less polymer from the sidewall, which produces more tapering of the profile. The systematic trends are difficult to discern, since the IEDs do not monotonically vary with phase difference $\Delta\phi_{30}$.

6.4   Plasma properties and IEDS in a triple- frequency CCP reactor

Since higher ion fluxes usually translate to higher etch rates, high plasma density reactors are typically employed for industrial processes. In order to attain high plasma densities in CCPs, a high frequency (>40 MHz) is commonly used as electron heating scales with ω^2. To investigate the EAE with quasi-independent control of the plasma density, the top electrode was

additionally powered at 60 MHz. The base case for the compuations is Ar, 20 mTorr with a

voltage waveform $V(t) = 100\sin(\omega_{15}t + 180^o) + 100\sin(\omega_{30}t + 180^o) + V_{60}\sin(\omega_{60}t + 270^o)$. The

voltage at 60 MHz was adjusted to deliver 150 W. The electron density and temperature,

ionization sources by bulk electrons and by secondary electrons are shown in Fig. 6.11. The

maximum electron density is 2.3×10^{11} cm^{-3} with an average $T_e = 3.4$ eV. With the addition of

the 60 MHz power, the plasma density of the TF-CCP is two times larger than that of the DF-

CCP. The majority of this increase comes from an increase in the bulk ionization source, a

consequence of more efficient electron heating at the higher frequency. The 60 MHz power is

approximately half the total. Since the 15 MHz and 30 MHz voltages are held constant, upon

applying the 60 MHz power which increases the ion current, the power at 15 MHz and 30 MHz

also increase.

While varying $\Delta\phi_{30}$ in the TF-CCP while keeping all other parameters constant, the

plasma uniformity at mid-gap was more sensitive to phase compared to the DF-CCF. These

trends are shown in Fig. 6.12 a. This sensitivity was most pronounced for $\Delta\phi_{30} = 0^o$ for the TF-

CCP (minimum in density) and $\Delta\phi_{30} = 270^o$ for the DF-CCP (maximum in density). When the

power at 60 MHz is increased from 50 to 600 W, the plasma density increases, though not

linearly. From 50 to 600 W (a factor of 12) the plasma density increased by a factor of 3, as

shown in Fig. 6.12 b. However, with higher power at 60 MHz, the plasma becomes more

uniform, likely a consequence of the electron heating at 60 MHz being less sensitive to the

electric field enhancement at the edge of the electrodes. The modulation in electron density with

$\Delta\phi_{30}$ persists for all 60 MHz powers though the value of $\Delta\phi_{30}$ which produces the maximum

density is sensitive to the 60 MHz power. At 50 W of 60 MHz power, $\Delta\phi_{30} = 270^o$ produces the

highest plasma density. For 600 W, $\Delta\phi_{30} = 90^o$ - 180° produces the highest plasma density.

There are two effects that may influence these trends. First, the higher plasma density produced by 600 W at 60 MHz results in a thinner sheath which would reduce the relative value of stochastic heating at 15 and 30 MHz compared to resistive heating. Therefore the contribution of the 30 MHz voltage to ionization may be disproportionately smaller. Second, the higher 60 MHz power requires a larger voltage at 60 MHz, which then adds more significant modulation to the sheath.

The phase setting of the 60 MHz voltage had a significant effect on plasma uniformity. The electron density at mid gap as a function of radius is shown in Fig. 6.13 for $\Delta\phi_{60} = 0^{\,o}$ to 270° for $\Delta\phi_{30} = 90^o$ and 270°. The electron density varies by 20% while changing $\Delta\phi_{60}$ with $\Delta\phi_{30}$ $=270^o$. The electron density varies by 35% for $\Delta\phi_{30} = 90^o$. The $\Delta\phi_{60}$ of the maximum density is also sensitive to $\Delta\phi_{30}$, and generally aligns with when the 30 MHz and 60 MHz voltages constructively interfere.

In order to verify that the EAE persists in TF-CCPs, we investigated the influence of $\Delta\phi_{30}$ on dc self-bias for Ar at 10 mTorr. The 60 MHz power was constant at 150 W. The ratio of voltages at 15 MHz and 30 MHz were $V_{15}/V_{30} = 1$, 2 and 3. The numerically and experimentally derived dc-biases are shown in Fig. 6.14. When adding the 60 MHz power, the EAE based on the voltages applied at 15 and 30 MHz (or 13.56 and 27.12 MHz in the experiment) still persists. However, the degree of modulation of the dc self-bias when changing $\Delta\phi_{30}$ is not as great as in the absence of the 60 MHz power (see Fig. 6.5) – a trend borne out in both the computed and experimental results. [Note that there is an unknown phase offset of the fundamental frequency in the experiment. So the experimental results ($V_{13}=V_{27}$ and $V_{13}=3V_{27}$) were shifted 90° to match the consistency, which then also align with the predictions as a function of phase offset.]

The simulation predictions match with experimental measurements well by comparing Fig. 6.14 a and b. The modulation in the dc self-bias is greatest for $V_{15} = 3V_{30,}$ and smallest for $V_{15} = V_{30}$. The magnitude of the dc self-bias increases as V_{15} increases. The modulation for $V_{15} = V_{30}$ is symmetric through the full cycle of $\Delta\Phi_{30}$ offset and is asymmetric for $V_{15} = 3V_{30.}$ The reduction in the depth of modulation of the dc self-bias when adding the 60 MHz power is attributable to its additional contributions to the rf current. The dc self-bias is ultimately determined by the relative currents collected by either side of the blocking capacitor. When adding the 60 MHz power, the fractional contribution to the current by the first and second harmonic is less. The higher plasma density provided by the 60 MHz also reduces the dependence of the sheath properties on the first and second harmonics. For example, the sheath thickness has less dependence on $\Delta\phi_{30}$ because the plasma density is sustained by the 60 MHz power somewhat independently of the power at the first and second harmonics.

The measured and simulated IEDs for $\Delta\phi_{30}$ varied from $0\,^{o}$ to 330° with 150 W of power at 60 MHz in a 10 mTorr Ar plasma are shown in Figs. 6.15 and 6.16 for $V_{15}/V_{30} = 1, 2$ and 3. The mean ion energy generally follows the modulation in the dc self-bias as $\Delta\phi_{30}$ is varied. The ions respond most directly to the oscillation of the sheath at the lowest frequency, and so the energy width of the IEDs increases in both the measured and simulated IEDs with larger V_{15}. From $\Delta\phi_{30} = 30\,^{o}$ to $180\,^{o}$, when $V_{15} = V_{30}$ the energy width of the IED reduces from 87 eV to 59 eV in the experiment and from 83 eV to 66 eV in the simulation. A similar trend has been reported by Coumou *et al.* [20] for DF-CCPs. Since the voltages of the lower frequencies are kept constant, the modulation in the energy width of the IED comes from a change in the sheath thickness. The plasma density and the portion of the cycle that is cathodic, varies with $\Delta\phi_{30}$. Higher plasma density (or a smaller fraction of the cycle that is cathodic) results in a thinner

sheath, a shorter ion transit time across the sheath and a wider IED. When V_{15}/V_{30} increases, the variation in the sheath thickness is less pronounced and so the width of the IED has less variation.

The mean ion energy generally follows the dc-bias as $\Delta\phi_{30}$ is varied. However the energy at the peak of the IED has less variation with phase, best shown in the computed and experimental results for $V_{15} = V_{30}$. This means that the energy of the peak of the IED changes its position from the lower portion of the IED with small $\Delta\phi_{30}$ to the higher portion of the IED for large $\Delta\phi_{30}$. This trend is less clear for $V_{15}/V_{30} = 2$ and 3. Although the experimental IEDs show this mode of modulation for all V_{15}/V_{30}, the simulation only captures this modulation when $V_{15}=V_{30}$. When the voltage ratio increases, the energy of the peak of the IED stays on either the low or high energy side of the IED. The mismatch may come from the unknown phase setting of 60 MHz in the experiment.

The measured and calculated IEDs of Ar at 20 mTorr with 150 W at 60 MHz for $\Delta\phi_{30} = 270^{o}$ and 90° are shown in Fig. 6.17. Since the phase shift of the 60 MHz voltage is unknown in the experiment, we investigated the influence of $\Delta\phi_{60}$ on the IEDs. With $\Delta\phi_{60}$ changing from 0 to 270° the energy of the maximum of the IED changed by approximately half the width of the IED, while the energy widths of the IEDs were modulated by about 15 eV. This modulation in the energy width of the IED most likely resulted from the variation in plasma density and so sheath thickness that occurs when varying $\Delta\phi_{60}$.

The influence of the 60 MHz power and value of $\Delta\phi_{60}$ on IEDs were numerically studied as $\Delta\phi_{30}$ was varied and the results are shown in Fig. 6.18. With a large 60 MHz power and a large plasma density, IEDs broadened due to the thinning of the sheath. The dc self-bias is still modulated by $\Delta\phi_{30}$ consistent with the EAE. When the 60 MHz power is large, its voltage amplitude is large enough to modulate the sheath potential. As such, changing $\Delta\phi_{30}$ with large

60 MHz power produces significant modulation of the peak and shapes of IEDs. (Compare the IEDs in Fig. 6.18 b and c.) However, for a constant 60 MHz power, the value of $\Delta\phi_{60}$ does not significantly affect the energy widths of the IEDs.

6.5 Concluding Remarks

The consequences of the EAE in DF- and TF-CCPs have been discussed with results from computational and experimental investigations. The experimental reactor was geometrically asymmetric, which naturally produced a large dc bias. The effect of the EAE on dc bias was therefore investigated in the context of geometrically asymmetric reactor having this natural negative dc bias as one might find in industry. The general trends of the EAE were also observed in this asymmetric system, however, the dependence of dc bias and so ion energy distributions were ultimately sensitive to the geometric asymmetry, rf voltage amplitudes and phases, and the phase offsets. The EAE has a first order effect on IEDs through not only the shift in the mean ion energy by modulation in the dc self-bias, but also in the shape of the IED, as represented by the energy of the peak of the IED. These trends persist in the TF-CCP where additional ionization is provided by a high frequency power source. Results from the model generally align with the experiments. Mismatches between the model and experiment may in part be explained by unknown phase offsets and phase shifts at 60 MHz.

The energy of the peak of the IEDs is found to shift between low and high energy as $\Delta\phi_{30}$ varies from 0 ^{o} to 330 ^{o}. The modulation in plasma density with changes in $\Delta\phi_{30}$ can modulate the sheath thickness and contribute to a modulation of the energy width of IEDs at certain phases. Although the consequences on plasma density with phase shift and its correlation with harmonic currents warrants further study, the computational and experimental results discussed here show that small changes of phase translate to significant changes in plasma properties and may provide

178

a means for customizing the shape of IEDs. These trends based on studies in argon also apply to multicomponent gas mixtures, through the trends are less clear due to the large variation in ion mass. Nevertheless, profile simulation of etching in complex gas mixtures using IEDs modulated by the EAE suggest that etching processes can be controlled through judicious choice of phase offsets between harmonic voltages.

6.6   Figures
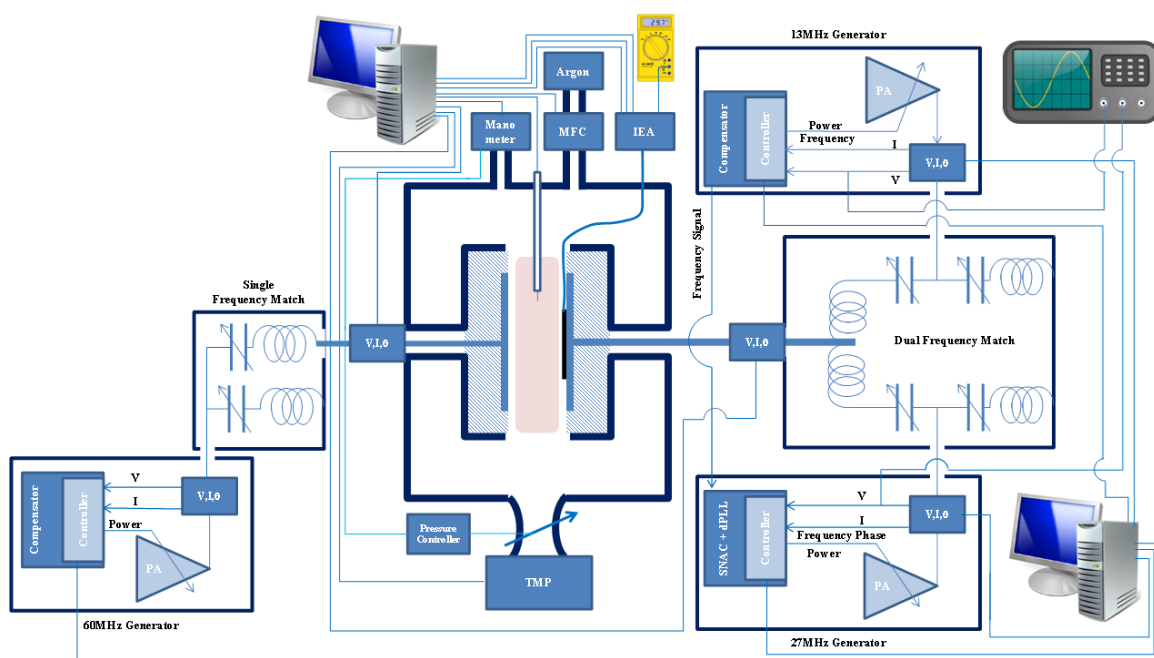
Fig. 6.1. Experimental setup for triple frequency CCP. Dual frequency setup is similar except that the top electrode is grounded.
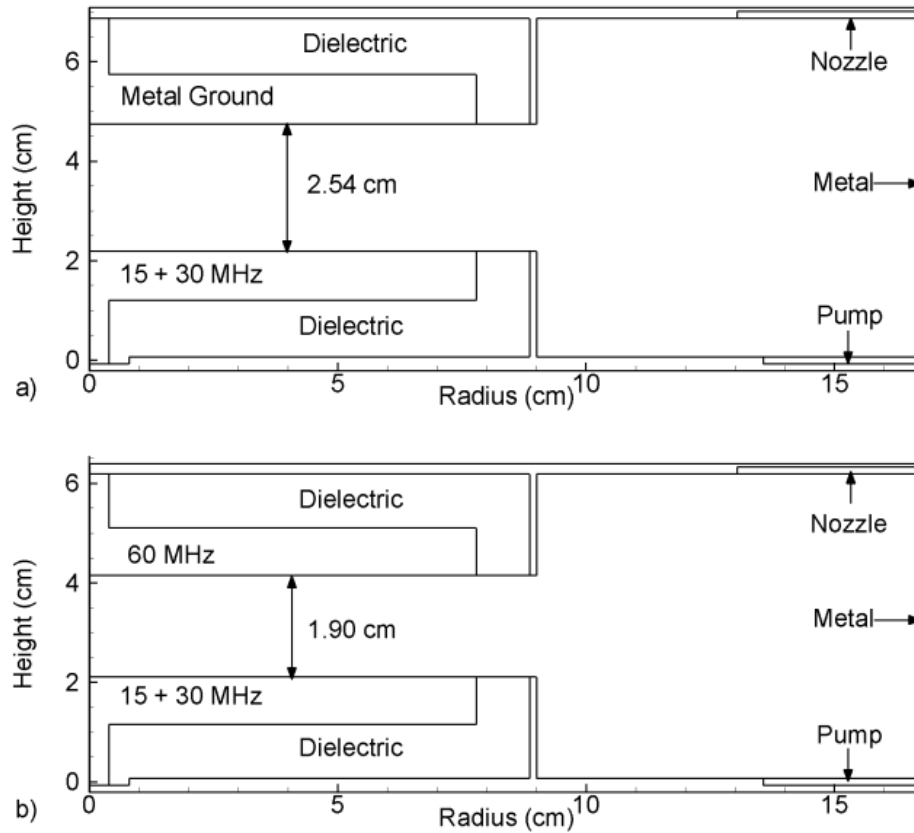
Fig. 6.2. Schematic of simulation geometries used in the model. a) Dual frequency CCP with both 15 and 30 MHz applied on the bottom electrode. The top electrode and metal chamber wall are grounded. The gap between two electrodes is 2.54 cm. b) Triple frequency CCP with 15 and 30 MHz applied on the bottom electrode, and 60 MHz applied on the top electrode. The electrode gap is 1.9 cm. The chamber wall is grounded.
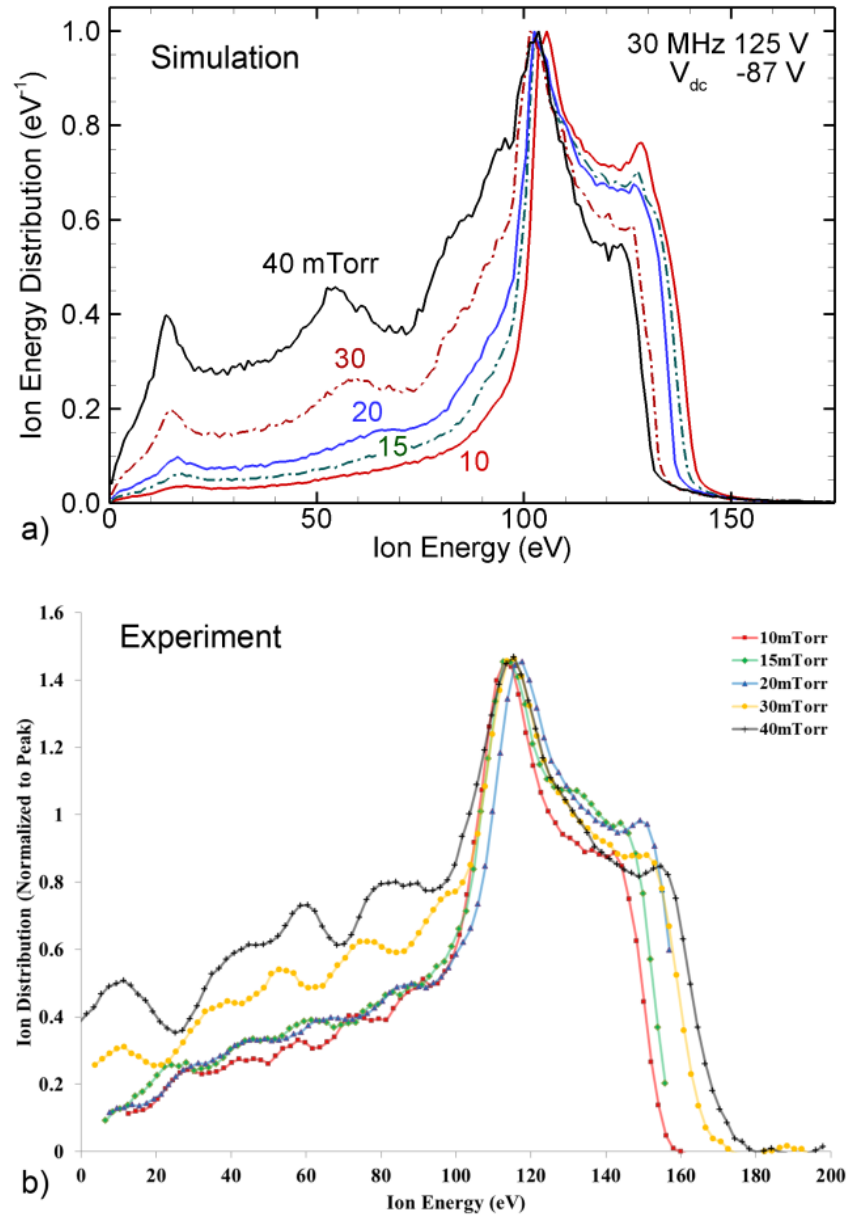
Fig. 6.3. IEDs for a single frequency CCP with pressure varying from 10 to 40 mTorr. Power was varied to provide constant dc self-bias voltage (-87 V) for each condition. a) Simulated IEDs for an Ar plasma with 30 MHz on the bottom electrode. b) Experimental results. [Data were reprinted with permission from D. J. Coumou et al., IEEE Trans. Plasma Sci. **42**, 1880 (2014).]
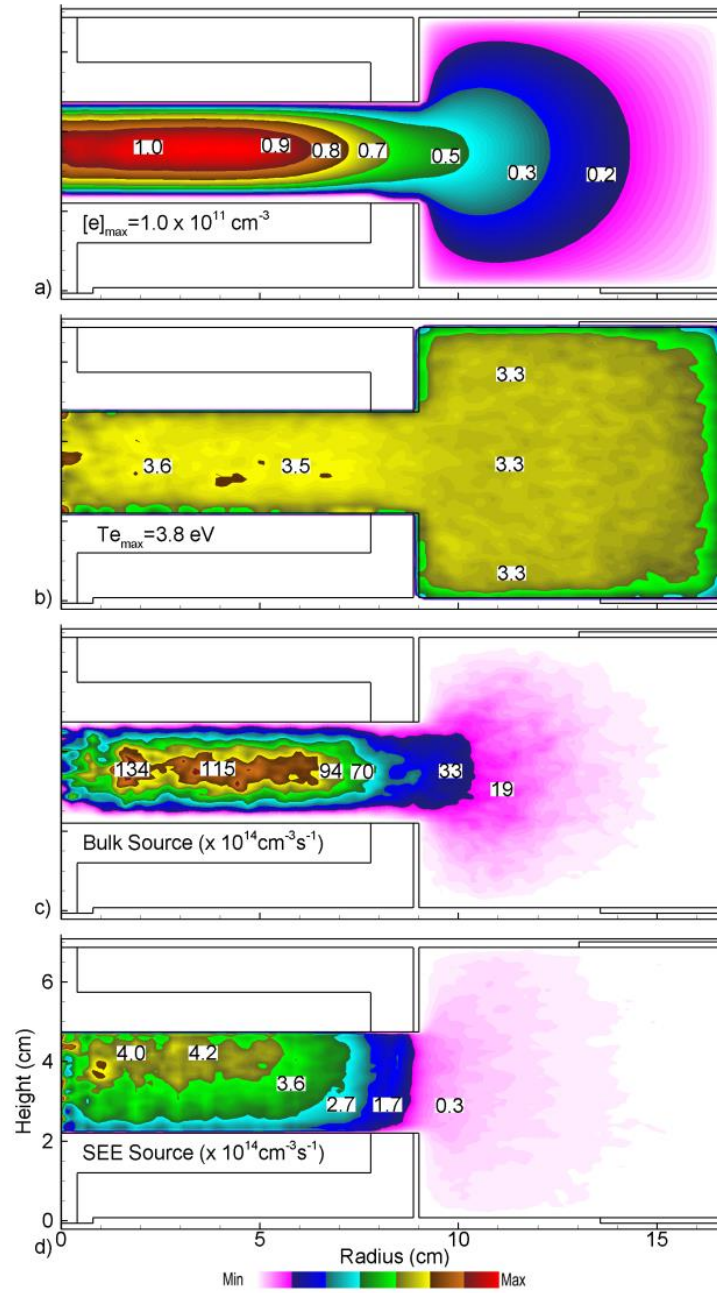
Fig. 6.4. Time averaged plasma properties for the DF-CCPs having base case conditions (Ar, 20 mTorr, 50 sccm, $V_{bottom}(t) = 100\sin(\omega_{15}t + 180^o) + 100\sin(\omega_{30}t + 180^o)$, no phase shift between two frequencies). a) Electron density, b) electron temperature, c) bulk electron ionization source and d) ionization by sheath accelerated secondary electrons. The plots use linear scales.
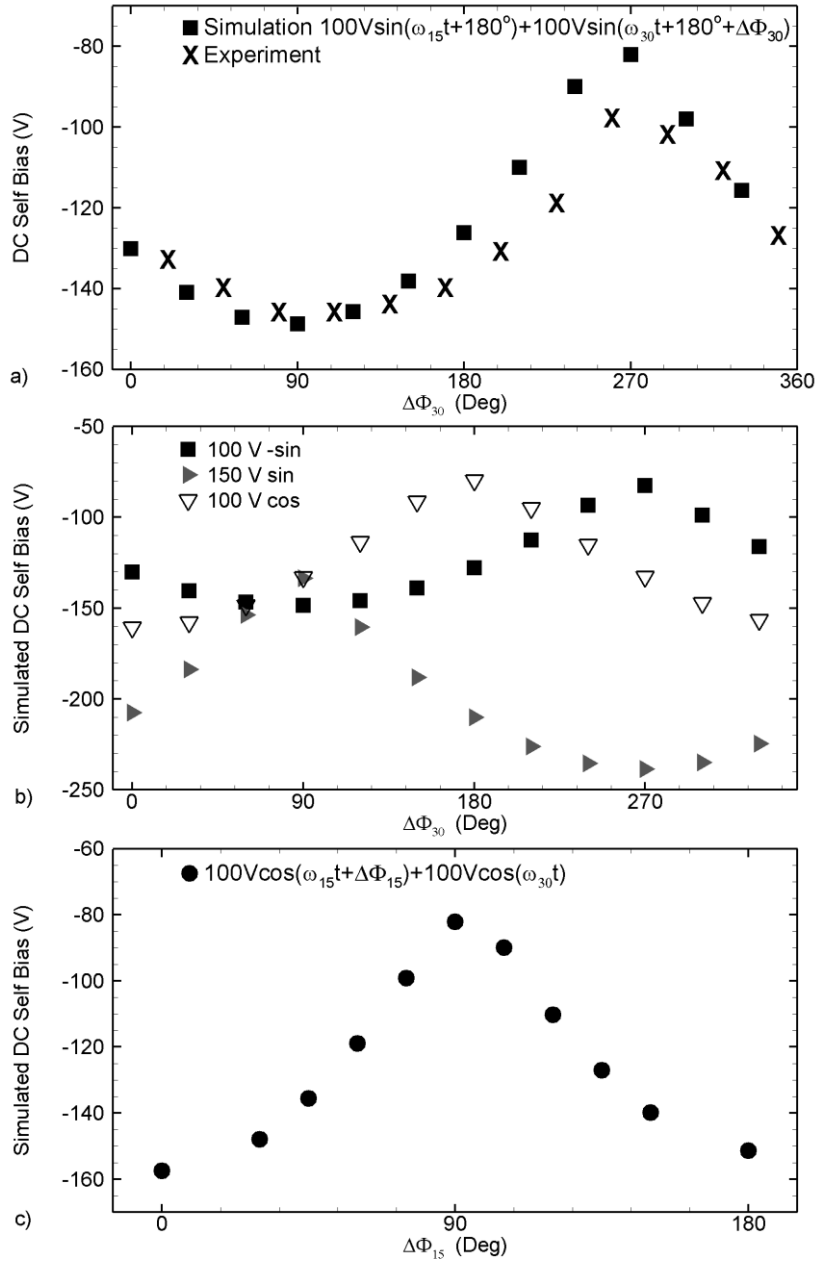
Fig. 6.5. Dc self-biases with a shift of phase $\Delta\phi_{30}$ from 0° to 360°. a) Simulated and measured dc self-biases for base case operating conditions. b) Simulated dc self-biases for different sinusoidal waveforms (different phase offset). The "100V –sin" represents $V_{bottom}(t) = 100V \sin(\omega_{15}t + 180^o) + 100V \sin(\omega_{30}t + 180^o + \Delta\phi_{30})$, the "150V sin" represents $V_{bottom}(t) = 150V \sin(\omega_{15}t) + 150V \sin(\omega_{30}t + \Delta\phi_{30})$, and "100V cos" represents $V_{bottom}(t) = 100V \cos(\omega_{15}t) + 100V \cos(\omega_{30}t + \Delta\phi_{30})$. c) Simulated dc self-biases for cosine functions with phase shift angle applied at the fundamental frequency: $V_{bottom}(t) = 100V \cos(\omega_{15}t + \Delta\phi_{15}) + 100V \cos(\omega_{30}t)$.

184
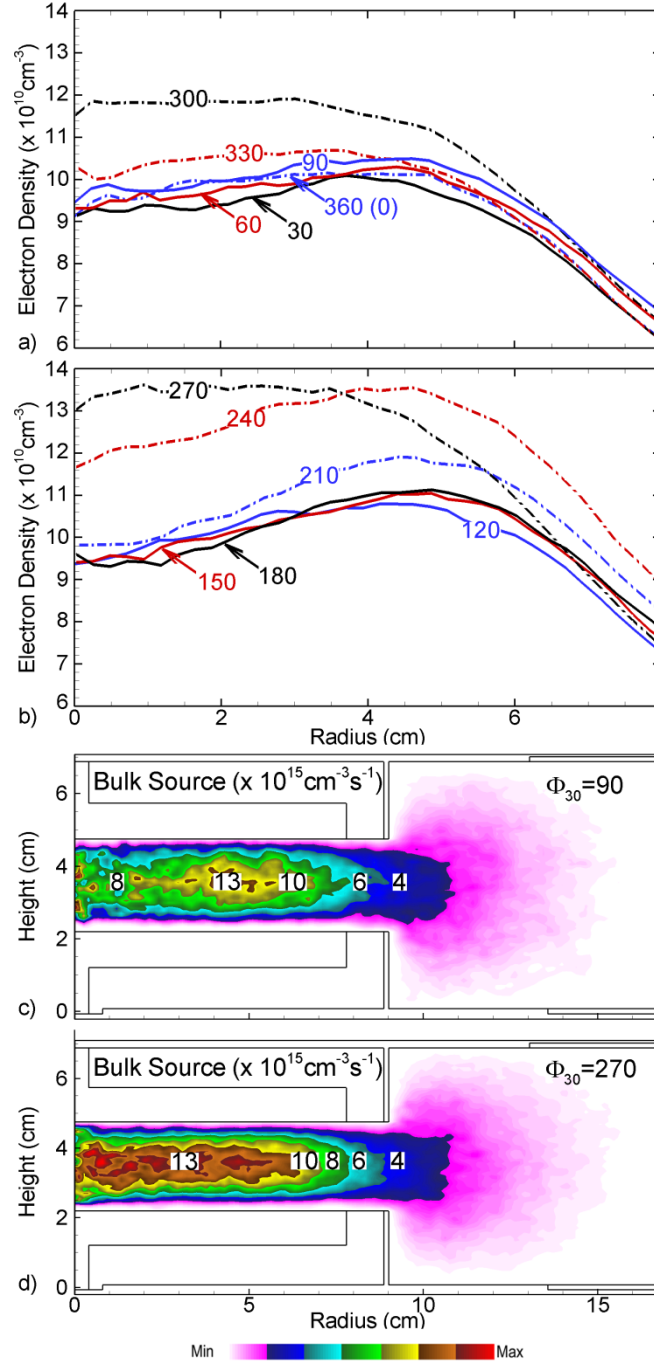
Fig. 6.6. Time averaged electron density in the middle of the electrodes (1.27 cm above substrate) from the center to the edge of the substrate for Ar, 20 mTorr, 50 sccm with rf bias: $V_{bottom}(t) = 100\sin(\omega_{15}t + 180^o) + 100\sin(\omega_{30}t + 180^o + \Delta\phi_{30})$ .a) $\Delta\phi_{30}$=300°, 330°, 360° (0°), 30°, 60°, 90° b) $\Delta\phi_{30}$=120°, 150°, 180°, 210°, 240° and 270°. Note that the range of density plotted is from 6×10^{10} to 14×10^{10} cm^{-3}. c) Cycle averaged bulk ionization source for $\Delta\phi_{30}$ =90° and d) $\Delta\phi_{30}$ =270°.

185
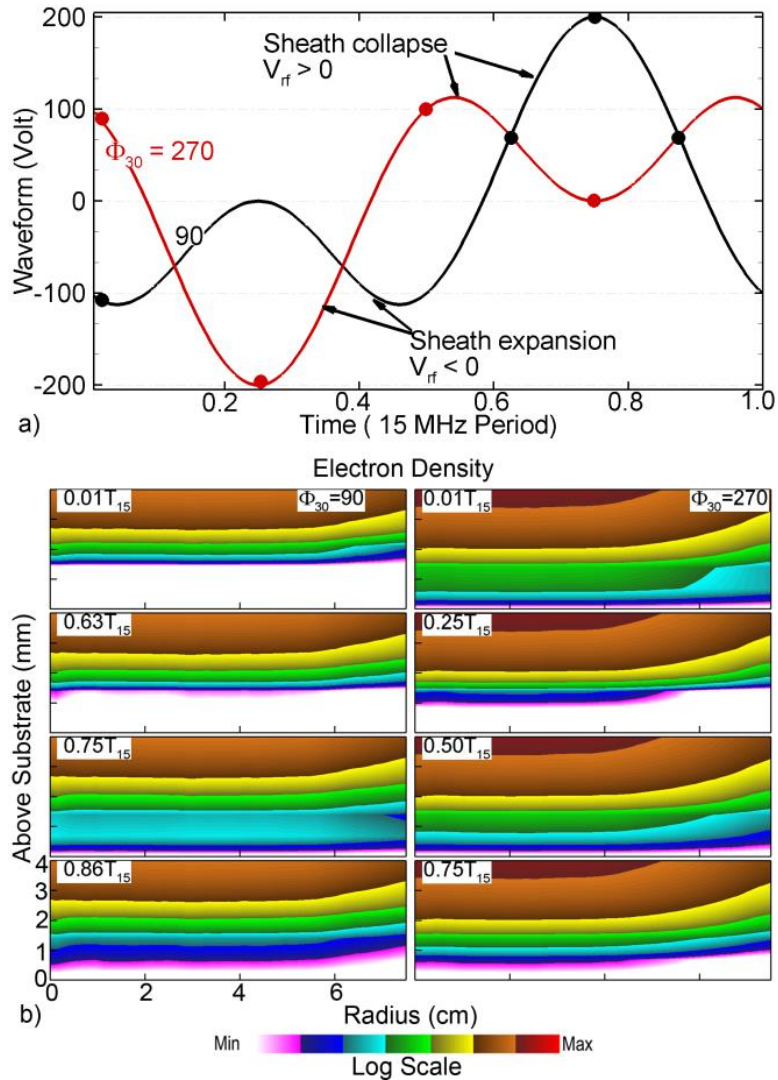
Fig. 6.7. Sheath dynamics for $\Delta\phi_{30}$ =90 and 270° during one 15 MHz period, T_{15}. a) rf waveform applied to the substrate. b) Electron density in the sheath region (radius from 0 to 7.5 cm and height from 0 to 4 mm above the substrate) for selected time points for (right) $\Delta\phi_{30}$ =90° and (left) $\Delta\phi_{30}$ =270°.
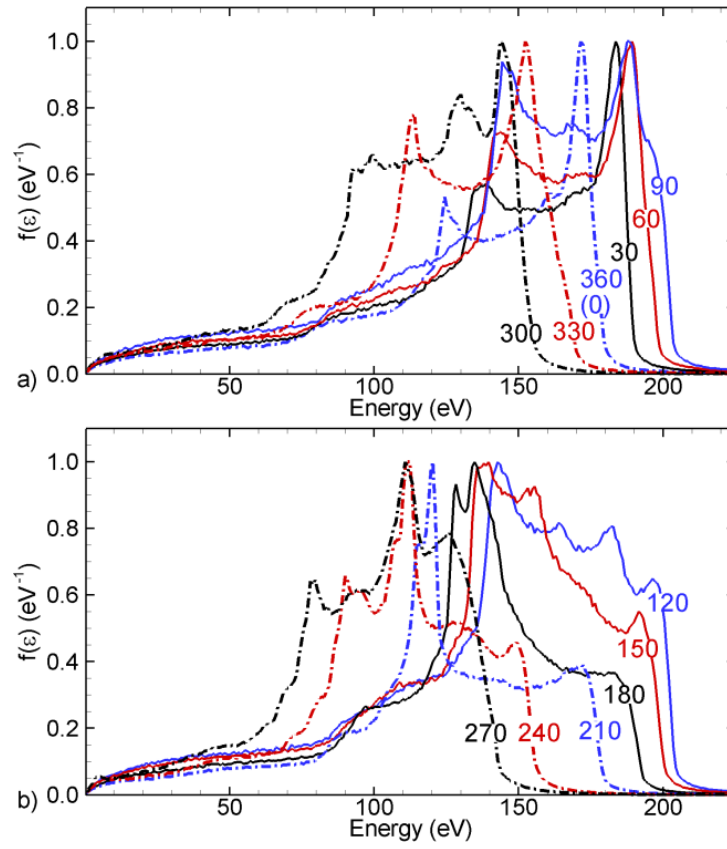
Fig. 6.8. Time averaged IEDs onto the substrate for Ar at 20 mTorr, 50 sccm with rf bias:
$V_{bottom}(t) = 100\sin(\omega_{15}t + 180^o) + 100\sin(\omega_{30}t + 180^o + \Delta\phi_{30})$. a) $\Delta\phi_{30} = 300^o$, 330°, 360° (0°), 30°, 60°, and 90°. b) $\Delta\phi_{30} = 120^o$, 150°, 180°, 210°, 240° and 270°.
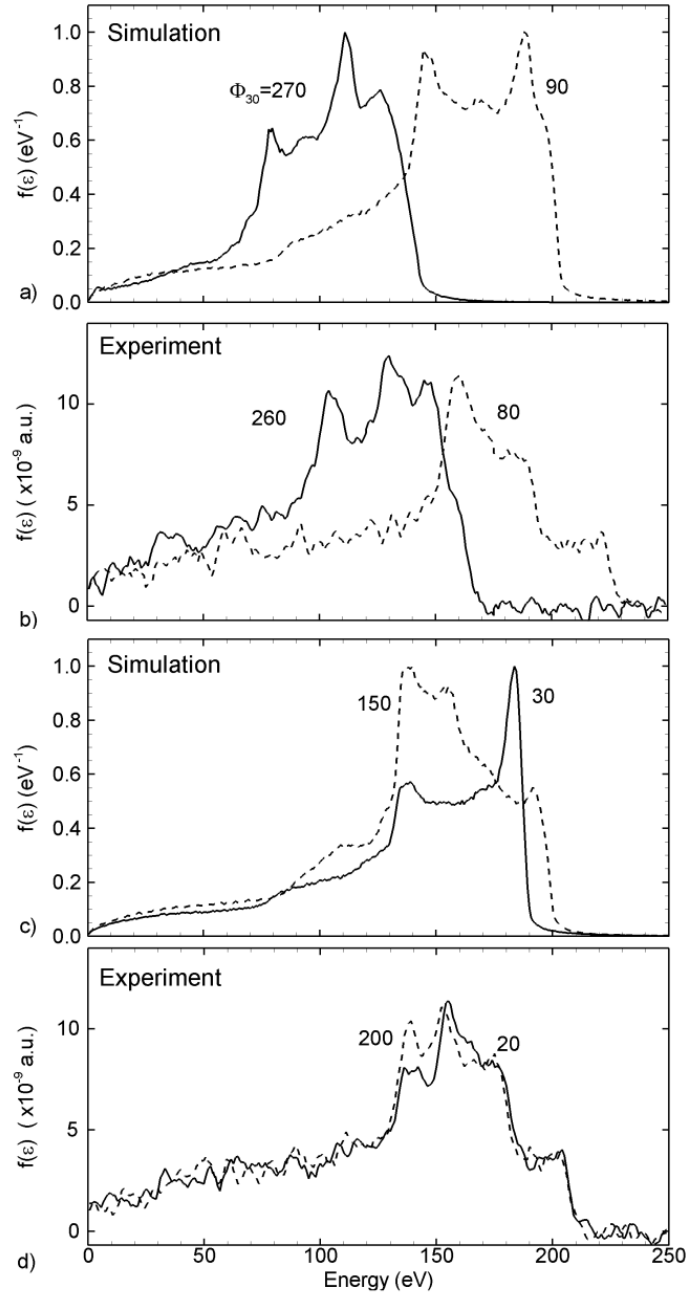
Fig. 6.9. Simulated and measured IEDs for operating conditions of Ar at 20 mTorr, 50 sccm, $V_{bottom}(t) = 100\sin(\omega_{15}t + 180^o) + 100\sin(\omega_{30}t + 180^o + \Delta\phi_{30})$. In the experiment, the phase delay is unknown. a) Simulated IEDs for minimum and maximum dc-bias phases. $\Delta\phi_{30} = 270^o$ and 90°. b) Measured IEDs for minimum and maximum dc-bias phases, $\Delta\phi_{30} = 260^o$ and 20°. c) Simulated IEDs at phases that have similar dc self-biases, $\Delta\phi_{30} = 150^o$ and 30°. d) Measured IEDs for phases having similar dc self-biases, $\Delta\phi_{30} = 200^o$ and 20°. The different shape of the IEDs suggests that the EAE not only affects mean ion energy but also ion sheath dynamics which modify IEDs.
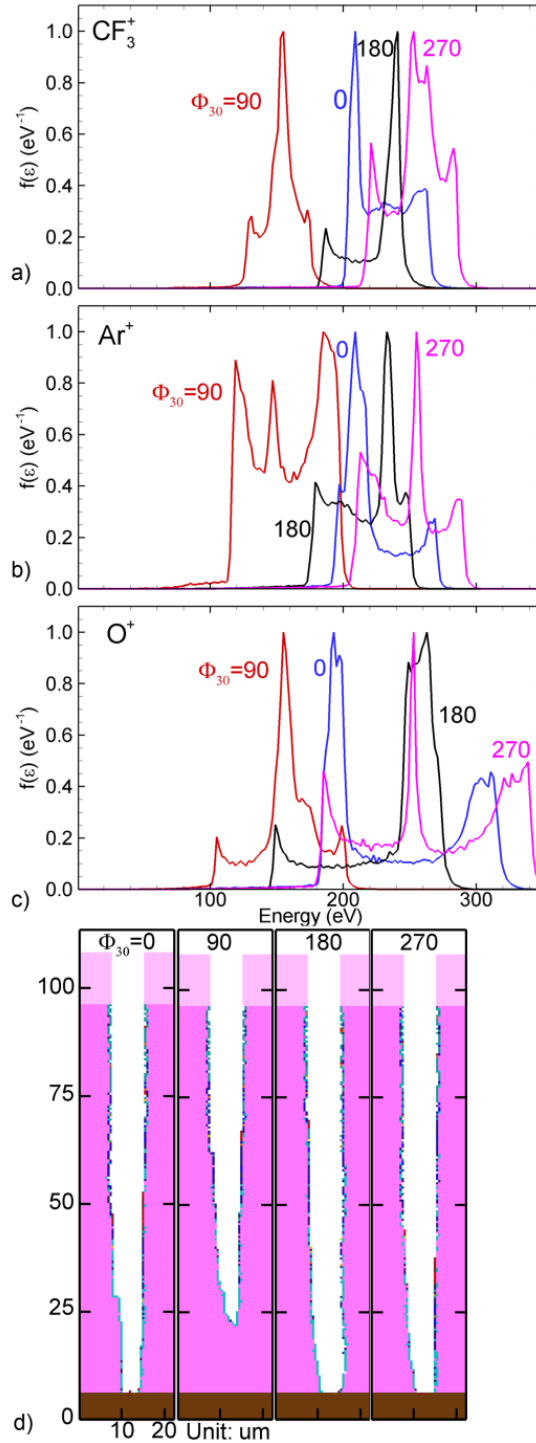
Fig. 6.10. Simulated IEDs and etch profiles for Ar/CF$_4$/O$_2$ = 75/20/5 at 20 mTorr with $V_{bottom}(t) = 100\sin(\omega_{15}t + 180^o) + 100\sin(\omega_{30}t + 180^o + \Delta\phi_{30})$, where $\Delta\phi_{30} = 0^o$, 90°, 180°, and 270°. a) CF$_3^+$ (heaviest ion), b) Ar$^+$ (major ion species), c) O$^+$ (lightest ion) and d) etch profiles when the $\Delta\phi_{30} = 270^o$ case reach 20% over-etch.

189
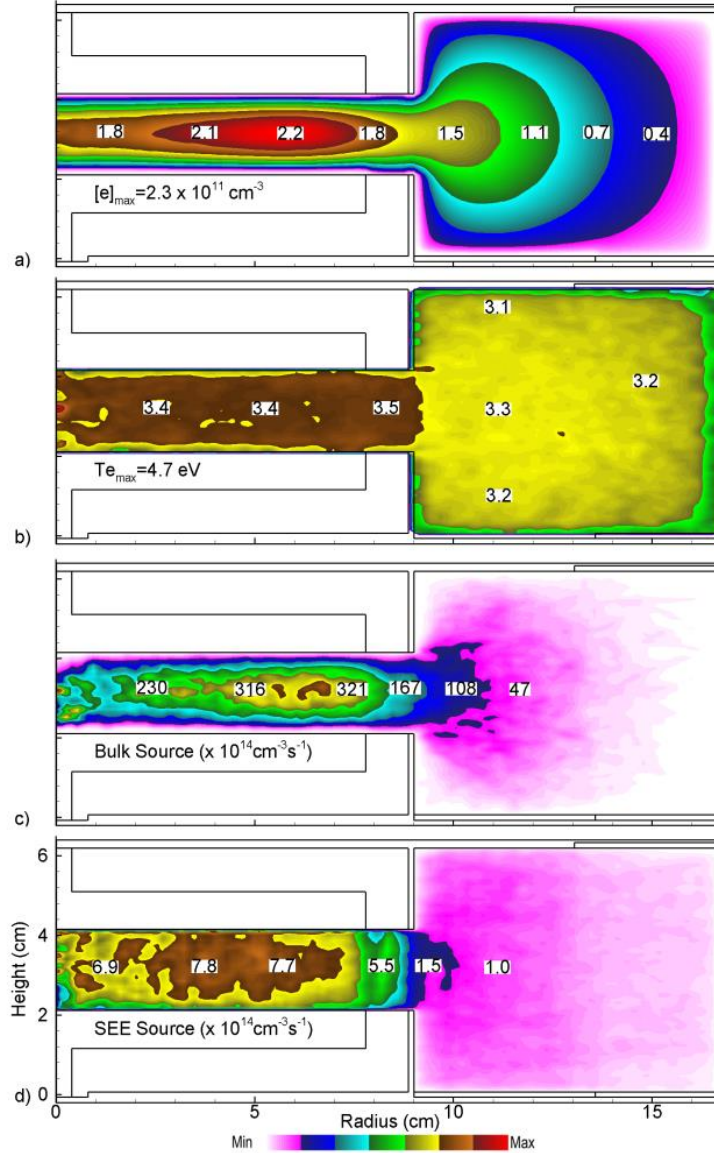
Fig. 6.11. Time averaged plasma properties for the TF-CCPs base case conditions (Ar, 20 mTorr, 50 sccm, $V(t) = 100\sin(\omega_{15}t + 180^o) + 100\sin(\omega_{30}t + 180^o) + P_{60}\sin(\omega_{60}t + 270^o)$ and $P_{60} = 150$ W). a) Electron density, b) electron temperature, c) bulk electron ionization source and d) ionization by sheath accelerated secondary electrons. The plots use linear scales.
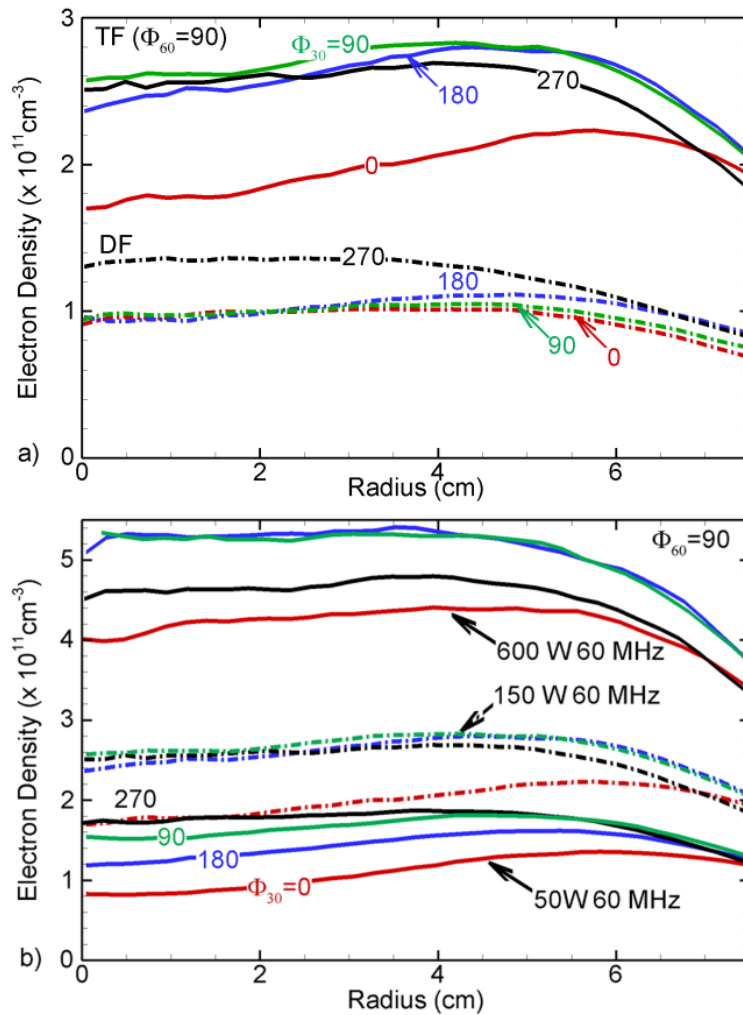
Fig. 6.12. Electron density at mid-gap from the center of the reactor to the edge of the electrode with bottom bias $V_{bottom}(t) = 100\sin(\omega_{15}t + 180^o) + 100\sin(\omega_{30}t + 180^o + \Delta\phi_{30})$ and $\Delta\phi_{30} = 0^o$, 30°, 60° and 90°. a) Comparison between no 60 MHz power on top electrode and 150 W at 60 MHz, b) 60 MHz power = 50, 150 and 600 W and with constant 60 MHz phase.
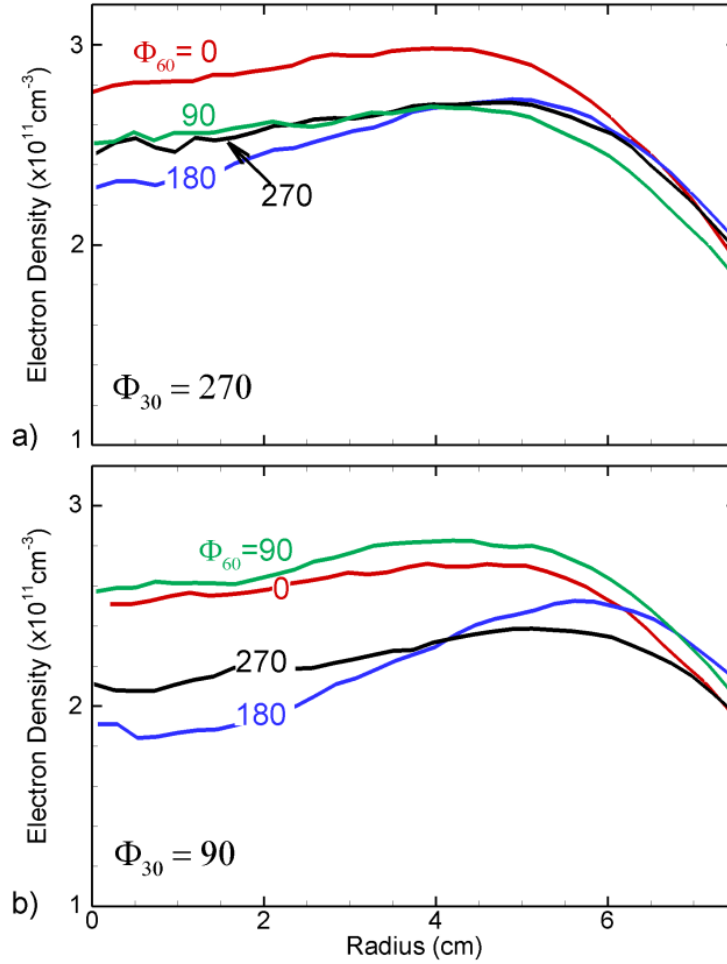
Fig. 6.13. Electron density at mid-gap from the center of the reactor to the edge of the electrode with bottom bias: $V(t) = 100\sin(\omega_{15}t + 180^o) + 100\sin(\omega_{30}t + 180^o + \Delta\phi_{30})$ and 150 W on the top electrode with voltage waveform $P_{60}\sin(\omega_{60}t + 180^o + \Delta\phi_{60})$ where $\Delta\phi_{60}$ =0°, 90°, 180° and 270°. a) $\Delta\phi_{30}$ =270° and b) $\Delta\phi_{30}$ =90°. Note that the electron density is plotted over a range of 1.0 × 10^{11} to 3.2 × 10^{11} cm^{-3}.
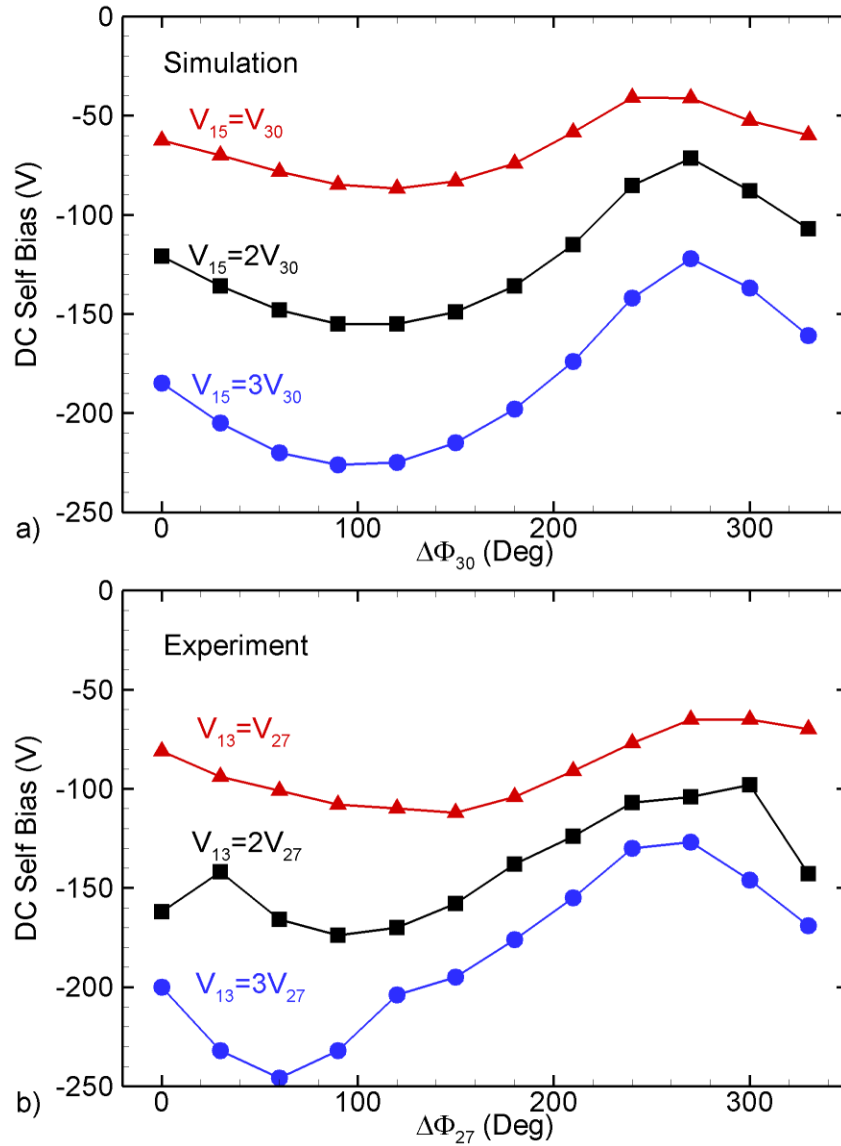
Fig. 6.14. EAE for TF-CCPs in Ar at 10 mTorr shown by the dc self-bias with $\Delta\phi_{30}$ varying from 0 to 330° for voltage ratios of $V_{30}/V_{15} = 1, 2$ and 3. Results from a) simulation and b) experiment. $V_{30} = 75$ V in the simulation and V_{27} in experiment has an average value of 59 V with a 15% variation. Both simulation and experiment find that larger V_{15} produces a more negative dc self-bias.
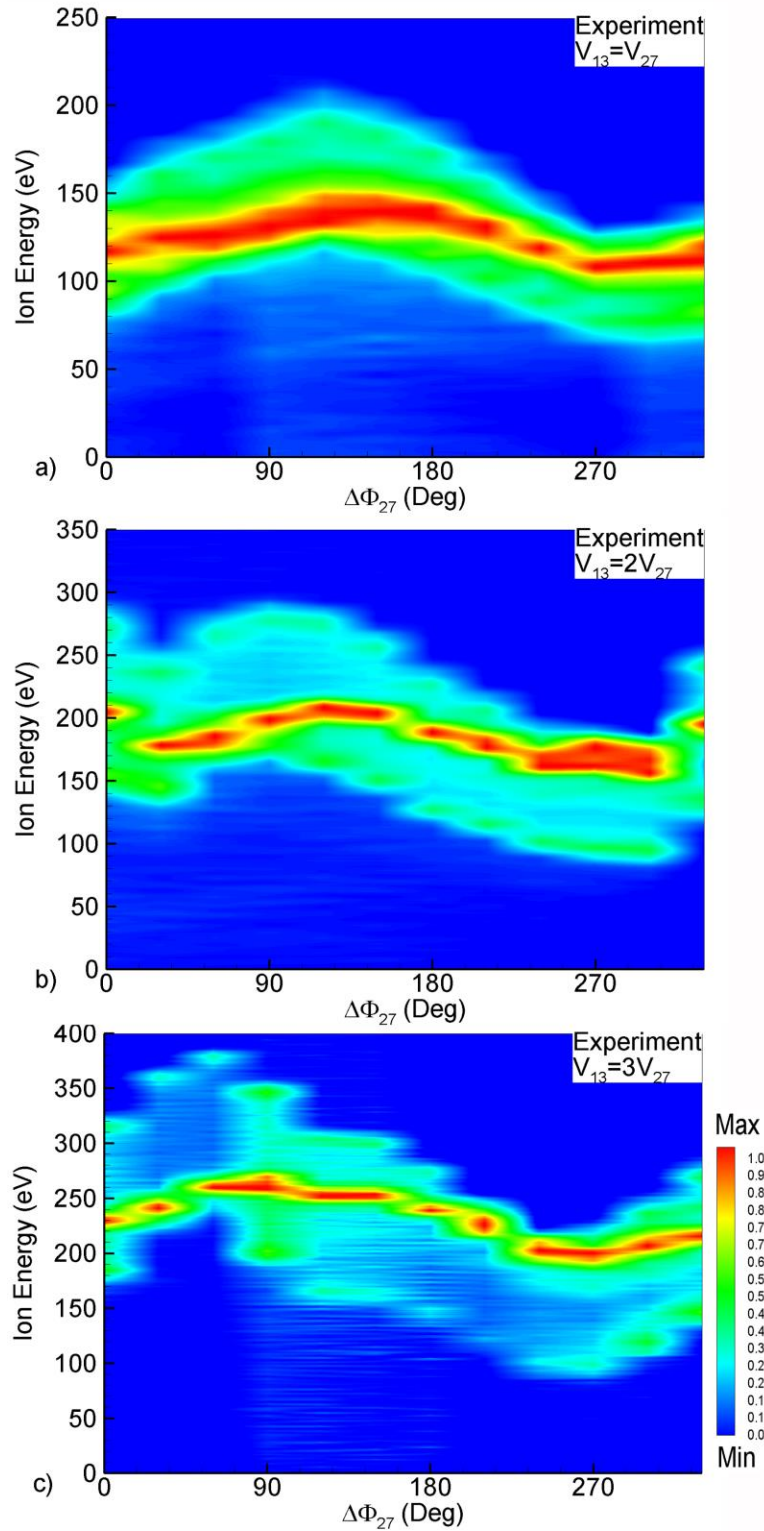
Fig. 6.15. Experimentally measured IEDs with $\Delta\phi_{27}$ varied from 0° to 330° for Ar at 10 mTorr. The distributions are normalized with respect to the maximum ion energy at each phase.

194
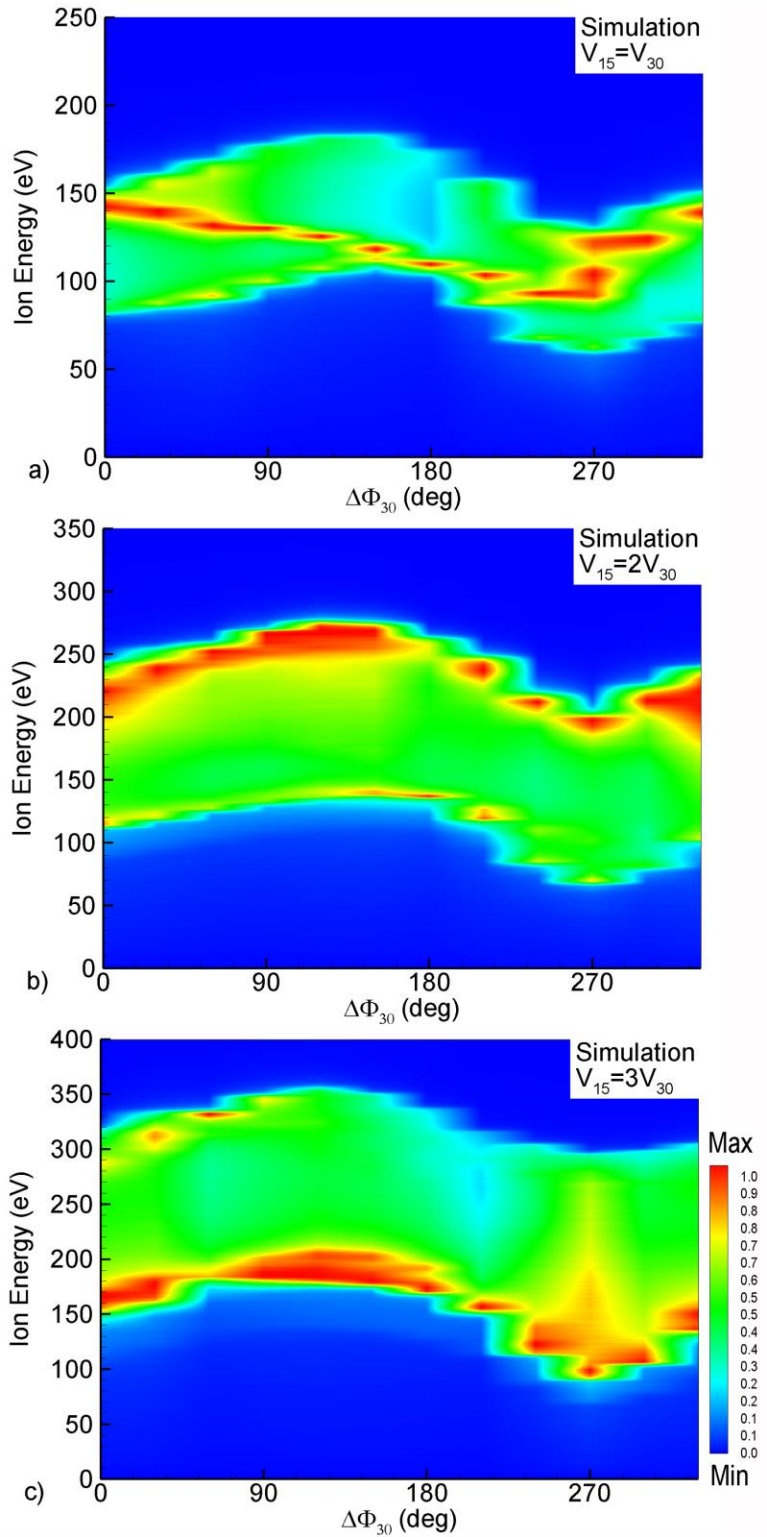
Fig. 6.16. Simulated IEDs with $\Delta\phi_{30}$ varied from 0° to 330° for Ar at 10 mTorr. The distributions are normalized with respect to the maximum ion energy at each phase.
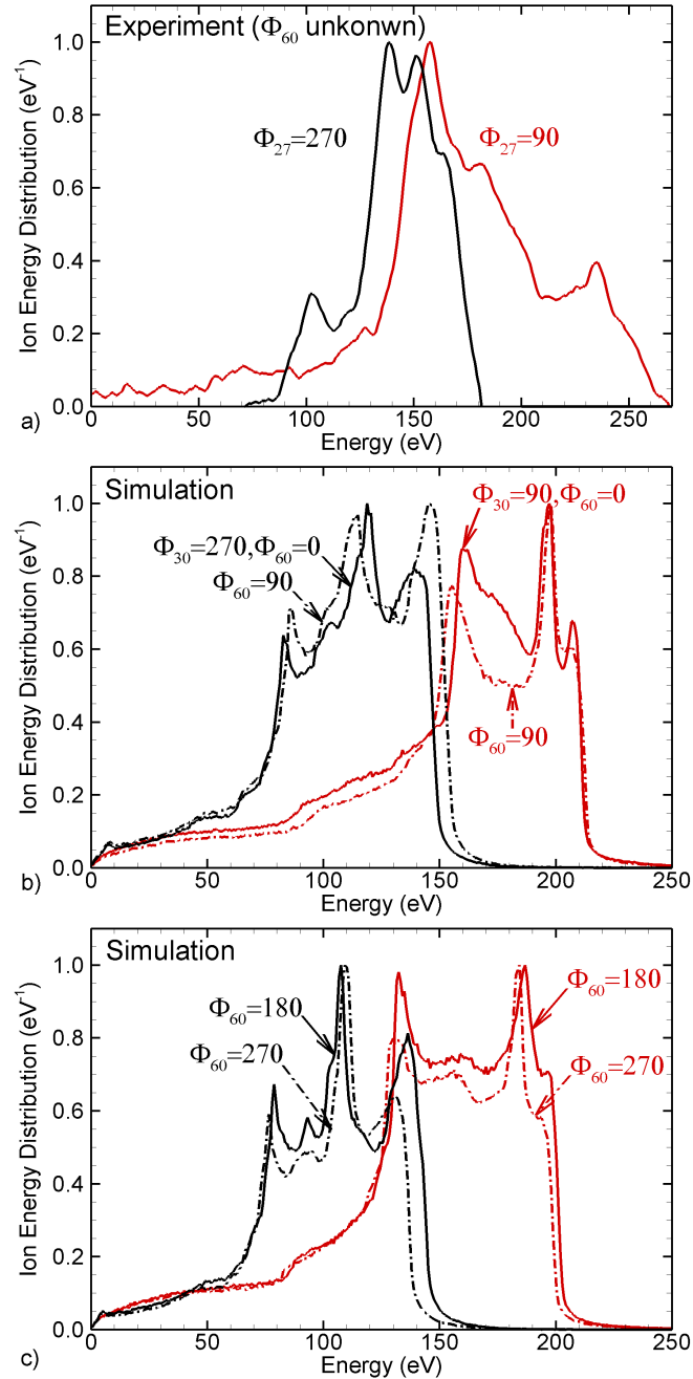
Fig. 6.17. IEDs with minimum and maximum dc self-bias ($\Delta\phi_{30} = 270^{o}$ and 90°) for Ar at 20 mTorr with 150 W power at 60 MHz and $V_{15}=V_{30}=$ 100 V. a) Experiment with no phase lock on 60 MHz and unknown phase offset from generator to electrode. Simulated IEDs with b) $\Delta\phi_{60}$ $=0^{o}$ and 90°, c) $\Delta\phi_{60}=180^{o}$ and 270°. In the simulation, the phase offset is estimated to be 180° for all frequencies.

196
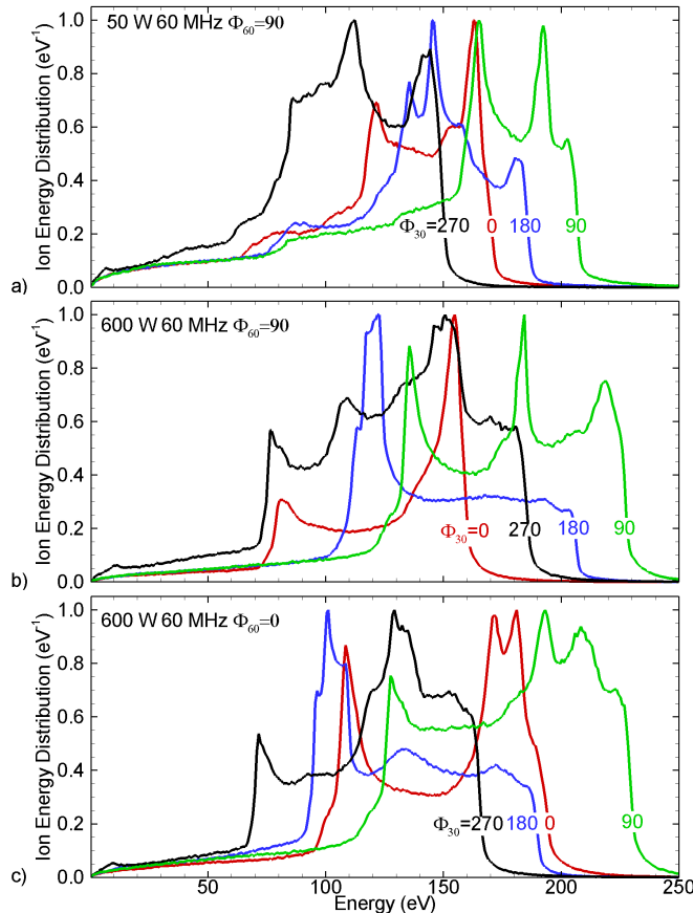
Fig. 6.18. IEDs with minimum and maximum dc self-bias ($\Delta\phi_{30} = 270^{\mathbf{o}}$ and 90°) for Ar at 20 mTorr with 150 W power at 60 MHz and $V_{15}=V_{30}= 100$ V. a) Experiment with no phase lock on 60 MHz and unknown phase offset from generator to electrode. Simulated IEDs with b) $\Delta\phi_{60}$ $=0^{\mathbf{o}}$ and 90°, c) $\Delta\phi_{60}=180^{\mathbf{o}}$ and 270°. In the simulation, the phase offset is estimated to be 180° for all frequencies.

6.7   References

1. B. G. Heil., U. Czarnetzki, R.P.Brinkmann, and T. Mussenbrock, J. Phys. D: Appl. Phys. **41**, 165202 (2008).
2. Z. Donkó, J. Schulze, B. G. Heil, and U. Czarnetzki, J. Phys. D: Appl. Phys. **42**, 025205 (2009).
3. J. Schulze, E. Schüngel, and U. Czarnetzki, J. Phys. D: Appl. Phys. **42**, 092005 (2009).
4. Q-Z. Zhang, W. Jiang, L-J. Hou and Y-N. Wang, J. Appl. Phys. **109**, 013308 (2011).
5. I. Korolov, Z. Donkó, U. Czarnetzki and J. Schulze, J. Phys. Appl. Phys. **45,** 465205 (2012).
6. T. Lafleur and J. P. Booth, Appl. Phys. Lett. **102**, 154104 (2013).
7. E. Schüngel, D. Eremin, J Schulze, T. Mussenbrock, and U. Czarnetzki, J. Appl. Phys. **112**, 053302 (2012).
8. S. Bienholz, T. Styrnoll and P. Awakowicz, J. Phys. D: Appl. Phys. **47,** 065201 (2014).
9. D. Hrunski, A. Janssen, T. Fritz, T. Hegemann, C. Clark, U. Schreiber, G. Grabosch, Thin Solid Films **532**, 56 (2013).
10. D. Hrunski, F. Mootz, A. Zeuner, A. Janssen, H. Rost, R. Beckmann, S. Binder, E. Schüngel, S. Mohr , D. Luggenhölscher, U. Czametzki and G. Grabosch, Vacuum **87**, 114 (2013).
11. B. Bruneau, T. Novikova, T. Lafleur, J. P. Booth and E. V. Johnson, Plasma Sources Sci. Technol. **23**, 065010 (2014).
12. B. Bruneau, T. Novikova, T. Lafleur, J. P. Booth and E. V. Johnson, Plasma Sources. Sci. Technol. **24**, 015021 (2015).
13. J. Schulze, E. Schungel, Z. Donk´o, and U. Czarnetzki, Plasma Sources Sci. Technol. **20**, 015017 (2011).
14. T. Lafleur, P. A. Delattre, E. V. Johnson and J. P. Booth, Appl. Phys. Lett. **101** 124104 (2012).
15. A. Derzsi, I. Korolov, E. Schüngel, Z. Donkó and J. Schulze. Plasma Sources Sci. Technol. **22**, 065009 (2013).
16. P. A. Delattre, T. Lafleur, E. Johnson and J.P. Booth, J. Phys. D: Appl. Phys. **46**, 235201 (2013).
17. A. V. Vasenkov, X. Li, G. S. Oehrlein and M. J. Kushner, J. Vac. Sci. Technol. A **22,** 511 (2004).
18. A. Vasenkov and M. J. Kushner, J. Appl. Phys. **95**, 834 (2004).
19. A. Sankaran and M. J. Kushner, J. Vac. Sci. Technol. A **22,** 1260 (2004).
20. D. J. Coumou, D. H.Clark, T. Kummerer, M. Hopkins, D. Sullivan and S. Shannon, IEEE Trans. Plasma Sci. 42, 1880 (2014).
21. G. F. Franklin, J. D. Powell and D. Workman, "Digital Control of Dynamic Systems", (Addison Wesley, Reading, MA, 1998).
22. D. J. Coumou, U.S. Patent 6522121, (2003).
23. A. V. Phelps, J. Phys. Chem. Ref. Data, **20**, 557 (1991).
24. M. A. Lewis, D. A. Glocker and J. Jorne, J. Vac. Sci. Technol. A **7**, 1019 (1989).
25. J. Schulze, E. Schüngel, U. Czametzki, and Z. Donkó, J. Appl. Phys. **106**, 063307 (2009).
26. J. Schulze, E. Schüngel, U. Czametzki, M. Gebhardt, R. P. Brinkmann and T. Mussenbrock, Appl. Phys. Lett. **98**, 031501 (2011).
27. S.-B. Wang and A. E. Wendt. J. Vac. Sci. Technol. A **19,** 2425 (2001).
28. D. C. Gray, I. Tepermeister and H. H. Sawin, J. Vac. Sci. Technol. B **11**, 1243 (1993).

Chapter 7 COMPUTATIONAL INVESTIGATION OF ION KINETICS IN PLASMA 3-DIMENSIONAL FEATURE ETCHING

7.1   Introduction

Plasma etching is an essential step in the fabrication of Micro Electro Mechanical System (MEMS) and Very Large Scale Integration (VLSI) circuits.[1-3] As current technology moves towards 14 nm and beyond, fabricating features with nanometer range critical dimensions (CD) and maintaining high aspect ratio (AR) structures becomes extremely challenging. Many phenomena occur to produce profile defects.[4] The most significant defects can be classified into three groups: 1) Etching yield angular dependent effects (e.g., mask faceting, micro-trenching, and slopped sidewalls) caused by the angular distributions of ion and neutral fluxes.[5-7] 2) Electron shading effects (e.g., notching, micro-trenching and electrical degradation) caused by the non-uniformed surface charging of the etched features.[8-10] 3) Effects (e.g., aspect ratio dependent etching (ARDE), undercut and micro-loading) caused by the transportation and depletion of chemical etching and inhibit reactants.[11-13] Moreover, new transistor structures involving 3-dimensional (3-d) integration technologies not only enable the continued miniaturization and performance improvement of future electronic systems, but also bring about new concerns in fabrication.[14,15] For example, the corners between the gates in a FinFET typically require extended over-etch time to be cleaned out. However, this over-etch

time may damage the underlying layer. Thus, this process requires high material selectivity to prevent potential damage.[16]

In order to achieve highly anisotropic structures, chlorine (Cl) based plasma chemistries are widely used. Because the spontaneous etch rate of Cl radical with Si at room temperature is relatively low, Cl_2 plasma etching is driven by the ion-induced chemistry.[17] Its etch products ($SiCl_n$, $n \leq 4$) have high reactivity and tend to redeposit on the sidewalls to prevent sidewall undercut.[18] Thus, Cl_2 etching silicon is able to produce a vertical profile. Other halogen species, such as fluorine (F) biased plasmas are also commonly used in reactive ion etching (RIE). Etching in F-based plasmas normally results in an isotropic etch rate and so anisotropy can be obtained through the formation of an inhibiting layer.[19] Oxide films are typically etched using a main etch recipe based on $C_xF_y/O_2/Ar$. The addition of a small amount of O_2 ($\approx 5\%$) to a fluorine-carbon mixture is found to increase the F radical density and thus promoting the F-based etching.[20] The polymer film can also be anisotropic etched by oxygen atom. Economou *et al.* reported etch rate up to 0.6 um/min of SiO_2 etching by oxygen atom with 100s eV energy.[21] In general, the anisotropic etching of silicon dioxide is mainly ion driven, as ions physically sputter passivation layers and allow radicals to react with silicon dioxide.

Although plasma reactive ion etching with halogen gas has been experimentally and computationally studied since the 1970s [22-25], controlling the quality of etching features continues to be challenging since the feature CD continuously shrinks with increases in AR. Kim *et al.* studied the effect of various oxide etching conditions during high aspect ratio contact (AR up to 14) for SiO_2 etching. Distortion of the contact pattern became significant when the aspect ratio of the etched oxide was increased. Improving mask material selectivity, increasing mask thickness, and adding an in-situ polymer removal step were found to reduce the pattern

distortion.[26] Chung investigated the geometry effect on RIE lag (i.e. smaller trenches etch at a lower rate than larger trenches during reactive ion etching) of etching Boron-doped p-Si while alternatively SF_6 and C_4F_8 during the Bosch process in an ICP reactor. He found that trenches with a larger dimension had higher etch rates. This aspect ratio dependent phenomenon was due to RIE lag.   His experimental results with different feature dimensions (2 to 100 μm) for rectangles, squares, and circles suggested that the primary factor for RIE lag was the feature width. The area and line width ratio of features were secondary factors.[27]

In additional to experimentally examining etch results, performing computational simulations in 3-d has shown great potential in understanding etching phenomena.[28-31] For example, surface roughness formation is one of the major problems of the controlling process. Tsuda *et al.* developed a 3-d Monte Carlo-based simulation to predict the evolution of nanoscale roughness surface features with different ion injection energies and angles. Their model was tested through plasma etching experiments of blank Si substrates in Cl_2. The comparison results showed that their model was capable of reproducing the surface roughness at incident ion energy less than 250 eV. Surface roughening and rippling were found to depend on the angle of ion incidence θ_i. When $\theta_i = 0^o$ (normal incidence), concavo-convex features randomly formed on the surface. With θ_i increased to 45° (oblique incidence), ripple structures formed perpendicularly to the direction of ion incidence. When $\theta_i > 75^o$, smaller ripples or grooves formed parallel to the direction of incidence. The deviation from the experimental results when incident energy $\varepsilon_i >$ 250 eV suggested that the plasma surface mechanisms of Tsuda *et al.* could be improved through molecular dynamic simulations and experimental demonstrations.

Diagnostic techniques have been employed for process monitoring.[32-34] However, many of these techniques focus on etch end point detection, and there is limited capability for

monitoring in-situ profile evolution. 3-d kinetic Monte Carlo profile models with validation from experimental work provide a way to study the ion kinetics in combination with the geometric effects on feature profile evolution. In this chapter, results from a computational study of an inductively coupled plasma reactor for etching of 3-d high aspect ratio features are discussed. The computational model and chlorine etching mechanism were tested with experimental results. The consequences on profile evolution of IEADs and the mask properties are discussed. The 'U' and 'L' shapes were used to investigate over-etch effects on corner etching and ARDE. Circular vias with aspect ratios of up to 30 were also studied for understanding the influence of the RIE lag, mask, IEADs and fluxes. Typical plasma etching phenomena such as undercutting, bowing, and aspect radio dependent etching were observed in our 3-d simulations. A description of the computational models is in Sec. 7.2. Validation of the models is discussed in Sec. 7.3. Predicted profiles for investigating CD control in 3-d features are discussed in Sec. 7.4. Concluding remarks are in Sec. 7.5.

7.2 Description of Models

The Hybrid Plasma Equipment Model (HPEM) was used for reactor scale simulation, which has been previously discussed in detail in Chapter 2. As a hybrid model, the HPEM has a hierarchical structure in which different modules address different physical phenomena. The main modules used in this study are: the Electron Magnetic Module (EMM), the electron Monte Carlo Simulation (eMCS), the Fluid Kinetics Poisson Module (FKPM) and the Plasma Chemistry Monte Carlo Module (PCMCM). The EMM computes the electromagnetic fields generated by the coils. Those fields are then transported to the eMCS for calculating the electron impact rate coefficients and source functions. The FKPM calculates the densities, fluxes, and energies of the charged and neutral particles. With the densities of charged particles, Poisson's

equation is solved in FKPM for the electrostatic potential. When a steady state is reached, the PCMCM is launched to obtain energy and angular distributions of neutrals and charged particles incident onto the substrate.

The 3-dimensional Monte Carlo Feature Profile Model (MCFPM 3-d) was applied for feature scale simulation, and was described in Chapter 3. The model utilizes a rectilinear mesh in 3-d having a fine enough resolution to address the dimensions of features. Each cell within the mesh may represent a different solid material or a mixture of materials, marked with different color in the figures. The model launches pseudo-particles representing gas phase species with energy and angular distributions produced by the PCMCM in the HPEM. The pseudo-particles are statistically weighted to represent the fluxes of radicals and ions to the feature surfaces. During the Monte Carlo integration, the trajectories of ion and neutral pseudo-particles are tracked within the feature until they either react or leave the computational domain.

7.3   Model Validation

For the purpose of validating MCFPM 3-d, an experimental study with He/Cl$_2$ etching of Si was performed to compare with the simulation predictions. The experiments were conducted in a commercial Lam Research ICP reactor, the geometry of which is simplified and simulated with the reactor scaled simulator HPEM as shown in Fig. 7.1 a. The reactor was 52 cm in diameter with a five turn coil on the top of the reactor and was operated at 500 W at 15 MHz. A conductive Si wafer, 30 cm in diameter, sat in electrical contact with the substrate which was surrounded by a dielectric focus ring. The substrate was powered with 500 W at 15 MHz rf source and the temperature of the wafer was maintained at 40 $^{\circ}$C. The operational pressure was 10 mTorr with 100 sccm Cl$_2$ injected from the center nozzles and 50 sccm He injected from a side nozzle. The reaction mechanism for He/ Cl$_2$ used for the reactor scale model, HPEM, is

listed in Appendix A, which is based on Refs. [35,36]. The species in the mechanism are: Cl_2, Cl, Cl_2^+, Cl^+, Cl^-, Cl^*, He, $He(2^3S)$, $He(2^1S)$, $He(2^3P)$, $He(2^1P)$, $He(3s)$, $He(3p)$, He^+, and e. The reaction mechanism includes electron impact excitation and ionization, electron ion recombination, heavy particle mixing, Penning ionization, charge exchange, and 3-body dimer formation.

The reactor scale plasma density is shown in Fig. 7.1 b and c. The peak plasma density is $n_e = 8.6 \times 10^{10}$ cm^{-3}, which is sustained by a bulk electron temperature of $T_e = 1.6$ -1.8 eV. The inductively coupled coils provide the majority of power deposition to maintain the plasma density. The substrate bias delivers the majority of its power to the sheath region and contributes to the ion acceleration through the sheath. This explains the ions on the wafer with high energy and narrow angular distributions. Energy and angular distributions for Cl_2^+ (flux: 9.8×10^{15} $cm^{-2}s^{-1}$), Cl^+(1.0×10^{15} $cm^{-2}s^{-1}$), Cl (4.4×10^{17} $cm^{-2}s^{-1}$) and He^+ (6.6×10^{13} $cm^{-2}s^{-1}$) are then transferred to MCFPM 3-d to determine the initial condition of the pseudo-particles.

The test feature for this study is a set of long trenches, which are typically used for shallow trench isolation. The trench feature has a line/pitch ratio= 50/100 nm with 60 nm oxide mask and 60 nm nitride mask stacked on a thick silicon substrate. In the simulation, a 3-dimensional rectangular mesh with repeating boundary condition is set up according to the test chips. The simulated region (x × y × z) is 210 × 87.5 × 560 nm with constant mesh resolution in each dimension $\Delta x = \Delta y = \Delta z = 1.25$ nm.

The experimental measurements and computed feature profile evolution are shown in Fig. 7.2. The masks show erosion with increasing etch time, which can be seen in the measured SEMs as shown in Fig. 7.2 a and the simulated results of x-z plane as shown in Fig. 7.2 b. With the thickness of mask continuing to decrease, ions with large horizontal velocities will bombard

the sidewalls of the feature, and thus causes sidewall etching. After ions strike on the surface, there will be high energy neutrals reflecting back to the plasma and bombarding the surface again. This high energy particle reflection brings about the necking and bowing effect as observed in the third column of Fig. 7.2. There is a difference of necking and bowing positions between the experimental measurements and the predicted simulation results. This is mainly due to the absence of reactor scale measurements to validate the ion energy and angular distributions and flux ratios. Simulation results in Sec. 7.4 reveal that a slight change in angular distribution may contribute significantly to different shape evolutions.

Overall, this comparison of the profile evolution between the experiment and simulation indicate that the MCFPM 3-d is capable of predicting shape evolution due to ion surface reflection including the effect of profile surface evolution. One the other hand, the MCFPM 3-d does not precisely reproduce the positions of the necking and bowing effect, which suggests further experimental validation in the prediction of the IEADs and fluxes on the wafer or using measured IEADs and fluxes as inputs in the MCFPM 3-d.

7.4   Predicted profiles and discussion

The Ar/Cl_2 mixture is applied in this part of the study to etch Si over SiO_2 to investigate the influence of IEADs in 3-d pattern etching. The plasma etching was performed in the same reactor that is described in Sec. 7.3 with its geometry shown in Fig. 7.1 a. The total 200 sccm Ar/Cl_2 mixture was injected through the center nozzle. The plasma was sustained in a 20 mTorr, Ar/Cl_2=80/20 mixture powered at 800 W 15 MHz with an rf bias of 100 V 15 MHz on the substrate. The reaction mechanism for Ar/Cl_2 plasma used in the HPEM is discussed in Refs. [35-37]. The species in the mechanism were Ar, Ar ($1s_5$, $1s_3$) metastable, Ar ($1s_2$, $1s_4$) radiative, Ar (4p,5d), Ar^+, Cl_2, Cl_2^*, Cl_2^+, Cl, Cl^+, Cl^-, Cl^* and e. The IEDs of Cl_2^+, Ar^+ and total ions are

shown in Fig. 7.3, with the sum of each distribution normalized to 1. The IEDs for each species have a double peak shape. The IED of total ions has a multiple peak distribution due to an overlap of the IEDs of Cl_2^+, Cl^+ and Ar^+. As the flux of Cl_2^+ is 5-7 times larger than the other two, the IED of total ions is similar to the Cl_2^+ case with extra minor peaks contributed from the Ar^+.

The bias voltage amplitude is increased to 300 V and 600 V for obtaining different IEADs as shown in Fig. 7.3 b. With larger rf biases, the angular distribution of total ions becomes narrower and the energy distribution is significantly increased. The flux of the main species at different bias condition is listed in Table. 7.1. The additional power promotes Cl_2 dissociation and thus an increment in Cl flux is observed. The ionization energy of Ar (16 eV) is higher than the ionization energy of Cl (12.99 eV) and Cl_2 (11.47 eV), and therefore the Ar^+ flux is smaller than the other ion fluxes.[38] Electron impact ionization does not increase with the bias voltage as a slightly modulation of ion fluxes is observed.

Table 7.1. Total fluxes of the reactants on the wafer with rf bias voltage adjusted.

Species	Flux ($cm^{-2}s^{-1}$)		
	Bias 100 V	Bias 300 V	Bias 600 V
Cl	4.8×10^{17}	5.6×10^{17}	8.0×10^{17}
Cl_2^+	6.7×10^{15}	6.7×10^{15}	6.9×10^{15}
Cl^+	1.2×10^{15}	1.2×10^{15}	1.3×10^{15}
Ar^+	8.9×10^{14}	8.7×10^{14}	8.8×10^{14}

7.4.1   3-d Pattern Etching

The impact of different $IEAD_S$ on 3-d pattern etching was studied by using MCFPM 3-d with the energy and angular distributions in Fig. 7.3 b. The test pattern is a 'U' shape hardmask (mask does not react with any incident species) with Si film over a SiO_2 substrate as shown in Fig. 7.4 a. The total computational region is $114 \times 210 \times 150$ nm with mesh resolution $\Delta x = \Delta y = \Delta z = 1$ nm. The boundary conditions of the front, back, left, and right faces are assumed to be

periodic. This implies that when a particle leaves the computational domain through the left boundary it appears on the right side. When a particle reaches the top and bottom boundary, it is assumed to be inactive and removed from the calculation. The Si film is 180 nm thick and the width between the sides of the 'U' is 18 nm. Therefore, the aspect ratio is 10 for the middle trench between the legs of the mask.

When the feature is etched with the IEAD of 100 V bias, it takes 700 seconds for the outside silicon to be totally etched. The time sequential profile evolution is shown in Fig. 7.4 c. In the beginning of the etching process, T=70 s, the etch rates inside and outside of the 'U' are close to each other. As the etching process proceeds, etch rates begin to differ, with higher rates outside the 'U' than inside. With the periodic boundary conditions, the four corners have a large area exposed to the plasma and fastest etch rate, due to the loading effect. Another 3-d effect due to the mask pattern is that the left and right side boundaries are concave. In contrast, the front side etch has a uniform etch front. Because the Cl-based RIE is angular dependent and has the fastest etch rate at 60°, the Si film is found to form slopes and result in a V-shape etch front inside the 'U' shape.

In order to etch out the inner Si film, at least 25% over-etch is needed. The feature profile with total 892 s etch time is shown in Fig. 7.4 b. From the cross section views in the middle and right, several phenomena occur. The film under the mask experience is undercut due to Cl spontaneous etching. The left and right sidewalls (marked as T_1 and T_2) of the middle trench are bowed due to energetic particle reflections. Because of the mask layout, the Cl radical is shadowed and has difficulty in reaching the corner of the 'U'. Therefore, the back sidewall (marked as T_3) has a tapered shape (i.e. inability to clear inner corners).

Since transistors or MEMS structures may be rotationally layout within a die, rotation of the pattern was investigated. The 'U' shape mask with the same dimension was rotated at 90°. The original pattern refers to the previously discussed 'U' shape etch results, which has the opening that aligns with the x axis. The rotated pattern refers to the mask opening that aligns with the y axis as shown in Fig. 7.5. Since particles are launched with azimuthally symmetric angular distribution, their horizontal velocities are uniform. The profile evolution is found to be almost independent of its orientation. Only a slight difference is observed on the shape of the sidewalls. The inner corner may be better cleaned with the rotated pattern due to the randomness of the Monte Carlo simulation.

When the ion angular distributions are twisted $\pm 3^o$ along the y axis, the IEADs become asymmetric. The 'U' pattern etching process then has an orientation dependent effect as shown in Fig. 7.6. When ion fluxes are injected slightly towards the left and right, the two long sidewalls are no longer perpendicular to the substrate. Instead, they have a significant slope etch as they experience more obliquely incident ion bombardment. This can be seen in the original pattern case from a vertical view or rear view. When the pattern is rotated at 90° aligned with the x axis, the back and front sides experience more direct ion trajectories and become slanted. The side view of the long sidewall shows this effect. The slope of the leaning sidewalls directly depends on the degree of angle asymmetry and direction. With a larger angular asymmetry or etching a higher aspect ratio feature, the sidewall may be etched though. These predicted feature profiles reveal the importance of reducing the oblique incident ions on the edge of the wafer.

The profiles etched with high energy distributions (bias increases from 100 V to 300, 600 V) are summarized in Fig. 7.7. A faster ion etch rate is obtained in the 600 V case. Since ion activation scales as $(\varepsilon_{ion} - \varepsilon_{th})^{1/2}$. Therefore, the etch rate of the 600 V bias case is about 29%

faster than the 300 V bias case. A comparison of the etched profiles of the 300 V and 600 V cases are shown in Fig. 7.7 c,d with the base 100 V case shown in Fig. 7.4 b. The profiles with high energy ion bombardment have less bowing and undercut, with their corners exhibiting a tapering effect. These improvements are a result of three factors. First, the IEADs in Fig. 7.7 a,b show that the 300 V and 600 V cases not only have higher energy, but also have narrower angular distributions. These narrower angular distributions effectively reduce ion sidewall reflection and thus inhibit the bowing effect. Second, the inner corners are better cleaned with high etch yield and fast etch rate due to higher energy ions. Third, since the total etch time and over-etch time are both reduced, the undercut of the mask caused by the Cl spontaneous etching of Si is suppressed.

7.4.2   Aspect Ratio Dependent Etching

The etch rate inside the 'U' shape shows a loading effect, a phenomenon of the aspect ratio depending etching (ARDE). When a feature becomes deeper, the etching species encounters a transport limit to reach the feature bottoms. With a small plasma view angle in the deep bottom of features, the neutrals are shadowed and while lead to a slow etch rate. In this part of the study, a hardmask with an 'L' shape trench was used to study the influence of the right angle corner etching and the loading effect with different feature layouts and etching gas mixture. The mask is 18 nm thick, with its longer and shorter sides measuring 90 nm and 66 nm. The trench has a 12 nm opening and the underlying Si film has a thickness of 150 nm. Therefore, the trench has an aspect ratio of 12.5. The entire computational region is $138 \times 138 \times 180$ nm with 1 nm mesh resolution. The etching condition is kept the same as the 'U' pattern base case: IEAD with 100 V bias in 20 mTorr, Ar/Cl_2=80/20, 200 sccm. Similar to the 'U' pattern case, the etch rate within the trench is smaller than the outside. Because the aspect ratio of the 'L' trench is higher, the

ARDE is much more significant. Even with 34% over-etch time, the trench bottom in Fig. 7.8 d is not cleaned. However, the sidewalls are close to collapsing due to the Cl spontaneous etching. Since the L pattern is diagonally symmetric, the left and back cross sections show similar concave etch front within the trench as shown in the middle and right columns of Fig. 7.8. This is also caused by the loading effect as the corner and ends of trenches have larger areas exposed to the plasma.

Using the same mask geometry and mesh dimensions, etching SiO_2 over Si was performed with $Ar/CF_4/O_2$ to investigate the ARDE with a passivating gas mixture. The operating conditions and reaction mechanism were described in Sec. 6. 3 with the IEADs with no phase shifting ($\Delta\phi_{30}$ =0) as plotted in Fig. 6. 10. With the addition of the passivating gas, polymer formation occurs on the surface. More polymers are found to deposit on the top and outside sidewall surfaces due to shadowing of the neutral particles. This passivation layer protects the sidewalls from the fluorine spontaneous etching and provides the reactants for removal of O from SiO_2, as shown in Fig. 7.9. Besides the high etch yield, grass-like residues and rough surface are observed in the $Ar/CF_4/O_2$ case as results of incomplete removal of the passivation components. On the other hand, there is more passivation in the outside of the 'L' trench than the inside of the trench, thereby balancing the etch rate differently and reducing the ARDE.

7.4.3   Circular Via Etching

ARDE appears in many etching processes. Etch rate depends on the mask opening area. Vias with a circular hole is one of the most common features used for many processes such as through-silicon-via and memory arrays. The MCFPM 3-d predicts ARDE, slow etch rate with small mask opening as shown in Fig. 7.10. The test feature has 3 aligned circular holes with 120

nm spacing. The diameter of the holes are 120, 180, and 240 nm with AR = 11.7, 7.8, and 5.8, respectively. With a higher aspect ratio, the left via has the slowest etch rate with undercut forming at 2330 s etch time. Since the undercut is only observed in the highest aspect ratio via case, it may be caused by the energetic particle reflected by the mask boundary instead of by spontaneous etching. The circular mask shape produces a 3-d ion reflection effect that enhances the undercut.

In order to verify this hypothesis, two circular vias with same aspect ratio (AR = 10), but different mask thickness were simulated. The mesh resolutions, mask dimension, and etching condition are kept the same. The circular via with 60 nm thick mask starts to form undercut at etch time = 1058 s as shown in Fig. 7.11 a. When the mask thickness increases to 120 nm (see Fig. 7.11 b), the undercut is reduced. Although the increased mask thickness to shadow neutrals with a slightly slow etch rate, the thick mask via has a better vertical sidewall slope than the thin mask case.

In many etching processes, masks can be sputtered by high energy particle bombardment and cause mask erosion. The via profile evolution of 60 nm thick mask with considerable mask erosion is shown in Fig. 7.12. With the mask thickness reduced during the etching process, the undercut becomes more significant and the position of ion reflection from the mask to the sidewalls changes. This reflection position shifting produces a bowing shape below the mask. A comparison of etched profiles with different mask thickness (60/ 180 nm) and materials (hardmask/ erosion mask) is in Fig. 7.12 b. This comparison points to the fact that mask properties are critical for high aspect ratio via etching. The thickness and slope of the mask interrupt the trajectories of incident particles. A non-optimized mask may cause side effects

such as bowing and undercut. Compared with the long trench features, circular feature etching needs to be addressed in 3-d, which can predict the 3-d particle reflection effect precisely.

Feature CDs controlling become extreme challenging when via aspect ratio increasing. Predicted results of etching high aspect ratio via (AR=30) with energy angular distributions (plotted in Fig. 7.3 b) and their fluxes (listed in Table. 1) with bias voltages = 100/ 300/ 600 V are shown in Fig. 7.13 b-d. The simulated profile has dimensions of 100 x 100 x 1380 nm with mesh resolution of 1 nm. The circular hole has a diameter of 40 nm with 150 nm thick hardmask. With low incident ion energies, the 100 (see Fig. 7.13 b) and 300 V (see Fig. 7.13 c) cases show significant bowing effect and unable to etch through the Si film. This bowing effect may come from the long life time of Cl atom. Since the ion energies are low, the etch yield of the etch front are small. The Cl atom can be reflected from the surface and cause sidewall spontaneous etching after thousands of reflections. Although the 600 V case etches through the Si film, its profile has significant undercut under the mask and bowing in the middle of the feature. We find that adjusting the fluxes can help improving feature critical dimensions. An example of profile etched with different flux is shown in Fig. 7. 13 e. By reducing the flux of Cl atoms from 8×10^{17} to 6×10^{17} cm^{-2}s^{-1} with all other operating condition same as the 600 V bias case, the undercut is reduced as shown in Fig. 7.13 e. An increment in etch rate is also observed due to the increased flux ratio between ions and neutrals. Because the pseudo-particles are statistically weighted to represent the fluxes of radicals and ions to the surface, the reduced Cl flux case has more ion particles with same amount of particles in simulations.

7.5   Concluding Remarks

The influences of ion kinetics and feature geometries have been investigated by developing a 3-d Monte Carlo Feature Profile Model, MCFPM 3-d. The profile model addresses

reaction mechanisms resulting in etching, sputtering, and deposition on the surface to predict profile evolution based on the fluxes of neutrals and charged particles provided by a reactor scale simulator, HPEM. The physics of the MCFPM 3-d was validated by comparing with experimental SEM results of silicon trench etching with He/Cl_2 plasma.

Etching of 3-d structures typically requires long over-etch time to clear corners and then places additional challenges on selectivity to maintain the feature CD. For understanding feature corner etching, 20 mTorr Ar/Cl_2 plasma sustained in an inductively coupled plasma reactor was used for Si over SiO_2 etching. The profiles obtained from the MCFPM 3-d suggest that etch profile defects such as bowing and tapering can be overcome through precisely controlling the IEADs. Ions with higher energy and narrower angular distribution are able to clear corners with short over-etch and subsequently reduce the Cl spontaneous etch on the sidewall. When the feature aspect ratio is increased, control of the ion angular distributions becomes important. The computed profiles with asymmetric incident ions are found to lie obliquely with their sidewall slope depending on the asymmetric direction.

The aspect ratio dependent etching occurs in many deep silicon etching processes and has many undesired complications in device fabrication. The simulated profile evolution results demonstrate that the MCFPM 3-d is capable of predicting the shadowing effect and transport limits in different features. In general, with a small plasma view angle, etching species experience a transport limitation in reaching the feature bottoms leading to a slower etch rate. The addition of passivation gases is found to balance the etch rate difference between features with different plasma view angles.

In simulating circular vias with different mask opening radii, the small mask opening results in a slow etch rate. The circular shape of mask is found to enhance ion reflection on the

213

surface. This 3-d reflection effect causes a worse undercut than typical trench etching. When the mask is sputtered by high energy particles, the ion reflection position shifts and results in a bowing shape under the mask. Controlling ion energy angular distributions and fluxes of incident species are important for high aspect ratio via etching. With low energy and broad angular distributions, etch profiles show significant bowing effect and unable to reach the bottom substrates. The undercut and etch rate can be improved by increasing ions neutrals flux ratio. The critical dimension of vias can be improved by changing its mask material, mask thickness, incident ion energy and angular distribution, and incident fluxes.
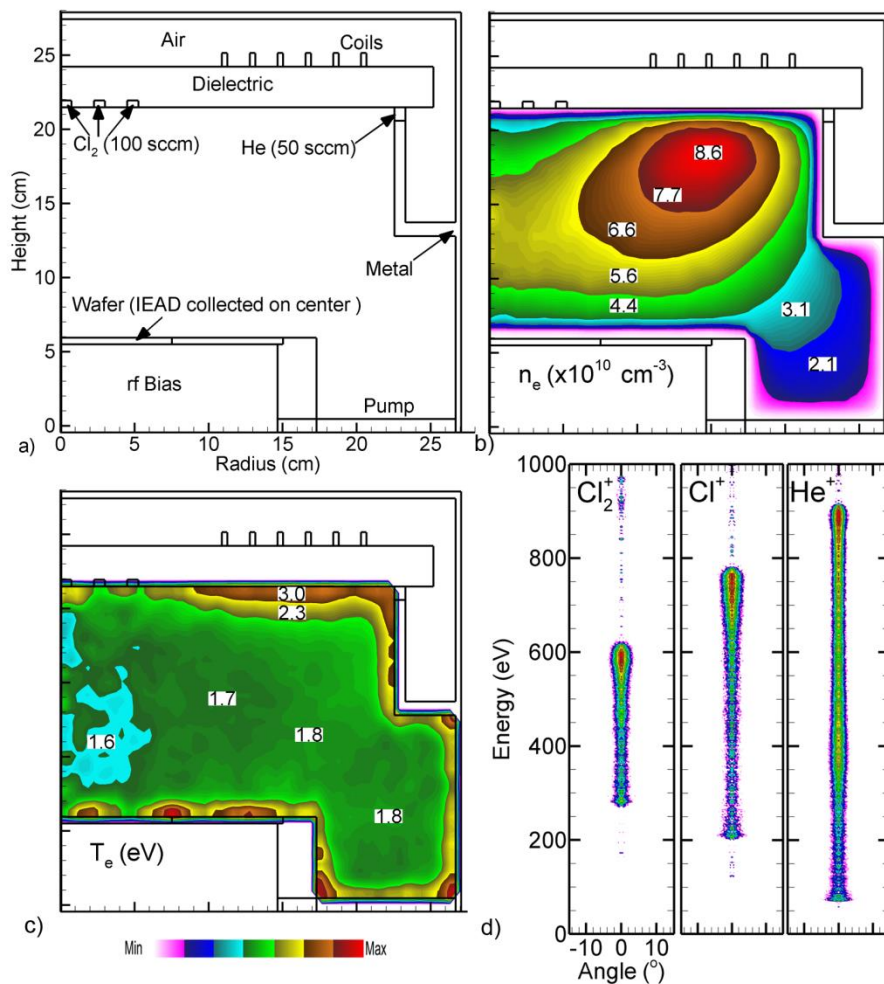
Fig. 7.1. Properties of the inductively coupled plasmas at 10 mTorr, with 100 sccm Cl_2 injection through center nozzle and 50 sccm He injection through side nozzle. The coils are powered with 500 W 15 MHz rf source and electrode is biased with 500 V 15 MHz rf source. a) Schematic of the reactor. Properties of He/Cl_2 plasmas showing b) time averaged electron density with a maximum of 8.6×10^{10} cm^{-3} with c) time averaged 1.6-1.8 eV electron temperature, and d) the ion energy angular distributions collected on wafer center and separately normalized at each species.
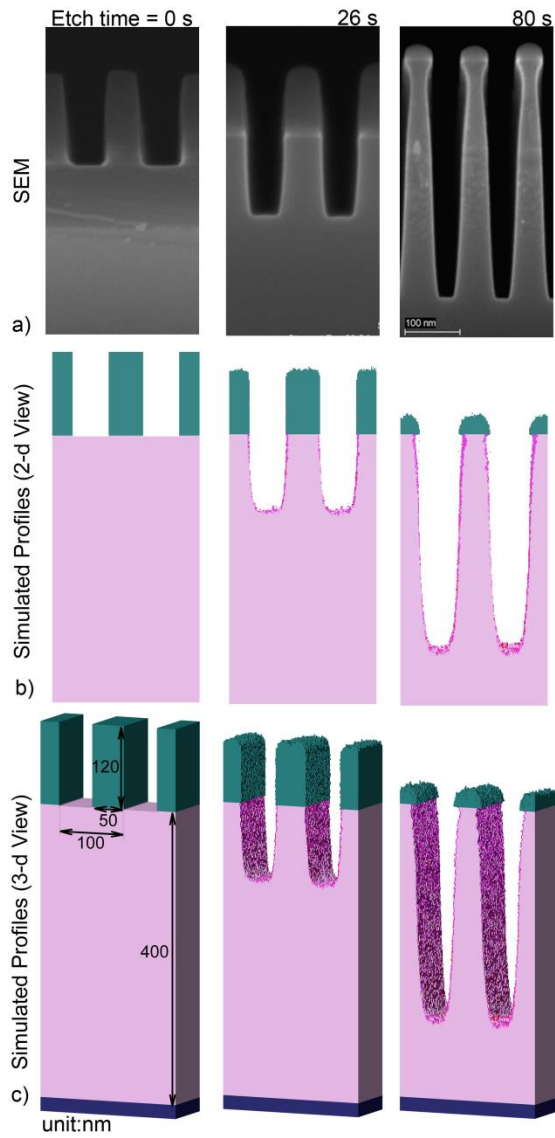
Fig. 7.2. Feature profiles with 10 mTorr He/Cl$_2$ mixture at etch time = 0, 26 and 80 second. a) SEM measured, b) Simulated profiles on x-z plane, and d) 3-d simulated profiles with z axis rotate 45$^\text{o}$.
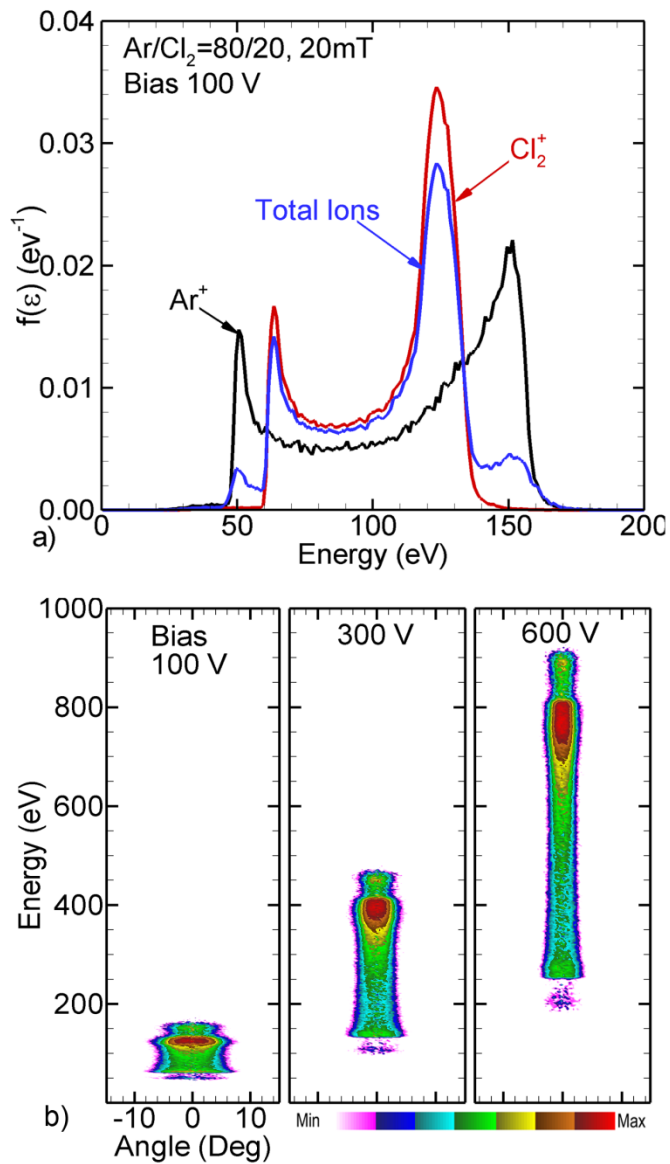
Fig. 7.3. HPEM computed properties of ions a) Ion energy distributions for Ar^+, Cl_2^+ and total ions incident onto the wafer for the base case ($Ar/Cl_2=80/20$, 20 mTorr, 200 sccm, 15 MHz coil power = 800 W and 100 V 15 MHz rf bias). b) Time averaged ion energy and angular distributions for total ions for rf bias = 100/ 300/ 600 V.
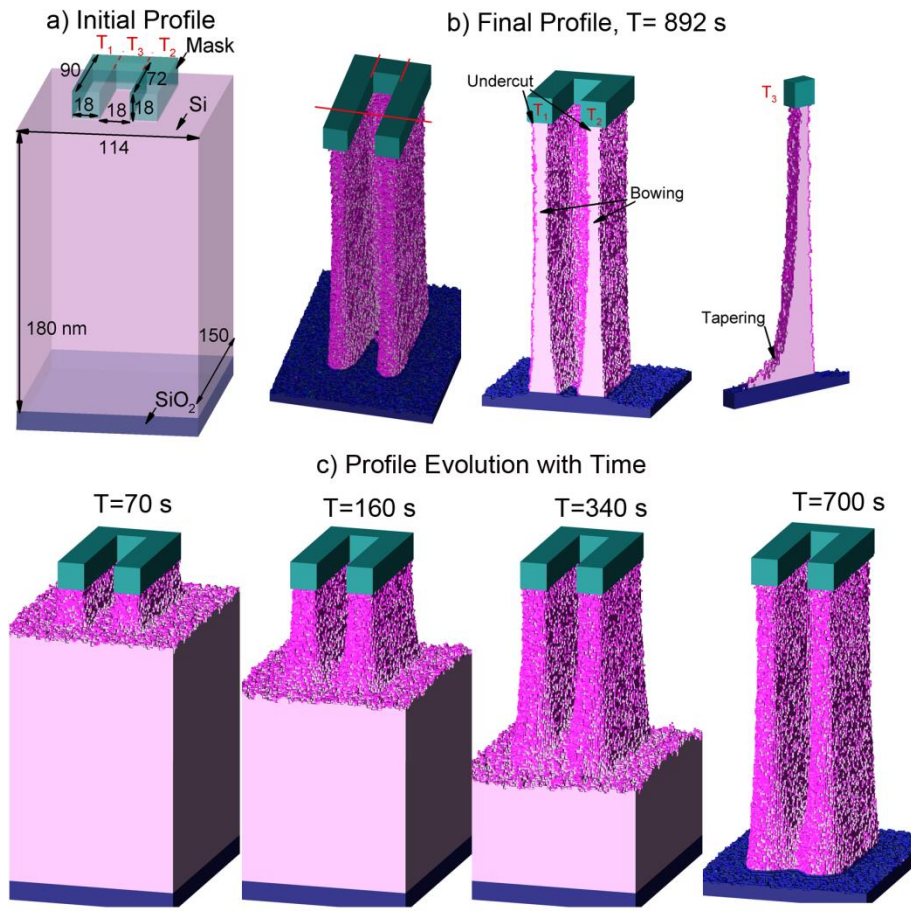
Fig. 7.4. MCFPM 3-d predicted profile evolution for Ar/Cl$_2$ etching Si film (pink) with hardmask (green) and SiO$_2$ substrate (navy) under the base case conditions (Ar Cl$_2$=80/20, 20 mTorr, 200 sccm, 15 MHz coil power = 800 W and 100 V 15 MHz rf bias) a) Initial profile after hardmask opening. b) Final feature profiles with 893 s etch time. Vertical view of entire feature (left), from middle cross section of paralleled trenches T$_1$ and T$_2$ (middle) and cross section of the center short trench T$_3$ (right). c) Profile evolution from etch time =70 s to 700 s.
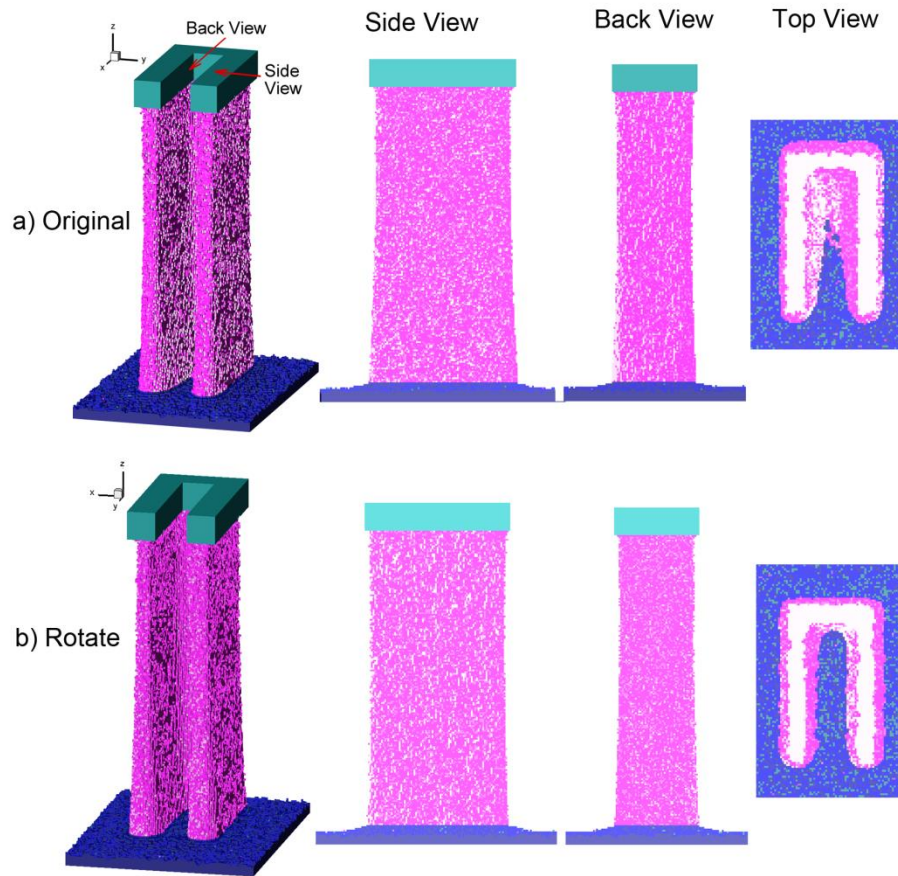
Fig. 7.5. Ar/Cl$_2$ etching Si film (pink) with hardmask (green) and SiO$_2$ substrate (navy). Profiles with base case fluxes (Ar Cl$_2$=80/20, 20 mTorr, 200 sccm, 15 MHz coil power = 800 W and 100 V 15 MHz rf bias) a) original layout with 'U' pattern along x axis b) rotated layout with u pattern along y axis.
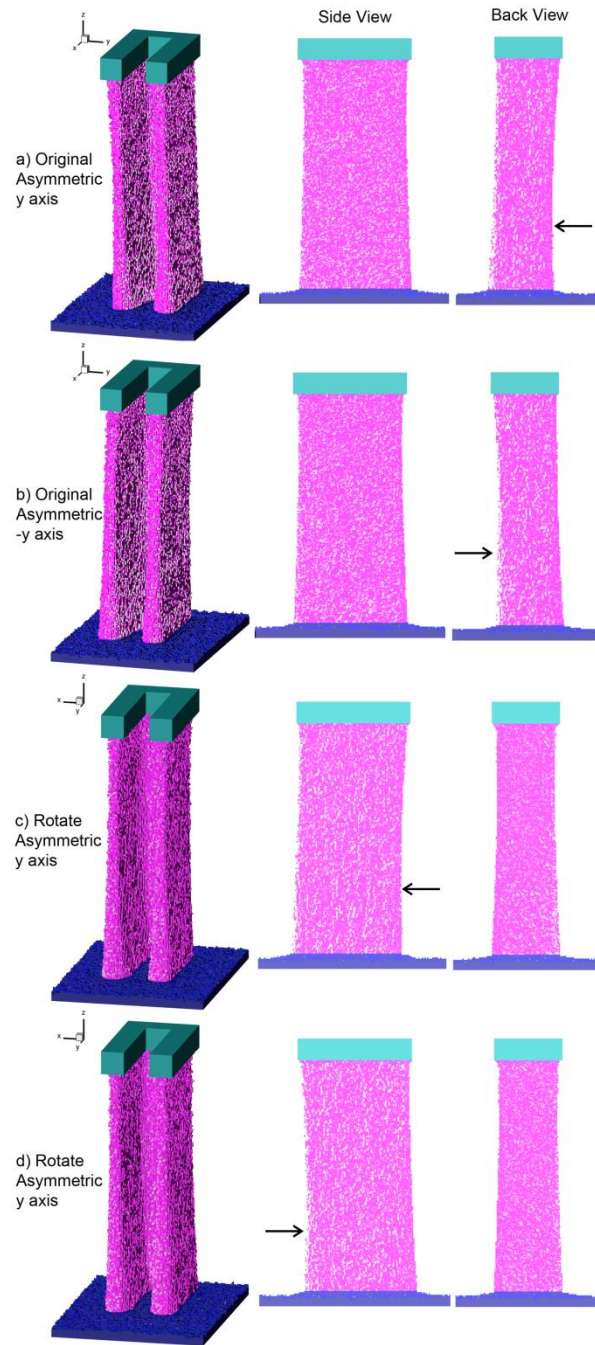
Fig. 7.6. Ar/Cl$_2$ etching Si film (pink) with hardmask (green) and SiO$_2$ substrate (navy). Profiles with 3° asymmetric ion angular distribution (IAD) for the base case (Ar Cl$_2$=80/20, 20 mTorr, 200 sccm, 15 MHz coil power = 800 W and 100 V 15 MHz rf bias). a) Original layout with U pattern along x axis and IAD 3° twist along y axis. b) Original layout with IAD 3° twist along -y axis. c) Rotational layout with IAD 3° twist along y axis, d) rotational layout with IAD 3° twist along -y axis.
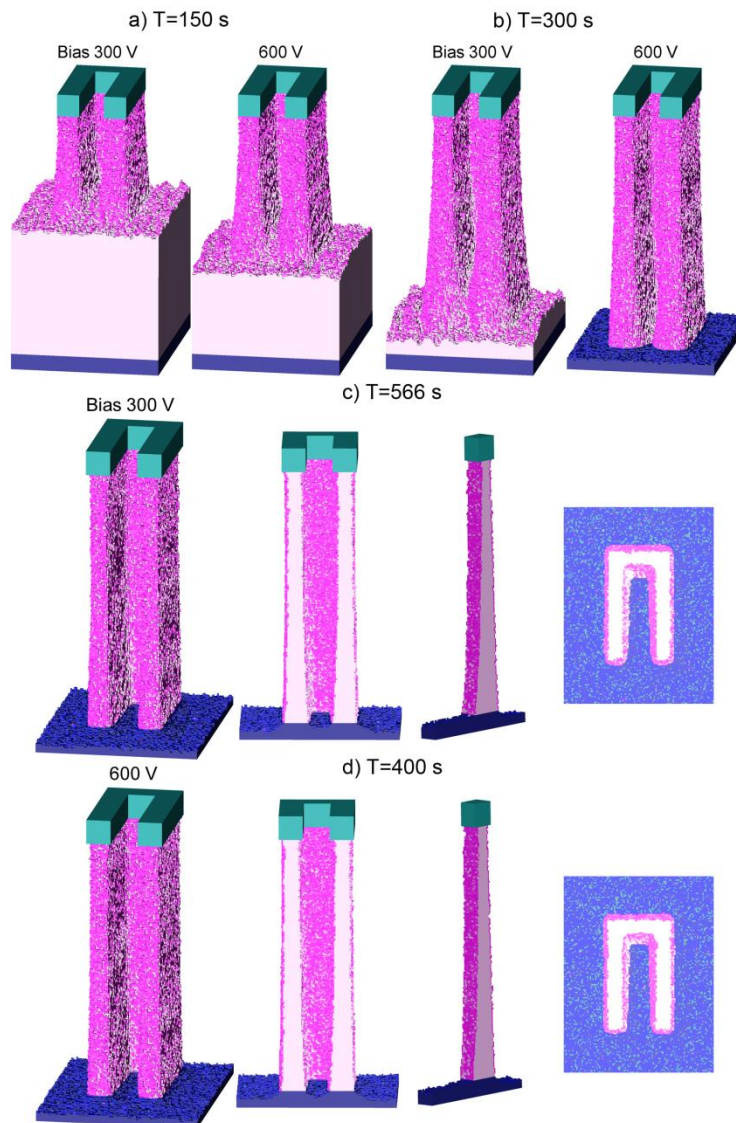
Fig. 7.7. Ar/Cl$_2$ etching Si film (pink) with hardmask (green) and SiO$_2$ substrate (navy). Profiles with 300 V bias and 600 V bias at etch time: a)150s and b) 300s. The etch rate of the 600 V bias case is much faster than the 300 V case as the ion assisted anisotropic etch yield scale with $\varepsilon_{ion}^{1/2}$. 20 % over-etch profiles with c) bias = 300 V IEDs and d) bias = 600 V.
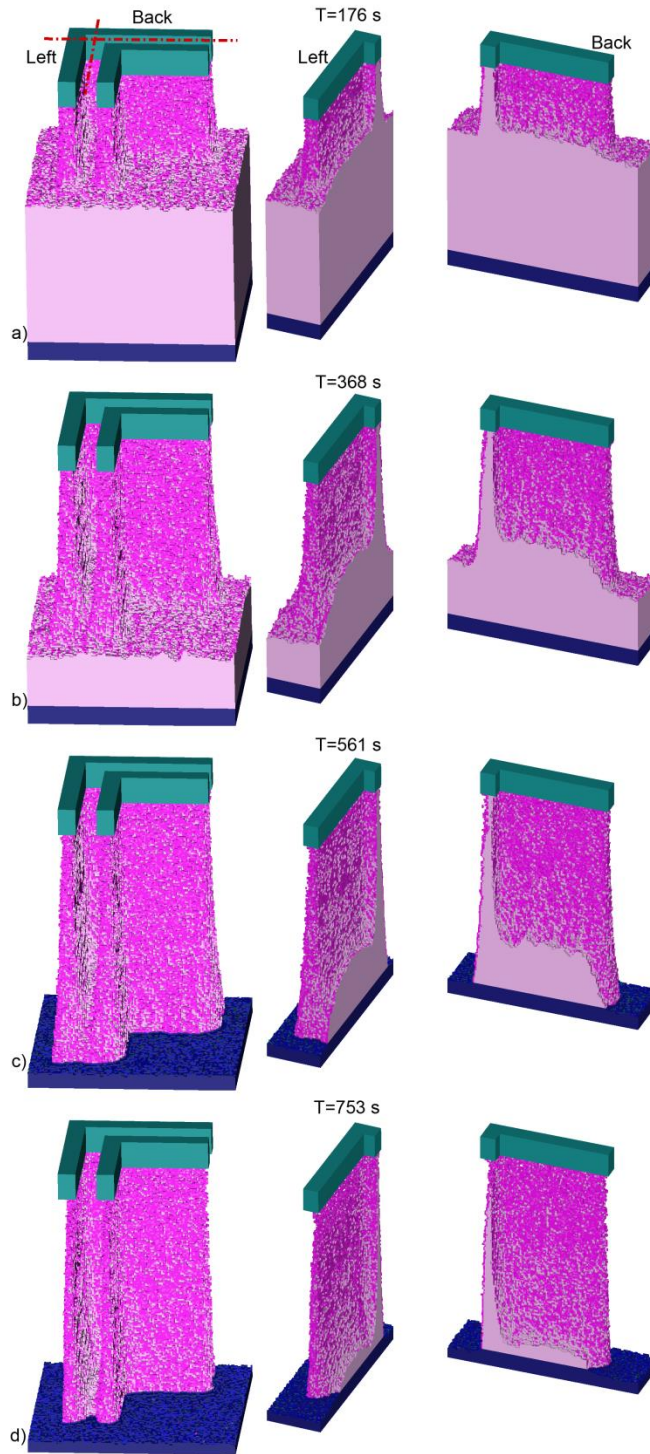
Fig. 7.8. Ar/Cl$_2$ etching Si film (pink) with hardmask(green) and SiO$_2$ substrate (navy). Time sequence profiles with the base case conditions (Ar Cl$_2$=80/20, 20 mTorr, 200 sccm, 15 MHz coil power = 800 W and 100 V 15 MHz rf bias) at etch time= a)176 s, b)338 s, c)561 s and d)753 s. Cross sections of left trench (middle column) and back trench (right column) shows the loading effect.
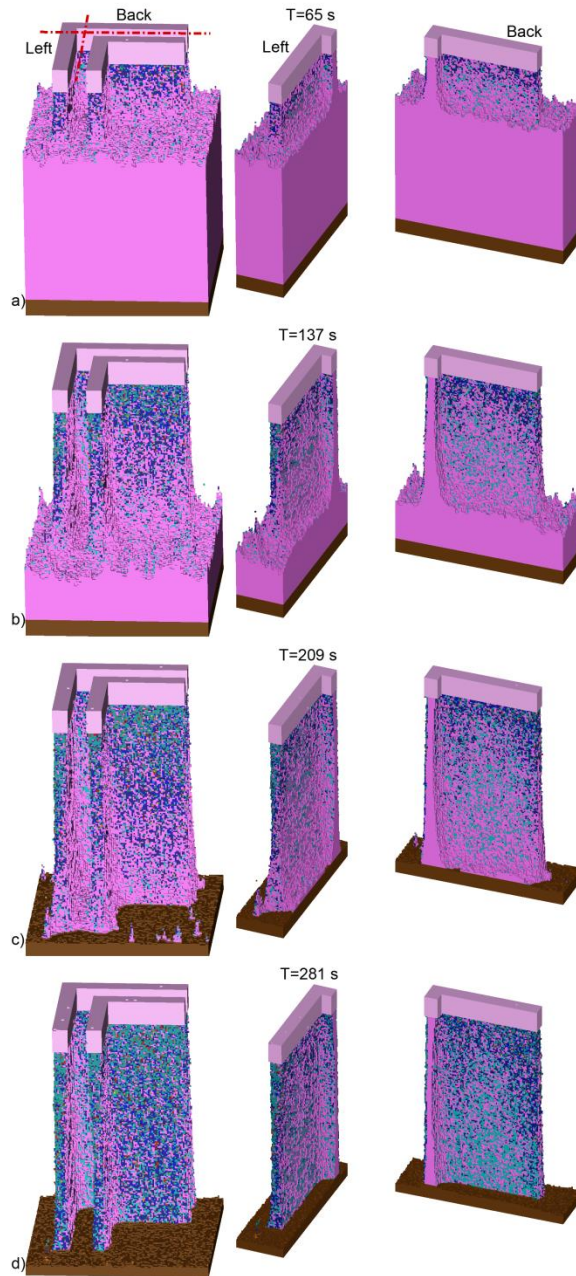
Fig. 7.9. Ar/CF$_4$/O$_2$ etching SiO$_2$ film (pink) with hardmask (light pink) and Si substrate (brown). Time sequence profiles with operating conditions (Ar/ CF$_4$/ O$_2$=75/20/5, 20 mTorr, 50 sccm, DF-CCPs with 150 V 15 MHz + 150 V 30 MHz on the bottom electrode) at etch time = a)65s, b)137 s, c)209 s and d)753s. The passivation gas mixture balances the etch rate difference.
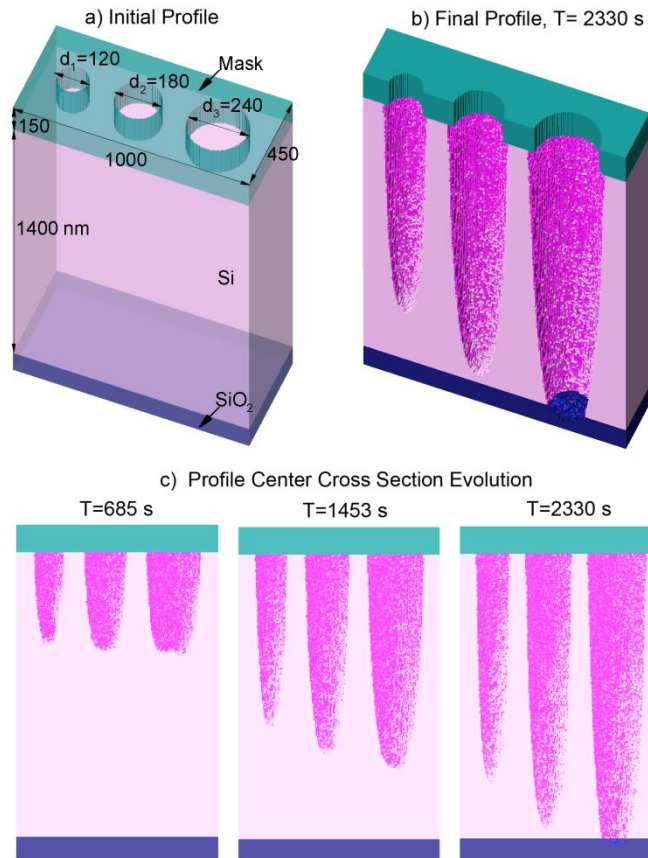
Fig. 7.10. Ar/Cl$_2$ etching Si vias (pink) with hardmask (green) and SiO$_2$ substrate (navy). The vias diameters = 120, 180 and 240 nm from left to right. a) Initial profile with mask opening, b)Vertical view of center cross section profile at etch time = 2330 s. c) Time sequential profile at center cross section.
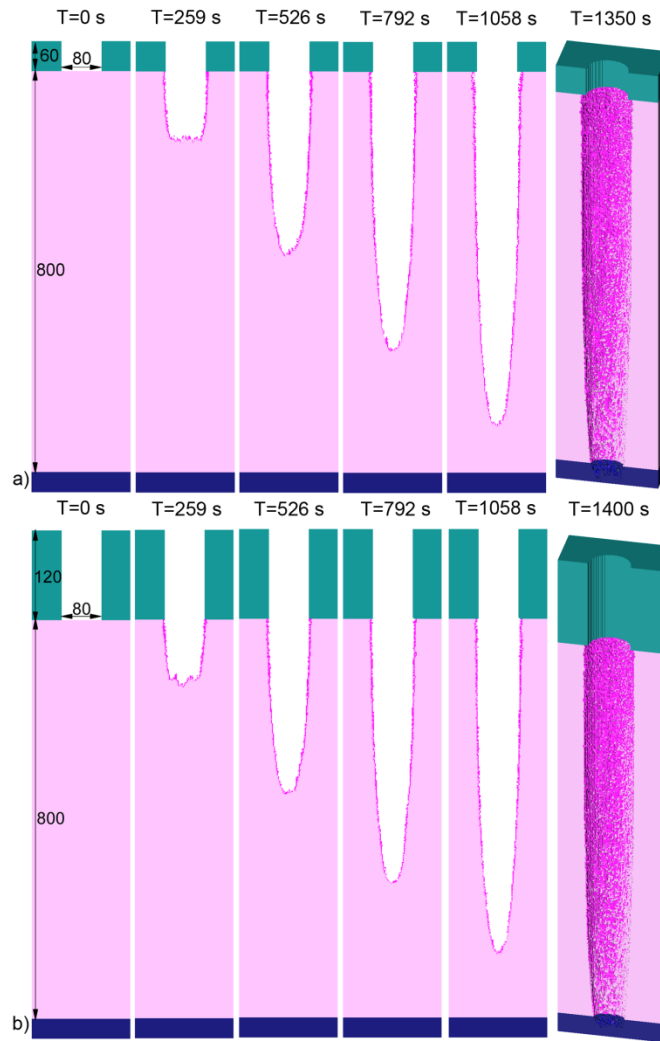
Fig. 7.11. Time sequential profiles of Ar/Cl$_2$ etching Si via with 60 nm thick hardmask and b) 180 nm thick hardmask for operating conditions (Ar/Cl$_2$=80/20, 20 mTorr, 200 sccm, 15 MHz coil power = 800 W and 600 V 15 MHz rf bias). The thicker mask brings an improvement in reducing the undercutting under the mask.
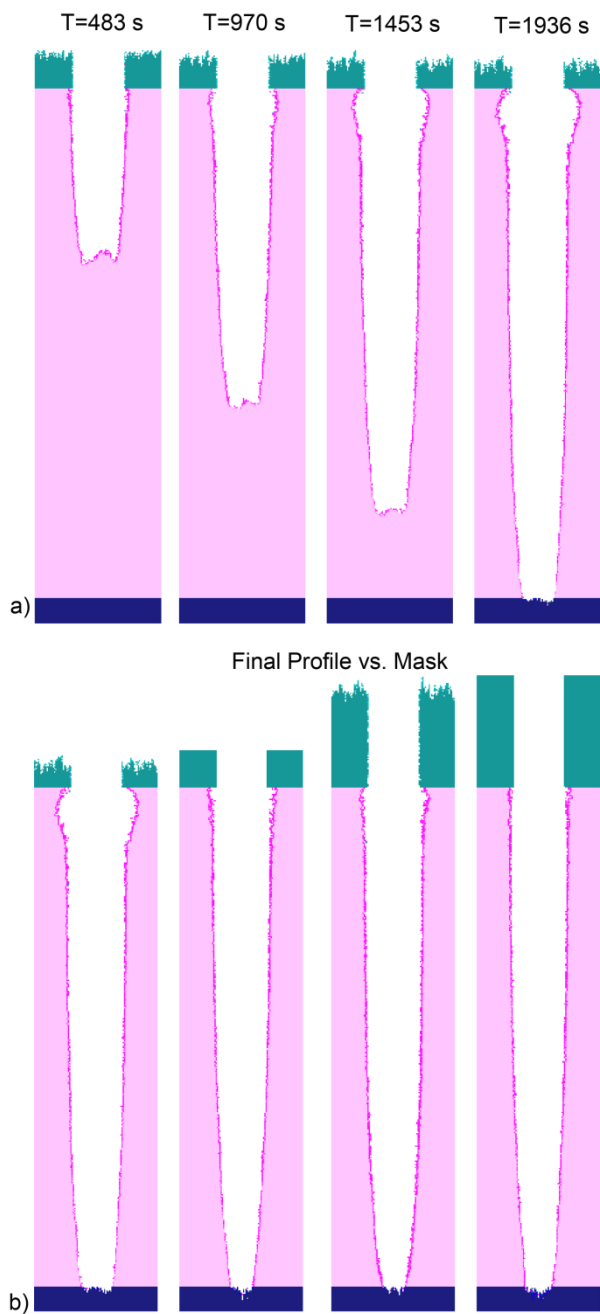
Fig. 7.12. Influence of profile with changing mask thickness and erosion for operating conditions (Ar/Cl$_2$=80/20, 20 mTorr, 200 sccm, 15 MHz coil power = 800 W and 600 V 15 MHz rf bias). a) Time sequential profiles of Ar/Cl$_2$ etching Si via with 60 nm thick mask considering mask erosion. b) 20% over etch profiles with 60 nm erosional mask, 60 nm hardmask, 180 nm erosional mask and 180 nm hardmask from left to right.
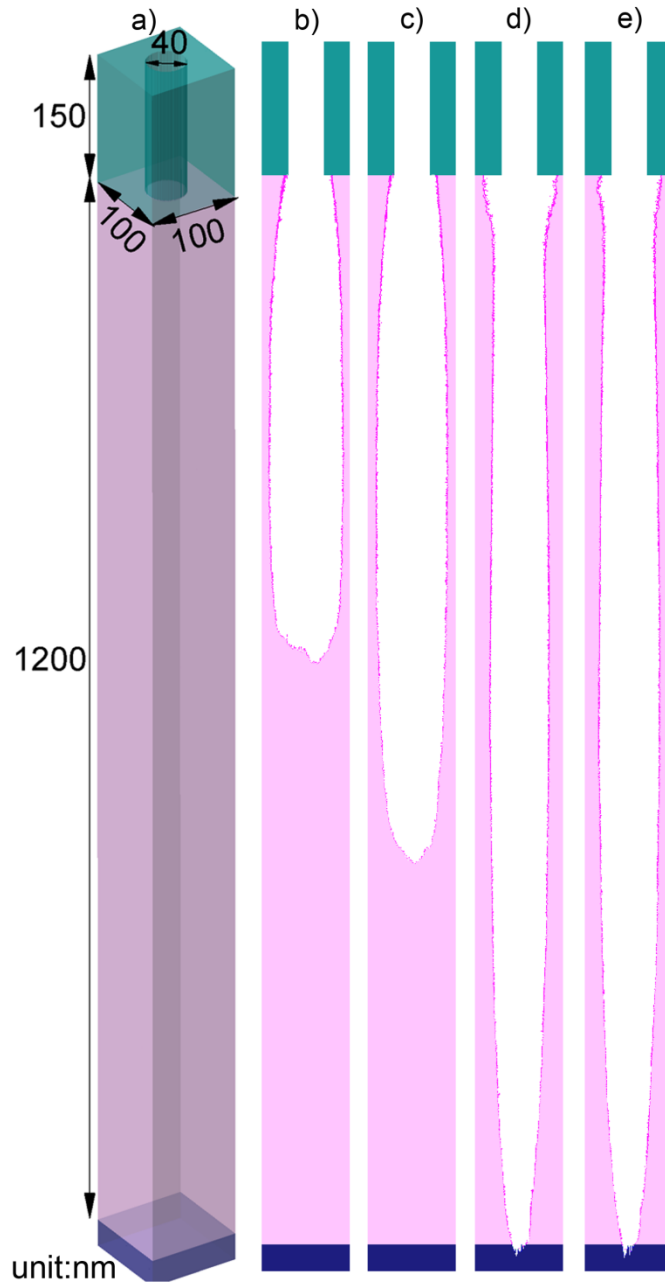
Fig. 7.13. Influence of high aspect ratio via profile with changing ion energy and flux ratios for operating conditions (Ar/Cl$_2$=80/20, 20 mTorr, 200 sccm, 15 MHz coil power = 800 W and 15 MHz rf bias) a) via has a 40 nm diameter with 150 nm thick hardmask and 1200 nm silicon film, AR=30. b) 100 V rf bias voltage, c)300V rf bias voltage, d) 600 V rf bias voltage and e) 600 V rf bias voltage with Cl flux decrease 25% (6×10^{17} cm^{-2}s^{-1}) .

7.7   References

1. H-D. Ngo, A. Hiess, V. Seidemann, D. Studzinski, M. Lange, J. Leib, D. Shariff, H. Ashraf, M. Steel, Li Atabo, J. Reast, Journal of Physics: Conference Series **34**, 271 (2006).
2. S K. Tolpygo and D. Amparo, Journal of Physics: Conference Series **97**, 012227 (2008).
3. S. F. Yoon, Microelectronic Engineering. **14**, 23(1991).
4. I. W. Rangelow, J. Vac. Sci. Technol. A **21**, 1550 (2003).
5. D. E. Hanson, A. F. Voter and J. D. Kress, J. Appl. Phys. **82**, 3553 (1997).
6. S. Ohki, M. Oda, H. Akiya, and T. Shibata, J. Vac. Sci. Technol. B **5**, 1611 (1987).
7. J. P. Chang, A. P. Mahorowala, H. H. Sawin, J. Vac. Sci. Technol. A **16**, 217 (1998).
8. J. Matsui, N. Nakano, Z. L. Petrovic, and T. Makabe, Appl. Phys. Lett. **78**, 883 (2001).
9. T. Ohmori, T.K. Goto, T. Kitajima, T. Makabe, Appl. Phys. Lett. **83**, 4637 (2003).
10. A. P. Mahorowala and H. H. Sawin, J. Vac. Sci. Technol. B **20**, 1084 (2002).
11. J. Yeom, Y. Wu, J. C. Selby, and M. A. Shannon, J. Vac. Sci. Technol. B **23**, 2319 (2005).
12. B. Wu, A. Kumar and S. Pamarthy, J. Appl. Phys. **108**, 051101 (2010).
13. C. J. Mogab, Journal of the Electrochemical Society. **124**, 1262 (1977).
14. V. M. Donnelly and A. Kornblit, J. Vac. Sci. Technol. A **31**, 050825 (2013).
15. M. Puech, J. M. Thevenoud, J. M. Gruffat, N. Launay, N. Arnal, and P. Godinat, "*Fabrication of 3D packaging TSV using DRIE*" In Design, Test, Integration and Packaging of MEMS/MOEMS 2008. Symposium on, pp 109-114. IEEE. (2008).
16. A. D. Baily III, M. C. M. van de Sanden, J. A. Gregus, and R. A. Gottscho, J. Vac. Sci. Technol. B **13**, 92 (1995).
17. W. -C. Tian, J. W. Weigold, and S. W. Pang, J. Vac. Sci. Technol. B **18** 1890 (2000).
18. I. W. Rangelow and H. Loschner, J. Vac. Sci. Technol. B **13** 2394 (1995).
19. H. Janse, H. Gardeniers, M. de Boer, M. Elwenspoek and J. Fluitman, J. Micromech. Microeng. 6 14 (1996).
20. R. D'Agostino, et al. J. Appl. Phys. **52** 1259 (1981).
21. S. Panda, D. J. Economou and L. Chen, J. Vac. Sci. Technol. A. **19**, 398 (2001).
22. J. W. Coburn and H. F. Winters, Appl. Phys. Lett. **55**, 2730 (1989).
23. S. A. Vitale, H. Chae, and H. H. Sawin, J. Vac. Sci. Technol. A **19**, 2197 (2001).
24. D. E. Hanson, J. D. Kress and A. F. Voter, J. Vac. Sci. Technol. A **17**, 1510 (1999).
25. M. E. Barone and D. B. Graves, J. Appl. Phys. **78**, 6604 (1995).
26. J. K. Kim, S. H. Lee, S. I. Cho and G. Y. Yeom, J. Vac. Sci. Technol. A **33**, 021303(2015).
27. C-K. Chung, J. Micromech. Microeng. **14**, 656 (2004)
28. H. Tsuda, N. Nakazaki, Y. Takao, K. Eriguchi and K. Ono, J. Vac. Sci. Technol. B **32**, 031212 (2014).
29. W. Guo and H. H. Sawin, J. Phys. D: Appl. Phys. **42**, 194014 (2009).
30. M. Fujinaga and N. Kotani, Electron Devices, IEEE Transactions on. **44**, 226 (1997).
31. P. Moroz and D. J. Moroz, J. Phys.: Conf. Ser. **550**, 012030 (2014).
32. J. P. Booth, Plasma Sources Sci. Technol. **8** 249 (1999).
33. F. H. Bell, O. Joubert and L. Vallier, J. Vac. Sci. Technol. B **14**, 1796 (1996).
34. M. Hübner, S. Zimmermann, S. E. Schulz, W. Buchholtz, J. Röpcke, and J. H. van Helden, Appl. Phys. Lett. **106**, 031102 (2015).
35. P. Tian and M. J. Kushner, "*Controlling VUV Photon Fluxes in Pulsed Inductively Coupled Plasmas*", unpublished paper.
36. P. Subramonium and M. J. Kushner, J. Vac. Sci. Technol. A **20**, 325 (2002).

37. P. Subramonium and M. J. Kushner, J. Vac. Sci. Technol. A **20**, 313 (2002).
38. R. Basner and K. Becker, New J. Phys. **6**, 118 (2004).

Chapter 8 CONCLUSION AND FUTURE WORK

8.1   Overview of Research

Low temperature plasma processing is an integral part of semiconductor fabrication. This dissertation investigated the plasma physics and plasma surface interactions in plasma etching chambers using a hybrid plasma equipment model to predict plasma properties and a Monte Carlo feature profile model to predict feature evolution.

Chapters 2 and 3 presented the algorithms, detailed descriptions, and fundamental physics in the Hybrid Plasma Equipment Model (HPEM) and the Monte Carlo Feature Profile Model (MCFPM). The Plasma Chemistry Monte Carlo Module in the HPEM was updated to capture the space- and phase- resolved ion sheath dynamics. The power contribution of multiple rf sources applied on the same electrode has been distinguished through computing the discrete Fourier components of the bias current. A 3-d surface advancement algorithm was developed in the MCFPM for investigating the influence of reactor scale plasma properties on complex nanoscale feature patterns.

In Chapter 4, ion dynamics were investigated in both single- and dual-frequency rf sheaths above a 300 mm diameter silicon wafer in an industrial inductively coupled plasma etching chamber. The simulated ion energy and angular distributions (IEADs) were compared with the ion velocity distribution measurements in Ar/O_2 plasma using a laser induced

fluorescence technique developed by collaborators. The IEADs on the substrate with single rf bias are found to differ dramatically at different phases. However, when the rf frequency is increased, the rf period is short than the ion sheath transit time. Therefore, ions incident onto the substrate encounter more cycles of rf periods and the phase dependency becomes weaker and finally the IEADs become independent of phase at 60 MHz. When a dual-frequency rf source is applied, the influence of the added high frequency (*HF)* needs to be taken into account. Time-averaged IEADs over one low frequency (*LF)* period show multi-peaks due to the *HF* modulation in sheath potential and sheath thickness. This *HF* modulation affects the ion sheath transition time and results in different ion response times at different phases.

In Chapters 5 and 6, control of ion energy and angular distributions in multi-frequency capacitively coupled plasmas (CCPs) are discussed. The consequences for etch profiles with different IEADs are also demonstrated. Varying relative voltages, powers and phases between multi-frequency rf sources are shown to serve as potential control mechanisms for the IEADs, and thus for the optimization of etching profiles. Increasing the voltage of the *HF* will increase the plasma density as well as shift the ion energies to higher energies. Increasing the voltage of the *LF* will mainly deposit the additional power within the sheath, and therefore, extend the width of the IEADs with little change in the composition of fluxes. Changing the power ratio between the *HF* and *LF* will also produce significant changes in the IEADs as well as plasma densities. If the *HF* power increases, the additional power will be deposited into the bulk plasma, producing a higher plasma density and thinner sheath. With the thinner sheath, the *HF* modulation of the IEADs increases. The *LF* voltage amplitude increases nearly linearly with power and produces similar energy width extension trends in the IEADs. A phase shifting technique shows great potential for controlling the IEADs and improving plasma uniformity.

Changing phases between the applied rf frequency and its second harmonic not only modifies the dc self-bias as the electrical asymmetry effects (EAE) predicts, but also changes the shape of ion energy distribution and plasma density. When phases are changed between the applied rf frequency and its higher harmonics, the EAE becomes less effective and ion energy distribution spikes at specific energies.

Chapter 7 discusses simulated profile evolutions that demonstrate the capability of the MCFPM 3-d. Phenomena such as bowing, tapering and aspect ratio dependent etching are discussed. The 3-d surface advancement algorithm is validated by comparison to experimental results. For demonstration of the MCFPM 3-d capabilities, He/Cl_2, Ar/Cl_2 and $Ar/CF_4/O_2$ plasmas are simulated for Si and SiO_2 etching in representative 3-d feature topographies. The results suggest that a long over-etch time is required to clear corners. This poses additional challenges on selectivity to maintain the critical dimensions of the features. The shape of the etched feature profiles is highly related to the ion energies and fluxes. A small change in ion angular distributions causes significant defects in the etching of certain feature patterns. With higher energy bombardment, a faster etch rate is observed. Through simulating circular vias, the mask erosion and thickness are shown to play an important role in optimizing feature profiles, as the shapes of the masks perturb particle trajectories.

The major contributions of this dissertation are:

1) Updated plasma equipment and profile models. These models provide insights into the complex physics and plasma surface interactions involved in low temperature plasma processing that may not be easily examined or studied through current experimental techniques. With the assistance of these computational models, the physical development time and manufacturing cost for developing new plasma process reactors can be reduced. A 3-d Monte Carlo feature profile model has been developed and integrated with the plasma equipment model to address the

complex feature pattern layout and to aid in the physical understanding of ion 3-d bombardment on surfaces. With this improved capability, correlation of the variability of plasma tool performance with variability of feature dimensions can be investigated.

2)   An enhanced description of ion sheath transition characteristics in multi-frequency CCPs. This description provides an understanding of multi-frequency rf sheath dynamics and suggests possible ways of controlling the complicated ion energy and angular distributions on wafers. These findings provide practical control parameters, such as adjusting phases, tuning frequencies and controlling voltage ratios, for process engineers in the microelectronics fabrication industry.

3)   Four validation sections testing the key physics reported here. Through the comparison with the actual experimental systems and measurements, the computational models are calibrated. Because computational models can never capture every detail of an experiment, the validation work shows the fundamental plasma physics and chemical reactions that need to be included in the models. Moreover, identifying mismatch between simulations and measurements helps both computational and experimental studies to improve their methodologies. For example, the mismatch of ion saturation current in DF-CCP (see Fig. 5.2 c) suggests future improvement of modeling assumptions such as including electromagnetic effects when 60 MHz power is large. On the other hand, the study of the Electric Asymmetry Effect in Chapter 6 shows the need to control or measure phase offsets in experiments.

8.2   Future Work

This dissertation has studied low temperature plasma physics and presented potential techniques for controlling ion energy angular distributions to meet the demands of highly controlled plasma processing. The following is an overview of future work that could provide further benefits in the area of low temperature plasma material processing.

1)   Inclusion of the electromagnetic effect in the presence of large high harmonics

The traditional CCP reactors typically have a 200-300 mm diameter electrode with a 1-10 cm electrode gap. If the driven frequency is below 60 MHz, the capacitive discharge is considered to operate in the electrostatic regime. The electrical characteristic of the CCPs can thus be described by Poisson's equation.[1] However, researchers have observed that the presence of higher harmonics of 60 MHz (power greater than 500 W) causes a center-peaked electron density in Ar plasma.[2] This suggests that the electromagnetic effect needs to be included in simulations when there exist large high harmonics of driving frequency greater than 40 MHz. Because the wafer sizes continue to increase, addressing this phenomenon will become necessary in the next generation plasma equipment design.

2)   Implementation of parallel computing for 3-d profile simulation

As computer processors become cheaper and more powerful, the computational plasma physics community has taken advantage of multicore computer architectures to perform parallel programming for complex or large scale simulations.[3,4] Because Monte Carlo algorithms often execute by averaging large numbers of computed values, it is logically straightforward to have multiple processors compute a certain number of pseudo-particle trajectories in the MCFPM 3-d and greatly improve the computational speed. In such algorithms, the communication between processors needs to be handled carefully to avoid numerical errors. The code parallelism can be performed either through a shared memory parallel application programming interface such as OPEN-MP[5] or a message passing interface (e.g. OPEN-MPI[6]).

3)   Investigation of high aspect ratio etching

In recent years, trough-silicon-via (TSV) etch application for 3-d integrated circuit stacking technology has been widely applied showing potential in further applications below 14 nm technology nodes. This TSV application requires etching vias in high aspect ratio with controllable profiles.[7] Moreover, microelectromechanical systems (MEMS) development requires research into plasma deep silicon etching to enable the fabrication of MEMS devices. Thus, the deep high aspect ratio etching as a special subclass of plasma ion assisted etching is growing in popularity. A typical deep etching process has two different gas compositions (SF_6 and C_4F_8) alternately injected in the reactor and is able to achieve an aspect ratio of 50.[8] The MCFPM 3-d that has been implemented in this thesis is a very powerful tool and it can be used for addressing 3-d via or any deep etching features to avoid reactive ion etching lag caused by pattern geometry[9].

8.3   References

1. Y-X. Liu, Y-R. Zhang, A. Bogaerts, and Y-N. Wang, J. Vac. Sci. Technol. A**. 33**, 020801 (2015).
2. R. R. Upadhyay, I. Sawada, P. L. G. Ventzek and L. L. Raja, J. Phys. D: Appl. Phys. **46**, 472001 (2013).
3. G. Stantchev, W. Dorland, and N. Gumerov. Journal of Parallel and Distributed Computing. 68, 1339 (2008).
4. A. Pukhov, Journal of Plasma Physics. **61**, 425 (1999).
5. Open MP: Open Multi-Processing website. Online at: http://www.openmp.org
6. Open MPI: Open Source High Performance Computing website. Online at: http://www.open-mpi.org/
7. B. Wu, A. Kumar, and S. Pamarthy, J. Appl. Phys. **108**, 051101 (2010).
8. K. J. Morton, G. Nieberg, S. Bai, and S. Y. Chou, Nanotechnology **19**, 345301 (2008).
9. C-K. Chung, J. Micromech. Microeng. **14**, 656 (2004).

Appendix A LIST OF REACTIONS OF He/Cl$_2$

Species

He	He(2^3S)	He(2^1S)	He(2^3P)	He(2^1P)	He(3s)
He(3p)	He2*	He$^+$	Cl$_2$	Cl$_2^+$	Cl$^-$
Cl	Cl$^+$	Cl*	e		

He(3p) is a lumped state of all higher states.

The reaction chemistry for He/Cl$_2$ gas mixture used in the HPEM for validation comparison is given below:

Reaction	Rate Coefficient [a]	Reference	-ΔH (eV) [a]
Radiative Transitions			
He(2^1P) ↔ He	1.8×10^9 s^{-1}	[1], b	
He(2^3P) → He(2^3S)	1.02×10^7 s^{-1}	[1]	
He(3p) → He(2^3S)	9.47×10^6 s^{-1}	[1]	
He(3p) → He(2^1S)	1.34×10^7 s^{-1}	[17]	
He(3s) → He(2^3P)	1.55×10^7 s^{-1}	[17]	
He(3s) → He(2^1P)	1.83×10^7 s^{-1}	[17]	
Electron Impact Processes			
e + He → He + e		[3]	d
e + He ↔ He(2^3S) + e	c	[3]	
e + He ↔ He(2^1S) + e	c	[3]	
e + He ↔ He(2^3P) + e	c	[3]	

237

Reaction	Rate	Ref
$e + He \leftrightarrow He(2^1P) + e$	c	[3]
$e + He \leftrightarrow He(3s) + e$	c	[3]
$e + He \leftrightarrow He(3p) + e$	c	[3]
$e + He \rightarrow He^+ + e + e$		[3]
$e + He(2^3S) \leftrightarrow He(2^1S) + e$	c	[3]
$e + He(2^3S) \leftrightarrow He(2^3P) + e$	c	[3]
$e + He(2^3S) \leftrightarrow He(2^1P) + e$	c	[3]
$e + He(2^3S) \leftrightarrow He(3s) + e$	c	[3]
$e + He(2^3S) \leftrightarrow He(3p) + e$	c	[3]
$e + He(2^3S) \rightarrow He^+ + e + e$	c	[4]
$e + He(2^1S) \leftrightarrow He(2^3P) + e$	c	[3]
$e + He(2^1S) \leftrightarrow He(2^1P) + e$	c	[3]
$e + He(2^1S) \leftrightarrow He(3s) + e$	c	[3]
$e + He(2^1S) \leftrightarrow He(3p) + e$	c	[3]
$e + He(2^1S) \rightarrow He^+ + e + e$	c	[4]
$e + He(2^3P) \leftrightarrow He(2^1P) + e$	c	[3]
$e + He(2^3P) \leftrightarrow He(3s) + e$	c	[3]
$e + He(2^3P) \leftrightarrow He(3p) + e$	c	[3]
$e + He(2^3P) \rightarrow He^+ + e + e$	c	[4]
$e + He(2^1P) \leftrightarrow He(3s) + e$	d	[3]
$e + He(2^1P) \leftrightarrow He(3p) + e$	d	[3]
$e + He(2^1P) \rightarrow He^+ + e + e$	d	[4]
$e + He(3s) \leftrightarrow He(3p) + e$	d	[3]
$e + He(3s) \rightarrow He^+ + e + e$	d	[4]
$e + He(3p) \rightarrow He^+ + e + e$	d	[4]
$e + e + He^+ \rightarrow He(2^3S) + e$	$2.69 \times 10^{-26} \, T_n^{-4}$	[5],[6]

Reaction	Rate	Ref.	
$e + He^+ \rightarrow He(2^3S)$	$6.76 \times 10^{-13} T_n^{-1/2}$	[7]	
$e + He^+ + He \rightarrow He(2^3S) + He$	$1.20 \times 10^{-33} T_n^{-4}$	[7]	
$e + He_2^+ \rightarrow He(2^3S) + He$	$1.6 \times 10^{-9} T_n^{-1/2}$	[8]	
$e + e + He_2^+ \rightarrow He(2^3S) + He + e$	$4.5 \times 10^{-25} T_n^{-1/2}$	[5],[6]	
$e + e + He_2^+ \rightarrow He_2^* + e$	$1.35 \times 10^{-26} T_n^{-4}$	[5],[6]	
$e + He_2^+ + He \rightarrow He(2^3S) + He + He$	$1.29 \times 10^{-28} T_n^{-1}$	[5],[6]	
$e + He_2^* \rightarrow He + He + e$	3.8×10^{-9}	[9]	

Heavy Particle Processes

Reaction	Rate	Ref.	
$He^+ + He \rightarrow He^+ + He$	6.08×10^{-10}	[10]	e
$He^* + He^* \rightarrow He^+ + He + e$	$4.5 \times 10^{-10} T_n^{1/2}$	[5],[6], f	
$He^* + He^* \rightarrow He_2^+ + e$	$1.05 \times 10^{-9} T_n^{1/2}$	[5],[6], f	
$He^* + He_2^* \rightarrow He^+ + He + He + e$	$2.25 \times 10^{-11} T_n^{1/2}$	[5],[6], f	
$He^* + He_2^* \rightarrow He_2^+ + He + e$	$1.28 \times 10^{-10} T_n^{1/2}$	[5],[6], f	
$He_2^* + He_2^* \rightarrow He^+ + 3He + e$	$2.25 \times 10^{-11} T_n^{1/2}$	[5],[6]	
$He_2^* + He_2^* \rightarrow He_2^+ + 2He + e$	$1.28 \times 10^{-10} T_n^{1/2}$	[5],[6]	
$He^+ + He + He \rightarrow He_2^+ + He$	$1.10 \times 10^{-31} T_n^{-0.38}$ $cm^6 s^{-1}$	[11]	
$He^* + He + He \rightarrow He_2^* + He$	$2 \times 10^{-34} cm^6 s^{-1}$	[6],[12], f	
$He + He_2^* \rightarrow He + He + He$	1.5×10^{-15}	[13]	

Cl$_2$ only Reactions

Reaction	Rate	Ref.
$e + Cl_2 \rightarrow Cl + Cl^-$	h	[14]
$e + Cl_2 \rightarrow Cl + Cl + e$	h	[14]
$e + Cl_2 \rightarrow Cl_2^+ + e + e$	h	[14]
$e + Cl \rightarrow Cl^* + e$	h	[14]
$e + Cl \rightarrow Cl^+ + e + e$	h	[14]
$e + Cl^* \rightarrow Cl^+ + e + e$	h	[14]
$Cl^* \rightarrow Cl$	$1 \times 10^5 \ s^{-1}$	g

$e + Cl^- \rightarrow Cl + e + e$	h	[14]
$e + Cl_2^+ \rightarrow Cl + Cl$	$1 \times 10^{-7} T_e^{-0.5}$	g
$Cl^- + Cl^+ \rightarrow Cl + Cl$	1×10^{-7}	g
$Cl^- + Cl_2^+ \rightarrow Cl + Cl + Cl$	1×10^{-7}	g
$Cl + Cl + Cl \rightarrow Cl_2 + Cl$	1.28×10^{-32} cm^{6}s^{-1}	[15]
$Cl + Cl + Cl_2 \rightarrow Cl_2 + Cl_2$	1.28×10^{-32} cm^{6}s^{-1}	[15]
$Cl^+ + Cl_2 \rightarrow Cl_2^+ + Cl$	5.4×10^{-10}	[16]g
$Cl^+ + Cl \rightarrow Cl + Cl^+$	1×10^{-9}	g
$Cl_2^+ + Cl_2 \rightarrow Cl_2 + Cl_2^+$	8×10^{-10}	g

Cl$_2$ and He Heavy Particle Processes

$He(2^3S) + Cl \rightarrow Cl^+ + He + e$	6.75×10^{-10} e$^{-684/Tg}$	[17]
$He(2^3S) + Cl^* \rightarrow Cl^+ + He + e$	6.75×10^{-10} e$^{-684/Tg}$	[17]
$He(2^3S) + Cl_2 \rightarrow Cl_2^+ + He + e$	1.0×10^{-9} e$^{-684/Tg}$	[17]
$He(2^1S) + Cl \rightarrow Cl^+ + He + e$	2.07×10^{-9} e$^{-684/Tg}$	[17],[18]
$He(2^1S) + Cl^* \rightarrow Cl^+ + He + e$	2.07×10^{-9} e$^{-684/Tg}$	[17],[18]
$He(2^1S) + Cl_2 \rightarrow Cl_2^+ + He + e$	4.0×10^{-9} e$^{-684/Tg}$	[17],[18]
$He(2^3P) + Cl \rightarrow Cl^+ + He + e$	2.07×10^{-9} e$^{-684/Tg}$	[17],[18]
$He(2^3P) + Cl^* \rightarrow Cl^+ + He + e$	2.07×10^{-9} e$^{-684/Tg}$	[17],[18]
$He(2^3P) + Cl_2 \rightarrow Cl_2^+ + He + e$	4.0×10^{-9} e$^{-684/Tg}$	[17],[18]
$He(2^1P) + Cl \rightarrow Cl^+ + He + e$	2.07×10^{-9} e$^{-684/Tg}$	[17],[18]
$He(2^1P) + Cl^* \rightarrow Cl^+ + He + e$	2.07×10^{-9} e$^{-684/Tg}$	[17],[18]
$He(2^1P) + Cl_2 \rightarrow Cl_2^+ + He + e$	4.0×10^{-9} e$^{-684/Tg}$	[17],[18]
$He(3s) + Cl \rightarrow Cl^+ + He + e$	2.07×10^{-9} e$^{-684/Tg}$	[17],[18]
$He(3s) + Cl^* \rightarrow Cl^+ + He + e$	2.07×10^{-9} e$^{-684/Tg}$	[17],[18]
$He(3s) + Cl_2 \rightarrow Cl_2^+ + He + e$	4.0×10^{-9} e$^{-684/Tg}$	[17],[18]
$He(3p) + Cl \rightarrow Cl^+ + He + e$	2.07×10^{-9} e$^{-684/Tg}$	[17],[18]

$He(3p) + Cl^* \rightarrow Cl^+ + He + e$	$2.07 \times 10^{-9} e^{-684/Tg}$	[17],[18]
$He(3p) + Cl_2 \rightarrow Cl_2^+ + He + e$	$4.0 \times 10^{-9} e^{-684/Tg}$	[17],[18]
$He^+ + Cl \rightarrow Cl^+ + He$	$5 \times 10^{-14} T_n^{1/2}$	[19],[20]
$He^+ + Cl^* \rightarrow Cl^+ + He$	$5 \times 10^{-14} T_n^{1/2}$	[19],[20]
$He^+ + Cl_2 \rightarrow Cl_2^+ + He$ lo	$1 \times 10^{-13} T_n^{1/2}$	[19],[20]

He mixing by Cl

$He(2^1S) + Cl \rightarrow He(2^3S) + Cl$	1.0×10^{-12}	g
$He(2^3P) + Cl \rightarrow He(2^3S) + Cl$	1.0×10^{-13}	g

He mixing by Cl_2

$He(2^1S) + Cl_2 \rightarrow He(2^3S) + Cl_2$	1.0×10^{-12}	g
$He(2^3P) + Cl_2 \rightarrow He(2^3S) + Cl_2$	1.0×10^{-13}	g

---

[a] Rate coefficients have units of cm^3-s^{-1} unless noted otherwise. T_e is electron temperature (eV). T_g is gas temperature (K), T_n is normalized gas temperature (T_g/300 K). -ΔH is the contribution to gas heating (eV).

[b] Rate shown is for emission. Absorption is addressed using a radiation trapping factor.

[c] Cross section is for forward reaction. Reverse cross section obtained by detailed balance.

[d] The rate of heating by elastic collisions is $k_m(3/2)k_B(2m_e/M)(T_e-T_g)$ eV-cm^3/s, for elastic rate coefficient k_m, electron mass m_e, neutral mass M and Boltzmann's constant k_B.

[e] The rate of gas heating of the neutral by charge exchange is $k_{ce}(3/2)k_B(T_{ion}-T_g)$ eV-cm^3/s, for charge exchange rate coefficient k_{ce} and ion temperature T_{ion}.

[f] He* represents any He excited state.

[g] Estimated.

[h] Rate coefficients are calculated from electron energy distribution obtained in the eMCS. T_e is the electron temperature (eV).

A.1 References

1. NIST Atomic Specular Database, Version 5, http://www.nist.gov/pml/data/asd.cfm.

2. M. Ohwa, T. J. Moratz and M. J. Kushner, J. Appl. Phys, **66**, 5131 (1989).

3. Biagi-v8.9 Database, www.lxcat.net, retrieved on July 2, 2012.

4. L. Vriens, Phys. Lett. **8**, 260 (1964).

5. R. Deloche, P. Monchicourt, M. Cheret, and F. Lambert, Phys. Rev. A **13**, 1140 (1976).

6. K. Niemi, J. Waskoenig, N. Sadeghi, T. Gans, and D O'Connell, Plasma Sources Sci. Technol. **20**, 055005 (2011).

7. M. A. Biondi, Chap.4, in "*Principles of Laser Plasmas*" ed. G. Bekefi (Wiley, New York, 1976).

8. A. W. Johnson, and J. B. Gerardo, Phys. Rev. A **5**, 1410 (1972).

9. R. Deloche, P. Monchicourt, M. Cheret, and F. Lambert, Phys. Rev. A **13**, 1140 (1976).

10. Atomic Data and Nuclear Data Tables, Vol. 17, No. 3 (1976)

11. R. Johnsen, A. Chen, and M. A. Biondi, J. Chem. Phys. **73**, 1717 (1980).

12. F. Emmert, H. H. Angermann, R. Dux, and H. Langhoff, J. Phys. D **21**, 667 (1988).

13. T. J. Miller, P. R. A. Farquhar, and K. Willacy, Astron. Astrophys. Suppl. Ser. **121** 139 (1997).

14. G. L. Rogoff, J. M. Kramer, and R. B. Piejak, IEEE Trans. Plasma Sci. 14, 103 (1986).

15. Y. Ikezoe, S. Matsuoka, M. Takabe, and A. Viggiano, "*Gas Phase Ion-Molecule Reaction Rate Constants Through 1986*", Ion Reaction Research Group, Tokyo, Japan (1987).

16. NIST Chemical Kinetics Database 17, Version 2Q98, http:// kinetics.nist.gov/index.php

17. W. Lindinger, A. L. Schmeltekopf and F. C. Fehsenfeld, J. Chem. Phys. **61**, 2890 (1974).

18. A. L. Schmeltekopf and F. c. Fehsenfeld, J. Chem. Phys. **53**, 3173 (1970).

19. J. D. C. Jones, D. G. Lister and N. D. Twiddy, J. Phys. B.**12**, 2723 (1979).

20. A. Bogaerts and R. Gijbels, J. Appl. Phys. **86,** 4124 (1999).

Appendix B Si ETCHING IN He/Cl$_2$: SURFACE REACTION MECHANISM

The main surface reactions for polysilicon etch mechanism with He/Cl$_2$ used in the present study is given below and the probability is estimated based on the previous work [1-5] of Cl$_2$ etching silicon.

Species definitions:

X   Gas phase species

X(s)   Surface site

Reaction[a,b,c]	Probability	Footnote
Formation of passivation layer:	p_0	
Cl + Si(s) → SiCl(s)	0.99	
Cl + SiCl(s) → SiCl$_2$(s)	0.6	
Cl + SiCl$_2$(s) → SiCl$_3$(s)	0.5	
Formation of etch blocks:		
Cl + SiCl$_3$(s) → SiCl$_4$	0.001	
Cl* + Si(s) → SiCl	0.001	
Cl* + SiCl (s) → SiCl$_2$	0.2	d
Cl* + SiCl$_2$(s) → SiCl$_2$ + Cl*	0.5	d
Cl* + SiCl$_3$(s) → SiCl$_3$ + Cl*	0.5	d

Reaction	Value	
$Cl^+ + Si(s) \rightarrow SiCl$	0.002	
$Cl^+ + SiCl(s) \rightarrow SiCl_2$	0.3	d
$Cl^+ + SiCl_2(s) \rightarrow SiCl_2 + Cl^*$	0.6	d
$Cl^+ + SiCl_3(s) \rightarrow SiCl_3 + Cl^*$	0.6	d
$Cl_2^* + Si(s) \rightarrow SiCl_2$	0.001	
$Cl_2^* + SiCl(s) \rightarrow SiCl + Cl_2^*$	0.2	d
$Cl_2^* + SiCl_2(s) \rightarrow SiCl_2 + Cl_2^*$	0.25	d
$Cl_2^* + SiCl_2(s) \rightarrow SiCl_3 + Cl^*$	0.25	d
$Cl_2^* + SiCl_3(s) \rightarrow SiCl_3 + Cl_2^*$	0.25	d
$Cl_2^* + SiCl_3(s) \rightarrow SiCl_4 + Cl^*$	0.25	d
$Cl_2^+ + Si(s) \rightarrow SiCl_2$	0.005	
$Cl_2^+ + SiCl(s) \rightarrow SiCl + Cl_2^*$	0.3	d
$Cl_2^+ + SiCl_2(s) \rightarrow SiCl_2 + Cl_2^*$	0.3	d
$Cl_2^+ + SiCl_2(s) \rightarrow SiCl_3 + Cl^*$	0.3	d
$Cl_2^+ + SiCl_3(s) \rightarrow SiCl_3 + Cl_2^*$	0.3	d
$Cl_2^+ + SiCl_3(s) \rightarrow SiCl_4 + Cl^*$	0.3	d
$He^* + SiCl(s) \rightarrow SiCl + He$	0.2	d
$He^* + SiCl_2(s) \rightarrow SiCl_2 + He$	0.5	d
$He^* + SiCl_3(s) \rightarrow SiCl_3 + He$	0.5	d
$He^+ + SiCl_2(s) \rightarrow SiCl + He$	0.2	d
$He^+ + SiCl_2(s) \rightarrow SiCl_2 + He$	0.5	d
$He^+ + SiCl_3(s) \rightarrow SiCl_3 + He$	0.5	d

Consumption of passivation layer

Reaction	Value
$Cl + SiCl_2(s) \rightarrow SiCl(s) + Cl_2$	0.02
$Cl + SiCl_3(s) \rightarrow SiCl_2(s) + Cl_2$	0.08
$Cl + Si_2Cl_2(s) \rightarrow SiCl(s) + SiCl_2$	0.008
$Cl + Si_2Cl_3(s) \rightarrow SiCl(s) + SiCl_2 + Cl$	0.008
$Cl + Si_2Cl_4(s) \rightarrow SiCl_2(s) + SiCl_2 + Cl$	0.008
$Cl^* + Si_2Cl_2(s) \rightarrow Si(s) + SiCl_2 + Cl$	0.8
$Cl^* + Si_2Cl_2(s) \rightarrow Si_2Cl_2(s) + Cl$	0.2
$Cl^* + Si_2Cl_3(s) \rightarrow SiCl(s) + SiCl_2 + Cl$	0.9
$Cl^* + Si_2Cl_3(s) \rightarrow Si_2Cl_3(s) + Cl$	0.1
$Cl^* + Si_2Cl_4(s) \rightarrow SiCl_2(s) + SiCl_2 + Cl$	0.9
$Cl^* + Si_2Cl_4(s) \rightarrow Si_2Cl_4(s) + Cl$	0.1
$Cl^+ + Si_2Cl_2(s) \rightarrow Si(s) + SiCl_2 + Cl$	0.9
$Cl^+ + Si_2Cl_3(s) \rightarrow SiCl(s) + SiCl_2 + Cl$	0.99
$Cl^+ + Si_2Cl_4(s) \rightarrow SiCl_2(s) + SiCl_2 + Cl$	0.99
$Cl_2^+ + SiCl_3(s) \rightarrow SiCl_3(s)_+ Cl_2$	0.4
$Cl_2^+ + Si_2Cl_2(s) \rightarrow Si(s) + SiCl_2 + Cl_2$	0.6
$Cl_2^+ + Si_2Cl_2(s) \rightarrow Si_2Cl_2(s)_+ Cl_2$	0.4
$Cl_2^+ + Si_2Cl_3(s) \rightarrow SiCl(s) + SiCl_2 + Cl_2$	0.6
$Cl_2^+ + Si_2Cl_3(s) \rightarrow Si_2Cl_3(s)_+ Cl_2$	0.4
$Cl_2^+ + Si_2Cl_4(s) \rightarrow SiCl_2(s) + SiCl_2 + Cl_2$	0.6
$Cl_2^+ + Si_2Cl_4(s) \rightarrow Si_2Cl_4(s)_+ Cl_2$	0.4
$He^* + Si_2Cl_2(s) \rightarrow Si(s) + SiCl_2 + He$	0.8
$He^* + Si_2Cl_3(s) \rightarrow SiCl(s) + SiCl_2 + He$	0.9
$He^* + Si_2Cl_4(s) \rightarrow SiCl_2(s) + SiCl_2 + He$	0.9

$He^+ + Si_2Cl_2(s) \rightarrow Si(s) + SiCl_2 + He$	0.9	
$He^+ + Si_2Cl_3(s) \rightarrow SiCl(s) + SiCl_2 + He$	0.99	
$He^+ + Si_2Cl_4(s) \rightarrow SiCl_2(s) + SiCl_2 + He$	0.99	

Deposition Mechanism (Source of Si_2Cl_n)

$SiCl + Si(s) \rightarrow SiCl(s) + Si(s)$	0.15	
$SiCl + SiCl(s) \rightarrow SiCl(s) + SiCl(s)$	0.15	
$SiCl + SiCl_2(s) \rightarrow SiCl(s) + SiCl_2(s)$	0.15	
$SiCl + SiCl_3(s) \rightarrow SiCl(s) + SiCl_3(s)$	0.15	
$SiCl_2 + Si(s) \rightarrow Si_2Cl_2(s)$	0.6	
$SiCl_2 + SiCl(s) \rightarrow Si_2Cl_3(s)$	0.6	
$SiCl_2 + SiCl_2(s) \rightarrow Si_2Cl_4(s)$	0.6	
$SiCl_2 + SiCl_3(s) \rightarrow SiCl_3(s) + SiCl_2(s)$	0.01	
$SiCl_2^+ + Si(s) \rightarrow Si_2Cl_2 + Si(s)$	0.5	d
$SiCl_2^+ + SiCl(s) \rightarrow Si_2Cl_3(s)$	0.5	d
$SiCl_2^+ + SiCl_2(s) \rightarrow Si_2Cl_4(s)$	0.5	d
$SiCl_2^+ + Si_2Cl_2(s) \rightarrow Si_2Cl_2(s) + SiCl_2(s)$	0.15	
$SiCl_2^+ + Si_2Cl_3(s) \rightarrow Si_2Cl_3(s) + SiCl_2(s)$	0.15	
$SiCl_2^+ + Si_2Cl_4(s) \rightarrow Si_2Cl_4(s) + SiCl_2(s)$	0.15	

Mask Resist Erosion:

$He^+ + Resist(s) \rightarrow Resist + He^*$	0.15	e
$He^* + Resist(s) \rightarrow Resist + He^*$	0.15	e
$Cl^+ + Resist(s) \rightarrow Resist + Cl*$	0.15	e
$Cl^* + Resist(s) \rightarrow Resist + Cl*$	0.15	e

Cl_2^+ + Resist(s) → Resist+ Cl_2*	0.15	e
Cl_2^* + Resist(s) → Resist+ Cl_2*	0.15	e

Resist Re-deposition

Si(s) + Resist→ Si(s) + Resist(s)	0.2
SiCl(s) + Resist→ SiCl(s) + Resist(s)	0.2
$SiCl_2$(s) + Resist→ $SiCl_2$(s) + Resist(s)	0.2
$SiCl_3$(s) + Resist→ $SiCl_3$(s) + Resist(s)	0.2

[a] Unless otherwise specified, all ions neutralize on surfaces, returning as their neutral counterparts.

[b] All gas phase species have units of flux ($cm^{-2}.s^{-1}$). All surface species have units of fractional coverage.

[c] In reactions with no chemical change, the gas species are reflected off the surface. These reactions are not shown in the table.

[d] The reaction probability κ is calculated by

If $\varepsilon_{incident} > \varepsilon_{th}$,
$$\kappa = \frac{p_0 \cdot (\varepsilon_{incident} - \varepsilon_{th})^{0.5}}{(\varepsilon_{ref} - \varepsilon_{th})^{0.5} \cdot f_{angle}} \quad ; \text{else } \kappa = 0.$$

where ε_{th}=16 eV and ε_{ref}=100 eV.

[e] Use the equation in d, with ε_{th}=15 eV and ε_{ref}=100 eV.

B.1   References

1. R. J. Hoekstra, M. J. Grapperhaus and M. J. Kushner, J. Vac. Sci. Technol. A. **15**, 1913 (1997).

2. A. Agarwal and M. J. Kushner, J. Vac. Sci. Technol. A. **26**, 498 (2008).

3. C. C. Cheng, K. V. Guinn, V. M. Donnelly, and I. P. Herman, J. Vac. Sci. Technol. A. **12**, 2630 (1994).

4. G. Cunge, M. Kogelschatz, O. Joubert and N. Sakeghi, Plasma Sources Sci. Technol. **14**, s42 (2005).

5. E. Meeks and J. W. Shon, IEEE Trans. Plasma Sci. **23**, 539 (1995).